# SUPPORTED TRANSITION METAL-BASED ELECTROCATALYSTS FOR ETHYLENE GLYCOL FUEL CELL

A Thesis

submitted in partial fulfilment of the requirements for the degree of

**Doctorate of Philosophy**

*by*

**SAPTARSHI GUPTA**

**(156151013)**

**School of Energy Science and Engineering**
**Indian Institute of Technology Guwahati**
**Guwahati-781039, Assam, India**

**January 2025**


# Dedicated to the Society

**INDIAN INSTITUTE OF TECHNOLOGY GUWAHATI**

**School of Energy Science and Engineering**

**Assam, Guwahati-781039**

# DECLARATION

I do hereby declare that the research findings in this thesis is the result of research work carried out by me in the School of Energy Science and Engineering, Indian Institute of Technology Guwahati, India, under the supervision of **Prof Mahuya De.**

I also declare that the contents of this thesis have not been the basis for award of any other degree, diploma, fellowship or any other similar title of any other University or Institution.

As per general norms of reporting research findings, due acknowledgments have been made, whenever findings of other researchers have been cited in this thesis.

Date:

Place: IIT Guwahati

**Saptarshi Gupta**

**INDIAN INSTITUTE OF TECHNOLOGY GUWAHATI**

**School of Energy Science and Engineering**

**Assam, Guwahati-781039**

# CERTIFICATE

This is to certify that the work described in the thesis entitled **"Supported Transition Metal-Based Electrocatalysts for Ethylene Glycol Fuel Cell**" is an authentic record of the results obtained from the research work carried out by **Saptarshi Gupta** in the School of Energy Science and Engineering, Indian Institute of Technology Guwahati, Assam, India, under my supervision and this work in part or as a whole has not been submitted elsewhere for the award of any other degree.

Date:

Place: IIT Guwahati

**Prof. Mahuya De**

(Thesis Supervisor)

# ACKNOWLEDGMENTS

*The PhD journey at IIT Guwahati has been an incredible life-altering experience. While writing this acknowledgment, I am experiencing déjà vu as if I'm revisiting the last eight years filled with delightful memories and invaluable moments of joy and tears, relentless hours of conducting experiments and publishing papers. This would have been impossible without the support, love, and encouragement of many individuals. I'm elated to convey my deepest gratitude to everybody who, voluntarily or involuntarily, supported and helped me over this notable voyage in my life.*

*First and foremost, I want to express my sincere gratitude and regards for my PhD supervisor,* ***Prof. Mahuya De.*** *I am grateful to her for all the technical guidance and knowledge, intuitive discussions and ideas, continuous support, and tolerance throughout my PhD journey. I thank her for providing the best possible resources and building a wonderful lab atmosphere to discuss and exchange numerous research ideas. She has encouraged me to work independently as a researcher and has always stimulated me to deliver my best. Her inquisitiveness for science, as well as her aptitude to multitask precisely and consistently, has motivated me to work hard. Her thorough editing was exceptionally helpful to complete this thesis. I am privileged to have a supervisor who nurtured me, and my work. Thank you so much for everything, Madam!!*

*I would also like to extend my sincere thanks to the doctoral committee members:* ***Prof. V.V. Goud, Dr. Prasanna R. Venkatesh and Dr. Shyam Prosad Biswas*** *for their constructive criticism and critical suggestions which helped me to cultivate a broader perception on my thesis. They have also generously invested their time to deliver me with constructive opinion on my work. I would also like to thank faculty members of Department of Chemical Engineering as well as School of Energy Science and Engineering for their valuable insights and encouragement towards my research.*

*I am grateful to the former and current heads of the School of Energy Science and Engineering,* ***Prof. Pranab Goswami, Prof. V. S. Mohalkar, Prof. Kaustabha Mohanty and Prof. V.V. Goud*** *for their support in providing all the departmental facilities during their tenure.*

*I also thank the School of Energy Science and Engineering, Department of Chemical Engineering, Central Instrumentation Facility, IIT Guwahati and the institute as a whole for providing the infrastructural resources needed to conduct my research. My deepest appreciation for the assistance provided by the office staff members especially* ***Dr. Lepakshi Barbora, Mr. Debarshi Baruah, Mr. Dhiren Huzuri, Mrs. Rashmi Baruah, Mr. Pranjal Bhuyan, Mr. Paragjyoti Sharma, Mr. Harsaraj Biswanath, Mr. Prasun Kumar Bhattacharjee, Mr. Ariful Hoque, Mr. Chandan Borgohain, Mr. Deep Manoram Baruah, Mr. Sujit Kumar Deb*** *and* ***Mr. Madhurjya Borah****. I am grateful for their continuous support.*

*I would like to thank the Ministry of Human Resource Development (MHRD), India and Indian Institute of Technology Guwahati for their financial support during my PhD tenure.*

*I'm in debt to all the former and current members of the Catalysis, Environment and Energy Research Lab family of which I have been a member for over eight years now. I thank my fellow lab-mates for the exciting discussions and for all the fun we had in the lab. I would like to thank my seniors* ***Dr. Ruhit Jyoti Kunwar, Dr. Sohan Bir Singh*** *and* ***Dr. Rishabh Saxena*** *for sharing their experience and knowledge with me. They helped me to learn new and exciting things about research and Ph.D life. I would like to thank my juniors* ***Yeshwanth, Rahul, Nilesh, Ankita, Ramanuj, Shubham*** *and* ***Arnab*** *for being constant sources of encouragement and help. A special thanks to* ***Shweta****, who without any hesitation and explanation always helped me in numerous ways throughout the journey and hence deserve a separate mention. Thanks to all the M.Tech and B.Tech students who was part of our lab, as mentoring them, I learned and developed insights about new field of research.*

*Apart from my lab members, I would also like to convey my appreciation towards seniors, friends and juniors associated with IIT Guwahati. Their support and assistance towards research as well as in my life made an impact which helped me to overcome many obstacles in day to day life in IIT Guwahati. My earnest gratitude* ***to Dr. Ashim Malakar, Dr. Anivash Kumar, Dr. Rupak Kishore, Dr. Satyannarayana Edubilli, Dr. Nilanjan Mondal, Dr. Atanu Kumar Paul, Dr. Mood Mohan, Dr. Robinson Timung. Dr. Pradip Das, Dr. Nabendu Paul, Dr. Rupam Sinha, Dr. Bitang Tripura, Dr. Barnali Bhui, Dr. Piyal Mondal, Dr. Subhajit Sanfui, Mr. Amritava Sarkar, Dr. Dipojjwal Ray, Dr. Aritra Mukherjee, Dr. Anirban Sikdar, Dr. Md. G Abdul Quadir, Dr. BhaskarJyoti Choudhury, Dr. Sutapa Das, Dr. Surabhi Patel, Dr. Jenasree Hazarika, Dr. Shibani Gupta, Milan Mahadani, Rupak Bhowmik,*** *and* ***Sumantra Choudhury*** *for being in my life.*

*The Ph.D journey would have not been possible without the motivation of* ***Dr. Srimanta Ray****, who moulded me towards research during my undergraduate days. His insights towards research inspired me to continue my career as researcher. A tribute to all my teachers, who helped me to develop the fundamentals in science and engineering and hence provide me the platform to conduct research.*

*I would also like to thank my school friends* ***Dr. Prajjal Dey and Dr. Ankita Mazumder****, who shared the journey with me, as they also completed the Ph.D degree in different fields in the similar timeline. They are always being my best buddies who cared for me during the toughest period of my life.*

*This degree would not have been possible without the continuous support, love and encouragement of* ***Dr. Rachayeeta Deb****, who was always beside me through the ups and down of my Ph.D career. Her relentless support and advice towards professional as well as personal growth made this journey look easier. You deserve a special mention.*

*Last but not least, I would like to convey my deepest regards to my **parents and family** for their unconditional support. From childhood, they were the support system and always backed me in doing things I wanted to perceive. Their relentless effort has made me who I am today and encouraged me to accomplish my dreams and goals. I am confident that nothing can ever go wrong for me because I am always protected by your blessings. I am strong because of your understanding and belief in me. Without you, I never would have progressed this far. All of you have contributed greatly to this, and this PhD is equally yours and mine.*

**Saptarshi Gupta**

# ABSTRACT

The expansion of economy and industry has made energy an integral part of daily life. The demand for energy generation is continuously increasing due to population growth and rapid development. There is an ongoing need for energy generation because of population growth and rapid development. The increasing consumption of fossil fuels led to their depletion at an alarming rate, thereby necessitating the quest for a new alternative *i.e.* complementary renewable energy sources. The most promising alternative for the generation of clean energy is the fuel cell (FC) owing to its additional benefits, which include increased efficiency, fuel selection flexibility, minimal carbon emissions, and a wide operating temperature range.

Fuel cell (FC) is a competent clean fuel technology where chemical energy generated during electrochemical reactions is directly converted to electrical energy. Among the different types of fuel cell, the direct alcohol fuel cell (DAFC) uses alcohol as the feed and oxygen serves as the oxidant. Monohydric alcohols like ethanol and methanol have been widely investigated as electrocatalysts for DAFC. However, polyhydric or higher order alcohols such as ethylene glycol (EG) can also be employed as an alternative since they have a higher volumetric energy density, are less flammable and have lower toxicity than ethanol and methanol. Research on the electro-oxidation of monohydric alcohols has primarily concentrated on the use of noble metals such as platinum (Pt), palladium (Pd), ruthenium (Ru), rhodium (Rh), silver (Ag), gold (Au), and iridium (Ir) as electrocatalysts. But a significant increase in current generation was observed when noble metal catalysts were utilised to oxidise polyhydric alcohol EG as compared to monohydric alcohols. Despite this, the noble metals also have disadvantages, such as sluggish oxidation kinetics due to carbon monoxide (CO) poisoning and a high cost. As a result, the focus shifted to the utilization of low-cost non-noble transition metals like nickel (Ni), cobalt (Co), copper (Cu), iron (Fe), molybdenum (Mo), manganese (Mn) and lead (Pb), which provide resistance to CO poisoning, thereby, improving the performance of electrocatalysts. However, the electro-oxidation of polyhydric alcohols using low cost transition metal-based catalysts with a systematic screening of different supports is still under investigation. Thus, our study aimed to conduct a comprehensive analysis of the electro-oxidation of polyhydric alcohols with several cost-effective transition metal-based catalysts and various supports that affects the energy output of the fuel cell.

Carbon-based supports namely activated carbon (AC), reduced graphene oxide (RGO), alumina -based templated carbon (ALS-TC) and vulcan carbon (VC), were employed in this study owing to their high surface area, good conductivity, availability and low cost. Transition

metals such as Cu, Ni, Co and Fe were chosen due to their reported excellent performance in the oxidation of lower alcohols. The effect of different support as well as different transition metal was compared for electro-oxidation of EG. To investigate the effect of metal loading, the most active transition metal was selected for the electro-oxidation of EG. The electro-oxidation was also performed using optimized loaded supported metal bimetallic catalysts. Furthermore, the effect of several process parameters such as temperature, varying concentrations of EG and KOH on the electro-oxidation of EG was investigated. Moreover, the efficacy of the best bimetallic catalyst was also studied for other polyhydric alcohol. Lastly, the fuel cell study was conducted with the same catalyst to understand it's behaviour for commercial application. The electrocatalysts were prepared by wetness impregnation technique and then subjected to thermal reduction in a hydrogen environment. The physical properties of the electrocatalysts was determined using surface area and pore analysis, X-ray diffraction (XRD), energy dispersive X-ray spectroscopy (EDX), field emission scanning electron microscopy (FESEM), field emission transmission electron microscopy (FETEM), X-ray photoelectron spectroscopy (XPS) and kelvin probe force microscopy (KPFM). Cyclic voltammetry (CV), chronoamperometry (CA) and electrochemical impedance spectroscopy (EIS) were used to assess the electrochemical characteristics in the presence or absence of EG.

The effect of various supports on the electro-oxidation of EG was first investigated with Cu as the active metal. The CV spectra of the supported Cu catalysts were compared in acidic and basic media. In acidic medium, the highest current density of 5.61 $mA/cm^2$ was generated by 20Cu-RGO, followed by 20Cu-VC (2.59 $mA/cm^2$). The current density in basic medium was as follows: 20Cu-ALS-TC (0.73 $mA/cm^2$) < 20Cu-AC (1.23 $mA/cm^2$) < 20Cu-VC (1.61 $mA/cm^2$) < 20Cu-RGO (2.78 $mA/cm^2$). The mass activity of 20Cu-RGO was 47.8 $mA/mg_{Cu}$ and 23.7 $mA/mg_{Cu}$ in acidic and basic media, respectively. The superior performance of 20Cu-RGO over other catalysts was attributed to its higher electrochemical surface area (ECSA), larger pore size and improved metal dispersion. EIS studies revealed that electrochemical reaction was a slower process than the charge transfer process, which was confirmed by the fact that the time constant for the electrochemical process was much higher than that of the charge transfer process for all catalysts. The presence of more oxygen-containing functional groups and a high work function were found to play an important role in the best performance of 20Cu-RGO. High work function and the presence of more oxygen-containing functional groups contributed significantly to the optimal performance of 20Cu-RGO.

The various transition metal (Cu, Ni, Co, or Fe)-based catalysts were then evaluated with low-cost commercial activated carbon (AC) support. The supported metal catalysts

outperformed individual components in the electro-oxidation of EG. The physical surface area of the catalysts varied between 379 to 615 $m^2/g$, whereas the ECSA ranged from 20.8 to 44.3 $m^2/g$. The average metal size ranged between 7.8 and 16.3 nm, validating the nano-metal structure. KPFM images showed variations in surface charge. The corresponding work function values of several electrocatalysts varied between 4.21 to 4.56 eV. The electrochemical activity was assessed in both acidic and basic environments, with and without EG. In the presence of EG, 20Ni-AC generated the maximum current density of 7.62 $mA/cm^2$ at 0.49 V and 11 $mA/cm^2$ at 1 V in acidic and basic media, respectively. Thus, in the presence of EG, Ni-AC with the highest specific ECSA (44.3 $m^2/g$) produced the maximum current density in all media. Work function values and the ability to form higher metal oxidation states also had a significant effect on the electrochemical performance of the catalysts. Time constants obtained from EIS analysis revealed that electrochemical process was slower in both medium.

The performance of various transition metals (Cu, Ni, Fe, and Co) for EG electro-oxidation was then evaluated on the most active support RGO. CV studies revealed that 20Ni-RGO exhibited the highest current density of 86 $mA/mg_m$, followed by 20Cu-RGO (61 $mA/mg_m$), 20Co-RGO (54 $mA/mg_m$) and 20Fe-RGO (39 $mA/mg_m$). The trend of the obtained current density was consistent with the increasing electrochemical surface area and decreasing Tafel slope. The charge transfer co-efficient also supported the observed current density trend. EIS analysis showed that electrochemical process was the slowest process for all the catalysts, which makes it the rate determining process. The time constants observed for electrochemical reaction in the electrocatalysts were inversely related to their average pore size.

In addition, the effect of metal loading in the range of 20 to 40 wt.% was examined in order to determine the best performing monometallic catalyst. The current density of Ni-RGO varied with the percentage of nickel loading. In the presence of EG, the current density increased to 102 and 106 $mA/mg_m$ for Ni loadings of 30 and 40%, respectively. At 30 and 40 wt.% Ni loading, EG exhibited Warburg resistance in EIS analysis due to its reduced surface area. Since, the enhancement in current density was minimal upon increasing the metal wt % from 30 to 40, hence, 30 wt.% was determined to be the most effective metal loading. As a result, detailed electrochemical analysis was performed to determine the surface coverage of redox species, diffusion coefficient of ethylene glycol molecule and mean electrocatalytic rate constant for 30Ni-RGO, which were $2.7\times10^{-8}$ $mol/cm^2$, $2.35 \times 10^{-5}$ to $2.35 \times 10^{-8}$ $cm^2/s$ and $1.48 \times 10^4$ $cm^3/mol.s$ respectively. Further analysis revealed that the electro-oxidation of EG

over 30Ni-RGO followed an electrochemical-chemical mechanism controlled by diffusion and accordingly a reaction mechanism for EG oxidation was postulated.

Ni was observed to be the most active metal with RGO as a support, hence Ni-based bimetallic catalysts were developed with Co, Cu and Fe as co-metals. The overall metal loading was maintained at 30 wt. %, with a Ni to co-metal ratio of 3:1. The bimetallic catalysts had surface areas ranging from 145 to 186 $m^2/g$ and a metal dispersion of approximately 14%. XRD and XPS spectra confirmed the incorporation of different metals into RGO supports. CV studies showed that NiCo-RGO had the maximum current density, followed by NiCu-RGO and NiFe-RGO. This observation was supported by the surface area measured for different catalysts. CA study also revealed that NiCo-RGO was a better catalyst in terms of stability in the presence of EG, producing a constant current of 1.83 $mA/cm^2$ after 3600 seconds. The ECSA of bimetallic catalyst increased in the order of NiFe-RGO < NiCu-RGO < NiCo-RGO. The increased ECSA directly correlated with the catalytic activity of bimetallic catalyst. The charge transfer coefficient value as well as Tafel slope also validated the performance of bimetallic catalyst for EG oxidation. EIS analysis showed lower impedance for NiCo-RGO followed by NiCu-RGO and NiFe-RGO. Time constant was higher for the electrochemical process than charge transfer process, indicating electrochemical process as rate determining step. So, it could be concluded that NiCo-RGO was the best catalyst for the electro-oxidation of EG. The detailed electrochemical analysis revealed that the surface coverage of redox species, diffusion coefficient of ethylene glycol molecule and mean electrocatalytic rate constant for NiCo-RGO were $1.5\times10^{-7}$ $mol/cm^2$, $9.53 \times 10^{-5}$ to $9.53 \times 10^{-8}$ $cm^2/s$ and $1.71 \times 10^5$ $cm^3/mol.s$ respectively. These parameters were significantly higher than that observed for Ni-RGO, thereby explaining the enhanced activity of bimetallic catalyst (NiCo-RGO).

The effect of process parameters such as temperature, concentration of KOH and EG concentration was also investigated studied using NiCo-RGO. The current density of the electrochemical process increased with increasing KOH concentration and temperature. However, when the concentration of ethylene glycol was changed, the same linearity was not observed. The current density gradually decreased after 0.75 M EG. EIS data also confirmed the CV findings. As a result, the optimal electro-oxidation conditions were determined to be 1 M KOH with 0.75 M EG at 75 °C. Furthermore, NiCo-RGO also showed significant activity for electro-oxidation of glycerol as well as propane-1,2-diol, making the catalyst suitable for the electro-oxidation of polyhydric alcohols.

Product analysis following a CA study confirmed the presence of glycoldehyde, glycolic, glyoxylic and oxalic acids. Glycoldehyde selectivity was the highest for all the

bimetallic catalysts. However, the selectivity of other products varied depending on the co-metal used. The catalyst also exhibited negligible CO poisoning effect, as demonstrated by CO stripping voltammetry. The analysis of the electrodes before and after EG oxidation suggested that the catalysts were both physically and chemically stable throughout the process. This study demonstrated the efficacy of supported transition metal catalysts for EG electro-oxidation, which can be implemented to direct alcohol fuel cells. The single cell fuel cell study of NiCo-RGO provided insight into the power generation of the best bimetallic catalyst. The study showed that ethylene glycol generated the highest power density (7.07 $mW/cm^2$), followed by glycerol (6.11 $mW/cm^2$) and propane-1,2-diol (3.71 $mW/cm^2$). Hence, the catalyst could be employed for commercial fuel cell application with polyhydric alcohol as fuel.

# LIST OF PUBLICATIONS

## Journals

1. **S. Gupta**, M. De 'Electro-oxidation of ethylene glycol over Cu/C catalysts using different forms of carbon' **J. Electrochem. Soc.** (2023), 170, 046501.
2. **S. Gupta**, M. De 'Role of metal (Cu/Ni/Fe/Co)-carbon composite in enhancing electro-oxidation of ethylene glycol' **J. Appl. Electrochem.** (2023), 53, 1-15.
3. **S. Gupta**, M. De 'Few layer graphene dispersed transition metals (Cu, Ni, Co or Fe) for augmented electro-oxidation of Ethylene Glycol' (Submitted).
4. **S. Gupta**, M. De 'Few layer graphene dispersed high performance nickel based bimetallic catalysts for ethylene glycol electro-oxidation' (To be submitted).

## International Conferences

1. **S. Gupta,** M. De 'Transition Metal (Ni/Cu) Based Bimetallic Catalyst for Glycerol Oxidation', '**244$^{th}$ ECS Meeting**', Oct 8-12, 2023.
2. **S. Gupta**, M. De 'Reduced and exfoliated graphene oxide supported Ni for Electro-Oxidation of Ethylene Glycol', '**14$^{th}$ International Green Energy Conference (IGEC-XIV)**', July 4-8, 2022.
3. **S. Gupta,** M. De, "Electro oxidation of ethylene glycol over supported copper catalyst: Effect of process parameters", **Virtual International Conference on Advances in Chemistry and Chemical Engineering**, Surat, India, 16$^{th}$-17$^{th}$ April 2021.
4. **S. Gupta,** M. De, "Copper based catalysts for electro oxidation of ethylene glycol in direct alcohol fuel cell", **International Conference on Engineering Sciences and Technologies for Environmental Care**, Jorhat, India, 20$^{th}$-22$^{nd}$ Feb 2020.

# TABLE OF CONTENTS

# LIST OF ABBREVIATIONS

**Abbreviations**

| | |
|---|---|
| AC | Activated carbon |
| AFC | Alkaline fuel cell |
| ALS-TC | Alumina-based templated carbon |
| BET | Brunauer-Emmett-Teller |
| CA | Chronoamperometry |
| CGCRI | Glass and Ceramic Research Institute |
| CHP | Combined heat and power |
| CNF | Carbon nanofiber |
| CPD | Contact potential difference |
| CPE | Constant phase element |
| CV | Cyclic voltammetry |
| DAFC | Direct alcohol fuel cell |
| EC | Electrochemical-chemical |
| ECSA | Electrochemical active surface area |
| EDX | Energy dispersive x-ray spectroscopy |
| EG | Ethylene glycol |
| EGO | Exfoliated graphene oxide |
| EIS | Electrochemical impedance spectroscopy |
| FC | Fuel cell |
| FCV | Fuel cell vehicles |
| FESEM | Field emission scanning electron microscopy |
| FETEM | Field emission transmission electron microscopy |
| FRA | Frequency response analyser |
| GC | Glassy carbon |
| $gC_3N_4$ | Carbon nitride |
| Gly | Glycerol |
| GO | Graphene oxide |
| HOPG | Highly oriented pyrolytic graphite |
| KPFM | Kelvin probe force microscopy |
| MCFC | Molten carbonate fuel cell |
| MEA | Membrane electrode assembly |
| MOF | Metal organic framework |

| | |
|---|---|
| Mt | Montmorillonite |
| MWCNT | Multiwall carbon nanotube |
| NLDFT | Non-linear density functional theory |
| OCP | Open circuit potential |
| PAFC | Phosphoric acid fuel cell |
| PEDOT | Poly(3,4-ethylenedioxythiophene) |
| PEMFC | Proton Exchange Membrane fuel cell |
| PPy | Polypyrrole |
| RF | Roughness factor |
| RGO | Reduced graphene oxide |
| SAED | Selected area electron diffraction |
| SDS | Sodium dodecyl sulphate |
| SOFC | Solid oxide fuel cell |
| SS | Stainless steel |
| TPR | Temperature programmed reduction |
| VC | Vulcan carbon |
| XPS | X-ray photoelectron spectroscopy |
| XRD | X-ray diffraction |

# LIST OF FIGURES

# LIST OF TABLES

# LIST OF APPENDICES

# *Chapter 1*
# *Introduction*

# 1. Introduction

## 1.1 Fuel cell scenario

Energy is becoming a basic necessity for daily life due to economic and industrial development. Population growth and rapid development have created a continual demand for energy generation. So far, fossil fuels like coal, oil, and natural gas have been the primary sources of energy production; however, their supply is limited and will deplete shortly. The survey of energy resources by World Energy Council provided clear insights about the supply and demand, as represented in Figure 1.1. According to the report, there would be a 1.5–3% increase in energy demand by 2050 compared to a 1.2–2% growth in population. It has become apparent that fossil fuels would deplete at an alarming rate in the future due to their increasing usage. Thus, there is a need to look for new alternatives or complementary renewable energy sources. On the other hand, fossil fuel-based energy technologies impart huge negative impact on the environment since they emit greenhouse gases during fuel production and utilization (Kordesch and Simader, 1996). These harmful environmental effects resulted in climate change, ozone layer depletion and acid rain kind of phenomena. Thus, global warming and the shortage of fossil fuels enhanced interests towards development of alternative clean energy sources and technologies (Boudghene Stambouli and Traversa, 2002). Additionally, various multinational companies have made significant contributions and investments in the field of alternative clean technologies to combat the depletion of fossil fuel reserves and the environmental consequences of the emission of conventional engines (Gottesfeld and Zawodzinski, 1997). Almost all the existing clean technologies such as solar, wind, biomass, geothermal, hydroelectric and tidal wave energy depend on the geographical location and can only be used in conjunction with the existing energy production technologies. Among the available alternatives, fuel cell (FC) is the promising choice for generating clean energy due to additional benefits such as higher efficiency than diesel engines, flexibility in fuel selection, low carbon emission and a wide range of operational temperature variations (Sharaf and Orhan, 2014). FC is a sustainable clean fuel technology in which chemical energy generated during an electrochemical reaction is directly converted to electrical energy. FC devices accept any chemicals as fuel, whether solid, liquid or gas, and oxidize them to produce energy. It even utilizes greenhouse gases, mainly CO and $CO_2$, as feed and converts them into non-toxic energy products (Coutanceau et al., 2006).

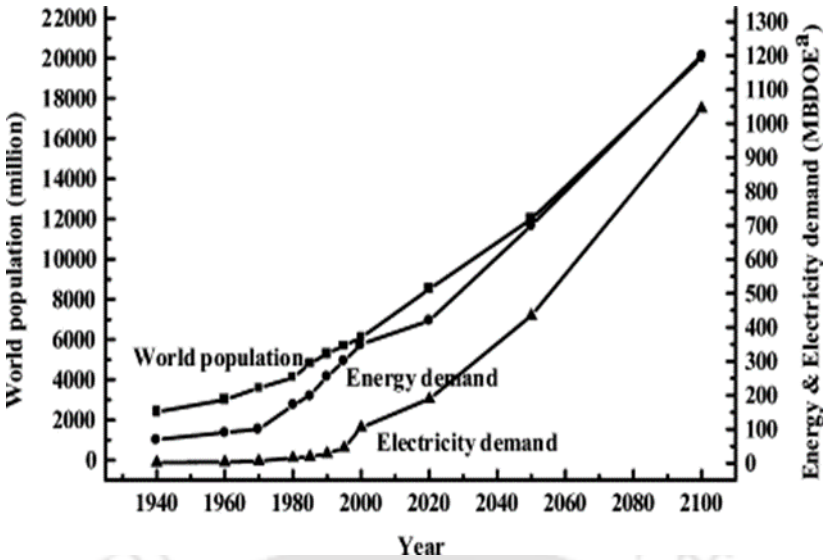


**Figure 1.1: Projection of world population, energy and electrical demands** ([a] Millions of barrels per day of oil equivalent) (Boudghene Stambouli and Traversa, 2002)

FCs have overcome many problems that conventional combustion engines and battery powered devices faced in terms of efficiency, modularity and static nature. The main operational advantage of FCs is a single step conversion to electrical energy, as compared to three step conversion in combustion engines. Unlike battery powered devices, FCs have a much longer lifespan due to the continuity in fuel supply. Benefits of FC are listed below (Boudghene Stambouli and Traversa, 2002; Sharaf and Orhan, 2014):

1. Combined heat and power (CHP) efficiency of FC is much higher compared to combustion engines and batteries.
2. FC runs at high stability, low noise and wide range of temperature which makes its use favorable.
3. FC does not emit $SO_X$, $NO_X$ and minimal emission of toxic gases and chemicals.
4. There is full fuel flexibility FC with zero dependency on fossil fuel.
5. FC operated with high modularity and low maintenance.

However, FC is still in the developmental stage and have some limitations. Extensive research and development is necessary to overcome the limitations of FC and make it fully economical and viable. Some of the limitations are enlisted below (Sharaf and Orhan, 2014):

1. FC have low durability because of fuel impurities, degradation mechanism and failure modes within FC components.
2. Storage of fuels is another intricacy for FC which prompts the use of liquid fuels.
3. Proper water balance maintenance in the membranes is a difficult task.

4. Satisfactory heat utilization and dissipation needs to be taken care of.
5. FC commercialization faces problem till date due to lack of economic feasibility.

FC has a wide range of applications, including stationary power supply, portable devices and engines for transport application (Sharaf and Orhan, 2014). FC is the most favorable power generation device in both residential and industrial areas. Moreover, it serves as the powerhouse in telecommunication systems (Varkaraki et al., 2003). FC is also used to generate power in off-grid areas such as forests, deserts, islands, rural villages and remote research labs (Liming, 2009). If cost and durability issues are resolved, FC would be efficient enough for distributive power generation in residential areas, industries, schools and colleges due to its static nature, high efficiency and lower emissions (Bauen et al., 2003). There is a market for FC in outdoor applications like camping, surveillance, traffic and street lighting. Furthermore, FC can be used in electronic devices such as laptops, mobile phones, radios and camcorders. However, FC faced huge competition in the portable sectors from lithium ion batteries. On the other hand, FC is the sole power generating technology used in space applications (Crowe, 1973). FC is also widely employed in defense sector for submarines, jet planes, radars, missile systems, military vehicles and portable military equipment (Cowey et al., 2004; Patil et al., 2004). In the transportation sector, FC is the leading clean technology and is used in personal light tracking vehicles such as scooters, motorbikes, wheelchairs, airport tugs and golf carts. It also finds application in cars, buses, heavy duty tracks and utility vans (Qi, 2009). Moreover, fuel cell vehicles (FCV) have been introduced to minimize carbon emissions, despite their high cost, which is five times that of diesel vehicles. Big industrial players like Toyota, Tesla, Tata, Mercedes-Benz, Honda, Hyundai, Nissan and Volvo are leveraging their resources to produce more cost-effective FCV.

FC sector continued to expand their empire with the active assistance of several government financial agencies. The favorable environmental and energy policies are also driving the growth of FC industry. In this context, China is providing complete scientific and technological support to drastically accelerate the expansion of FC. Japan and Korea are involving their major corporate entities in this area. In Europe and North America, progress is moving forward at a rapid pace through ample support provided by industrial companies. However, it is insufficient to drive the actual commercialization of FC (World Energy Council, 2016). But there is an increasing tendency in the marketization of FC in all aspects, in terms of megawatts of energy produced, the number of FC units utilized, FC units in different

applications and adoption of FC units in different continents. The FC market has grown at an exponential rate over the past few years (The Fuel Cell Industry Review, 2021).

India is also gradually expanding its momentum into FC research by attempting to commercialize this technology. Around 150 FC has been imported into India for application in the telecom sectors. Bharat Heavy Electrical Limited has imported a 200 KW phosphoric acid fuel cell (PAFC), installed it and is presently operational with LPG as fuel. This organization also develops its own 50 KW PAFC technology using hydrogen, a by-product of the Chlor-Alkali industry. The Naval Materials Research Laboratory demonstrated its own 15 KW PAFC system for field applications. The Central Glass and Ceramic Research Institute (CGCRI) uses a new bi-polar stack design to fabricate a 1 KW solid oxide fuel cell (SOFC) stack (Hydrogen Energy and Fuel Cells In India–A Way Forward, 2016). Apart from CGCRI, Bhabha Atomic Research Centre, National Aeronautical Lab, Institute of Minerals and Materials Technology are focusing on various aspects of SOFC. Moving on to direct alcohol fuel cell (DAFC), the SPIC Science Foundation has already introduced a 250-watt stack that uses methanol as an alcohol feed (Report on Fuel Cell Development in India, 2016). DAFC is still in research phase in India, and no commercialization has been made so far. However, the private automotive sectors of India are coming forward for the implementation of FCV in India. Mahindra & Mahindra, Tata Motors and Ashok Leyland are trying to introduce FCVs into the Indian market and also have been partially successful. Tata Motors, in association with ISRO, introduces India's first FCV in 2017 (CarAndBike Team An NDTV Ventrure, 2017). In India, various premier institutes are collaborating with research organizations and top-tier industrial investors in energy applications to explore the research potential in FC domain. The Ministry of New and Renewable Energy has already allocated a proposed budgetary estimate of Rs 750 crore for development of complete fuel cells up to the financial year 2022-2023 (Report on Fuel Cell Development in India, 2016).

## 1.2 Types of fuel cell

Fuel cell (FC) is a device which undergoes electrochemical reactions to produce electricity and heat. The concept of FC is fundamentally the reverse mechanism of an electrolytic reaction. The main components of FC are anode, cathode, electrolyte and external circuit. FC uses any potent chemical as feed to split up into ions and electrons by oxidation at the anode. The resulting ions then permeate through the membrane, while electrons flow through the external circuit to the cathode. On the cathode side, an oxidant is supplied, which absorbs the electron

and reacts with the ions passing through the membrane to get reduced, thus completing the reaction (Larminie et al., 2003). The different types of FC are as follows:

**Alkaline fuel cell (AFC)** produces electricity by using an alkaline electrolyte, preferably potassium hydroxide in aqueous solution. The main contributing charge transfer agent is hydroxyl ions, which flows through the anion exchange membrane thereby making a complete circuit by harvesting electricity. When hydrogen is supplied as the feed to anode, it gets oxidized by hydroxyl ions to produce water and electrons.

**Phosphoric acid fuel cell (PAFC)** employs liquid phosphoric acid ($H_3PO_4$) as the electrolyte and operates at temperatures ranging from 150 to 220°C. This operational temperature range is due to the high ionic conductivity of $H_3PO_4$ at high temperatures. At the anode, hydrogen is divided into hydrogen ($H^+$) ions and electrons. Here, $H^+$ ions operate as the charge transfer agent, which pass through the electrolyte from anode to cathode and release electrons that flow across the external circuit. Water is formed due to the reaction of electrons at the cathode.

**Proton exchange membrane fuel cell (PEMFC)** usually utilize polymeric proton exchange membrane as the electrolyte. The hydrogen ions and electrons are formed by splitting the hydrogen molecule at the catalyst surface. It operates at low temperatures ranging from 60 to 100°C. The $H^+$ ions are transported across the membrane, whereas the ejected electrons travel across the external circuit to the cathode side to form water.

**Molten carbonate fuel cell (MCFC**) is classified as high temperature fuel cell. Molten carbonate is employed as the electrolyte and carbonate is the contributing ion which transfer through the electrolyte. Methane and water are supplied as feed to the anode, where they react to produce carbon monoxide (CO) and hydrogen. CO further oxidizes to $CO_2$ and $H_2$. However, $H_2$ and CO produced undergoes electrochemical reaction simultaneously and react with carbonate ions to produce $H_2O$, $CO_2$ and electrons. Carbonate ions are formed at the cathode by the reaction of oxygen, $CO_2$ and electrons passing across the external circuit. Carbonate ions are generated and transported to the anode via the molten carbonate electrolyte.

**Solid oxide fuel cell (SOFC)** uses a solid metallic oxide ceramic-based electrolyte membrane and hydrocarbon as feed. Hydrocarbon is internally reformed to produce hydrogen and carbon monoxide (Ormerod, 2003). The produced hydrogen reacts with oxygen provided as an oxidant to generate electricity. Yttria stabilized zirconia is the most common SOFC electrolyte due to its high thermal and chemical stability, as well as ionic conductivity (Singhal, 2000). At the cathode, oxygen is oxygen is oxidized at 1000°C to form oxide ions, while at the anode, hydrogen reacts with the oxide ions to produce water and electrons.

**Direct alcohol fuel cell (DAFC)** is the advanced version of PEMFC which uses alcohol as a liquid fuel. DAFC generally operates at low temperatures with enhanced lifetime and fast refuelling attachments. Methanol and ethanol are commonly explored as fuels for DAFC. Alcohol oxidizes at the anode to produce $H^+$ ions and electrons which generate electricity.

## 1.3 Direct alcohol fuel cell

Direct alcohol fuel cell (DAFC) uses alcohol as a feed and oxygen as an oxidant. The alcohol is supplied to the anodic side to react with the electrocatalysts to form $H^+$ ions and electrons. The $H^+$ ions permeate through the membrane to the cathodic side and react with the oxidant to form water. The electrons generated at the anodic side pass through the external circuit to generate electricity. The reactions are catalyzed by noble metal catalyst, with polymeric membrane serving as the electrolyte. The membrane provides low permeability to fuels while maintaining high proton conductivity. Moreover, the membrane provides thermal and chemical stability, allowing proper functioning of DAFC. Nafion® is commonly used as the electrolytic membrane. This type of FC can be used in portable and transport applications. Typically, methanol and ethanol have been mainly investigated as alcohol fuels for DAFC. The reactions involving both methanol and ethanol electro-oxidation are represented below.

Methanol electro-oxidation (Mekhilef et al., 2012):

$$\text{At anode: } CH_3OH + H_2O \rightarrow CO_2 + 6H^+ + 6e^- \quad (1.1)$$

$$\text{At cathode: } (3/2)O_2 + 6H^+ + 6e^- \rightarrow 3H_2O \quad (1.2)$$

Ethanol electro-oxidation (Kamarudin et al., 2013):

$$\text{At anode: } C_2H_5OH + 3H_2O \rightarrow CO_2 + 12H^+ + 12e^- \quad (1.3)$$

$$\text{At cathode: } 3O_2 + 12H^+ + 12e^- \rightarrow 6H_2O \quad (1.4)$$

However, research is also being conducted on utilising polyhydric alcohols such as ethylene glycol (EG), glycerol, propylene glycol and glucose as fuels for DAFC. These polyhydric alcohols, also termed as polyhydric alcohols, have a high volumetric energy density, low flammability, low toxicity, are easy to handle and also renewable in nature.

## 1.4 Electrocatalysts for direct alcohol fuel cell

Monohydric alcohols have been widely studied as electrocatalysts for DAFC. These studies mostly focused on noble metal-based catalysts, preliminary Pt-based catalysts, for the electro-oxidation of alcohols. Other noble metals such as Pd, Ru, Rh, Ag, Au and Ir, were also

investigated as catalysts for methanol and ethanol electro-oxidation. The same noble metal catalysts were used for the electro-oxidation of polyhydric alcohols, preferably EG and glycerol, and the results showed better current generation than monohydric alcohols. However, these noble metals underwent sluggish oxidation kinetics due to poisoning of the catalysts. The oxidation of alcohols on the electrode surface resulted in the generation of CO, which gets adsorbed on the catalyst surface. The adsorption of CO formed a passivation layer on the catalyst surface, thereby deactivating it. To address the aforementioned issue and improve the performance of catalysts, a variety of noble metal-based bimetallic catalysts were introduced for the electro-oxidation of alcohols. The use of noble metals as catalysts imparts significant expenses to the electrochemical oxidation process. Thus, co-doped noble metals were replaced by low-cost transition metals such as Ni, Cu, Co, Fe, Zn, Mo, Mn, Sn, Bi. These transition metals were very resistant to CO poisoning, thereby enhancing the performance of electrocatalysts. Further research was conducted by introducing different low-cost conductive supports made by using various forms of carbon and $TiO_2$. The use of multiple supports increased the surface area of the catalysts as well as metal dispersion. The supported catalysts (both monometallic and bimetallic) improved the performance of alcohol oxidation by reducing the mass transfer effect. The supported catalysts also became economically more viable as the metal loading got reduced. In recent years, researchers have focussed on replacing the noble metals completely with non-noble metals. Several transition metals, such as Ni, Co, Cu, Fe, Mo, Mn and Pb, were utilized as catalysts in various combinations for methanol and ethanol oxidation. Similarly, these metals were also introduced for polyhydric alcohols and require further investigation for viable commercialization. Hence, there is a huge scope of research opportunities with low cost transition metal-based supported and unsupported catalysts for the electro-oxidation of polyhydric alcohols in DAFC.

# *Chapter 2*
# *Literature Review*

# 2. Literature review

The electro-oxidation of monohydric alcohols such as methanol and ethanol with various noble metal catalysts has been studied and reported extensively. These alcohols are renewable, non-toxic and have a high volumetric energy density, making them highly desirable fuels. The study of noble metal catalysts for alcohol oxidation pointed out that CO adsorption on the noble metal surfaces led to the poisoning of the catalysts. This phenomenon also slowed down the rate of alcohol oxidation. To counteract this effect, various combinations of bimetallic catalysts were developed for alcohol oxidation. Though there was certain improvement in the performance, the use of noble metals as catalysts still caused higher cost for energy generation, questioning the economic feasibility of the process. To reduce the cost, transition metals were introduced as co-metals to noble metals. Furthermore, reduction of cost can also be achieved by replacing the noble metals completely with transition metals.

The majority of research on alcohol oxidation has focused on only methanol and ethanol. So, there remains a scope for exploring polyhydric alcohols like EG and glycerol. EG has generated significant interest in liquid fuels due to its high electron transfer rate of up to 80%. EG provides a number of advantages over monohydric alcohols in FC applications. EG has a theoretical capacity higher than monohydric alcohols. The higher boiling point of EG as compared to monohydric alcohols, makes it safer to work with. The supply chain of EG is already established, as it is widely used in the automotive industry. All of these advantages make EG-based FCs a promising source of alternative energy. However, mainly noble metal catalysts were explored for the electro-oxidation of polyhydric alcohols. There is potential for research into completely replacing noble metal catalysts with transition metal catalysts. Moreover, vulcan carbon (VC) has been primarily explored as a support material for electrocatalysts for alcohol oxidation. The study on the use of other type of supports such as graphene, reduced graphene oxide (RGO), mesoporous carbon, carbon nitride ($gC_3N_4$), titanium dioxide *etc*. are limited. The following literature review is primarily categorized into noble and transition metal catalysts. Each section provides a detailed review of various supported and unsupported catalysts used for the electro-oxidation different type of alcohols.

## 2.1 Monometallic catalysts for alcohol oxidation

### 2.1.1 Noble metal catalysts

The electro-oxidation of alcohols was primarily explored with noble metal based catalysts. The mostly used catalysts for electro-oxidation of alcohols was Pt, Pd, Ru, Ir, Au, and Ag. Among these noble metals Pt and Pd was most explored for electro-oxidation of alcohols. Extensive studies were reported about modifications of these metals for its use in alcohol electro-oxidation to enhance the activity of the catalyst. Detailed literature review regarding the same was discussed in subsequent sections.

#### 2.1.1.1 For monohydric alcohols

Methanol is the most thoroughly researched alcohol used as a fuel for FCs. The electro-oxidation of methanol was primarily accomplished using noble metal-based electrocatalysts. The most commonly used noble metals for the electro-oxidation of methanol were Pt, Pd, Ag and Au. Li et al., (2010) introduced Pt on graphene and multiwall carbon nanotubes (MWCNT) for methanol oxidation in a sulphuric acid medium. In the presence of methanol, the Pt/graphene and Pt/MWCNT generated current densities of approximately 30 and 25 $mA/cm^2$. The addition of support lowered the poisoning effect, making the catalyst more efficient (Li et al., 2010). Functionalized graphene was used as a support to Pt catalysts for methanol oxidation (Vulcu et al., 2021; Yang et al., 2014). The functional groups of graphene had a positive effect on the electrocatalytic activity of the catalyst (Table 2.1). Yang et al., (2019) developed graphene supported Pd nanoplates for methanol oxidation in basic environment to extract current density of 1.86 $mA/cm^2$, which was higher than VC supported Pd catalyst (1.31 $mA/cm^2$). The use of composites as support was a very promising approach for improving the performance of the catalysts. Estudillo-Wong et al., (2013) employed $TiO_2$ and VC composites to support Pd catalysts for methanol oxidation in a basic environment. The performance of Pd/$TiO_2$-VC was 3.3 times better than Pd/VC. The use of g$C_3N_4$-RGO and g$C_3N_4$-VC composites as supports amplified the mass activity of Pd catalysts for methanol electro-oxidation (Table 2.1) (Qian et al., 2015; Zhang et al., 2014a). Guo et al., (2012) prepared Ag/RGO and Au/RGO catalysts for electro-oxidation of methanol in basic medium, generating 19 $mA/mg_{Ag}$ and 34 $mA/mg_{Au}$ respectively. Du et al., (2021) incorporated Rh into several supports for methanol oxidation in basic medium. The g$C_3N_4$-graphene composite-supported Rh showed better catalytic activity of 701 mA/mg, followed by N-graphene, graphene, CNT and carbon black-supported Rh.

**Table 2.1: Comparison of different noble metal-based monometallic catalysts for alcohol oxidation**

| Catalyst | Electrolyte (Conc.) | Type of Alcohol (Conc.) | Current density ($mA/cm^2$) | References |
|---|---|---|---|---|
| **Monohydric alcohols** | | | | |
| Pt/graphene | $H_2SO_4$ (0.2 M) | Methanol (1 M) | 30 | Li et al., 2010 |
| Pt/MWCNT | NaOH (0.2 M) | Methanol (1 M) | 25 | Li et al., 2010 |
| Pt/S-graphene | KOH (1 M) | Methanol (0.5 M) | 28.6 | Yang et al., 2014 |
| Pt/S-graphene | NaOH (1 M) | Methanol (1 M) | 644* | Vulcu et al., 2021 |
| Pd/$gC_3N_4$-RGO | NaOH (1 M) | Methanol (1 M) | 1550* | Zhang et al., 2014a |
| Pd/$gC_3N_4$-VC | KOH (0.5 M) | Methanol (1 M) | 1720* | Qian et al., 2015 |
| Pd/graphene<br>Pd/VC | NaOH (0.5 M) | Methanol (0.5 M) | 1.86<br>1.31 | Yang et al., 2019 |
| Ag/RGO<br>Au/RGO | KOH (1 M) | Methanol (5 M) | 19*<br>34* | Guo et al., 2012 |
| Rh/$gC_3N_4$-RGO | KOH (1 M) | Methanol (1 M) | 701* | Du et al., 2021 |
| Pt single crystal | NaOH (0.1 M) | Ethanol (0.2 M) | 37 | Busó-Rogero et al., 2014 |
| Pt/graphene | $H_2SO_4$ (0.5 M) | Ethanol (1 M) | 180* | Li et al., 2016 |
| Pt/graphene | $HClO_4$ (0.1 M) | Ethanol (0.1 M) | 520* | Liu et al., 2016b |
| Pt/carbon fiber | $H_2SO_4$ (0.5 M) | Ethanol (1 M) | 370* | García-Mateos et al., 2017 |
| Pt/C | KOH (0.5 M) | Ethanol (0.5 M) | 30 | Ruiz-Camacho et al., 2019 |
| Pd Nanosheets | KOH (0.1M) | Ethanol (0.5M) | 30* | Farsadrooh et al., 2018 |
| Pd/$TiO_2$-Carbon black | NaOH (0.5M) | Ethanol (2.44M) | 17.6 | Akbarfallahi et al., 2020 |
| Pd/N–Carbon nano onions | KOH (1M) | Ethanol (1 M) | 17.4 | Sikeyi et al., 2021 |
| Pd nanofilms<br>Pd nanosheets<br>Pd nanomeshes | KOH (1 M) | Ethanol (1 M) | 2960*<br>2150*<br>1790* | Fan et al., 2023 |
| Au/carbonfiber | NaOH (0.5 M) | Ethanol (1 M) | 12 | Yang et al., 2013 |

| | | | | |
|---|---|---|---|---|
| $Au/MoO_3$ | KOH (1 M) | Ethanol (1 M) | 1713.7* | Karuppasamy et al., 2017 |
| **Polyhydric alcohols** | | | | |
| Pd/VC | KOH (0.1 M) | EG (0.5 M) | 348* | Yang et al., 2015a |
| Pd/3D graphene | KOH (2 M) | EG (3 M) | 60 | Krittayavathananon and Sawangphruk, 2016 |
| Pd/C | KOH (0.1 M) | EG (0.5M) | 320* | Wang et al., 2018 |
| Pd/ PPy -RGO | KOH (1 M) | EG (1 M) | 30 | Xie et al., 2022b |
| Pd/CeO-C | KOH (1 M) | EG (1 M) | 68.5 | Sankar et al., 2019 |
| Au nanoparticles | Phosphate buffer (0.06 M) | EG (0.5 M) | 27.9 | Łuczak and Bułat, 2016 |
| Au aerogels | KOH (1 M) | EG (0.5 M) | 94.5 | Wang et al., 2020a |
| Pt/VC<br>Au/VC | KOH (1 M) | EG (0.5 M) | 38<br>15 | Xin et al., 2012 |
| Pt/C<br>Pd/C<br>Au/C | NaOH (0.3 M) | EG (0.5 M) | 212.7<br>239.1<br>234.5 | Habibi, 2017 |
| Pd/carbon paper<br>Pt/carbon paper | KOH (2 M) | EG (0.3 M) | 23#<br>17.2# | Arjona et al., 2022 |
| Pt/VC | KOH (1 M) | Glycerol (1 M) | 19.6 | Frota Jr. et al., 2017 |
| Pt/Carbon | $H_2SO_4$ (0.5 M) | Glycerol (2 M) | 3.92 | Lee et al., 2019 |
| Au/VC | KOH (0.1 M) | Glycerol (0.1 M) | 23.6 | Qi et al., 2014 |
| AuNP/PVPGraphene | KOH (0.5 M) | Glycerol (0.5 M) | 2500* | Wang et al., 2015 |
| Pd/MWCNT | KOH (0.5 M) | Glycerol (0.1 M) | 6.3 | Ahmad et al., 2020 |
| Ag electrode | KOH (0.1 M) | Glycerol (1 M) | 2.3 | Suzuki et al., 2016 |
| Pt/VC<br>Pd/VC<br>Au/VC | KOH (1 M) | Glycerol (0.5 M) | 27.4<br>20.9<br>117.2 | Zhang et al., 2013 |

*current density in $mA/mg_{metal}$, #current density at 60°C

The most explored alcohol after methanol was ethanol. The electrochemical oxidation of ethanol, like that of methanol, had been extensively studied using noble metal *i.e.* Pt and Pd-

based catalysts. Busó-Rogero et al., (2014) developed a Pt single crystal electrode for the electro-oxidation of ethanol in basic medium, achieving a maximum current density of 37 $mA/cm^2$. Different carbon supports, such as graphene, mesoporous and biomass-derived carbon, improved the catalytic activity of the Pt catalyst, as shown in Table 2.1 (García-Mateos et al., 2017; Li et al., 2016; Ruiz-Camacho et al., 2019). According to Liu et al., (2016b) modulating the particle size of a graphene-supported Pt catalyst increased the catalytic activity by about 1.7-fold. Farsadrooh et al., (2018) utilized Pd nanosheets to harvest 30 $mA/mg_{Pd}$ from the electro-oxidation of ethanol in basic medium, which was higher than the activity found with Pd black. The addition of different supports like $TiO_2$ nanofibers and carbon black composite, nitrogen-doped oxygen functionalized carbon nano onions, to Pd catalysts improved the extraction of current density from ethanol in basic medium (Table 2.1) (Akbarfallahi et al., 2020; Sikeyi et al., 2021). Fan et al., (2023) discovered that structural modifications to Pd catalysts had an impact on their performance. Pd nanofilms (2.96 A/mg) performed better, followed by Pd nanosheets (2.15 A/mg), Pd nanomeshes (1.79 A/mg) and commercial Pd/C (1.14 A/mg) in electro-oxidation of ethanol. Yang et al., (2013) electrodeposited Au on carbon fiber cloth for ethanol electro-oxidation, resulting in a current density of approximately 12 $mA/cm^2$ in basic medium. Karuppasamy et al., (2017) employed $MoO_3$-supported Au catalysts for ethanol oxidation in basic environment and obtained catalytic activity of 1713.7 $mA/mg_{Au}$.

### 2.1.1.2 For polyhydric alcohols

The electro-oxidation of polyhydric alcohols was explored less as compared to monohydric alcohols. The simplest form of polyhydric alcohols is ethylene glycol (EG). The electrocatalytic reaction of EG was mostly carried out using noble metal-based catalysts, with Pd being the most extensively studied active metal. The use of Pd metal electrodes in 0.1 M NaOH environment generated a current density of 5.7 and ~3 $mA/cm^2$ from 0.1 M and 1 M EG, respectively (Dalbay and Kadirgan, 1990; Lin et al., 2013). On the other hand, the Pt metal electrodes used for the oxidation of 0.51 M EG in 1 M KOH generated ~47.5 $mA/cm^2$ current density (Sitta and Varela, 2010). In another study, the same group reported a current density of 22 $mA/cm^2$ at pH 14 from the electro-oxidation of EG with Pt electrodes (Sitta et al., 2013). Moreover, various types of support played a crucial role in improving the performance of the catalysts. In fact, both functional and structural modifications to the support also had an impact on catalyst activity. Yang et al., (2015a) used phenanthroline-modified VC to support Pd nanoparticles for the electro-oxidation of EG in 0.1 M KOH, with a mass activity of 348 $mA/mg_{Pd}$. The Pd/phenanthroline-modified VC showed higher activity than Pd/VC and

Pd/phenanthroline-derived carbon. Similarly, replacing polypyrrole (PPy) and VC with PPy-modified RGO increased catalytic activity (Xie et al., 2022b). Moreover, the structurally modified RGO also improved the current density generation from EG. The Pd/3D-RGO demonstrated the maximum current density of 60mA/cm$^2$, followed by Pd/2D-RGO, Pd/GO and pure Pd (Krittayavathananon and Sawangphruk, 2016). Wang et al., (2018) investigated riboflavin-derived carbon as a support for Pd catalyst to oxidize EG in basic medium, resulting in an activity of 0.32 A/mg$_{Pd}$. The use of a carbon-ceria composite supported Pd catalyst resulted in a current density of 68.5 mA/cm$^2$ from 1 M EG oxidation in 1 M KOH medium. The study also focused on the impact of composite ratio on the catalytic activity (Sankar et al., 2019). Au nanoparticles were modified to electro-oxidize EG at pH 7, resulting in a current density of 27.9 mA/cm$^2$ (Łuczak and Bułat, 2016). The influence of (111) and (110) facets of Au aerogels increased the catalytic activity up to 94.5 mA/cm$^2$ for EG oxidation (Wang et al., 2020a).

There were few studies that compared several noble metals for EG oxidation. (Xin et al., (2012) examined the performance of Pt/VC and Au/VC for electrochemical oxidation of EG in alkaline medium, producing 38 and 15 mA/cm$^2$ current density, respectively. Another study found that the activity of catalysts followed the order as: Pd/C (239.1 A/g) > Au/C (234.5 A/g) > Pt/C (212.7 A/g) (Habibi, 2017). Arjona et al., (2022) electrodeposited Pd and Pt on Toray carbon paper to assess the performance of catalyst for EG oxidation. The study also investigated the effect of different electrolytes, varying concentrations of EG and various temperatures on catalytic activity.

Glycerol is the most studied polyhydric alcohols after EG. The most used noble metals for glycerol oxidation were Pt, Pd Ag and Au. Frota Jr. et al., (2017) experimented with Pt/VC to determine the optimal Pt loading into VC support for glycerol oxidation in alkaline medium. The maximum current density was observed at 60 wt.% Pt loading (19.6 mA/cm$^2_{Pt}$), and the current density dropped with a decrease in Pt concentration. The 3D graphene-like mesoporous carbon was employed to support Pt nanoparticles, resulting in a current density of 3.92 mA/cm$^2$ from 2 M glycerol electro-oxidation in 0.5 M $H_2SO_4$. The obtained activity was 1.6 times higher than that of Pt/VC (Lee et al., 2019). Qi et al., (2014) utilised Au/VC as anode catalyst to harvest a current density of 23.6 mA/cm$^2$ from 0.1 M glycerol in 0.1 M KOH. The use of poly(4-vinylpyridine) functionalized graphene as a support for Au nanoparticles in glycerol oxidation yielded a mass activity of 2.5 A/mg$_{Au}$ (Wang et al., 2015). The effect of Pd loading on MWCNT for glycerol oxidation in 0.5 M KOH indicated that increase in Pd loading up to 20 wt.%, boosted current density but it decreased with further increase in Pd loading. The

optimum 20 wt.% Pd/MWCNT extracted current density of 63.44 A/$m^2$ from the electro-oxidation of glycerol (Ahmad et al., 2020). The polycrystalline Ag electrode for generated 2.3 mA/$cm^2$ current density from glycerol oxidation (Suzuki et al., 2016). Zhang et al., (2013) evaluated the performance of Pt/VC, Pd/VC and Au/VC for the electro-oxidation of glycerol in 1 M KOH. The Au/VC (117.2 mA/$cm^2$) performed best, followed by Pt/VC (27.4 mA/$cm^2$) and Pd/VC (20.9 mA/$cm^2$). Moreover, an increase in temperature boosted the catalytic activity towards glycerol oxidation.

#### 2.1.1.3 Comparison between different alcohols

**For Monohydric alcohols**

Hu et al., (2012) incorporated Pd nanocrystals on helical carbon nanofiber (CNF) for methanol and ethanol oxidation, resulting in twice the current density of a VC-supported Pd catalyst. Sikeyi et al., 2019 synthesized Pd/CNF catalysts with low Pd concentration for methanol and ethanol oxidation in basic medium. The Pd/CNF demonstrated higher catalytic activity than the commercial Pd/C catalyst, generating 1.21 and 1.16 mA/$cm^2$ current densities for methanol and ethanol respectively.

**For combination of monohydric and polyhydric alcohols**

The performance of methanol, ethanol, EG and glycerol oxidation was compared using bis (dibenzylidene acetone) palladium (0) catalyst (Zhiani et al., 2015). EG had the highest current density (28.4 mA/$cm^2$), followed by ethanol (20.7 mA/$cm^2$), glycerol (15.8 mA/$cm^2$) and methanol (5.2 mA/$cm^2$) (Zhiani et al., 2015). Li et al., (2014) compared the performance of Pd/RGO for EG and glycerol oxidation, which had catalytic activities of 33.7 and 25.1 mA/mg respectively. Pd/RGO showed better catalytic activity than Pd/VC and pure Pd. Karuppasamy et al., (2020) prepared a carbon nanosphere-supported spherical and hexagonal Pd catalyst for the oxidation of ethanol and EG. The spherical Pd catalyst performed better than the hexagonal Pd catalyst for both the alcohols. Moreover, the catalysts generated higher current density for the oxidation of EG than for ethanol (Karuppasamy et al., 2020). Hu et al., (2020) used Pt nanoparticles to oxidize methanol, ethanol and EG in alkaline medium. The Pt nanoparticle with dominant (111) facets produced current densities of 15.29, 14.24 and 15.51 mA/$cm^2$ for methanol, ethanol and EG oxidation, respectively (Hu et al., 2020). Mesoporous carbon with self-doping defects was used as support for Pd catalysts to obtain mass activity of 3044.3 and 4002 mA/mg from the electro-oxidation of ethanol and EG, respectively (Chen et al., 2021). The composite of PPy and nitrogen doped graphene was also used as a support for Pd catalyst

(Xie et al., 2022a). The mass activity of Pd/PPy-N-graphene for EG, methanol and ethanol oxidation was 2176.7, 1192.7 and 498.9 mA/$mg_{Pd}$, respectively (Xie et al., 2022a).

### 2.1.2 Transition metal catalysts

The use of transition metals as catalyst for alcohol electro-oxidation was primarily introduced for economic feasibility regarding energy production. But, using transition metal as a catalyst also reduced the amount of CO adsorption on the catalyst surface due to alcohol oxidation. Thus, transition metal catalysts had an added advantage over noble metal catalysts due to less catalyst poisoning. However, these catalysts exhibited sluggish kinetics for alcohol oxidation. Nickel (Ni) was the most used transition metal as a catalyst for alcohol oxidation. In addition to Ni, copper (Cu) and cobalt (Co) were also explored as catalysts.

#### 2.1.2.1 For monohydric alcohols

The demand for transition metal catalysts originated from the necessity to reduce the cost of FC catalysts while lowering the CO poisoning effect. The electro-oxidation of monohydric alcohols such as methanol and ethanol, was mostly conducted using supported and unsupported Ni-based catalysts. Table 2.2 shows the activity of different transition metal-based catalysts for alcohol oxidation. Different supported nickel catalysts were used for methanol oxidation. Rahim et al., (2004) employed Ni-modified graphite for methanol oxidation in 1 M KOH to generate 150 mA/$cm^2$ current density. The Ni/VC, Ni/3D porous graphene and Ni/MWCNT generated 32, 64.6 and 15.94 mA/$cm^2$ current density, respectively for electro-oxidation of methanol in basic medium (Askari et al., 2019; Hameed and El-Sherif, 2015; Zhu et al., 2017). The N-doped CNF supported NiO showed improved activity for methanol oxidation, with a current density of 300 mA/$cm^2$ (Al-Enizi et al., 2014). Moreover, a sulfonated PPy-supported Ni catalyst showed mass activity of 7.4 mA/g in acidic medium, whereas Ni/RGO was reported to exhibit an activity of 1600 mA/mg for methanol oxidation in basic medium (Das et al., 2016; Sun et al., 2018). The various Ni metal organic framework (MOF)-based composites were also used as catalysts to harvest current densities of 275.85 mA/$cm^2$ and 267.77 mA/$cm^2$ from methanol electro-oxidation (Noor et al., 2019; Yaqoob et al., 2021). Ullah et al., (2019) examined the performance of Ni and Co on 3D porous graphene for methanol oxidation in 1 M KOH, generating current densities of 147.1 mA/$cm^2$ and 53 mA/$cm^2$, respectively. The core shell $Co_3O_4$/PPy nanohybrid was used as an anode catalyst, producing 111 mA/$cm^2$ current density at 0.5 V from methanol oxidation in 1 M KOH medium (Khalafallah et al., 2018). Thamer et al., (2017) utilized Co on CNF to achieve current density of 72.78 mA/$cm^2$. The Co

MOF and GO composite were used as catalyst, generating 72.78 mA/cm$^2$ current density in basic medium (Mehek et al., 2017). PPy-graphene oxide-supported $Cu_2O$ delivered current density of 7.9 mA/g for the electro-oxidation of 2 M methanol in acidic medium (Pattanayak et al., 2018). Anantharaj et al., (2020) prepared $Cu(OH)_2$-CuO/Cu via potentiostatic anodization for 60 s and implemented it for the oxidation of 0.5 M methanol, resulting in 42 mA/cm$^2$ current density in basic medium.

The oxidation of ethanol was also investigated thoroughly using transition metal-based electrocatalysts. Similar to methanol oxidation, electro-oxidation of ethanol was carried out primarily using several supported Ni-based catalysts. Soliman et al., (2016) electrodeposited Ni on a graphite electrode for the oxidation of 1 M ethanol in 0.5 M NaOH, producing a current density of 162 mA/cm$^2$. Biomass-derived hydrothermally processed activated carbon (AC) was used as a support for Ni catalyst to generate 28.5 mA/cm$^2$ current density from ethanol oxidation (Cuña et al., 2017). Moreover, nitrogen-doped carbon supported Ni catalyst produced 327 mA/cm$^2$ current density, whereas graphitized carbon supported NiO catalyst generated 21.59 mA/cm$^2$ current density (Hameed, 2019; Shi et al., 2017). On the other hand, Ni/RGO extracted a current density of 12 mA/cm$^2$ from ethanol oxidation (Li et al., 2019a). Santos et al., (2019) introduced RGO support for nickel(II)-bis(1,10-phenanthroline) to achieve a current density of ~16 mA/cm$^2$ from 0.1 M ethanol oxidation in 1 M NaOH. Hassen et al., (2016) hydrothermally synthesized $Co_3O_4$ from biomass sources with various morphologies. This $Co_3O_4$ catalyst was capable to produce 200 mA/cm$^2$ current density from ethanol electro-oxidation. The use of electrochemically deposited Co on graphite for ethanol oxidation in alkaline medium yielded a current density of 29.40 mA/cm$^2$ (El-Jemni et al., 2022). El Attar et al., (2020) also electrodeposited $Cu_2O$/Ppy on glassy carbon electrodes and achieved ~18 mA/cm$^2$ current density from electrochemical oxidation of 5 M ethanol in 0.1 M NaOH.

#### 2.1.2.2 For polyhydric alcohols

Polyhydric alcohols have received less attention than monohydric alcohols with transition metals being used as catalysts. The electrochemical oxidation of ethylene glycol and glycerol was mostly investigated using Ni-based catalyst. The Ni nanofibers were used to electro-oxidize 0.03 M EG, yielding a current density of 10 mA/cm$^2$ in 0.2 M NaOH at 0.63 V (Hosseini et al., 2017). Eshagh-Nimvari and Karim Hassaninejad-Darzi, (2021) used a composite of nano zeolite beta and MWCNT as support for $Ni(OH)_2$ for the electro-oxidation of 0.14 M ethylene glycol in 1.6 M NaOH, thereby extracting 12.52 mA/cm$^2$. The study also revealed that composite support showed better activity than individual nano zeolite beta and

MWCNT support, as well as unsupported $Ni(OH)_2$. The surfactant-based Ni catalyst was investigated as an anodic catalyst for ethylene glycol oxidation. Ni, sodium dodecyl sulphate (SDS) poly(o-aminophenol) was electrochemically deposited into carbon paste electrode to oxidize 0.28 M ethylene glycol in basic medium, generating 11.1 $mA/cm^2$ current density (Ojani et al., 2009). The same group also electrodeposited Ni, SDS, poly (p-aminoacetanilide) and Ni, Trition X-100, poly (m-toluidine) into carbon paste electrode to produce 5.9 $mA/cm^2$ and 10.6 $mA/cm^2$ current densities, respectively from ethylene glycol oxidation in NaOH medium (Table 2.2) (Ojani et al., 2013; Ojani et al., 2011).

**Table 2.2: Comparison of different transition metal-based monometallic catalysts for alcohol oxidation**

| Catalyst | Electrolyte (Conc.) | Type of Alcohol (Conc.) | Current density ($mA/cm^2$) | References |
|---|---|---|---|---|
| **Monohydric alcohols** | | | | |
| Ni/Graphite | KOH (1 M) | Methanol (0.5 M) | 150 | Rahim et al., 2004 |
| NiO/N-CNF | KOH (6 M) | Methanol (1 M) | 300 | Al-Enizi et al., 2014 |
| Ni/VC | KOH (0.5 M) | Methanol (0.4 M) | 32 | Hameed and El-Sherif, 2015 |
| Ni/SPPy | $H_2SO_4$ (0.05 M) | Methanol (2 M) | 7.4* | Das et al., 2016 |
| Ni/3D Porous graphene | KOH (1 M) | Methanol (0.75 M) | 64.6 | Zhu et al., 2017 |
| Ni/RGO | KOH (1 M) | Methanol (4 M) | 1600* | Sun et al., 2018 |
| Ni/MWCNT | KOH (0.1 M) | Methanol (0.7 M) | 15.94 | Askari et al., 2019 |
| 5%RGO/NiO-MOF | KOH (1 M) | Methanol (3 M) | 275.85 | Noor et al., 2019 |
| $NiNH_2BDC$/5%RGO | KOH (1 M) | Methanol (3 M) | 267.77 | Yaqoob et al., 2021 |
| Ni/3D Porous graphene<br>Co/3D Porous graphene | KOH (1 M) | Methanol (0.75 M) | 147.1<br>53 | Ullah et al., 2019 |
| $Co_3O_4$/PPy | KOH (1 M) | Methanol (2 M) | 111 | Khalafallah et al., 2018 |
| Co/CNF | KOH (1 M) | Methanol (3 M) | 72.78 | Thamer et al., 2017 |
| 5%GO/Co-MOF | KOH (1 M) | Methanol (3 M) | 29.1 | Mehek et al., 2017 |
| $Cu_2O$/PPy-graphene oxide | $H_2SO_4$ (0.05 M) | Methanol (2 M) | 7.9 | Pattanayak et al., 2018 |
| $Cu(OH)_2$-CuO/Cu | KOH (1M) | Methanol (0.5 M) | 42 | Anantharaj et al., 2020 |

| | | | | |
|---|---|---|---|---|
| Ni /Graphite | NaOH (0.5 M) | Ethanol (1 M) | 162 | Soliman et al., 2016 |
| Ni/ Biomass derived C | NaOH (1 M) | Ethanol (1 M) | 28.5 | Cuña et al., 2017 |
| Ni/ N doped C | NaOH (0.1 M) | Ethanol (1 M) | 327 | Shi et al., 2017 |
| Nickel(II)-bis(1,10-phenanthroline)/RGO | NaOH (1 M) | Ethanol (1 M) | 16 | Santos et al., 2019 |
| Ni/RGO | NaOH (1 M) | Ethanol (1 M) | 12 | Li et al., 2019a |
| NiO/Graphitized carbon | NaOH (0.5 M) | Ethanol (1 M) | 21.59 | Hameed, 2019 |
| Co/Graphite | NaOH (0.5 M) | Ethanol (1 M) | 29.40 | El-Jemni et al., 2022 |
| $Co_3O_4$ | NaOH (0.5 M) | Ethanol (1 M) | 200 | Hassen et al., 2016 |
| $Cu_2O$/ppy | NaOH (0.1 M) | Ethanol (5 M) | 18 | El Attar et al., 2020 |
| **Polyhydric alcohols** | | | | |
| Ni SDS poly(o-aminophenol)/C | NaOH (0.1 M) | EG (0.28 M) | 11.1 | Ojani et al., 2009 |
| Ni SDS (p-aminoacetanilide)/C | NaOH (0.1 M) | EG (0.25 M) | 5.9 | Ojani et al., 2011 |
| Ni Trition X-100, poly (m-toluidine) | NaOH (0.1 M) | EG (0.06 M) | 10.6 | Ojani et al., 2013 |
| Ni nanofibers | NaOH (0.2 M) | EG (0.03 M) | 10 | Hosseini et al., 2017 |
| $Ni(OH)_2$ /nano zeolite beta and MWCNT | NaOH (1.6 M) | EG (14 M) | 12.52 | Eshagh-Nimvari and Karim Hassaninejad-Darzi, 2021 |
| Ni electrode | KOH (1 M) | Glycerol (0.1 M) | 16 | Houache et al., 2018 |
| Ni/ N doped C | NaOH (1.0 M) | Glycerol (50 mM) | ~ 4 | Wang et al., 2020b |
| Ni -poly-Eriochrome Black T | NaOH (0.1 M) | Glycerol (3 mM) | 0.015[#] | Radi et al., 2022 |
| Ni NPs | KOH (1M) | Glycerol (0.1 M) | 42.6 | Houache et al., 2021 |
| Ni/ Graphaite pencil | NaOH (1 M) | Glycerol (0.1 M) | 36.5 | Nacef et al., 2021 |
| CuO | $Na_2B_4O_7$ (0.1 M)<br>NaOH (0.1 M) | Glycerol (0.1 M) | 2.5<br>9.5 | Liu et al., 2020 |
| $MnO_2$ | $Na_2B_4O_7$ (0.1 M) | Glycerol (0.1 M) | 6 | Tran et al., 2021 |

[*]Current density in mA/$mg_{metal}$, #current in mA

The electro-oxidation of glycerol was mostly studied using supported and unsupported Ni electrodes. Houache et al., (2018) modified a polycrystalline Ni electrode for glycerol oxidation in alkaline medium to achieve a current density of approximately 16 mA/cm$^2$. The same group improved the performance of Ni by modifying its morphologies, resulting in a current density of 42.6 mA/cm$^2$ (Houache et al., 2021). Different carbon supports, such as graphite pencil and nitrogen-doped mesoporous carbon, were employed for Ni catalysts with high catalytic activity (Table 2.2) (Nacef et al., 2021; Wang et al., 2020b). Radi et al., (2022) deposited Ni and poly-Eriochrome Black T electrochemically for glycerol oxidation in a basic medium. The behaviour of CuO for glycerol oxidation in basic medium was studied at pH 9 and 13, with current densities of 2.5 mA/cm$^2$ and 9.5 mA/cm$^2$, respectively (Liu et al., 2020). Tran et al., (2021) employed $MnO_2$ catalyst for electro-oxidation of glycerol to achieve current density of 6 mA/cm$^2$.

#### 2.1.2.3 Comparison among different alcohols

**For monohydric alcohols**

Shamsipur et al., (2013) studied MWCNT supported NiO for the electro-oxidation of methanol, ethanol, 1-propanol, 1-butanol and 1-pentanol. The NiO/MWCNT showed similar activity towards all the alcohols. Guo et al., (2019a) developed a 3D porous nickel film for methanol and ethanol oxidation, generating 59 mA/cm$^2$ and 45 mA/cm$^2$ respectively in basic medium.

**For polyhydric alcohols**

Lin et al., (2017) employed Ni/Indium tin oxide to compare the activity for the electro-oxidation of ethylene glycol and glycerol in 0.2 M NaOH, generating 0.8 and 0.46 mA current at 0.64 V respectively. Sun et al., (2017) studied the effect of different alcohols (glycerol, 1,2 propane diol, 1,3 propane diol, 1 propanol and 2 propanol) on electro-oxidation in alkaline environment using a $Co_3O_4$ catalyst. Glycerol had the highest activity, followed by 1,2 propane diol, 1,3 propane diol, 1 propanol and 2 propanol. It was also observed that higher KOH concentration facilitated the activity for all the alcohols.

## 2.2 Bimetallic catalysts for alcohol oxidation

### 2.2.1 Noble metal catalysts

The noble metal based bimetallic catalyst was introduced to improve the performance of alcohol oxidation. The co-metals were anticipated to offer a synergistic effect while also

reducing the poisoning effect of CO adsorption. Different combination of noble metals was used as bimetallic catalyst in order to overcome the above mentioned issue.

#### 2.2.1.1 For monohydric alcohols

Among noble metal-based bimetallic catalysts, the most explored catalysts for methanol oxidation were Pt-based bimetallic catalysts. Zhang et al., (2014b) synthesized PtPd bimetallic nanoparticles on graphene and obtained 2.7 $mA/cm^2$ current density via methanol oxidation. Similarly, polycrystalline PdPt and $TiO_2$ supported PtPd performed better in the presence of methanol (Maksic et al., 2015; Xu et al., 2021). The bimetallic catalysts also performed better than the monometallic catalysts for methanol oxidation. Moreover, $TiO_2$ was found to be a better support than carbon black. Hernandez-Fernandez et al., (2015) evaluated the performance of commercial PtRu/C catalyst to Pt/C catalyst for methanol oxidation and observed that bimetallic catalysts exhibited higher catalytic activity than monometallic catalysts (Table 2.3). Various types of PtRu catalysts were investigated for methanol oxidation. The mesoporous and graphitic carbon supported PtRu bimetallic catalysts exhibited a mass activity of approximately 375 and 1674.2 mA/mg respectively, whereas PtRu/$TiO_2$ generated a current density of 12.3 $mA/cm^2$ for methanol oxidation (Liu et al., 2017; Zhang et al., 2020a; Zheng et al., 2020). Li et al., (2017a) used hydrothermal treatment to prepare PtRu nanocrystals for the electro-oxidation of methanol. The bimetallic PtRu catalysts showed better performance than Pt and Ru catalysts in acidic medium containing 1 M methanol. The PtAu/RGO composite had a mass activity of 0.81 $A/mg_m$ for methanol oxidation in basic medium, while electrochemically synthesized PtAu/graphene produced 7.3 $mA/cm^2$ current density (Chang et al., 2018; Feng et al., 2017). On the other hand, 3D PtAu nanoframes harvested 250 mA/mg current density from methanol oxidation in acidic medium (Yoo et al., 2019). $Pd_{10}Ag_{10}$/CNT, with a current density of 731.2 $mA/mg_{Pd}$, was observed to be the best performing catalyst among the other PdAg combinations, while the hollow porous PtAg double-shelled nanocage structured catalyst had 2.2 times higher activity than Pt black (Satyanarayana et al., 2018; Yao et al., 2021). Kumar et al., (2020) incorporated PdAu into N-doped graphene to yield a current density of 1510 $mA/mg_{Pd}$ during methanol oxidation in basic medium. The AuAg alloy employed for methanol oxidation had 16.3 times more mass activity than Au in basic medium (Yu et al., 2020).

The most commonly used noble metal-based bimetallic catalysts for ethanol oxidation were Pt and Pd-based catalysts. $Pt_{30}Pd_{70}$/VC was found to exhibit higher catalytic activity than Pt/VC and Pd/VC. It was also observed that increase in temperature improved the oxidation

performance of the catalysts (Dutta and Datta, 2013). Similarly, $Pt_{23}Pd_{77}$/C demonstrated enhanced catalytic activity than monometallic catalysts in both acidic and basic media. The electrochemical performance was superior in basic medium for all the catalysts. The $Pt_{23}Pd_{77}$/C produced 2453.7 mA/mg current density in basic medium (Zhang et al., 2020b). Acetylene black was modified with $HNO_3$ treatment and used as a support for PtRu catalyst, thereby generating a current density of 78.4 $mA/cm^2$ from ethanol oxidation in acidic medium (Choudhary and Pramanik, 2020). The PtAu/VC was used to electro-oxidize ethanol in an acidic medium, resulting in a mass activity of 240.1 $mA/mg_m$, which was twice as good as the monometallic counterpart (Zhou et al., 2014). The carbon supported PdAu catalysts was proved to be promising for ethanol oxidation (Qin et al., 2014). Chen et al., (2016) modified Pd by depositing Au on carbon to form a core-shell catalyst. The bimetallic catalyst demonstrated 5.4 times better catalytic activity than Pd/C catalyst for ethanol oxidation in a basic environment, producing 36.1 $mA/cm^2$ current density. The $Pd_{67}Au_{33}$/C used for ethanol oxidation generated approximately 130 $mA/cm^2$ current density in basic medium, which was much higher than that obtained from Pd/C (Dutta et al., 2017). Carrión-Satorre et al., (2016) synthesized PdRu/VC for ethanol oxidation in basic medium, resulting in a current density of 0.425 $mA/cm^2\mu g^{-1}_m$. Bimetals Ag and Au were electrodeposited on carbon fiber electrodes for the electro-oxidation of ethanol, extracting 1834 mA/mg current in basic medium (Wang et al., 2022a).

### 2.2.1.2 For polyhydric alcohols

The oxidation of polyhydric alcohol was mostly executed using Pt and Pd-based bimetallic catalysts. The Pt-based bimetallic catalysts were rigorously employed for the electro-oxidation of EG, out of which PtPd bimetallic catalyst was mostly reported. The supported PtPd catalyst was found to be efficient for ethylene glycol oxidation (Table 2.3). Ju et al., (2016) developed RGO supported PtPd alloyed nanoflower using a bio-directed one-pot synthesis technique. In basic medium, PtPd/RGO (134.51 $mA/cm^2$) showed better catalytic activity than PtRu/C (59.82 $mA/cm^2$), Pt/C (60.34 $mA/cm^2$), Pt/RGO (53.25 $mA/cm^2$), Pd/RGO (10.68 $mA/cm^2$) and Pt black (23.68 $mA/cm^2$) for ethylene glycol oxidation. Ren et al., (2018) reported similar observations when RGO supported core shell PdPt nanocluster was used for ethylene glycol oxidation, which produced 128.96 $mA/cm^2$ current density. Moreover, the hydrothermally synthesized 3D N-doped RGO hydrogel supported PtPd catalyst exhibited a mass activity of 1115.5 $mA/mg_m$ in the presence of ethylene glycol, which was higher than the activity of Pt/3D-N-RGO, Pd/3D-N-RGO, Pt/C and Pd/C (Shi et al., 2019). The use of agro-waste derived carbon

as support to bimetallic PdPt catalyst was observed to be beneficial for ethylene glycol electro-oxidation (Kasturi et al., 2020). Zheng et al., (2014) reported the use of RGO supported porous PtRu nanodendrites for ethylene glycol oxidation in basic medium. The findings revealed that PtRu/RGO (1058.9 $mA/mg_m$) outperformed Pt/RGO (245.7 $mA/mg_m$) and commercial PtRu/C (352 $mA/mg_m$) catalysts. The PtAg catalyst had a mass activity of 5042.9 mA/mg for ethylene glycol oxidation, whereas hollow AgPt nanotubes generated a current density of 75.23 $mA/cm^2$ in basic environment (Gao et al., 2018; Zhu et al., 2018). In case of Pd-based bimetallic catalysts, several supported PdAg catalysts were found to be effective for ethylene glycol oxidation (Table 2.3). The PdAg/VC catalysts synthesized using the polyol reduction method showed higher catalytic activity (956 $mA/mg_{Pd}$) than Pd/VC (197 $mA/mg_{Pd}$) (Yang et al., 2015b). Similarly, PdAg/VC with Pd (100) facets generated 196.26 $mA/cm^2$ current density during electro-oxidation of ethylene glycol (López–Coronel et al., 2019). Further, nitrogen-doped graphene supported PdAg nanoflower and nanocapsule demonstrated mass activities of 5304.1 and 6118.3 $mA/mg_{Pd}$ respectively for ethylene glycol oxidation (Li et al., 2019b; Zhai et al., 2019). The activity of the above-mentioned catalysts was 1.4 and 5.4 to 5.8 times higher than PdAg and commercial Pd/C catalyst respectively. counterparts Liu et al., (2016a) synthesized AuPd core shell nanocrystals for efficient electro-oxidation of ethylene glycol to generate 96.1 $mA/cm^2$. The bimetallic catalysts had significantly higher activity than their monometallic.

Glycerol oxidation was reported less as compared to ethylene glycol, where mainly Pd-based bimetallic catalysts were used. Lam et al., (2015) evaluated the performance of carbon black supported PdAu and PdAg catalysts for glycerol oxidation, thereby generating 14 and 6 $mA/cm^2_{Pd}$ current densities respectively. The MWCNT supported PdAg catalyst was designed to electro-oxidize glycerol in an alkaline environment, producing approximately 40 $mA/cm^2$ (Benipal et al., 2017). Moreover, the use of Au as a promoter for Pt/VC and Pd/VC favoured the oxidation of glycerol in basic medium (Table 2.3) (Li et al., 2017b). The activity of poly(3,4-ethylenedioxythiophene) (PEDOT) supported $Pd_5Ru_1$ catalyst (4.3 $mA/cm^2$) was investigated for the oxidation of 0.1 M glycerol in 1 M NaOH (Dash and Munichandraiah, 2015). On the other hand, Au was electrodeposited on Ag/RGO at concentrations ranging from 0.3 to 2.3 wt.%, resulting in a maximum current density of 49.6 $mA/cm^2$ from glycerol oxidation (Jin et al., 2016). In the presence of glycerol, the RGO supported PtPd core shell catalyst yielded a mass activity of 1533.49 $mA/mg_{metal}$ (Yang et al., 2018). Velázquez-Hernández et al., (2021) examined PdPt/VC, PdIr/VC and PdRu/VC for the oxidation of pure and crude glycerol. PdPt/VC demonstrated the highest activity for both pure and crude glycerol,

followed by PdRu/VC and PtIr/VC. However, the catalysts showed lower performance in crude than in pure glycerol.

**Table 2.3: Comparison of different noble metal-based bimetallic catalysts for alcohol oxidation**

| Catalyst | Electrolyte (Conc.) | Type of Alcohol (Conc.) | Current density ($mA/cm^2$) | References |
|---|---|---|---|---|
| **Monohydric alcohols** | | | | |
| PtPd /Graphene | NaOH (1 M) | Methanol (0.5 M) | 2.7 | Zhang et al., 2014b |
| PdPt | KOH (0.1 M) | Methanol (0.4 M) | 20.4 | Maksic et al., 2015 |
| $PtPd/TiO_2$ | NaOH (0.5 M) | Methanol (0.1M) | 62.7 | Xu et al., 2021 |
| PtRu/C | $HClO_4$ (0.1 M) | Methanol (0.5 M) | ~ 375* | Hernandez-Fernandez et al., 2015 |
| PtRu | $H_2SO_4$ (0.5 M) | Methanol (1 M) | 1.54 | Li et al., 2017a |
| PtRu/C | $H_2SO_4$ (0.5 M) | Methanol (1 M) | 170.2# | Liu et al., 2017 |
| PtRu/ Graphitic support | $HClO_4$ (0.1 M) | Methanol (0.5 M) | 1674.2* | Zhang et al., 2020a |
| $PdRu/TiO_2$ | NaOH (0.5 M) | Methanol (1 M) | 12.3 | Zheng et al., 2020 |
| PtAu/RGO | KOH (0.5M) | Methanol (2 M) | 810* | Feng et al., 2017 |
| PtAu/Graphene | NaOH (1 M) | Methanol (0.5 M) | 7.3 | Chang et al., 2018 |
| 3D PtAu nanoframe | $H_2SO_4$ (0.1 M) | Methanol (1 M) | 250* | Yoo et al., 2019 |
| PtAg double shelled nanocage | $H_2SO_4$ (0.5 M) | Methanol (1 M) | 566* | Yao et al., 2021 |
| $Pd_{10}Ag_{10}/CNT$ | KOH (1 M) | Methanol (0.5 M) | 731.2* | Satyanarayana et al., 2018 |
| PdAu/N - graphene | NaOH (0.5 M) | Methanol (1 M) | 1510* | Kumar et al., 2020 |
| AuAg | NaOH (0.5 M) | Methanol (2 M) | 15* | Yu et al., 2020 |
| $Pt_{30}Pd_{70}/VC$ | NaOH (0.5 M) | Ethanol (1 M) | 270$ | Dutta and Datta, 2013 |
| $Pt_{23}Pd_{77}/C$ | KOH (1 M) | Ethanol (1 M) | 2453.7 | Zhang et al., 2020b |
| PtRu/ acetylene black with $HNO_3$ treatment | $HClO_4$ (0.1 M) | Ethanol (2 M) | 78.4 | Choudhary and Pramanik, 2020 |
| PtAu/VC | $HClO_4$ (0.1 M) | Ethanol (1 M) | 240.1* | Zhou et al., 2014 |
| PdAu/VC | KOH (1 M) | Ethanol (1 M) | ~25 | Qin et al., 2014 |
| PdAu/carbon | NaOH (1 M) | Ethanol (1 M) | 36.1 | Chen et al., 2016 |
| $Pd_{67}Au_{33}/C$ | NaOH (0.5 M) | Ethanol (1 M) | 130 | Dutta et al., 2017 |
| PdRu/VC | KOH (1 M) | Ethanol (1 M) | 0.425@ | Carrión-Satorre et al., 2016 |

| | | | | |
|---|---|---|---|---|
| AgAu/Carbon | KOH (1 M) | Ethanol (1 M) | 1834* | Wang et al., 2022a |
| **Polyhydric alcohols** | | | | |
| PtPd/RGO | KOH (1 M) | EG (0.5 M) | 134.51 | Ju et al., 2016 |
| PdPt/RGO | KOH (1 M) | EG (0.5 M) | 128.96 | Ren et al., 2018 |
| PdPt/3D N-RGO | KOH (0.5 M) | EG (0.5 M) | 1115.5* | Shi et al., 2019 |
| $Pd_1Pt_{0.5}$/C | $H_2SO_4$ (0.5 M) | EG (0.5 M) | 80 | Kasturi et al., 2020 |
| PtRu/RGO | KOH (1 M) | EG (1 M) | 1058.9* | Zheng et al., 2014 |
| PtAg | KOH (1 M) | EG (1 M) | 5042.9* | Gao et al., 2018 |
| AgPt nanotube | KOH (0.5 M) | EG (0.5 M) | 75.23 | Zhu et al., 2018 |
| PdAg/N-graphene | KOH (1 M) | EG (1 M) | 5304.1* | Li et al., 2019b |
| PdAg /N-graphene | KOH (1 M) | EG (1 M) | 6118.3* | Zhai et al., 2019 |
| PdAg/VC | KOH (1 M) | EG (1 M) | 196.26 | López–Coronel et al., 2019 |
| Au Pd core shell nanocrystals | KOH (0.5 M) | EG (0.5 M) | 96.1 | Liu et al., 2016a |
| PdAu/carbon black<br>PdAg/carbon black | KOH (1 M) | Glycerol (0.5 M) | 14<br>6 | Lam et al., 2015 |
| PdAg/ MWCNT | KOH (1 M) | Glycerol (0.1 M) | 40 | Benipal et al., 2017 |
| PtAu/VC<br>PdAu/VC | KOH (1 M) | Glycerol (1 M) | 96.3<br>74.4 | Li et al., 2017b |
| $Pd_5Ru_1$/ PEDOT | NaOH (1 M) | Glycerol (1M) | 4.3 | Dash and Munichandraiah, 2015 |
| $Au_{1.2}$Ag/RGO | NaOH (0.5 M) | Glycerol (0.1M) | 49.6 | Jin et al., 2016 |
| PtPd/RGO | KOH (0.5 M) | Glycerol (0.5 M) | 1533.49* | Yang et al., 2018 |
| PdPt/VC<br>PdIr/VC<br>PdRu/VC | KOH (1 M) | Glycerol (1 M) | 200*<br>115*<br>120* | Velázquez-Hernández et al., 2021 |

*current density in $mA/mg_{metal}$, #current density at 60°C, $current density at 80°C, @current density in $mA/cm^2\mu g^{-1}{}_m$

### 2.2.1.3 Comparison with different alcohols

**For monohydric alcohols**

The bimetallic PdRu/CNF used for the electro-oxidation of methanol and ethanol generated 1.38 and 1.39 $mA/cm^2$ current density respectively, which was higher than Pd/CNF and Pd/C (Sikeyi et al., 2020). Kottayintavida and Gopalan, (2021) employed PdAu nanowire for

methanol and ethanol oxidation in basic environment. The catalyst generated 2256.9 and 2932.5 $mA/mg_{Pd}$ current densities for methanol and ethanol, respectively.

**For polyhydric alcohols**

Xu et al., (2017b) ultrasonically synthesized an N-doped graphene supported PdAu catalyst for the electro-oxidation of ethylene glycol and glycerol. The supported bimetallic catalyst performed better than unsupported bimetallic and supported monometallic catalysts. The PdAu/N-doped graphene produced 12.87 and 8.7 $A/mg_{Pd}$ current density from ethylene glycol and glycerol oxidation, respectively. Chen et al., (2018) utilized AuPd nanocrystals for electro-oxidation of ethylene glycol and glycerol in a basic environment, producing 58.67 and 50.64 $mA/cm^2$ current density respectively, which was significantly higher than the Pd catalyst. Wang et al., (2020c) modulated the shape of PtRh to form nanoassembly and nanodendrites for ethylene glycol and glycerol oxidation. The PtRh nanossembly performed better than PtRh nanodendrites and monometallic catalysts, with mass activity of 2.16 and 2.02 A/mg for ethylene glycol and glycerol oxidation, respectively.

**For combination of monohydric and polyhydric alcohols**

The $Pd_1Au_3$ nano-snowflakes developed for ethanol and ethylene glycol oxidation yielded 317 and 365 $mA/mg_{metal}$, respectively. Moreover, the bimetallic catalyst demonstrated higher activity than the monometallic Au and Pd catalysts (Yang et al., 2017). Xu et al., (2018c) made PdIr nanoporous aggregates for ethylene glycol and methanol oxidation in basic medium. The synthesized bimetallic catalyst performed better than PdIr nanoparticles, pure Pd and Pd/C catalysts. The PdIr nanoporous aggregates extracted 79.95 and 134.91 $mA/cm^2$ current densities from 1 M methanol and 0.5 M ethylene glycol, respectively. Silva et al., (2019) investigated the effect of Pt/Ru ratio on the PtRu/VC bimetallic catalyst for ethanol and ethylene glycol oxidation in a basic environment. $Pt_{50}Ru_{50}$/VC showed higher activity for ethanol oxidation, while $Pt_{70}Ru_{30}$/VC performed best for ethylene glycol oxidation. Moreover, ethylene glycol had a higher current density than ethanol oxidation. Gao et al., (2022) synthesized 0D-2D PdPt nanocrystals for ethanol and ethylene glycol oxidation to harvest mass activity of 7.84 and 5.55 $A/mg_{metal}$, respectively.

### 2.2.2 Noble metal/transition metal catalysts

The bimetallic catalysts formed by the combination of noble and transition metals were used for alcohol oxidation to reduce the catalyst cost associated with the use of noble metals as well as to reduce the catalyst poisoning effect. Pt and Pd were the most commonly used noble metals, with various transition metals serving as co metals for bimetallic catalysts.

### 2.2.2.1 For monohydric alcohols

Methanol oxidation was carried out extensively using Pt and Pd as the key metals in bimetallic catalysts. Transition metals such as Cu, Ni, Fe, Co, V, Mn, Mo and W, were employed as co-metals with noble metals to create bimetallic catalysts. Hosseini et al., (2015) used Pt-Cu/poly-(o-Anisidine) composite to study methanol oxidation in both acidic and basic media. The study revealed that the supported catalyst performed better in basic medium (4.5 $mA/cm^2$) than in acidic medium (1.1 $mA/cm^2$). It was also observed that supported catalyst had higher catalytic activity than unsupported Pt-Cu in both the media conditions. The RGO and MWCNT supported PtCo catalyst showed prominent performance for methanol oxidation (Table 2.4). In another study, PtCo(1:9)/RGO showed enhanced catalytic activity (38.02 $mA/cm^2$) than other Pt/Co ratios as well as Pt/RGO, whereas PtCo/MWCNT had a mass activity of 616.7 $mA/mg_{Pt}$ which was higher than Pt/MWCNT (280.6 $mA/mg_{Pt}$) and commercial Pt/C (241.2 $mA/mg_{Pt}$) (Baronia et al., 2017; Zhang et al., 2017b). The addition of W, Mo and V as bimetals to Pt/RGO increased the electrochemical activity for methanol oxidation when compared to monometallic catalysts. However, among the bimetallic catalysts tested, PtW/RGO outperformed the others (Kianfar et al., 2021). On the other hand, the effect of ordered and disordered structure was observed when a carbon supported PtFe catalyst was used for methanol oxidation. The ordered bimetallic catalyst performed better (357.9 $mA/mg_{Pt}$) than the disordered catalyst (235.1 $mA/mg_{Pt}$) and commercial catalyst (83.6 $mA/mg_{Pt}$) (Nie et al., 2021). Amin et al., (2014) found that PdNi/VC, yielding 7.64 $mA/cm^2$ current density, exhibited increased activity than Pd/VC for methanol electro-oxidation. The effect of various transition metals, such as Co, Ni and Cu, to RGO supported Pd catalysts were investigated for methanol oxidation in basic medium (Table 2.4). The activity for different catalysts followed the order as: PdNi/RGO (1092.5 $mA/mg_{Pd}$) > PdCo/RGO (1004.1 $mA/mg_{Pd}$) > PdCu/RGO (911.3 $mA/mg_{Pd}$) > Pd/RGO (400.2 $mA/mg_{Pd}$)> commercial Pd/C (142.7 $mA/mg_{Pd}$) (Ji et al., 2018). In another study PdMn/RGO and PdFe/RGO demonstrated mass activity of 885.1 and 855.9 $mA/mg_{Pd}$, respectively in the presence of methanol (He et al., 2020). Atar et al., (2015) engineered $Fe_3O_4$@Ag nanoparticles on L-cystine/RGO to produce a current density of 14.6 $mA/cm^2$ at 0.6 V in 0.5 M methanol and 1 M KOH.

Pt and Pd-based catalysts were also extensively studied for ethanol oxidation. Sedighi et al., (2017) electrochemically deposited Pt and $CeO_2$ on MWCNT for ethanol oxidation in basic environment. The $PtCeO_2$/MWCNT catalyst produced a current density of 163 $mA/cm^2$, which was higher than that of Pt/MWCNT (53 $mA/cm^2$). For ethanol oxidation, the performance of PtCu/VC, PtNi/VC and PtCo/VC core shell catalysts were compared and they

generated 9.882, 13.909 and 13.309 mA/cm$^2$ current density, respectively (Hameed et al., 2019). Tian et al., (2020) investigated the effect of different types of support on PtW core shell catalysts for ethanol oxidation in acidic medium. The PtW/CNT performed best with a current density of 31.72 mA/cm$^2$. Sn was added to Pd for enhancing the performance of the catalyst for ethanol electro-oxidation. The use of MWCNT as a support to PdSn further enhanced the activity compared to carbon support (Geraldes et al., 2015). PdNi/VC also proved to be an efficient catalyst for ethanol oxidation in basic environment (Table 2.4) (Nguyen et al., 2021; Obradović et al., 2016). The use of support increased the catalytic activity of the catalyst. Moreover, exfoliated graphene oxide (EGO) supported PdNi bimetallic catalyst showed better performance than VC supported and unsupported PdNi catalysts (Tan et al., 2017). Almeida et al., (2019) observed that PdFe/VC and PdNi/VC had higher catalytic activity than Pd/VC, with mass activities of 30 and 20 A/$g_{Pd}$, respectively. Upon ethanol oxidation, PdCu nanowire extracted a mass activity of 1598 mA/mg, whereas PdZn/C showed an activity of 1500 mA/$mg_{Pd}$ (Gong et al., 2019; Kien et al., 2022).

#### 2.2.2.2 For polyhydric alcohols

The oxidation of higher alcohols was mostly carried out using Pt and Pd-based bimetallic catalysts. The Pt-$TiO_2$ hybrid catalysts with varying Pt-$TiO_2$ ratios were used for electro-oxidation of 0.1 M ethylene glycol in 0.1 M KOH. The optimum Pt/$TiO_2$ ratio was observed to be 1:5, which yielded 4.82 mA/cm$^2$ current density (Corchado-García and Cabrera, 2014). Ni and Pt were sequentially electrodeposited on a glassy carbon electrode to investigate the electrochemical activity towards ethylene glycol oxidation. The bimetallic catalyst performed better than its monometallic counterparts. Moreover, the study demonstrated that increase in temperature and pH increased the activity of the catalyst (El-Nowihy et al., 2017). PtCu nanocrystals and nanocubes were found effective for ethylene glycol oxidation in basic medium (Table 2.4) (Chen et al., 2019; Xu et al., 2018b). The effect of shape on the performance of electro-oxidation of ethylene glycol was studied extensively. Pd-based catalysts were also thoroughly investigated for ethylene glycol oxidation. Both supported and unsupported PdCu bimetallic catalysts were active in the presence of ethylene glycol (Guo et al., 2019b; Hu et al., 2018; Mukherjee et al., 2021). Shu et al., (2022) examined the performances of PEDOT supported PdCu and PdNi bimetallic catalysts for ethylene glycol oxidation in basic medium. The bimetallic catalysts showed better performance than monometallic Pd/PEDOT and Pd/C. $Pd_1Cu_3$/PEDOT and $Pd_7Ni_3$/PEDOT demonstrated mass activities of 2301.6 and 2435 mA/$mg_{Pd}$ respectively from the electro-oxidation of ethylene

glycol. Moreover, the $Pd_1Ni_1$ hollow nanospheres and $Pd_{70}Ni_{30}$ nanocubes showed high catalytic activity for ethylene glycol oxidation (López-Coronel et al., 2020; Zhang et al., 2018a). Other studies reported $Pd_{69}Co_{31}$ nanosheets to produce 85.23 mA/cm$^2$ current density in acidic medium, whereas PdCo/VC had 2373.75 mA/mg$_{Pd}$ mass activity in 1 M ethylene glycol and 1 M KOH (Liu et al., 2022; Yu et al., 2018). $PdFe_2O_3/gC_3N_4$ was employed for ethylene glycol oxidation in a basic medium, yielding 3.47 A/cm$^2$ current density. The incorporation of Fe into $Pd/gC_3N_4$ significantly increased its activity to oxidize ethylene glycol (Mari et al., 2020). The $Pd_{65}Pb_{35}$ nano-chain shaped catalysts also efficiently generated mass activity of 4.47 A/mg$_{Pd}$ from ethylene glycol oxidation in 1 M KOH, which had higher activity than other PdPb combinations and Pd/C (Zou et al., 2022).

**Table 2.4: Comparison of different noble/transition metal-based bimetallic catalysts for alcohol oxidation**

| Catalyst | Electrolyte (Conc.) | Type of Alcohol (Conc.) | Current density (mA/cm$^2$) | References |
|---|---|---|---|---|
| **Monohydric alcohols** | | | | |
| PtCu/poly- (o Anisidine) | NaOH (0.5M)<br>$H_2SO_4$ (0.5 M) | Methanol (2.78 M) | 4.5<br>1.1 | Hosseini et al., 2015 |
| PtCo(1:9)/RGO | $H_2SO_4$ (1 M) | Methanol (2 M) | 38.02 | Baronia et al., 2017 |
| PtCo/MWCNT | $H_2SO_4$ (0.5 M) | Methanol (0.5 M) | 616.7* | Zhang et al., 2017b |
| PtW/RGO<br>PtMo/RGO<br>PtV/RGO | $H_2SO_4$ (0.25 M) | Methanol (0.1 M) | 12.64<br>9.77<br>9.24 | Kianfar et al., 2021 |
| PtFe | $H_2SO_4$ (0.5 M) | Methanol (0.5 M) | 357.9* | Nie et al., 2021 |
| PdNi/VC | NaOH (0.5M) | Methanol (0.6 M) | 7.64 | Amin et al., 2014 |
| PdNi/RGO<br>PdCo/RGO<br>PdCu/RGO | KOH (0.5 M) | Methanol (2 M) | 1092.5*<br>1004.1*<br>911.3* | Ji et al., 2018 |
| PdMn/RGO<br>PdFe/RGO | KOH (0.5 M) | Methanol (2 M) | 885.1*<br>855.9* | He et al., 2020 |
| Fe3O4@Ag/ L-cystine/RGO | KOH (1 M) | Methanol (0.5 M) | 14.6 | Atar et al., 2015 |
| $PtCeO_2$/MWCNT | KOH (1 M) | Ethanol (1 M) | 163 | Sedighi et al., 2017 |
| PtCu/VC<br>PtNi/VC<br>PtCo/VC | NaOH (0.5 M) | Ethanol (0.5 M) | 9.882<br>13.909<br>13.309 | Hameed et al., 2019 |
| PtW/CNT | $H_2SO_4$ (0.5 M) | Ethanol (1 M) | 31.72 | Tian et al., 2020 |
| PdNi/VC | NaOH (0.1 M) | Ethanol (0.5 M) | 2010* | Obradović et al., 2016 |

| | | | | |
|---|---|---|---|---|
| PdNi/EGO | NaOH (0.1 M) | Ethanol (1 M) | 770.6* | Tan et al., 2017 |
| PdNi/VC | KOH (1 M) | Ethanol (1 M) | 7999* | Nguyen et al., 2021 |
| PdFe/VC<br>PdNi/VC | NaOH (1 M) | Ethanol (1 M) | 20*<br>30* | Almeida et al., 2019 |
| PdCu | KOH (1 M) | Ethanol (1 M) | 1598* | Gong et al., 2019 |
| PdZn | KOH (1 M) | Ethanol (1 M) | 1500* | Kien et al., 2022 |
| **Polyhydric alcohols** | | | | |
| Pt-$TiO_2$ | KOH (0.1 M) | EG (0.1 M) | 4.82 | Corchado-García and Cabrera, 2014 |
| PtNi/GC | NaOH (0.5 M) | EG (0.5 M) | 13 | El-Nowihy et al., 2017 |
| PtCu nanocrystal | KOH (1 M) | EG (1 M) | 4259.2* | Xu et al., 2018b |
| PtCu nanosphere | KOH (1 M) | EG (1 M) | 2146.9* | Chen et al., 2019 |
| PdCu | KOH (1 M) | EG (0.5 M) | 1648.4* | Hu et al., 2018 |
| $Pd_2Cu$ nanoflower | KOH (1 M) | EG (1 M) | 4714.1* | Guo et al., 2019b |
| Pd@CuO/VC | KOH (1 M) | EG (3 M) | 284.5 | Mukherjee et al., 2021 |
| $Pd_1Cu_3$/PEDOT<br>$Pd_7Ni_3$/PEDOT | KOH (1 M) | EG (1 M) | 2301.6*<br>2435* | Shu et al., 2022 |
| PdNi | KOH (1 M) | EG (1 M) | 3121* | Zhang et al., 2018a |
| $Pd_{70}Ni_{30}$ | KOH (2 M) | EG (1 M) | 320.32<br>501# | López-Coronel et al., 2020 |
| $Pd_{69}Co_{31}$ | $H_2SO_4$ (0.5 M) | EG (0.5 M) | 85.23 | Yu et al., 2018 |
| PdCo/VC | KOH (1 M) | EG (1 M) | 2373.75* | Liu et al., 2022 |
| $PdFe_2O_3/gC_3N_4$ | KOH (0.5 M) | EG (0.5 M) | 3470 | Mari et al., 2020 |
| $Pd_{65}Pb_{35}$ | KOH (1 M) | EG (1 M) | 4470* | Zou et al., 2022 |
| PtCu/VC<br>PtNi/VC<br>PtCo/VC | KOH (0.5 M) | Glycerol (0.5 M) | 33.5*<br>26.6*<br>23.9* | Caglar et al., 2021 |
| $PtNi_2$/VC | KOH (1 M) | Glycerol (1 M) | 1940* | Luo et al., 2022 |
| PdSn | KOH (1 M) | Glycerol (0.1 M) | 1000* | Zalineeva et al., 2015 |
| $Pd_{17}Bi_{83}$/VC | KOH (1 M) | Glycerol (1 M) | 370.75* | Velázquez-Hernández et al., 2022 |
| $AuCeO_2$/C | KOH (1 M) | Glycerol (1 M) | 75.4 | Zhang et al., 2016 |
| $AgCo_3O_4$ | KOH (1 M) | Glycerol (0.1 M) | 20 | Ashok and Kumar, 2021 |

*current density in $mA/mg_{metal}$, #current density at 50°C

The research on glycerol oxidation using noble/transition metal-based bimetallic catalysts was very limited. Caneppele et al., (2017) decorated Sb to Pt/VC for electro-oxidation of glycerol in acidic medium, which increased the current density by 41.7 times over Pt/VC. Caglar et al., (2021) examined a VC supported Pt-based bimetallic catalyst for glycerol oxidation. The study indicated that the activity of the catalysts followed the trend as: PtCu/VC (33.5 $mA/mg_{metal}$) > PtNi/VC (26.6 $mA/mg_{metal}$) > PtCo/VC (23.9 $mA/mg_{metal}$) > Pt/VC (22.3 $mA/mg_{metal}$). Moreover, the Pt/Ni ratio had a significant effect on glycerol oxidation. The $PtNi_2$/VC showed the highest activity (1.94 $A/mg_{Pt}$), followed by $PtNi_3$/VC (1.19 $A/mg_{Pt}$), Pt/VC (0.99 $A/mg_{Pt}$) and $PtNi_1$/VC (0.96 $A/mg_{Pt}$) (Luo et al., 2022). A self-supported PdSn catalyst resulted in more than 1000 $A/g_{Pd}$ mass activity from the electro-oxidation of 0.1 M glycerol in 1 M KOH (Zalineeva et al., 2015). The incorporation of Bi into Pd/VC also enhanced its activity for the electro-oxidation of pure and crude glycerol in alkaline medium. The bimetallic catalyst performed better in pure glycerol (370.75 $mA/mg_{Pd}$) than in crude glycerol (237.67 $mA/mg_{Pd}$) (Velázquez-Hernández et al., 2022). Zhang et al., (2016) added $CeO_2$ to Au/C, which increase the current density from 20.4 to 75.4 $mA/cm^2$ for glycerol oxidation, whereas $AgCo_3O_4$ produced approximately 20 $mA/cm^2$ current density (Ashok and Kumar, 2021).

### 2.2.2.3 Comparative study of different alcohols

**For monohydric alcohols**

The PdNi/MWCNT used for methanol and ethanol oxidation in basic medium had better catalytic activity, lower CO poisoning effect and lower over potentials than monometallic Pd/MWCNT catalyst (Chen et al., 2015).

**For polyhydric alcohols**

(Xu et al., 2018a) investigated Au-Cu nano-prism catalysts for ethylene glycol and glycerol oxidation, which had catalytic activity of 2263 and 2873 $mA/mg_{Au}$ respectively (Xu et al., 2017a). PdPb nanocubes were also developed for ethylene glycol and glycerol oxidation to extract current density of 16.8 and 9.2 $mA/cm^2$.

**For combination of monohydric and polyhydric alcohols**

Fathirad et al., (2017) studied the PdMo/VC bimetallic catalyst for various alcohols such as methanol, ethanol, ethylene glycol and glycerol in basic medium. For all the alcohols, the bimetallic catalyst outperformed Pd/VC in terms of catalytic activity. Among the studied alcohols, ethylene glycol had the highest current density (234.8 $mA/cm^2$), followed by glycerol (182.6 $mA/cm^2$), ethanol (121.2 $mA/cm^2$) and methanol (71.2 $mA/cm^2$). Various combinations

of NiAg nanoalloy supported on RGO were synthesized for alcohol oxidation in basic medium. The best performing $Ni_{66}Ag_{34}$/RGO catalyst generated 60.6 and 43.4mA/cm$^2$ current density in the presence of ethylene glycol and ethanol respectively (dos Santos et al., 2022).

### 2.2.3 Transition metal catalysts

The study regarding the use of low cost transition metal as bimetallic catalyst for alcohol oxidation was the recent approach. This approach was taken to completely replace noble metals for further reduction of cost and to omit the CO adsorption issue. However, the use of transition metal as catalyst had catalytic activity lower than noble metal based bimetallic catalysts. Researchers were trying to engineer the transition metal based bimetallic catalyst to enhance the catalytic activity for alcohol oxidation.

#### 2.2.3.1 For monohydric alcohols

One of the most recent research topics has been the study of alcohol oxidation using transition metal bimetallic catalysts. The methanol oxidation was mostly carried out with Ni-based bimetallic catalysts. Among the numerous Ni-based catalysts, NiCo-based bimetallic catalysts were most commonly used for electrochemical conversion of methanol to extract energy. Tarrús et al., (2014) electrochemically synthesized CoNi alloy and employed it for methanol oxidation, extracting 25 mA/cm$^2$ current density in 0.5 M NaOH. Other studies reported the use of NiCo as anodic catalyst to generate 58 and 160 mA/cm$^2$ from methanol oxidation in basic medium (Table 2.5) (Arunachalam et al., 2017; Cui et al., 2015). Moreover, they found that unsupported NiCo performed better than pristine Ni and Co for methanol oxidation (Cui et al., 2015). The effect of hydroxides and oxides of electrodeposited NiCo bimetallic catalyst with respect to their composition on methanol oxidation was investigated in basic medium. It was observed that bimetallic oxides with Ni content of 46% showed best catalytic activity (250 A/g approx.) in presence of methanol (Sun and Xu, 2015). The supported $Ni_3Co_1$/C-N/CNT and NiCo nanoporous carbon composite based on mixed metallic Ni-Co-MOF were also observed to be efficient electrocatalysts for methanol oxidation, harvesting 213 and 178 mA/cm$^2$ current density respectively (Deng et al., 2017; Rezaee and Shahrokhian, 2019). Core shell NiCo/graphene catalyst prepared by microwave irradiation was used for methanol oxidation to extract 48.1 µA current (Mohanapriya and Gopi, 2022). The Ni and NiCu nanoparticle were electrodeposited on glassy carbon to study their behaviour in the presence of methanol. NiCu performed better than Ni in basic medium with a current density of approximately 320 mA/cm$^2$ (Danaee et al., 2009). The $gC_3N_4$ supported NiCu showed lower

activity than Ni/g$C_3N_4$, but higher activity than Cu/g$C_3N_4$. The poor performance of NiCu/ g$C_3N_4$ was attributed to the unoptimized composition of Ni and Cu in the bimetallic catalyst (Pieta et al., 2019). Tammam et al., (2015) used a bimetallic catalyst based on $NiO_x$ and $MnO_x$ for methanol oxidation, where the use of $MnO_x$ enhanced the catalytic performance. The NiSn alloy nanoparticle was incorporated into CNF to study the effect of calcination temperature and Sn content on the electro-oxidation of methanol. The bimetallic catalyst with 10% Sn content showed the highest catalytic activity (85 mA/cm$^2$) for 2 M methanol oxidation with a significant effect of calcination temperature (Barakat et al., 2018). Jia et al., (2020) developed NiSe/RGO at different temperatures and found that a calcination temperature of 550°C was optimal for better electrochemical oxidation of methanol. The ZnO/$CeO_2$dots@/CNF was used as an anodic catalyst to produce 16.3 mA/cm$^2$ current density from methanol (Ghouri et al., 2016). Zhang et al. electrochemically synthesized $Fe_2(MoO_4)_3$ with varied morphologies by altering synthesised parameters and used them for methanol electro-oxidation in basic environment. The observed electrochemical activity of $Fe_2(MoO_4)_3$ nanotubes in 0.1 M KOH and 1 M methanol was 3.27 mA/cm$^2$ (Zhang et al., 2017a).

The study of ethanol oxidation by transition metal based bimetallic catalysts was less extensive than that of methanol. Similar to methanol, electro-oxidation of ethanol was conducted mostly using Ni-based bimetallic catalysts, with NiCo being the most commonly reported. Ni and Co on nitrogen-doped RGO was used to generate 40 mA/cm$^2$ current density for ethanol oxidation. In addition, the use of bimetallic NiCo/RGO increased the current density to 80 mA/cm$^2$ under the same conditions (Kakaei and Marzang, 2016). The $Ni_3Co_1$/C-N/CNT catalyst extracted 181 mA/cm$^2$ current density from ethanol oxidation in 1 M NaOH medium, whereas NiCo/RGO used as anode material yielded a current density of ~30 mA/cm$^2$ (Deng et al., 2017; Hassanzadeh et al., 2019). The performance of nickel, cobalt and iron oxyhydroxides was investigated for ethanol oxidation and it was observed that nickel oxyhydroxides performed better than the other metal hydroxides. Moreover, the bimetallic nickel cobalt oxyhydroxides showed better results, but nickel iron oxyhydroxides exhibited lower performance than nickel oxyhydroxides (Martín-Yerga et al., 2019). The synthesized Ni and $MnO_2$-based bimetallic catalyst demonstrated a mass activity of 4.3 A/$mg_{Ni}$ for the oxidation of 0.5 M ethanol in 1 M KOH (Nakayama et al., 2019). The effect of varied weight percentages of W in Ni/CNF on the electro-oxidation of ethanol was studied in alkaline media. The 10 wt.% WNi/CNF achieved the maximum current density of 124.65 mA/cm$^2$ upon electro-oxidation of 2 M ethanol in 1 M KOH. The increased temperature and ethanol concentration favoured the higher activity of the catalyst (Zaher et al., 2020). Moreover, the rod-shaped CuNi alloy

and electrochemically modified Cu-doped NiOOH were highly active towards ethanol oxidation in 1 M KOH (Table 2.5) (Miao et al., 2021; Wang et al., 2022b). VC supported NiMo-based catalysts were also used for ethanol electro-oxidation in 0.05 M NaOH, resulting in a current density of 11.4 mA/cm$^2$ (Kazan and Bayramoğlu, 2021).

### 2.2.3.2 For polyhydric alcohols

Studies regarding the electro-oxidation of polyhydric alcohols using transition metal-based bimetallic catalysts is quite limited. The reported studies mainly focused on the Ni-based bimetallic catalysts for ethylene glycol oxidation. Sun et al., (2015) electrodeposited NiCo spinel oxides on a stainless steel (SS) substrate to generate 75 mA current from 0.5 M ethylene glycol in 1 M KOH. The NiTi/ITO was used to oxidize 0.7 M ethylene glycol, thereby generating 1.4 mA current at 1 V (Yu et al., 2019). Both supported and unsupported NiMn were effective for electro-oxidation of ethylene glycol in basic medium (Table 2.5). The addition of support enhanced the performance of the catalyst compared to the unsupported catalyst (Hefnawy et al., 2021). The incorporation of Mn improved the performance of the bimetallic catalysts and showed better performance than monometallic catalysts (Hameed et al., 2022). Sultan et al., (2023) observed that Ni-$PbO_2$/graphene (172 mA/cm$^2$) showed higher current density than Ni-$PbO_2$ (87 mA/cm$^2$) and Ni (68 mA/cm$^2$) when oxidizing 1 M ethylene glycol. The Fe/VC catalyst was also very active for ethylene glycol oxidation, thereby producing 14.6 mA/cm$^2$ current density, which increased to 28.2 and 32.6 mA/cm$^2$ on introducing Co and Ni as co-metals respectively (Gayathri et al., 2022). Abbaci et al., (2022) added CoMn to montmorillonite (Mt) to extract approximately 2 mA/cm$^2$ from 0.8 M ethylene glycol oxidation.

The Ni-based bimetallic catalysts outperformed other transition metal-based bimetallic catalysts for glycerol oxidation. The VC supported NiCo catalysts were effective for glycerol oxidation in basic medium (Table 2.5). The observed mass activity for NiCo/VC from the oxidation of 0.1 M glycerol was 65 mA/$g_{metal}$, whereas porous $NiCoO_2$/VC exhibited a current density of 23 mA/cm$^2$ (Ashok et al., 2018; Oliveira et al., 2013). Oliveira et al., (2014) used Ni-based bimetallic catalyst for glycerol oxidation in basic environment. The NiFe/VC generated higher current density than NiCo/VC. However, Ni/VC had the highest activity for glycerol oxidation. The effect of Bi loading on glycerol oxidation was studied by investigating the activity of NiBi bimetallic catalyst. The $Ni_{90}Bi_{10}$ catalyst had the highest activity of 96.2 mA/cm$^2$, followed by $Ni_{95}Bi_5$, $Ni_{98}Bi_2$ and Ni (Houache et al., 2020). The AC supported NiCu and NiCu mesoporous films produced current densities of 11.7 and 60.8 mA/cm$^2$ respectively

from electro-oxidation of glycerol (Rizk and Abd El-Moghny, 2021; Zhang and Shen, 2021). Oh et al., (2023) electrochemically synthesized CuCo oxide for glycerol oxidation, exhibiting a mass activity of 21.3 $mA/mg_{catalyst}$. The bimetallic oxide-based catalyst showed higher activity than monometallic oxides. Another study used different Co-based spinel oxides for electro-oxidation of glycerol. The highest activity was observed for $CuCo_2O_4$, followed by $NiCo_2O_4$, $CoCo_2O_4$, $FeCo_2O_4$, $ZnCo_2O_4$ and $MnCo_2O_4$ (Han et al., 2020).

**Table 2.5: Comparison of different transition metal-based bimetallic catalysts for alcohol oxidation**

| Catalyst | Electrolyte (Conc.) | Type of Alcohol (Conc.) | Current density ($mA/cm^2$) | References |
|---|---|---|---|---|
| **Monohydric alcohols** | | | | |
| CoNi | NaOH (0.5 M) | Methanol (1.2 M) | 25 | Tarrús et al., 2014 |
| NiCo | NaOH (1 M) | Methanol (0.5 M) | 58 | Cui et al., 2015 |
| NiCo | KOH (1 M) | Methanol (0.5 M) | 250* | Sun and Xu, 2015 |
| NiCo | KOH (1 M) | Methanol (1 M) | 160 | Arunachalam et al., 2017 |
| $Ni_3Co_1$/C-N/CNT | NaOH (1 M) | Methanol (1 M) | 213 | Deng et al., 2017 |
| NiCo/C | NaOH (0.5 M) | Methanol (0.5 M) | 178 | Rezaee and Shahrokhian, 2019 |
| NiCu | NaOH (1 M) | Methanol (0.7 M) | 320 | Danaee et al., 2009 |
| $NiCu/gC_3N_4$ | NaOH (1 M) | Methanol (3 M) | 1.6 | Pieta et al., 2019 |
| $NiO_xMnO_x$ | NaOH (0.5 M) | Methanol (1 M) | 12.7 | Tammam et al., 2015 |
| NiSn/CNF | KOH (0.5 M) | Methanol (2 M) | 85 | Barakat et al., 2018 |
| NiSe/RGO | KOH (1 M) | Methanol (0.5 M) | 59.8 | Jia et al., 2020 |
| $ZnO/CeO_2$dots@/CNF | KOH (1 M) | Methanol (3 M) | 16.3 | Ghouri et al., 2016 |
| $Fe_2(MoO_4)_3$ | KOH (0.1 M) | Methanol (1 M) | 3.27 | Zhang et al., 2017a |
| NiCo/RGO | KOH (1 M) | Ethanol (0.5 M) | 80 | Kakaei and Marzang, 2016 |
| $Ni_3Co_1$/C-N/CNT | NaOH (1 M) | Ethanol (1 M) | 181 | Deng et al., 2017 |
| NiCo/RGO | pH 13 | Ethanol (0.25 M) | 30 | Hassanzadeh et al., 2019 |
| $Ni_{0.69}Co_{0.31}O_xH_y$ | NaOH (0.1 M) | Ethanol (1 M) | 40 | Martín-Yerga et al., 2019 |

| | | | | |
|---|---|---|---|---|
| $NiMnO_2$ | KOH (1 M) | Ethanol (0.5 M) | 4300* | Nakayama et al., 2019 |
| NiW/CNF | KOH (1 M) | Ethanol (2 M) | 124.65 | Zaher et al., 2020 |
| CuNi | KOH (1 M) | Ethanol (0.2 M) | 86.1 | Miao et al., 2021 |
| Cu-NiOOH | KOH (1 M) | Ethanol (1 M) | 233 | Wang et al., 2022b |
| $NiMo_2C$/C | NaOH (0.05 M) | Ethanol (0.5 M) | 11.4 | Kazan and Bayramoğlu, 2021 |
| **Polyhydric alcohols** | | | | |
| NiCo/SS | KOH (1 M) | EG (0.5 M) | 75 | Sun et al., 2015 |
| NiTi/ITO | KOH (1 M) | EG (0.7 M) | 7 | Yu et al., 2019 |
| NiMn/RGO | KOH (1 M) | EG (1 M) | 38 | Hefnawy et al., 2021 |
| NiMn/CNF | NaOH (4 M) | EG (1 M) | 15.95 | Hameed et al., 2022 |
| $NiPbO_2$/graphene | NaOH (1 M) | EG (1 M) | 172 | Sultan et al., 2023 |
| FeNi/VC | KOH (0.5 M) | EG (1 M) | 32.6 | Gayathri et al., 2022 |
| FeCo/VC | KOH (0.5 M) | EG (1 M) | 28.2 | Gayathri et al., 2022 |
| CoMn/Montmorillonite | NaOH (0.1 M) | EG (0.8 M) | 2 | Abbaci et al., 2022 |
| NiCo/VC | NaOH (0.1 M) | Glycerol (0.1 M) | 65* | Oliveira et al., 2013 |
| $NiCoO_2$/VC | KOH (1 M) | Glycerol (0.1 M) | 23 | Ashok et al., 2018 |
| NiFe/VC | NaOH (0.1 M) | Glycerol (0.1 M) | 70* | Oliveira et al., 2014 |
| $Ni_{90}Bi_{10}$ | KOH (1 M) | Glycerol (0.1 M) | 96.2 | Houache et al., 2020 |
| NiCu/AC | NaOH (0.1 M) | Glycerol (0.1 M) | 11.7 | Zhang and Shen, 2021 |
| NiCu | NaOH (0.3 M) | Glycerol (0.1 M) | 60.8 | Rizk and Abd El-Moghny, 2021 |
| CuCo | KOH (0.1 M) | Glycerol (0.1 M) | 21.3* | Oh et al., 2023 |

*current density in $mA/mg_{metal}$

## 2.3 Knowledge gap and motivation

The detailed literature review as discussed above provided an overview about the various types of electrocatalysts used for the electro-oxidation of different alcohols. The most commonly used noble metal catalysts for alcohol electro-oxidation were Pt and Pd. These metals, however, were subjected to CO poisoning during alcohol reaction due to adsorption of CO on the metal surfaces. Even, the bimetallic noble metal based catalysts were unable to mitigate the issue of CO adsorption on the catalytic surface completely. On the other hand, these metals imparted cost to the alcohol oxidation process, rendering their use economically less feasible.

Both the above issues were initially addressed with the incorporation of various supports with high surface area (VC, RGO, CNF, AC, mesoporous carbon and graphene) as well as low cost transition metals (Ni, Cu, Co, Fe, Mn, Mo, Sn, W and Bi). These approaches helped in reducing CO adsorption on the catalyst surface while reducing the cost of catalysts. To make the electro-oxidation of alcohol more economically viable for fuel cell, the noble metals were completely replaced by transition metals as catalysts. The activity of transition metal-based catalysts was significantly lower than that of noble metals. There lies a scope of research where improvement in catalytic activity was required for alcohol oxidation. In terms of alcohol, methanol and ethanol were explored to some extent for electro-oxidation using transition metal catalysts. It was also observed that electro-oxidation of polyhydric alcohols, such as ethylene glycol and glycerol, generated high current density compared to monohydric alcohols, owing to high volumetric density of the former. But only a few studies have been conducted using transition metal catalysts for the electro-oxidation of polyhydric alcohols. The studies till date showed poor electrocatalytic activity. There is also lack of comparative studies regarding the effect of various supports and transition metals on the electro-oxidation of polyhydric alcohols in both acidic and alkaline media. The activity of low cost transition metals need to be enhanced so to make it feasible for fuel cell application So, in this thesis, a detailed study using various transition metals was carried out to explore the most active electrocatalysts for polyhydric alcohol oxidation. This study also explored the effect of incorporation of different supports with active metal. The support is expected to increase the catalytic activity of the catalyst. There is also a need of optimizing different operating parameters such as alcohol concentration, electrolyte concentration, temperature and type of polyhydric alcohols. The novelty of this thesis is the systematic study to find out the most suitable supported low cost catalysts as well as process conditions required for electro-oxidation of polyhydric alcohols

using various supports and transition metals. The present study sought to achieve these by formulating the following objectives.

## 2.4 Objectives of the thesis

The primary objective of this study was to develop highly active and stable low cost transition metal based catalysts for the electro-oxidation of polyhydric alcohols. This study also conducted to determine the best operating parameters for the developed catalysts for electro-oxidation of polyhydric alcohols. Ethylene glycol was selected as the polyhydric alcohol. Detailed objectives are discussed below:

1. Study the effect of incorporation of various supports such as activated carbon, vulcan carbon, alumina-based templated carbon and reduced graphene oxide into transition metal-based catalysts.
2. Investigation of supported transition metals such as Cu, Ni, Co and Fe based catalysts for the electro-oxidation of ethylene glycol.
3. Development of supported bimetallic electrocatalysts for the oxidation of ethylene glycol.
4. Determination of the most suitable operating parameters for the developed catalysts.
5. Application of the developed catalyst to fuel cell study.

# *Chapter 3*
# *Experimental Details*

# 3. Experimental details

## 3.1 Materials

Copper nitrate trihydrate [$Cu(NO_3)_2.3H_2O$, Merck LifeScience Pvt Ltd], nickel nitrate hexahydrate [$Ni(NO_3)_2.6H_2O$, Merck LifeScience Pvt Ltd], iron (III) nitrite nonahydrate [$Fe(NO_3)_3.9H_2O$, Merck LifeScience Pvt Ltd], cobalt nitrate hexahydrate [$Co(NO_3)_2.6H_2O$, Merck LifeScience Pvt Ltd] were used as metal precursors. Aluminium nitrate nonahydrate [$Al(NO_3)_3.9H_2O$, Merck LifeScience Pvt Ltd], sodium dodecyl sulphate [SDS, Merck LifeScience Pvt Ltd] and ammonia solution [Merck LifeScience Pvt Ltd] were used for the preparation of the alumina template. Acetonitrile [$CH_3CN$, Spectrochem] was employed as a carbon precursor to prepare alumina-based templated carbon [ALS-TC] for use as catalyst support. Hydrofluoric acid [HF, Merck LifeScience Pvt Ltd] was used as a template remover from template-carbon composite. Graphite [Sigma Aldrich], sulphuric acid [$H_2SO_4$, Merck LifeScience Pvt Ltd], sodium nitrate [$NaNO_3$, Merck LifeScience Pvt Ltd], potassium permanganate [$KMnO_4$, Merck LifeScience Pvt Ltd], hydrogen peroxide [$H_2O_2$, Merck LifeScience Pvt Ltd], hydrochloric acid [HCl, Merck LifeScience Pvt Ltd] and hydrazine hydrate [$N_2H_4.H_2O$, Sigma Aldrich] were used for RGO preparation, to be used as suppport for the catalysts. Activated carbon (AC) [C9157, Sigma Aldrich] and vulcan carbon (VC) [XC72R, Cabot Corp] were purchased directly to be also used as support materials. Nafion® solution [Sigma Aldrich] was used as the binder for electrode preparation. The potassium hydroxide [KOH, Merck LifeScience Pvt Ltd] was used in electrochemical studies. Ethylene glycol [Merck LifeScience Pvt Ltd], glycerol [Merck LifeScience Pvt Ltd] and propane-1,2-diol [Merck LifeScience Pvt Ltd] were used as different polyhydric alcohols. All the chemicals were used in as-received conditions.

## 3.2 Preparation of different carbon supports

### 3.2.1 Preparation of reduced graphene oxide (RGO)

Graphene oxide (GO) was prepared from the oxidation of graphite powder by modified Hummers method (Singh and De, 2020). GO was reduced chemically using hydrazine as a reducing agent. The desired amount of GO was dissolved in deionized water, maintaining a concentration of 3 mg/ml. The resulting suspension was stirred for 4 h followed by 2 h of sonication. The temperature of the suspension was gradually increased to 90 °C with the addition of required amount of hydrazine. Under these conditions, the solution mixture was

stirred for 4 h and then cooled to room temperature. The solution was then filtered, washed several times and dried to obtain black powder as the desired RGO.

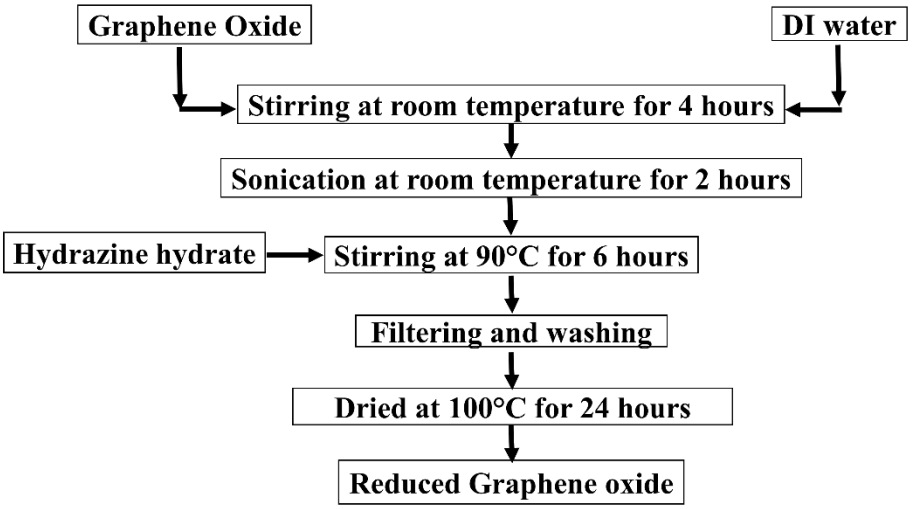


**Figure 3.1: Preparation steps of reduced graphene oxide (RGO)**

### 3.2.2 Preparation of templated carbon (ALS-TC)

Surfactant-modified alumina-based templated carbon was prepared using the method described in the literature (Singh and De, 2018). The desired amount of SDS-modified alumina was taken in a quartz boat and placed inside a horizontal tubular furnace. Carbon deposition was done at 750 °C for 3 h. Acetonitrile was used as a carbon source. The argon was used as a carrier gas, and its flow rate was maintained at 50 ml/min to keep the gas phase concentration of acetonitrile at 70 ppm.

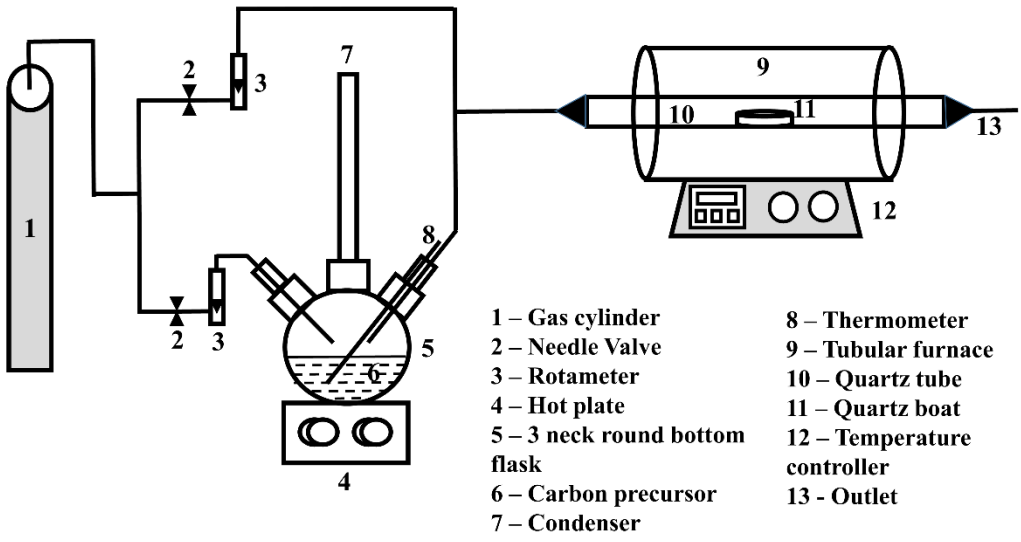


**Figure 3.2: Schematic of experimental set up for preparation of templated carbon**

Deposition of carbon was followed by treatment of the carbon-template composite in an inert environment at 800 °C for 2 h. The final composite sample was then cooled down to room temperature. The carbon-template composite was then treated with an excess amount of 48% HF to dissolve the template. It was finally filtered and washed by deionized water. The final carbon sample obtained was dried overnight at 150 °C. It is referred to as templated carbon and abbreviated as ALS-TC.

## 3.3 Preparation of monometallic electrocatalysts

Different metal-based electrocatalysts with various supports were synthesized using the wetness impregnation method with subsequent reduction in a 10% $H_2$/Ar environment. Typically required amount of metal precursor was dissolved by continuous stirring in an adequate amount of deionized water, which is equivalent to 3.5 times the support pore volume. The precursor solution was added to 1.6 g of supports under constant stirring. The stirring was continued for 2 h. The slurry was then dried overnight at 100 °C. The dried sample was grinded and placed in a quartz boat inside a horizontal tubular furnace to reduce in hydrogen environment at respective temperature for 2 h. The reduction temperatures were determined based on temperature programmed reduction (TPR) study (Appendix A). The temperature of the furnace was gradually increased at a heating rate of 10 °C/min under the flow of 10% $H_2$/Ar until the reduction temperature was reached.

To study the effect of catalyst supports using Cu as the active metal (dicussed in section 4.2), the Cu metal precursor (copper nitrate) was loaded on RGO, AC, ALS-TC and VC supports at a metal loading of 20 wt.%. The obtained catalysts were denoted as 20Cu-RGO, 20Cu-AC, 20Cu-ALS-TC and 20Cu-VC. To study the effect of various metals using activated carbon and RGO as supports, metal loading was again maintained at 20 wt.% and catalysts were designated as 20M-AC and 20M-RGO, respectively, where M = Cu, Ni, Co, or Fe. To investigate the effect of metal loadings on electrocatalysts, nickel was employed as the active metal with RGO as the support. The nickel content was varied as 20, 30 and 40 wt.%. These samples are designated in the text as xNi-RGO where x = 20, 30, & 40 wt.%.

## 3.4 Preparation of bimetallic electrocatalysts

The bimetallic catalysts were prepared in a similar manner as monometallic catalyst. For preparation of bimetallic catalysts, the required amounts of different metal precursors in fixed ratio were dissolved in deionised water which is equivalent to 3.5 times the support pore volume. The ratio of nickel to other metals (Cu, Co, and Fe) was maintained at 3:1. The overall

metal loading was fixed at 30 wt.%. The metal salt solution was added to RGO support, and the slurry was stirred for 2 h. The obtained sample was dried overnight at 100 °C and reduced at 350 °C for 2 h under $H_2$/Ar environment. The sample obtained was termed NiCu-RGO, NiFe-RGO, and NiCo-RGO.

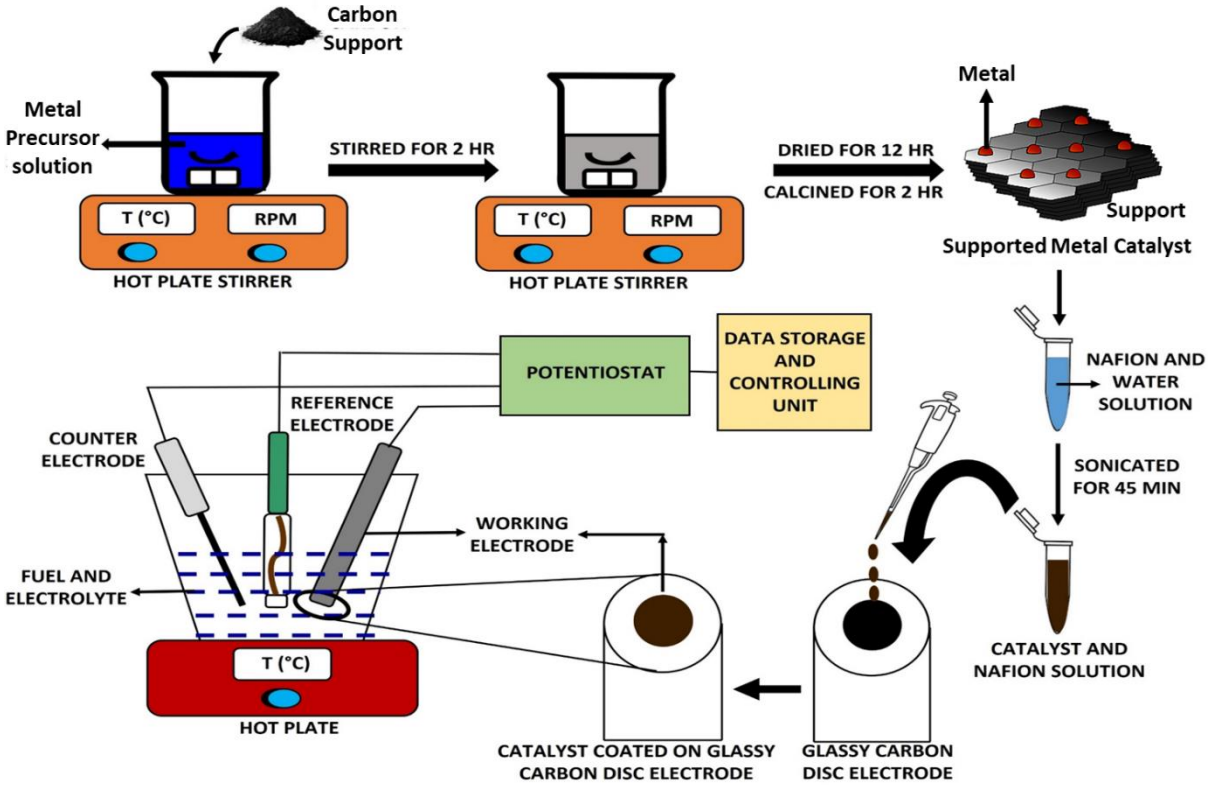


**Figure 3.3: Schematic representation depicting the preparation of catalyst and electrochemical characterization procedure**

## 3.5 Characterization techniques

### 3.5.1 Physical characterization

The physical characterization of all the electrocatalysts was carried out using surface area and pore analysis, X-ray diffraction (XRD), field emission scanning electron microscopy (FESEM), energy dispersive x-ray spectroscopy (EDX), field emission transmission electron microscopy (FETEM), X-ray photoelectron spectroscopy (XPS) and kelvin probe force microscopy (KPFM).

Surface area and pore analysis of different supports and electrocatalysts were carried out with the help of Autosorb-iQ (Quantachrome) by developing nitrogen adsorption-desorption isotherm at -196°C (77 K) as per standard procedure (Singh and De, 2018). The samples were dried overnight and degassed at 150 °C under helium environment for 3 h before

analysis. The surface area was calculated using the Brunauer-Emmett-Teller (BET) method over a relative pressure range ($P/P_0$) of 0.05 to 0.3. The pore volume was determined at $P/P_0$ = 0.99. The pore size distribution was determined using the non-linear density functional theory (NLDFT) method.

The XRD patterns were recorded using Rigaku Spectralab having Cu Kα wavelength of 0.154 nm (40KV, 112mA). The scan rate was maintained at 0.33°/s and a step size of 0.02° scanned over 2θ range of 5 to 90°. The crystallite size ($D_c$) from XRD was calculated using the Scherrer formulae

$$D_C = \frac{K\lambda}{\beta\cos\theta} \tag{3.1}$$

Where K is the dimensionless shape factor, λ is the wavelength, β is the full width half maxima of the peak and θ is the Bragg's angle

The morphological study of various supports and supported catalysts was performed with the help of a 1430VP Zeiss FESEM at different magnifications. The elemental composition of the samples was analysed using EDX equipped with FESEM. The FETEM images were captured by 2100F JEM (JEOL). The metal particle size distribution was calculated from FETEM images of the supported electrocatalysts by ImageJ software. Metal dispersion ($D_{TEM}$) of electrocatalysts was calculated from respective mean particle size obtained from FETEM images by the following formula (Iida and Igarashi, 2006):

$$D_{TEM} = \frac{C}{d} \tag{3.2}$$

where, d = mean diameter of metal particles (m) calculated from FETEM images and

$$C = \frac{6 \times M}{N \times \rho \times \delta} \tag{3.3}$$

where, M = atomic weight of the metal, N = Avagadro's no, ρ = density of different metals ($g/m^3$), and δ = cross-sectional area of different metal atoms ($m^2$). The calculated values of parameter C as defined by Equation 3.2 for Cu, Ni, Fe and Co were 1.23, 0.942, 0.924 and 0.909 nm, respectively.

The XPS spectra of the catalysts were recorded using PHI 5000 Versa Probe II (FEI Inc). The catalysts were subjected to high vaccum of $10^{-8}$ mbar. AlKα was used as the exication source. The XPS Peak Fit software was used to deconvolute the spectrum of different elements.

KPFM analysis was performed using Cypher (Oxford) equipped with Pt/Ir conducting tip in non-contact mode. The tip was calibrated at 74 Hz with a modulation voltage of 3 V to record the surface potential of different catalysts. Before acquiring measurements for the

samples, the work function of the Pt/Ir tip was calibrated using highly oriented pyrolytic graphite (HOPG). The tip recorded the contact potential difference (CPD) as surface potential. The CPD is defined as the difference in the work function of the tip ($\phi_{tip}$) and sample ($\phi_{sample}$) and is given by the following formula:

$$CPD = \frac{(\phi_{tip} - \phi_{sample})}{e} \quad (3.4)$$

The work function of HOPG was 4.5 eV and the CPD value between HOPG and tip was 0.26 V. Using these values, the work function of the tip was calculated to be 4.76 eV from Equation (3.4).

### 3.5.2 Electrochemical characterization

The electrochemical analysis was performed using a bi-potentiostat, M204 Autolab-Metrohm, associated with a frequency response analyser (FRA) module and 20A booster. A three-electrode cell, consisting of glassy carbon (GC) with 0.196 $cm^2$ area as the working electrode, Pt as a counter electrode, and a double junction Ag/AgCl as the reference electrode was used to perform the electrochemical studies. The catalyst ink was prepared by sonicating 5 mg of the prepared electrocatalyst in 1 ml of water and 40 µl of 5% Nafion® for 45 min. 20 µl of the catalyst ink was drop casted on the GC electrode to form a uniform layer which was then dried at 100 °C for 30 min. Before drop casting, GC was sonicated for 10 min in 0.1 M nitric acid solution and polished with 0.05 µm alumina slurry. Each catalyst was tested in nitrogen saturated 0.1 M $H_2SO_4$ and 0.1 M KOH to simulate the acidic and alkaline environments of proton exchange and anion exchange membrane FCs. The $N_2$-saturated environment was created to minimize the participation of dissolved oxygen in the oxidation reaction. Cyclic voltammetry (CV) studies were conducted at a scan rate of 50 mV/s both in acidic (0.1 M $H_2SO_4$) and alkaline (0.1 M KOH) media. Chronoamperometry (CA) studies were conducted at the peak potential of respective catalysts in both acidic and alkaline media with EG, keeping all the parameters same as CV. The current density was calculated by normalising current with respect to geometric surface area. Electrochemical impedance spectroscopy (EIS) of the supported catalysts was done in acidic and basic medium both in the presence and absence of EG. All the experiments were performed potentiodynamically at open circuit peak potentials from 20 kHz to 0.01 Hz with a single sinusoidal amplitude of 10 mV.

To calculate the electrochemical active surface area (ECSA), CVs were performed at different scan rates for the supported electrocatalysts. The ECSA was calculated using the following formula:

$$\text{ECSA (cm}^2\text{)} = \frac{C_{dl}}{c_s} \tag{3.5}$$

where, $C_{dl}$ is double layer capacitance and is defined as the slope between current and scan rate for different electrocatalysts, $c_s$ is the specific charge density and is taken as 0.04 mF/cm$^2$ for all the catalysts (McCrory et al., 2013).

The roughness factor (RF) was obtained from ECSA using the following equation:

$$\text{RF} = \frac{\text{ECSA (cm}^2\text{)}}{\text{SA (cm}^2\text{)}} \tag{3.6}$$

where, SA is the geometrical cross-sectional area of the electrode.

The charge transfer coefficient was calculated using Butler-Volmer equation:

$$\text{Log } i = \text{Log } i_0 + \alpha nF\eta/2.303RT \tag{3.7}$$

The $i_o$ is the exchange current density, R is the universal gas constant, F is Faraday constant, T is temperature in K, $\eta$ is overpotential, $\alpha$ is charge transfer coefficient and n is the number of electrons transferred. The electron transferred in basic medium was considered to be 1.

The surface coverage of the redox species ($\Gamma^*$) could be calculated by the following equation when linearity was achieved between peak current density and scan rate (Ma et al., 2021):

$$I_P = \frac{n^2F^2}{4RT}\nu A\Gamma^* \tag{3.8}$$

where, $I_P$ and A are peak current and electrode area respectively.

The diffusion coefficient ($D_0$) of ethylene glycol molecules can be calculated using the following Randels -Sevcik equation (Lin et al., 2017):

$$I_P = 2.69 \times 10^5\ n^{3/2}AD_0^{1/2}\nu^{1/2}C_0 \tag{3.9}$$

where, $C_0$ is the concentration of EG. The diffusion coefficient of ethylene glycol molecule calculated from above Equation, when n was varied between 1 and 10.

Dual potential chronoamperometry was performed at the peak potential observed for different catalysts. This technique was used to explore the electrochemical-chemical (EC) mechanism and also to find out the electrocatalytic rate constant of the catalyst for alcohol oxidation. The electrocatalytic rate constant was calculated using the Cottrell equation (Azizi et al., 2013):

$$\frac{I_{cat}}{I_L} = \pi^{1/2}(k_{cat}C \times t)^{1/2} \tag{3.10}$$

where, $I_{cat}$ and $I_L$ is the current in presence and absence of ethylene glycol, $k_{cat}$ is the electrocatalytic rate constant, C is the concentration of EG and t is the elapsed time.

The adsorption of CO on the catalyst surface during alcohol oxidation was studied using CO stripping voltammetry. The solution was purged with $N_2$ gas for 30 min for CO stripping voltammetry. The CO gas was then introduced for 30 min to get adsorbed on the catalyst surface at an applied potential of 0.1 V in an acidic medium and -0.9 V in basic medium. $N_2$ gas was purged again for 30 min to remove the excess CO from the solution. Two cycles of CV were conducted in both acidic and basic media. The first cycle corresponded to the peak associated with CO electro-oxidation, whereas the second cycle represented the basic CV in the corresponding medium. The difference in peak intensity of the first and second cycles accounted for the CO adsorption on the catalyst surface (Duan et al., 2020).

## 3.6 Fuel cell study

The single fuel cell study was conducted to replicate the behaviour of the catalyst for commercial applications. FC study was done with a single cell assembly of 9 $cm^2$ area consisting of home-made membrane electrode assembly (MEA), graphitic flow plate having serpentine flow channels, copper current collector and stainless-steel end plate. The temperature was maintained at 75 °C with a temperature controller and provided with two heating rods placed into the endplates. The liquid fuel was fed through a peristaltic flow pump on the anode side varying flow rate from 0.5 ml/ min, while oxygen flow was controlled by a mass flow controller at a fixed flow rate of 200 ml/min. The MEA was made with anion exchange membrane (Fumasep FAA 50) sandwiched between coated catalyst gas diffusion layer (Toray carbon paper). The catalyst ink was prepared by sonication, a mixture catalyst and binder (polyfluoroethylene) with a ratio of 9:1 in 1:1 water ethanol solvent. The anode catalyst (in-house catalyst) was coated on the carbon paper with active metal loading ranging from 0.5 $mg/cm^2$. The cathodic catalyst (20 wt.% Pt/VC) was coated on the carbon paper with a fixed Pt loading of 1 $mg/cm^2$. The experiment under any parametric condition was carried out after stable open circuit potential (OCP) was reached. The linear polarisation curve was obtained by sweeping potential from OCP with a scan rate of 1 mV/s.

# *Chapter 4*
# *Results and Discussions*

# 4. Results and Discussions

## 4.1 Analysis of supports

The $N_2$ adsorption-desorption isotherms obtained for various supports at -196 °C are shown in Figure 4.1a. The profiles showed wide variation in the extent of $N_2$ adsorption and nature of isotherms, thereby indicating significant differences in the porous structure of the supports. The ALS-TC and VC followed type IV and type III isotherms, respectively, while RGO and AC followed type II isotherm. The hysteresis loop for templated carbon was of H2 type, which corresponded to the complex structure of interconnected pores. The AC did not show significant hysteresis loop, suggesting the presence of micropores. The VC and RGO exhibitedH4 type hysteresis loop, representing a slit-shaped pore structure. The volume of adsorbed $N_2$ was significantly higher for ALS-TC than the other supports, with the following order: ALS-TC > AC> RGO> VC. Accordingly, ALS-TC had the highest surface area and total pore volume, followed by AC, RGO, and VC. The surface area, total pore volume, micropore area and average pore size of the samples are tabulated in Table 4.1. All of the samples showed the presence of micropores, with AC having the highest area of 231 $m^2/g$. The value is within the wide range of micropore areas (100 - 2124 $m^2/g$) reported in literature for activated carbon prepared from different sources (Kumar and Jena, 2015, Li et al. 2024).

**Table 4.1: Physico-chemical properties of different supports**

| Sample ID | BET surface area ($m^2/g$) | Total pore volume ($cm^3/g$) | Micropore area ($m^2/g$) | Average pore size (nm) | C d-spacing (nm) |
|---|---|---|---|---|---|
| AC | 986 | 0.6 | 231 | 2.6 | 0.335 |
| RGO | 487 | 0.5 | 67 | 4 | 0.362 |
| ALS-TC | 1262 | 1.3 | 64 | 4 | 0.342 |
| VC | 207 | 0.4 | 32 | 9 | 0.368 |

The pore size distribution of different supports is shown in Figure 4.1b. The pores in ALS-TC ranged upto to 8 nm, with the majority of them being larger than 2 nm. AC exhibited pores up to about 4 nm, with significant fraction was less than 2 nm. RGO showed the narrowest pore size distribution in the mesoporous range of 2.5 to 4.5 nm with the highest intensity. VC had the least number of pores as intensity of the peaks was very low. The widest pore in VC was up to 15 nm, though most of the pores were smaller than 5 nm. The average pore size of VC was highest at 9 nm. This was consistent with the lowest surface area and pore volume of VC. RGO and ALS-TC had similar average pore sizes of 4 nm, whereas AC had the least average pore size of 2.6 nm, which is consistent with the presence of a larger fraction of micropores.

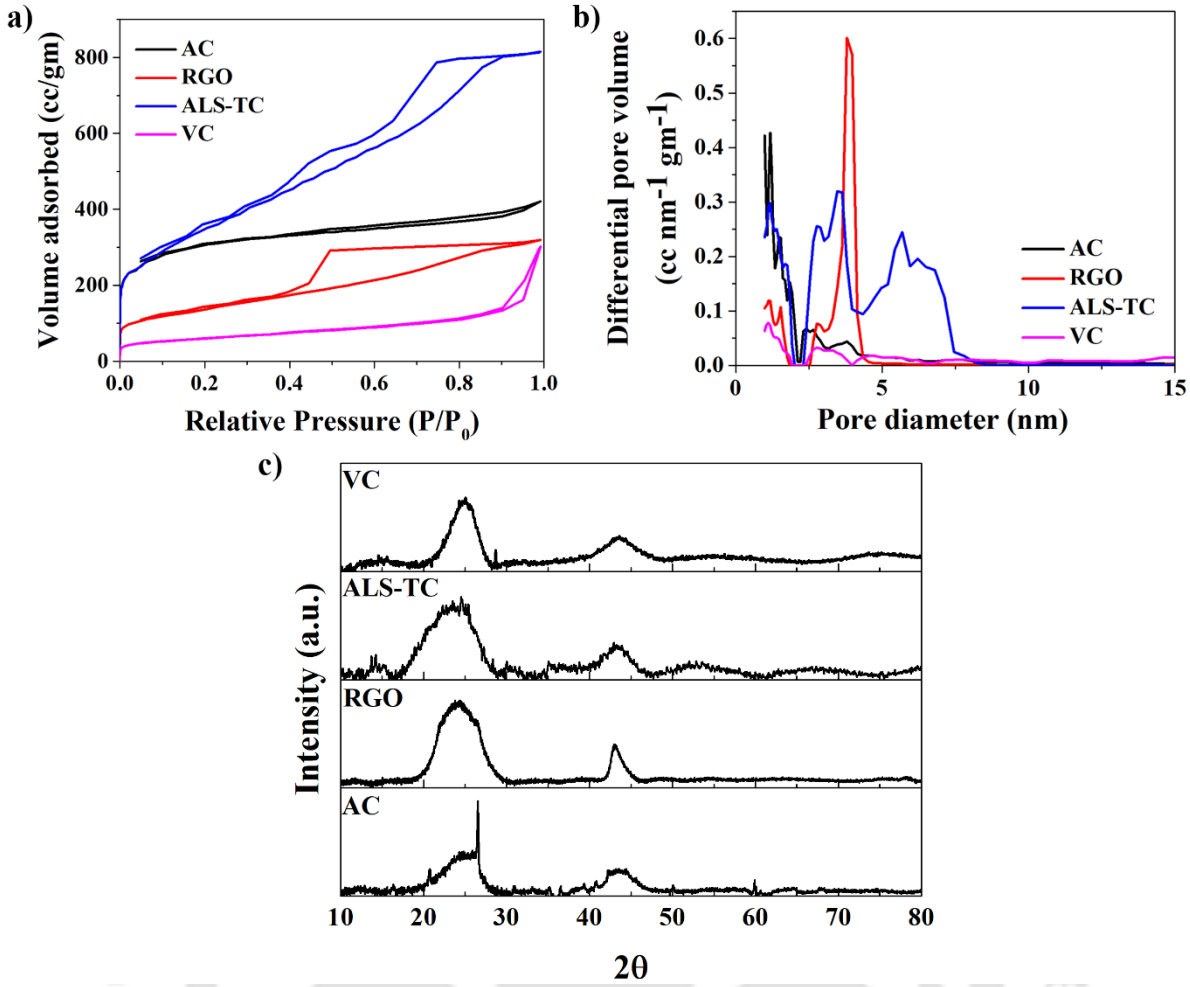


**Figure 4.1: a) $N_2$ adsorption-desorption isotherms, b) pore size distributions and c) XRD profile for different supports, respectively. (In all the isotherms the lower curves are for adsorption process and the upper curves for desorption process.)**

The XRD patterns of different carbon supports are shown in Figure 4.1c. All the samples exhibited a broad peak between 24° to 27°, which corresponded to the graphitic plane (002) (Singh and De, 2018). The broad and low intensity graphitic peak for different carbon supports suggested their mainly amorphous nature, with presence of intermittent small graphitic zones. The other peak at around 44.4° corresponded to the graphitic plane (101). The absence of an alumina peak in the ALS-TC profile confirmed the removal of alumina template from carbon sample. The d-spacing of all supports are represented in Table 4.1. The d-spacing of different supports varied from 0.335 to 0.368 nm. AC has the lowest d-spacing, followed by ALS-TC, RGO and VC.

The FESEM images in Figure 4.2a-d demonstrate the morphology of various supports The AC and ALS-TC had agglomerated structures. RGO formed a structure with randomly orientated stacked layers. A distinct spherical, agglomerated and interconnected structure was observed for VC. FETEM images of different support are shown in Figure 4.2e-f. The AC

support had random agglomerated sheet, whereas RGO had oriented sheet structure. ALS-TC exhibited an interconnecting tubular network, while VC displayed interconnected globular network.

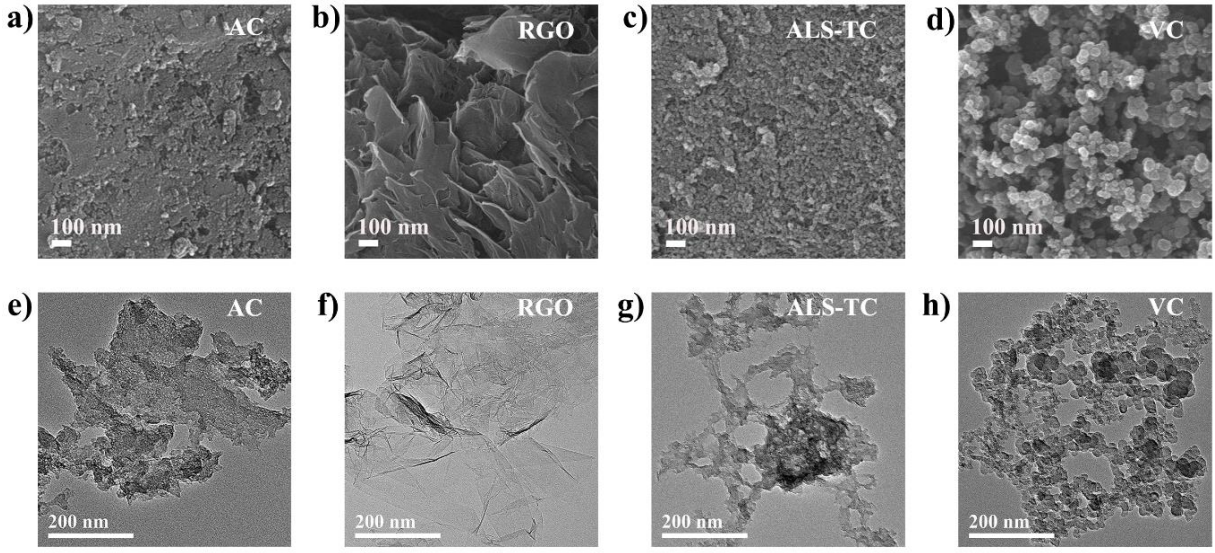


**Figure 4.2: a-d) FESEM and e-f) FETEM images different supports.**

The CV of different supports in acidic ($H_2SO_4$) and basic (KOH) medium containing 0.5 M EG was shown in Figure 4.3. In the presence of EG, the different supports showed negligible redox activity in both the media conditions. This suggested that the supports were inactive towards electro-oxidation of EG.

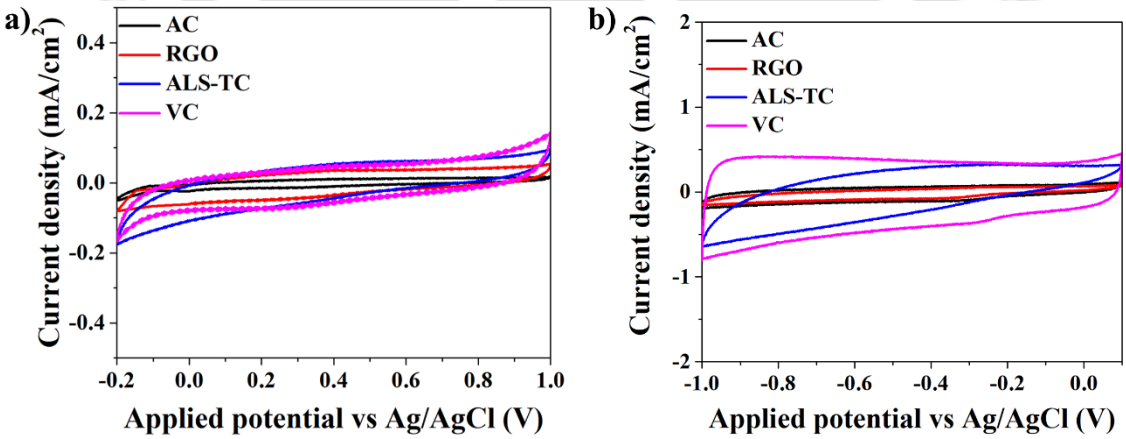


**Figure 4.3: Cyclic voltammetry of different supports in a) 0.1 M $H_2SO_4$ and b) 0.1 M KOH medium with 0.5 M EG.**

## 4.2 Different supported copper catalysts

### 4.2.1 Physical characterization

The composition of electrocatalysts as determined by EDX analysis is shown in Table 4.2. The copper loading ranged from 21.6 to 24.7 wt.%. The oxygen content in various supported catalysts varied from 8.5 to 11.1%, with 20Cu-VC having the lowest value. The 20Cu-ALS-TC also showed the presence of nitrogen, as acetonitrile was used in its preparation.

**Table 4.2: Elemental composition of supported copper catalysts**

| Sample ID | Cu (wt.%) | C (wt.%) | O (wt.%) | N (wt.%) |
|---|---|---|---|---|
| 20Cu-AC | 23.3 | 65.9 | 10.8 | - |
| 20Cu-RGO | 24.7 | 65.1 | 10.2 | - |
| 20Cu-ALS-TC | 21.6 | 65.2 | 11.1 | 2.1 |
| 20Cu-VC | 22.1 | 69.5 | 8.5 | - |

Figure 4.4a shows the $N_2$ adsorption-desorption isotherms of all supported copper electrocatalysts. The nature of isotherms was similar to their respective supports. The volume of $N_2$ adsorbed decreased for each of the supported copper electrocatalysts compared to their respective supports, indicating a decrease in surface area and pore volume due to metal doping. The decrease could be attributed to partial blockage of pores or space between layers due to the presence of metal clusters. The BET surface area, total pore volume, micropore area and average pore size are summarised in Table 4.3. All the catalysts showed almost similar percentage reduction in surface area, except for 20Cu-RGO. The surface area of 20Cu-RGO reduced by around 70% upon the incorporation of copper. The significant reduction in surface area incurred by 20Cu-RGO might be explained by higher metal loading, the presence of more clusters and layered structure, which results in increased blocking of spaces between the graphene layers.

**Table 4.3: Physico-chemical properties of different supported copper catalysts**

| Sample ID | BET surface area ($m^2/g$) | Total pore volume ($cm^3/g$) | Micropore area ($m^2/g$) | Average pore size (nm) | C d-spacing (nm) | Cu d-spacing (nm) | $D_{TEM}$ (%) |
|---|---|---|---|---|---|---|---|
| 20Cu-AC | 566 | 0.3 | 95 | 2.8 | 0.366 | 0.208 | 16 |
| 20Cu-RGO | 142 | 0.2 | 11 | 5.8 | 0.346 | 0.207 | 10 |
| 20Cu-ALS-TC | 658 | 0.7 | 0 | 4.5 | 0.350 | 0.209 | 4 |
| 20Cu-VC | 135 | 0.5 | 17 | 17.5 | 0.358 | 0.209 | 9 |

The pore size distribution of the supported copper catalysts is shown in Figure 4.4b. The total pores in supported copper electrocatalysts reduced compared to their corresponding supports

due to the blocking of pores or spaces between layers by the metal particles. The overall pore size distribution for catalysts remained similar to that of their respective supports, with a decrease in peak intensity and a shift towards the larger pore sizes. Accordingly, the average pore size of all the catalysts increased as compared to their supports. This could be explained by blocking of smaller pores by deposited metals. Copper loading on AC has minimal effect on porous structure apart from a reduction in the number of pores. The pores were within the same range of 1 - 5 nm, similar to AC support. The average pore size increased slightly to 2.8 nm for 20Cu-AC from 2.6 nm for AC. The number of pores in 20Cu-VC was above 8 nm, which was slightly higher as compared to its support, possibly because of the agglomerated deposition of copper on VC. The average pore size increased drastically from 9 nm for VC to 17.5 nm for 20Cu-VC.

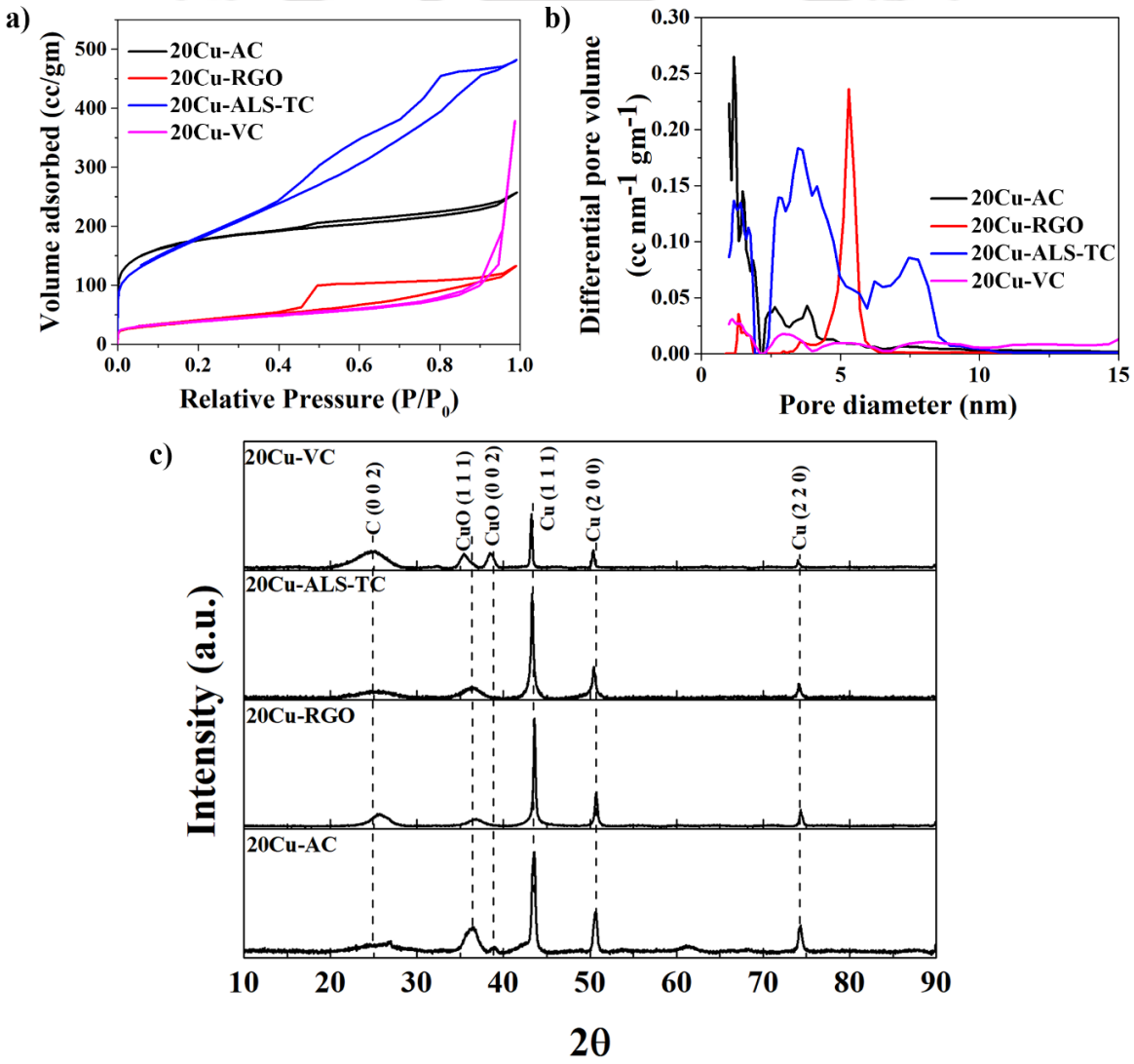


**Figure 4.4: a) $N_2$ adsorption-desorption isotherms, b) pore size distributions and c) XRD profile for different supported copper catalysts. (In all the isotherms the lower curves are for adsorption process and the upper curves for desorption process.)**

The porous structure of RGO and ALS-TC changed significantly due to copper loading. The pores of 20Cu-RGO increased to 4.4 - 6.2 nm in size, when compared to RGO (2.5 - 4.39 nm). As stated earlier, this shift in pore size could be attributed to partial blockage of spaces between the layers. The average pore size accordingly increased from 4 nm for RGO to 5.8 nm for 20Cu-RGO (Table 4.1 and 4.3). However, as observed in Figure 4.1b and 4.4b, 20Cu-RGO retained the narrow pore size distribution, similar to RGO. This could be attributed to the higher separation of layers in 20Cu-RGO caused by the presence of metal clusters between the layers. The pore size distribution of 20Cu-ALS-TC also shifted towards higher values, with an average pore size of 4.5 nm.

The XRD profiles of different supported copper catalysts are shown in Figure 4.4c. The peak corresponding to different supports was observed between 24° to 27°, representing the graphitic plane (002) (Singh and De, 2018). Each supported copper catalyst exhibited multiple peaks representing the Cu and CuO planes. The copper peaks were observed at 43.47°, 50.37° and 74°, corresponding to the (111), (200) and (220) planes respectively in all electrocatalysts (Ghouri et al., 2017). A small peak of CuO was found at 36.8°, corresponding to the (111) plane (Priya and Berchmans, 2012). The peak at 38.5° was detected only for 20Cu-VC, corresponding to the (002) plane of CuO. The intensity of peaks due to copper impregnation varied in different electrocatalysts. The intensity of copper peak at 43.47° increased in the following order: 20Cu-ALS-TC, 20Cu-AC, 20Cu-VC and 20Cu-RGO. The intensity variations indicated the formation of different sizes of copper crystals on various supports. The average crystal size of metal was highest for 20Cu-RGO (27.9 nm), followed by 20Cu-VC (23.5 nm). The 20Cu-ALS-TC showed an average crystal size of 17.5 nm, whereas 20Cu-AC had the smallest average crystal size of 13.5 nm. The incorporation of metals reduced the d-spacing of the VC and RGO carbon matrix while increasing it for AC and ALS-TC. The addition of metals to VC and RGO carbon matrix with low porosity (Figure 4.4 & Table 4.3) and layered structure (for the latter) limited the space within the carbon matrix, which in turn reduced the carbon d-spacing. But since AC and ALS-TC already have a highly porous carbon matrix, placing metal crystallites in appropriate openings of the carbon matrix increases the availability of larger d-spacings, thereby increasing the carbon d-spacing of the samples. The metal d-spacing values for different supported copper catalysts remained in the same range of 0.207 - 0.209 nm, indicating that metal crystal arrangement was similar in nature for all the supports. The crystallite size of different supported copper catalysts was between 17.9 to 34.4 nm.

The morphology of various supports and corresponding supported copper catalysts are depicted in FESEM images in Figure 4.5a-d. AC and ALS-TC depicted agglomerated

structures. RGO formed a structure with randomly orientated stacked layers. A distinct spherical, agglomerated and interconnected structure was observed for VC. The incorporation of metal particles on different supports resulted in the appearance of a spherical entity on the surface of the supports, indicating the formation of a spherical metal structure in catalysts. Metal spheres were clearly visible in 20Cu-ALS-TC.

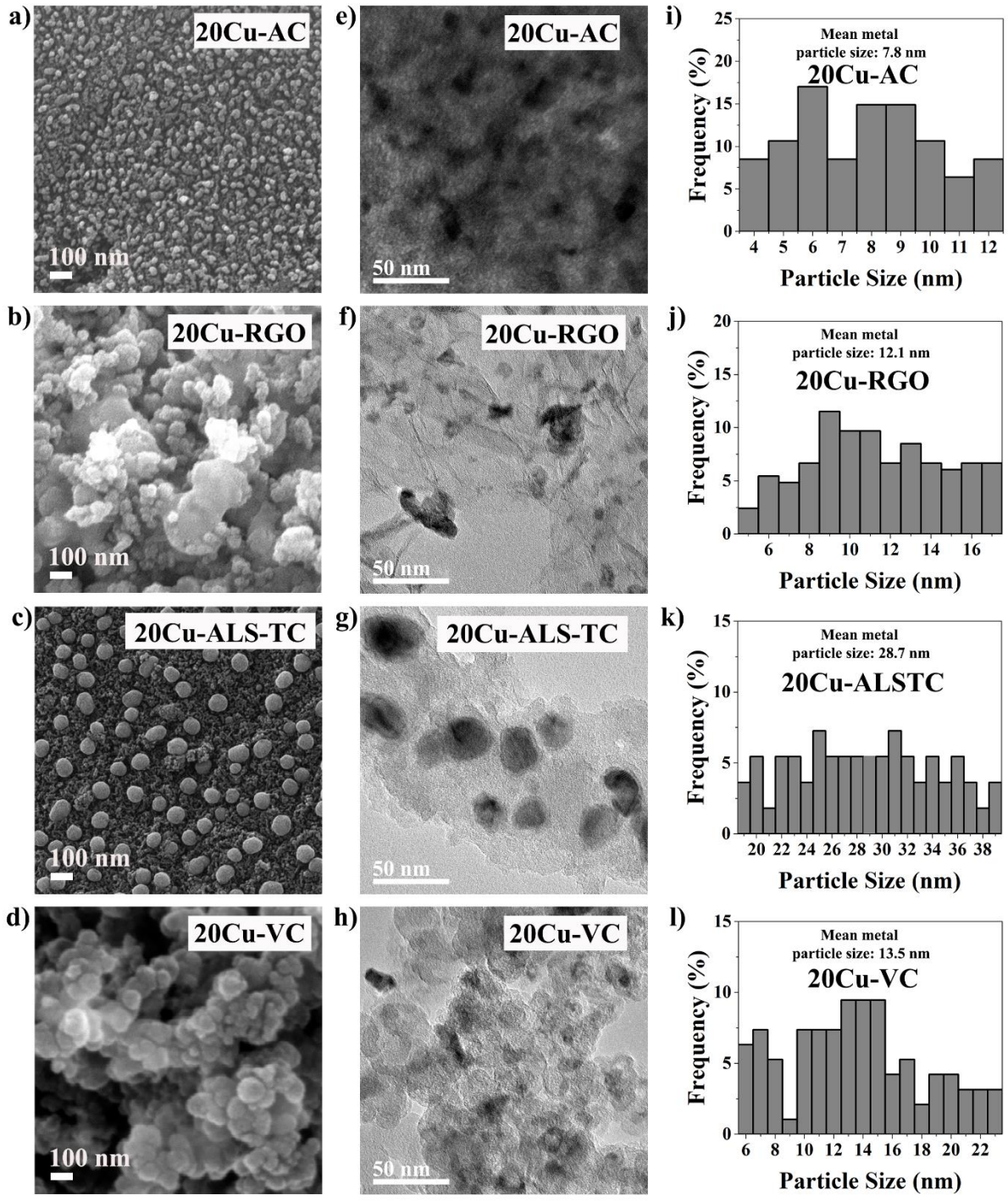


**Figure 4.5: a-d) FESEM, e-h) FETEM images and i-l) particle size distribution of respective supported copper catalysts.**

The FETEM images of supported catalysts together with their metal particle size distributions are shown in Figure 4.5e-h. The copper metal particles were represented by the dark spherical spots, as shown in Figure 4.5e-h. The particle size of the metal particles incorporated was significantly influenced by the supports. The corresponding average metal particle sizes of 20Cu-AC, 20Cu-RGO, 20Cu-VC and 20Cu-ALS-TC were 7.8 nm, 12.1 nm, 13.5 nm and 28.7 nm, respectively. The metal dispersion ($D_{TEM}$) calculated from the average particle sizes of 20Cu-AC, 20Cu-RGO, 20Cu-VCand 20Cu-ALS-TC was 16, 10, 9 and 4%, respectively (Table 4.3). The FESEM image of 20Cu-ALS-TC clearly depicted lowest dispersion which corresponds to the distinct formation of metal spheres (Figure 4.5c). The dotted circular ring formations in the selected area electron diffraction (SAED) patterns suggested polycrystalline nature for all the catalysts (Figure 4.6a-d). The d-spacing of metal crystallites of different supported catalysts obtained from TEM images (Figure 4.6e-h) showed a slight deviation from XRD d-spacing values (Table 4.3). The 20Cu-AC and 20Cu-VC exhibited d-spacing values of 0.25 nm, whereas 20Cu-RGO and 20Cu-ALS-TC displayed d-spacing values of 0.26 and 0.24 nm, respectively. The d-spacing observed from TEM corresponded to the CuO (111) plane. This difference in d-spacing values might be due to the influence of different supports.

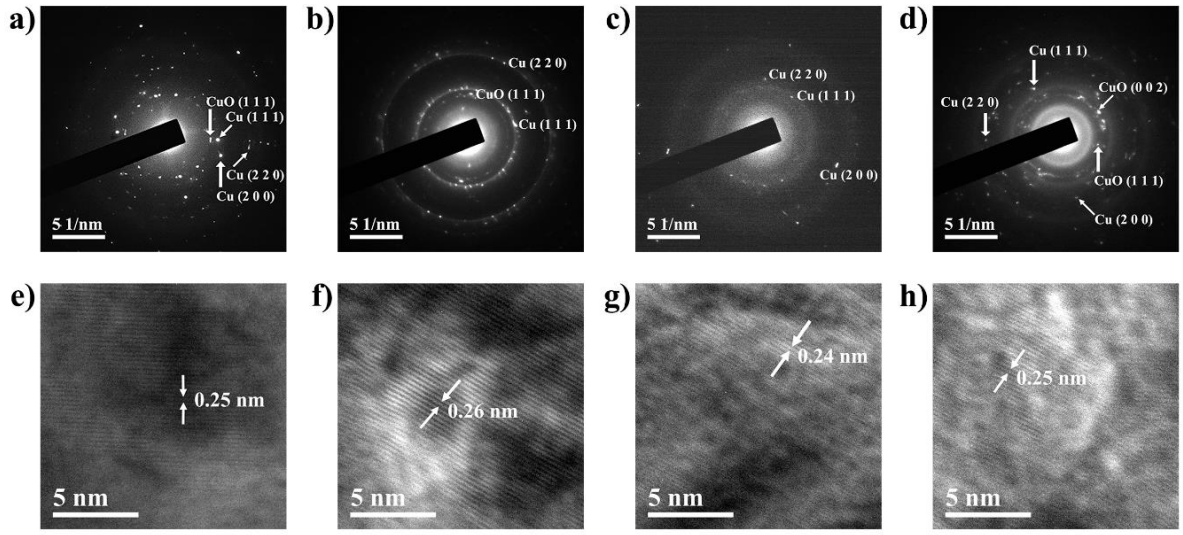


**Figure 4.6: SAED patterns from FETEM of a) 20Cu-AC, b) 20Cu-RGO, c) 20Cu-ALS-TC, and d) 20Cu-VC. High resolution FETEM images of e) 20Cu-AC, f) 20Cu-RGO, g) 20Cu-ALS-TC, and h) 20Cu-VC.**

Figure 4.7 depicts the results of XPS analysis for different catalysts. Deconvolution of C1s spectra of various samples suggested the presence of various functional groups on the surface of different supports (Figure 4.7a, c, e, and g).

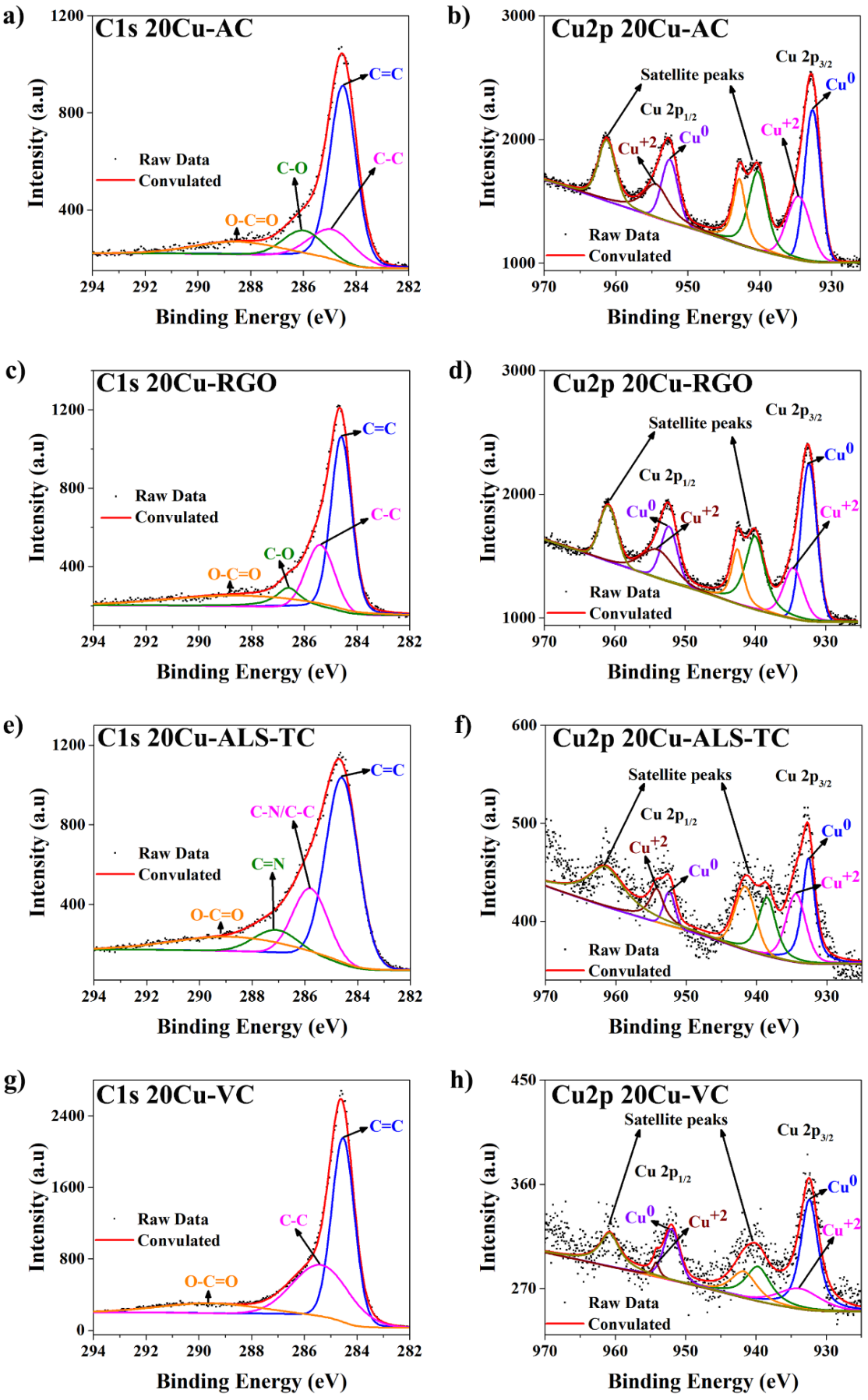


**Figure 4.7: XPS spectra of different supported copper catalysts.**

All the supports showed the presence of C=C, C-C, and O=C-O containing groups. The C-O group was present only in 20Cu-AC and 20Cu-RGO. The 20Cu-ALS-TC showed C-N/C=N group. The peak position of different functional groups and their percent contribution is tabulated in Table 4.4. All the catalysts had slight deviation in peak positions for different functional groups (except for C=C). This difference might have resulted from the interaction of copper with various supports. The total percent contribution of oxygen-containing functional groups was observed to be highest for 20Cu-RGO (28%), followed by 20Cu-AC (26%), 20Cu-VC (12%) and 20Cu-ALS-TC (11%).

Cu2p spectra of all the supported copper catalysts showed a similar pattern with variations in the relative percentages of $Cu^0$ and $Cu^{+2}$ (Figure 4.7b, d, f, and h). $Cu2p_{3/2}$ spectra yielded the peaks for $Cu^0$, $Cu^{+2,}$ and two satellite peaks at around 932.7 eV, 934.7 eV, 940.3 eV and 942.8 eV, respectively. $Cu2p_{1/2}$ spectra disclosed $Cu^0$, $Cu^{+2,}$ and one satellite peak at 952.5 eV, 954.6 eV and 961.3 eV, respectively (Table 4.4) (Xu et al., 2018b). In all the catalysts, there was a positive shift in the binding energy of copper with respect to metallic copper. This shift indicated a strong interaction of copper with the respective supports. The percentages of $Cu^0$ and $Cu^{+2}$ varied for different catalysts. The percentages of $Cu^0$ for 20Cu-AC, 20Cu-RGO, 20Cu-ALS-TC and 20Cu-VC were observed to be 35, 39, 30 and 45%, respectively (Table 4.4).

**Table 4.4: XPS Analysis of all the Cu/C catalysts**

| Sample ID | C=C eV (%)* | C-C eV (%) | C-O eV(%) | O=C-O eV (%) | C=N eV (%) | $Cu^0$ eV (%) | $Cu^{+2}$ eV (%) |
|---|---|---|---|---|---|---|---|
| 20Cu-AC | 284.5 (59) | 285 (16) | 286 (13) | 288.7 (13) | 0 | 932.7 (35) | 934.7 (65) |
| 20Cu-RGO | 284.6 (49) | 285.8(23) | 286.6 (9) | 288.4 (19) | 0 | 932.4 (39) | 934.7 (61) |
| 20Cu-ALS-TC | 284.6 (55) | 285.8 (22) | 0 | 289.4 (11) | 287.1 (12) | 932.6 (30) | 934.5 (70) |
| 20Cu-VC | 284.5 (53) | 285.4 (35) | 0 | 289.4 (12) | 0 | 932.4 (45) | 934.2 (55) |

*the percent contribution of each peak is given in bracket.

KPFM was conducted to determine the surface potentials of the supported copper catalysts. Figure 4.8 shows CPD mapping images with the distribution of potential in their respective insets. The mapping images displayed that different electrocatalysts varied significantly in surface charge. The average CPD values were in the following ascending order: 20Cu-RGO (0.279 V) < 20Cu-VC (0.292 V) < 20Cu-ALS-TC (0.310 V) < 20Cu-AC (0.345 V) (Figure 4.8). Except for 20Cu-VC, the overall surface charge variation for all catalysts was about 20

mV, whereas 20Cu-VC showed a 50 mV variation in surface charge (inset figure 4.8). This variation in surface charge of the electrocatalysts resulted from varying interactions of the supports with different oxidation states of copper (as established by XPS studies) present in different catalysts. The work function, calculated by Equation (3.4), increased with decreasing values of average CPD. The work function of various supported copper (Cu) catalysts ranged from 4.415 to 4.481 eV, with 20Cu-AC having the lowest and 20Cu-RGO having the highest value (Figure 4.8). As increased work function value is associated with the better catalytic activity (Patel et al., 2016), the 20Cu-RGO (4.481 eV) and 20Cu-VC (4.468 eV) with higher work function values exhibited better activity (shown in the latter part of the study) as compared to the other two catalysts. Since the metal element and loadings were similar for all the catalysts, this difference in work function may be attributed to the effect of different forms of carbon used as support materials.

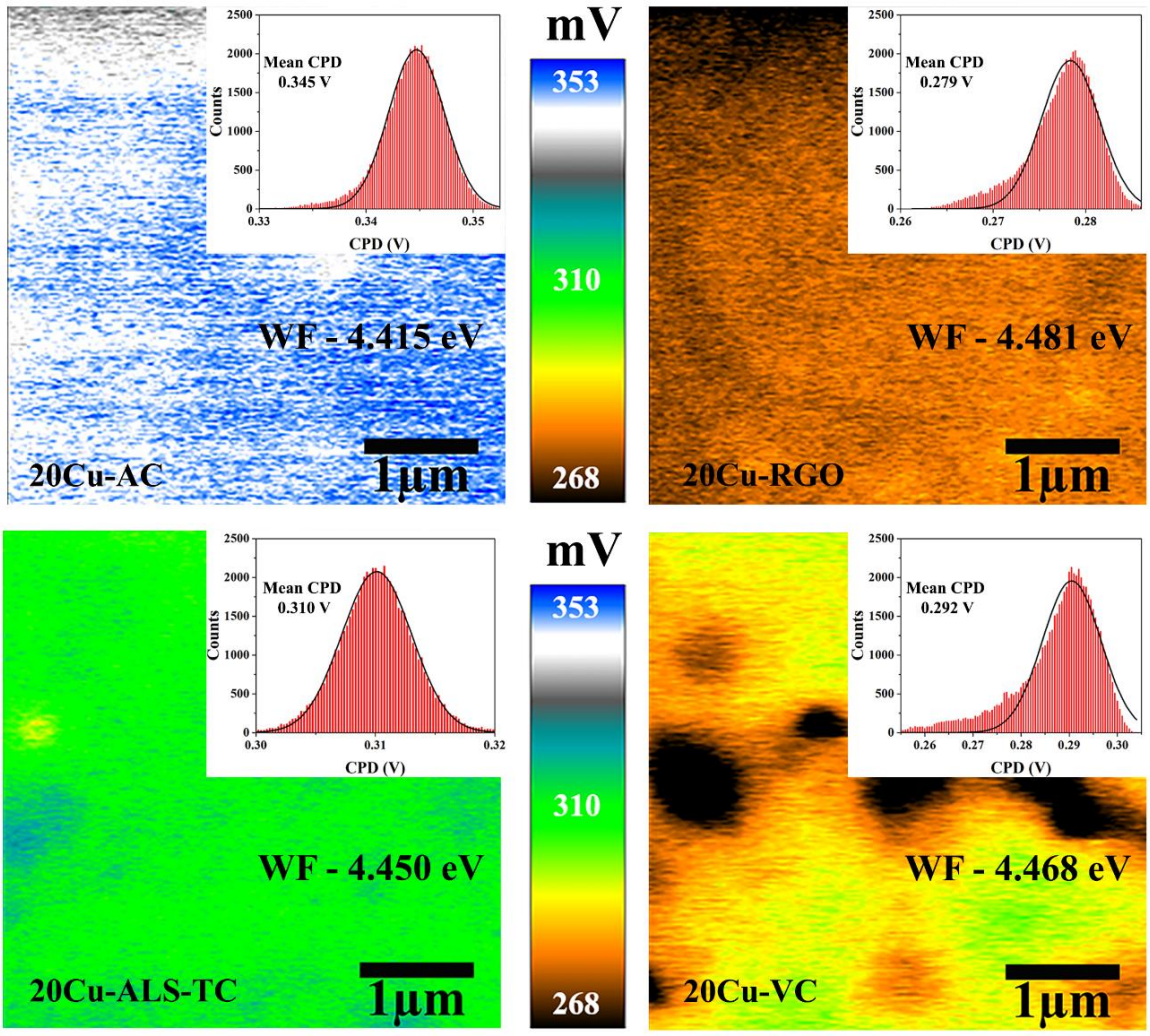


**Figure 4.8: KPFM images of different supported copper (Cu) catalysts and their contact potential difference (CPD) distribution (inset).**

### 4.2.2 Electrochemical studies

The CV of supported copper catalysts was conducted in both acidic (0.1 M $H_2SO_4$) and alkaline (0.1 M KOH) media, and the corresponding curves at the 50$^{th}$ scan are shown in Figure 4.9. The current density of supported copper catayst for EG was higher compared to that of pure copper catalyst as well as only RGO support, in both acidic and alkaline media (Figure 4.10). Higher surface area and metal dispersion of 20Cu-RGO might have resulted in its higher acivity than that of pure Cu. No activity of RGO support can be explained based on the absence of any active metal site present on the support.

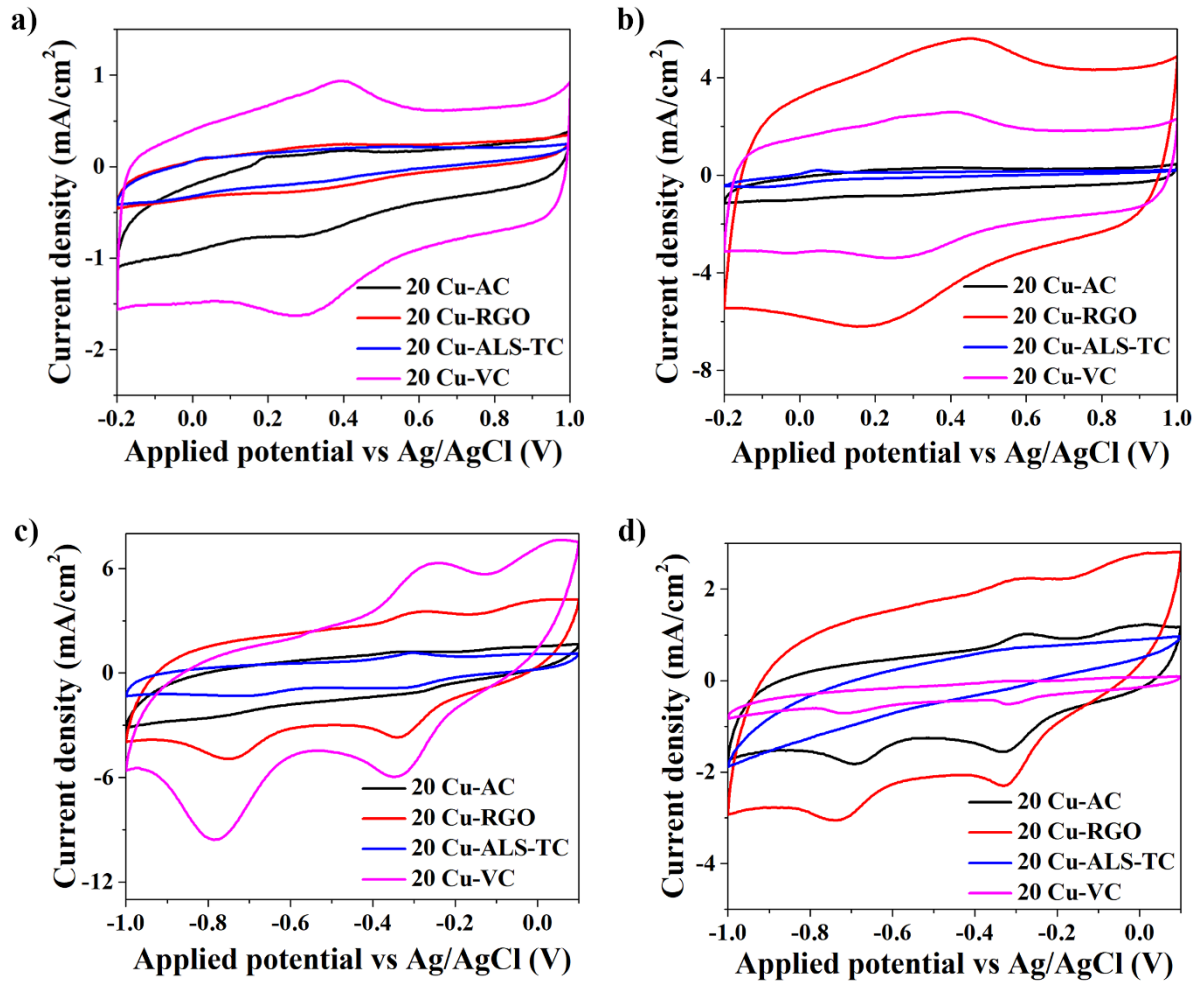


**Figure 4.9: Cyclic voltammetry of different supported copper catalysts a, c) in the absence of EG and b, d) presence of EG using a, b) 0.1 M $H_2SO_4$ and c, d) 0.1 M KOH as electrolytes.**

The anodic onset potentials are tabulated in Table 4.5, whereas the peak potential values and current density are depicted in Table 4.6. The potential at which current density started to increase towards peak formation was considered as the onset potential. In the acidic medium, the forward anodic peak was observed between 0.2 and 0.6 V, and the onset potential was in the range of 0.09 - 0.15 V (Table 4.5). The maximum current density peak was observed at

around 0.4 V. The anodic current densities were between 0.18 and 0.94 mA/cm$^2$. The highest current density observed for 20Cu-VC (0.94 mA/cm$^2$) followed by that of 20Cu-RGO (0.25 mA/cm$^2$) (Table 4.5).

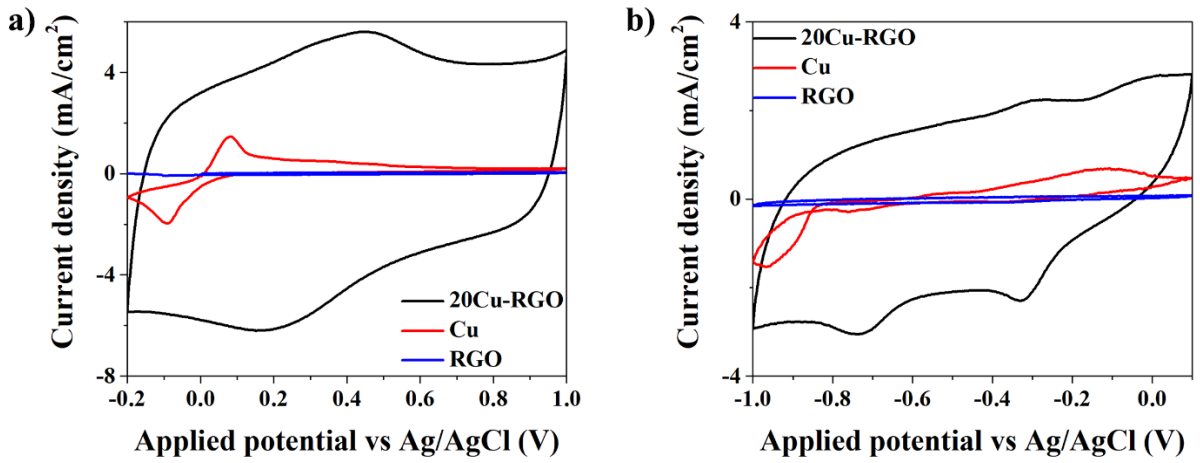


**Figure 4.10: Cyclic voltammetry of 20Cu-RGO, Cu, and RGO in the presence of EG in a) 0.1 M $H_2SO_4$ and b) 0.1 M KOH.**

In the $H_2SO_4$ environment, the copper may undergo the following reactions at the electrode-electrolyte interface (Moreira et al., 1993).

$$2Cu + H_2O \rightleftarrows Cu_2O + 2H^+ + 2e^- \quad (4.1)$$

$$Cu_2O + H_2O \rightleftarrows 2CuO + 2H^+ + 2e^- \quad (4.2)$$

Thus copper can be oxidized in two stages, first is the formation of cuprous oxide followed by cupric oxide. However, the CV profiles for all the samples, except for 20Cu-AC, showed only one broad peak around 0.4 V. In the acidic medium, two distinct but small peaks were observed in 20Cu-AC at 0.19 V and 0.41 V. The formation of these copper ions could also be correlated with the Pourbaix diagrams of copper. However, no distinct peaks were observed for 20Cu-ALS-TC under the studied conditions, indicating negligible activity at this applied potential.

**Table 4.5: Anodic onset potential observed from cyclic voltammetry of different supported copper catalysts in acidic and basic medium**

| Sample ID | In $H_2SO_4$ (V) | In $H_2SO_4$ + EG (V) | In KOH (V) | In KOH + EG (V) |
|---|---|---|---|---|
| 20Cu-AC | 0.15 | 0.15 | -0.41 | -0.35 |
| 20Cu-RGO | 0.11 | 0.09 | -0.39 | -0.39 |
| 20Cu-ALS-TC | - | - | -0.43 | -0.38 |
| 20Cu-VC | 0.09 | 0.18 | -0.42 | -0.47 |

The onset potential in the acidic medium was around 0.1 V, suggesting that there was an initial rise in current density corresponding to the conversion of $Cu/Cu^{+}$ as per Equation (4.1), followed by $Cu^{+}/Cu^{2+}$ step around 0.4 V according to Equation (4.2) (Grishina et al., 2002; Moreira et al., 1993; Tromans and Ahmed, 1998). Except for 20Cu-AC, the appearance of a broad peak could be attributed to overlapping of peaks or instability of cuprous ions in acidic solution resulting in their fast conversion to cupric ions. The peaks merged due to a high scan rate of 50 mV/s, as anodic peak potentials of cuprous and cupric ion formation are relatively close, and their conversion process is fast (Elgrishi et al., 2018). Interestingly, the onset potential observed for all the electrocatalysts was lower than that for pure $Cu^{+}$ formation. The reduced onset potential could be due to the influence of supports. This indicated that the incorporation of support lowered the energy required for oxidation. The highest peak intensity for 20Cu-VC in acidic medium compared to other catalysts suggested easy transformation of cuprous oxide to cupric oxide for this catalyst. All the samples exhibited a reverse reduction peak in the acidic medium at around 0.2 - 0.30 V, except 20Cu-ALS-TC.

**Table 4.6: Anodic peak potential and current density observed from cyclic voltammetry of different supported copper catalysts in acidic and basic medium**

| Sample ID | In $H_2SO_4$ | | In $H_2SO_4$ + EG | | In KOH | | In KOH + EG | |
|---|---|---|---|---|---|---|---|---|
| | $E_{Pa}$ (V) | $J_{Pa}$ (mA/cm$^2$) | $E_{Pa}$ (V) | $J_{Pa}$ (mA/cm$^2$) | $E_{Pa}$ (V) | $J_{Pa}$ (mA/cm$^2$) | $E_{Pa}$ (V) | $J_{Pa}$ (mA/cm$^2$) |
| 20Cu-AC | 0.41 | 0.18 | 0.40 | 0.32 | 0.04 | 1.49 | 0.02 | 1.23 |
| 20Cu-RGO | 0.40 | 0.25 | 0.45 | 5.61 | 0.04 | 4.21 | 0.04 | 2.78 |
| 20Cu-ALS-TC | - | - | - | - | -0.31 | 1.15 | -0.28 | 0.73 |
| 20Cu-VC | 0.40 | 0.94 | 0.40 | 2.59 | 0.04 | 7.61 | 0.04 | 1.61 |

$E_{Pa}$ is anodic peak potential, $J_{Pa}$ is the anodic current density

In basic environment, the copper at the electrode-solution interface may undergo following reaction, *i.e.* Equation (4.3) in addition to reactions [Equation **Error! Reference source not found.** and (4.2)] (Kautek and Gordon, 1990).

$$Cu_2O + 3H_2O \rightleftarrows 2Cu(OH)_2 + 2H^{+} + 2e^{-} \quad (4.3)$$

Figure 4.9c and d depict the CV peaks of supported copper catalysts in KOH medium. The corresponding anodic peak potential and current density are summarized in Table 4.6. All supported catalysts had similar onset potential at around -0.4 V (Table 4.5). The maximum current density was observed at around 0.04 V for all the samples except 20Cu-ALS-TC, which showed a prominent peak at -0.31 V. According to the Pourbaix diagram, this peak could be

associated with $Cu(OH)_2$ formation. The anodic current densities ranged from 1.15 to 7.61 $mA/cm^2$, following the increasing order of 20Cu-ALS-TC (1.15 $mA/cm^2$) < 20Cu-AC (1.49 $mA/cm^2$) < 20Cu-RGO (4.21 $mA/cm^2$) < 20Cu-VC (7.61 $mA/cm^2$). Thus VC supported copper catalyst had the highest anodic current density, whereas ALS-TC supported catalyst had the lowest. In contrast to acidic environment, reduction at the cathodic region in alkaline medium was observed to be distinctly two-step process. The first reverse peak, which was detected over a range of -0.28 to -0.34 V depending on the type of support, could be attributed to $Cu^{2+}/Cu^{+}$ reduction. The second reverse peak observed between -0.7 and -0.78 V might be due to the reduction of $Cu^{+}/Cu$. Similar observations has also been documented in the literature (Habekost, 2016; Kautek and Gordon, 1990).

The variation in current density produced by different supported catalysts might be associated with the differences in their average pore size. Larger pore size would facilitate the diffusion and adsorption of the ionic species. This would, in turn, enhance the electrochemical reactions of the ionic species resulting in high current density. Among the supported catalysts, the 20Cu-VC catalyst with the largest pore size (17.5 nm) exhibited the highest activity in both acidic and basic media. The 20Cu-RGO, with the second largest average pore size of 5.8 nm, displayed the second highest activity in both the media conditions. The comparatively smaller average pore sizes of the AC and ALS-TC supported catalysts may account for their lower current density values in both media.

The interaction of copper at the anodic region in KOH medium led to the formation of $Cu_2O$ at a potential below -0.4 V. As the potential increased, the $Cu_2O$ converted to CuO between -0.35 and -0.25 V (Kautek and Gordon, 1990). In the basic medium, at similar potential, $Cu_2O$ had the capacity to generate $Cu(OH)_2$ at the electrode-solution interface, as shown in Equation **Error! Reference source not found.** (Kautek and Gordon, 1990). The higher current density generated in the basic medium might be due to $Cu(OH)_2$ formation (Habekost, 2016; Xia et al., 2024). However, the higher current density in basic medium compared to that in acidic medium might also be attributed to the ease of copper oxidation in the former. The ease of oxidation was observed to be influenced by the copper-support interaction, with the onset potential of supported copper being lower than that of pure form. The ease of oxidation, as indicated by the corresponding current density, further demonstrated that the nature of support also played an important role in determining the electrocatalytic activity of the catalysts. Copper dispersion on different supports also appeared to play a crucial role in increased catalytic activity, which resulted in higher current density. Both 20Cu-VC and 20Cu-RGO showed higher catalytic activity with 9% and 10% dispersion, respectively. The

smallest average pore size of 20Cu-AC (2.8 nm) might account for its reduced activity, even with a maximum metal dispersion of 16%. The poorer activity of 20Cu-ALS-TC could be attributed to its low metal dispersion of 4% and the second lowest average pore size (Table 4.3). Thus, both pore size and metal dispersion seemed to have an effect on current generation by ionic species. The CV of the supported copper catalysts was performed at different scan rates (10 to 80 mV/s) between 0.1 and 0.4 V (Figure 4.11a-d). All of the catalysts showed a linear relationship between current and scan rate (Figure 4.11e). This suggested that the current density depended on the capacitance of the electrocatalysts at the mentioned potential range.

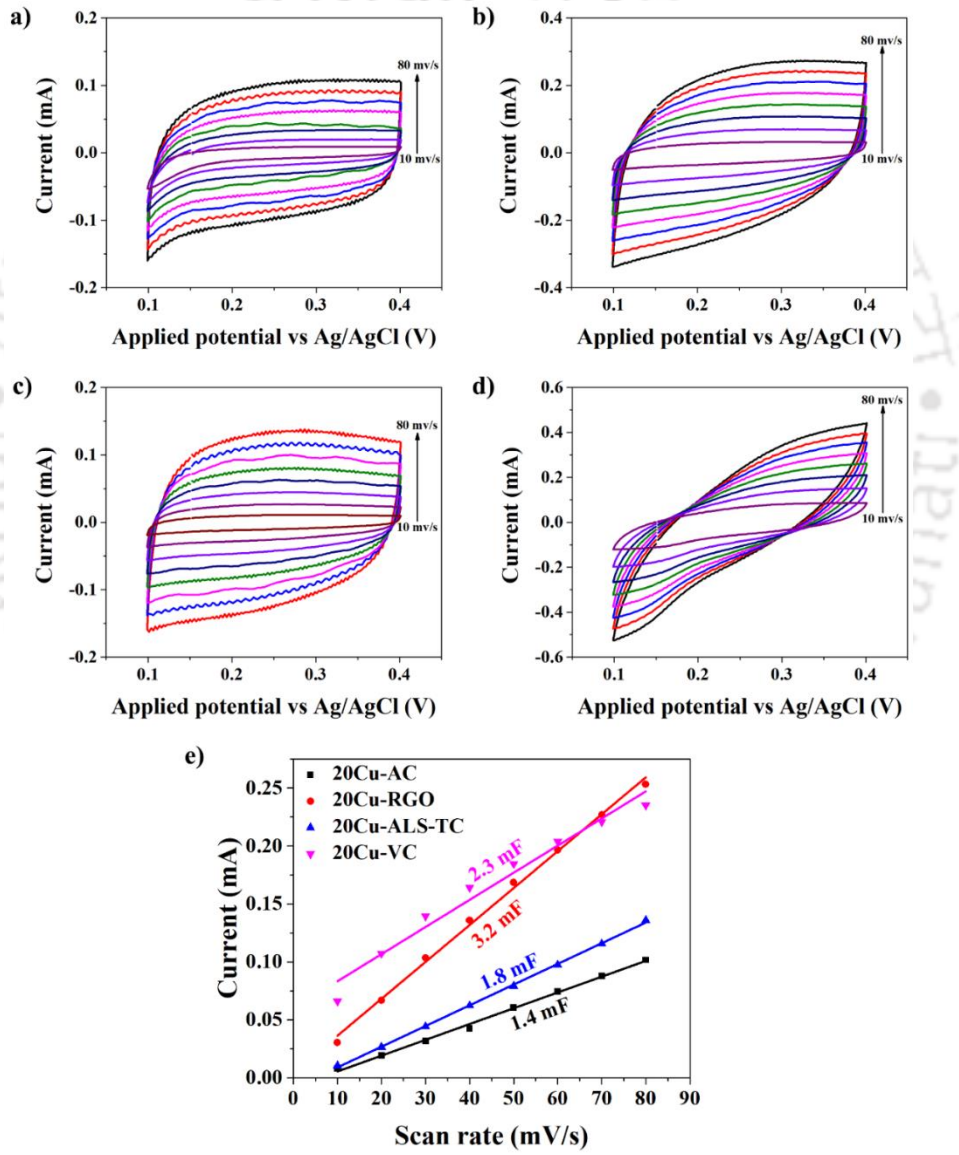


**Figure 4.11: Cyclic voltammetry of a) 20Cu-AC, b) 20Cu-RGO, c) 20Cu-ALS-TC, d) 20Cu-VC at different scan rates and e) relation of current density and scan rates for supported copper catalysts.**

The electrochemical active surface area (ECSA) and roughness factor (RF) calculated using Equation (3.5) and (3.6) are tabulated in Table 4.7. It was observed that 20Cu-RGO had the highest ECSA (80 $cm^2$), followed by 20Cu-VC (57.5 $cm^2$), 20Cu-ALS-TC (45 $cm^2$) and 20Cu-AC (35 $cm^2$). The RF for different copper catalysts ranged from 178.6 to 408.2.

**Table 4.7: Electrochemical properties and catalytic activity of supported copper catalysts**

| Sample ID | ECSA ($cm^2$) | Specific ECSA ($m^2/g$) | RF | Mass activity ($mA/mg_{Cu}$) | |
|---|---|---|---|---|---|
| | | | | $H_2SO_4$ medium | KOH medium |
| 20Cu-AC | 35 | 36.5 | 178.6 | 2.85 | 11 |
| 20Cu-RGO | 80 | 83.3 | 408.2 | 47.8 | 23.7 |
| 20Cu-ALS-TC | 45 | 46.9 | 229.6 | - | 7.2 |
| 20Cu-VC | 57.5 | 59.9 | 293.4 | 24.2 | 15 |

The CV studies were also conducted in the presence of 0.5 M EG, with all the other parameters being same as discussed above. Figure 4.11a-d displays the CV graphs of the supported copper catalysts in the presence of 0.5 M EG. The corresponding peak potential and current density are summarized in Table 4.6. In acidic medium, the presence of EG had no significant effect on the anodic peak potential of 20Cu-AC and 20Cu-VC (0.40 V), however, it shifted to 0.45 V for 20Cu-RGO. In the basic medium, the anodic peak potential remained same (0.04 V) for 20Cu-RGO and 20Cu-VC upon introduction of EG, but it shifted to 0.02 V for 20Cu-AC. On the other hand, the current density generated for the supported copper catalysts increased upon addition of EG, indicating that the presence of EG improved catalytic activity. With the highest current density of 5.61 $mA/cm^2$, 20Cu-RGO exhibited the highest activity in presence of EG, followed by 20Cu-VC (2.59 $mA/cm^2$). The mass activity of various catalysts is tabulated in Table 4.7. 20Cu-RGO exhibited the maximum mass activity in acidic medium (47.8 $mA/mg_{Cu}$). The mass activity decreased in the same manner as current density. The activity of different catalysts was also proportional to their ECSA. However, the overall current density for all supported copper catalysts decreased when EG was added to the basic medium, as compared to that observed in KOH. The order of current density among the electrocatalysts was 20Cu-ALS-TC (0.73 $mA/cm^2$) < 20Cu-AC (1.23 $mA/cm^2$) < 20Cu-VC (1.61 $mA/cm^2$) < 20Cu-RGO (2.78 $mA/cm^2$). The mass activity also showed the same trend as follows: 20Cu-ALS-TC (7.2 $mA/mg_{Cu}$) < 20Cu-AC (11 $mA/mg_{Cu}$) < 20Cu-VC (15 $mA/mg_{Cu}$) < 20Cu-RGO (27.5 $mA/mg_{Cu}$). 20Cu-RGO and 20Cu-VC had higher ECSA as compared to other electrocatalysts, which might be attributed to their higher current density and mass activity.

$Cu^{2+}$ ions are converted into higher order $Cu^{3+}$ ions during the oxidation of organic molecules in the presence of copper ions (Dantas et al., 2012; Habekost, 2016; Marioli and Kuwana, 1992). The EG oxidation at the copper surfaces might also follow a similar mechanism. The reaction of EG with higher order copper ions may be represented as (Dantas et al., 2012):

$$CH_2OH\text{-}CH_2OH + 2CuO_2^- \rightarrow CH_2OH\text{-}CHOH + CuO + 2OH^- \quad (4.4)$$

The variation in the formation of higher order $Cu^{3+}$ ions from $Cu^{2+}$ ions in the acidic and basic medium might have accounted for the difference in current density generated in these medium conditions. The transformation of $Cu^{2+}$ to higher order copper ions was reported as the rate-determining step for the oxidation of organic molecules at copper surfaces (Fleischmann et al., 1972; Hosseini et al., 2017). Hence, higher concentration of $Cu^{3+}$ ions are expected to result in a faster rate of EG oxidation reaction and subsequent increase in current density. Thus, a higher current density for all the catalysts in the acidic medium as compared to the basic medium suggested a higher concentration of $Cu^{3+}$ ions in the former. The presence of a higher concentration of positively charged $H^+$ ions in acidic medium might have facilitated the removal of negatively charged electrons from $Cu^{2+}$ ions to generate $Cu^{3+}$ ions in contrast to basic medium, which has higher concentration of negatively charged $OH^-$ ions. The addition of EG to the basic medium resulted in a decrease in current density, indicating that the formation of $Cu^{3+}$ ions was not favoured in the presence of EG at the studied potential. However, when the study was conducted at a higher potential range of -1 to 1 V (Figure 4.12a), there was a steep increase in current density in the presence of EG at a potential above 0.5 V (onset potential). In basic medium, above 0.5 V, the formation of $Cu^{3+}$ ions were facilitated, which eased the EG oxidation process. The more EG oxidation resulted in steep increase in current density. At 1 V, in the presence of 0.5 M EG and 0.1 M KOH, 20Cu-RGO exhibited a current density of 7.5 $mA/cm^2$. The results revealed that in the presence of EG, a higher potential was required to generate active $Cu^{3+}$ ions in the basic medium.

The RGO supported copper catalyst exhibited the highest activity upon addition of EG, followed by VC supported catalyst. As discussed earlier, higher average pore size might have contributed to the higher activity of the catalysts. Another dominating factor for higher current generation was the highest ECSA observed for 20Cu-RGO. The role of larger pore size seemed to be more important in the presence of EG, which itself is a larger molecule and contributed to the significantly higher activity of these catalysts (Goyal et al., 2022). Larger pore size might have facilitated the diffusion of the EG molecule to the active site. Despite lower pore size and

similar metal dispersion, the considerably higher activity of RGO supported catalysts compared to VC supported catalysts might be attributed to more oxygen-containing surface functional groups on the RGO supported catalysts (Table 4.4). The presence of surface oxygen functional groups increases the wettability of the pore surface, which facilitates surface diffusion of fuel and electrolyte molecules, thereby contributing to the reaction process (Li et al., 2020).

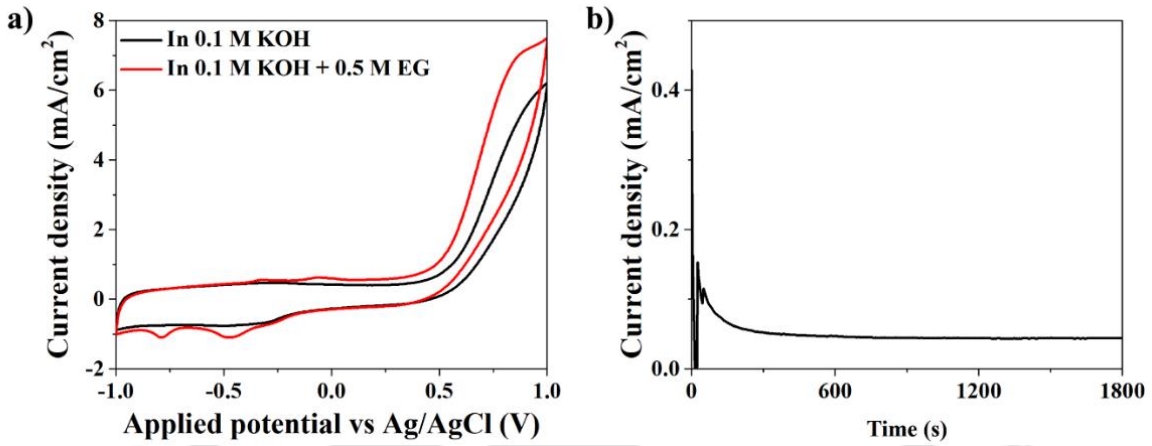


**Figure 4.12: a) Cyclic voltammetry of 20Cu-RGO in basic medium b) chronoamperometry of 20Cu-RGO at 0.6 V in basic medium.**

Figure 4.13 depicts the CA curves of supported copper catalysts generated in acidic and alkaline media with 0.5 M EG. In acidic medium, 20Cu-RGO had the highest current density, followed by 20Cu-AC and 20Cu-VC (Figure 4.13a). This contradicts the observation from CV study, which showed that under comparable circumstances, the current density for 20Cu-VC was higher than that for 20Cu-AC.

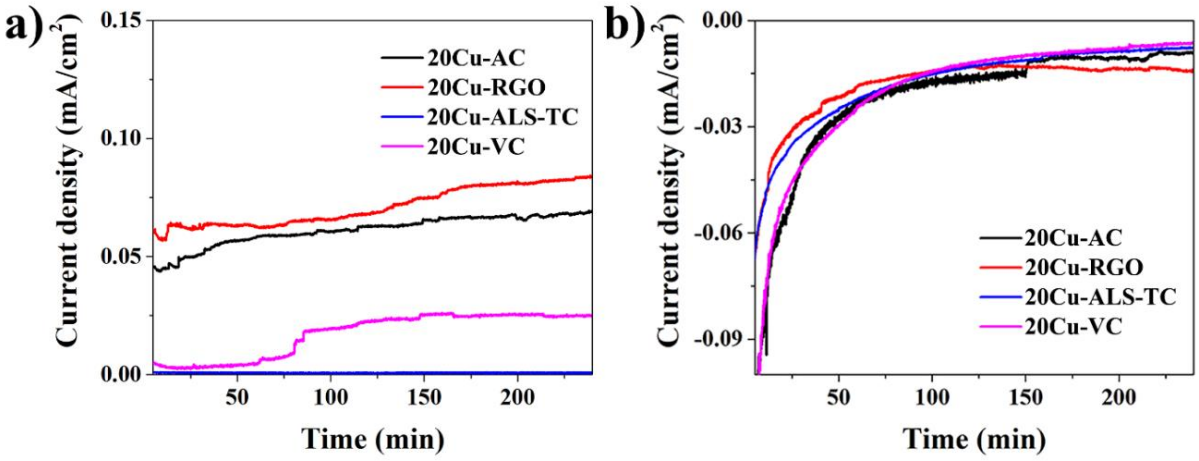


**Figure 4.13: Chronoamperometry of different supported copper catalysts with 0.5 M EG in $N_2$ saturated environment using a) 0.1 M $H_2SO_4$ and b) 0.1 M KOH as electrolyte.**

These results indicated that 20Cu-AC outperformed 20Cu-VC in longer duration of the study. 20Cu-ALS-TC displayed very low current density in acidic medium. On the contrary, all the supported copper (Cu) catalysts exhibited lower current density in basic medium. Nonetheless, a positive current density was achieved when CA was performed in the basic medium at a constant higher applied potential of 0.6 V (Figure 4.13b). Also, upon applying negative potential (-0.28 V) for CA studies according to the peak potential, a negative current density was observed in basic medium. The lower current density in the basic medium might be explained by partial passivation of electrodes by $Cu(OH)_2$ owing to longer exposure during CA studies.

The electrochemical impedance spectroscopy (EIS) spectra of the supported copper catalysts in 0.1 M $H_2SO_4$ in the absence and presence of EG are shown in Figure 4.14a and c, respectively. All the impedance spectra in Figure 4.14a displayed the same behaviour with a small depleted semicircle in the higher frequency zone and a bigger arc tending to form a semicircle in the lower frequency zone.

The experimental data were fitted with $[R_S(R_1Q_1)(R_2Q_2)]$ where $R_S$ is the solution resistance, $R_1$ is the charge transfer resistance and $Q_1$ is the constant phase element (CPE) developed due to double layer. In the absence of EG, $R_2$ and $Q_2$ evolved due to the transport of ionic species from bulk to the solid-electrolyte interface. In the presence of EG, the $R_2$ and $Q_2$ are the resistance and CPE generated, respectively, due to the electrochemical reaction. Each CPE has two components: admittance (Y), which is opposite of impedance and signifies the ease of charge transfer and n, which denotes the phase angle. Depending on the value of n, the working of CPE can be assigned to resistance (n = 0), capacitance (n = 1) or inductance (n = -1). Time constant ($\tau$) was calculated from corresponding R.Q components of the equivalent circuit using the following equation:

$$\tau = (Y \times R)^{\frac{1}{n}} \quad (4.5)$$

Time constant could be directly co-related to the rate of different processes occurring during electrochemical reaction. Here $\tau_1$, calculated from $R_1Q_1$ components, represented the time required for charge transfer and $\tau_2$, calculated from $R_2Q_2$ components, described the time required for transport of ionic species. In the presence of EG, $\tau_2$ indicated the time required for electrochemical reactions. The overall rate of electrochemical process, however, depended on

the simultaneous contribution of both $\tau_1$ and $\tau_2$. The fitted values of circuit for all the supported copper (Cu) catalysts in acidic medium are shown in Table 4.8.

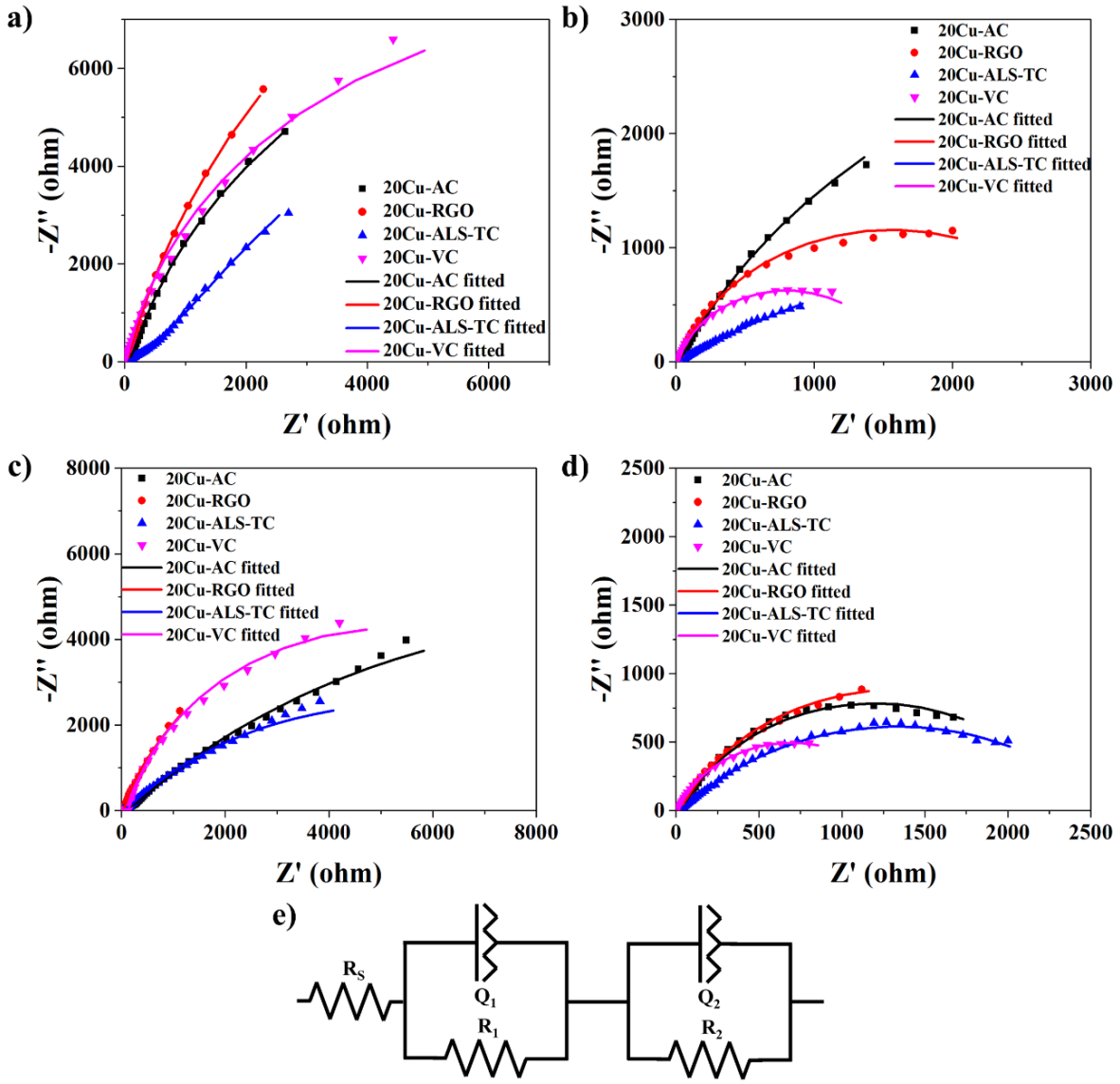


**Figure 4.14: Electrochemical impedance spectra of different supported copper catalysts in a, b) without EG and c, d) with 0.5 M EG in 0.1 M $H_2SO_4$ and 0.1 M KOH respectively and e) corresponding equivalent circuit diagram.**

The solution resistance ($R_S$) values for the supported copper catalysts were between 10 and 17.2 Ω. The 20Cu-RGO had the lowest resistance, whereas the other three catalysts exhibited almost similar resistance. The lower resistance of 20Cu-RGO could be attributed to its significantly larger average pore size (Table 4.3) and higher number of pores (Figure 4.4b) when compared to the remaining three catalysts. The charge transfer resistance, $R_1$, followed the trend as 20Cu-VC (11.3 Ω) < 20Cu-RGO (44.5 Ω) < 20Cu-AC (300 Ω) < 20Cu-ALS-TC

(2209 Ω). Under all conditions, the generation of lower current density of 20Cu-AC and 20Cu-ALS-TC was consistent with their extremely high charge transfer resistance. The admittance ($Y_1$) value components of $Q_1$ were between $16.2 \times 10^{-5}$ and $763 \times 10^{-5}$ $\Omega^{-1}$ $s^n$, whereas $n_1$ values ranged from 0.18 to 0.49. The values of the $n_1$ component of $Q_1$ suggested that the impedance developed from double layer formation at the electrode-electrolyte interface showed mixed behavior of capacitance and resistance. This behavior of double layer was mainly due to the porous structure of different carbon supports.

**Table 4.8: Parameters of equivalent circuits for different supported copper catalyst in 0.1 M $H_2SO_4$ medium**

| Sample ID | $R_S$ (Ω) | $R_1$ (Ω) | $Q_1$ | | $\tau_1$ (ms) | $R_2$ (KΩ) | $Q_2$ | | $\tau_2$(s) |
|---|---|---|---|---|---|---|---|---|---|
| | | | $Y_1 \times 10^{-5}$ ($\Omega^{-1}s^n$) | $n_1$ | | | $Y_2 \times 10^{-5}$ ($\Omega^{-1}s^n$) | $n_2$ | |
| 20Cu-AC | 15.1 | 300 | 653 | 0.26 | 13230 | 18.7 | 191 | 0.87 | 61.0 |
| 20Cu-RGO | 10 | 44.5 | 763 | 0.18 | 2.261 | 32.2 | 180 | 0.87 | 108.9 |
| 20Cu-ALS-TC | 14.7 | 2210 | 146 | 0.34 | 31589 | 23.6 | 236 | 0.74 | 223.5 |
| 20Cu-VC | 12.5 | 11.3 | 16.2 | 0.49 | 0.002 | 16.7 | 119 | 0.90 | 28.1 |
| 20Cu-AC* | 22.1 | 114 | 4.8 | 0.70 | 0.563 | 19.9 | 41.9 | 0.53 | 53.1 |
| 20Cu-RGO* | 10 | 27.5 | 278 | 0.23 | 0.011 | 11.0 | 376 | 0.84 | 82.3 |
| 20Cu-ALS-TC* | 23.9 | 40.2 | 2.2 | 0.76 | 0.100 | 13.1 | 36.6 | 0.54 | 18.7 |
| 20Cu-VC* | 26.8 | 108 | 5.51 | 0.70 | 0.420 | 10.3 | 103 | 0.89 | 14.6 |

* In presence of 0.5 M EG

The time constant ($\tau_1$) calculated from $R_1Q_1$ components ranged from 0.002 to 31589 ms. The 20Cu-VC had least $\tau_1$ value (0.002 ms), followed by 20Cu-RGO (2.261 ms), 20Cu-AC (13230 ms) and 20Cu-ALS-TC (31589 ms). Therefore, it can be concluded that the overall charge transfer process of 20Cu-AC and 20Cu-ALS-TC was much slower than the other two catalysts. In the absence of EG, the $R_2$ and $Q_2$ corresponded to the transport of ionic species from bulk to electrode-electrolyte interface (Kien et al., 2022). The rate of transport of ionic species to the solid-electrolyte interface was estimated using the time constant ($\tau_2$) calculated from $R_2$ and $Q_2$. For different catalysts, the $\tau_2$ values varied between 28.1 and 223.5 s, and the values followed a similar trend as $\tau_1$. The values of $\tau_1$ were much lower than that of $\tau_2$, irrespective of the catalysts, indicating that the transport of ionic species was the limiting factor in the overall electrochemical process. It was also evident that the catalysts with low $\tau_1$ and $\tau_2$ values would perform better, as the overall process was faster. Therefore, 20Cu-VC having lower $\tau_1$ and $\tau_2$ generated the highest current density in CV (Table 4.8).

The EIS spectra of all catalysts in acidic medium, consisting of two semicircles, in the presence of EG was similar to that without EG (Figure 4.14c). The obtained EIS spectra were fitted with the same equivalent circuit as done in the spectra without EG. Changes in the values of different circuit components were observed, as tabulated in Table 4.8. All supported copper catalysts, except 20Cu-RGO, showed an increase in the values of $R_S$ in acidic medium with the addition of EG and the values ranged from 10 to 26.8 Ω. The values of $R_1$ decreased for all the catalysts, except for 20Cu-VC. The $R_1$ for 20Cu-VC increased to 108 Ω from 11.3 Ω in the presence of EG, whereas there was a noticeable reduction to 43.3 Ω from 2210 Ω for 20Cu-ALS-TC. The admittance ($Y_1$), developed due to double layer capacitance, decreased for all the catalysts and ranged from 2.2 to 278 $\Omega^{-1}s^n$. The shape of the depressed semicircle, as measured by $n_1$, increased and was in the range of 0.23 to 0.76. This implied that the presence of EG increased the dominance of the capacitive behaviour of the double layer that formed at the electrode-electrolyte interface. This increase in capacitive behaviour was caused due to the adsorption of EG on the surface of the catalysts. The $\tau_1$ calculated for all catalysts decreased in presence of EG. However, the $\tau_1$ values for 20Cu-VC increased drastically due to increase in $R_1$. In acidic medium in the presence of EG, 20Cu-RGO exhibited the lowest $\tau_1$. Thus, it can be concluded that the charge transfer process for 20Cu-RGO was faster compared to the other catalysts in the presence of EG. These observations revealed that the introduction of EG in acidic medium altered the interaction behaviour of the adsorbed species at the solid-electrolyte interface of the supported copper catalysts. The $R_2$-$Q_2$ combination accounted for the electro-oxidation process in the presence of EG. The $\tau_2$ values for different catalysts increased as: 20Cu-VC (14.6 s) < 20Cu-ALS-TC (18.7 s) < 20Cu-AC (53.1 s) < 20Cu-RGO (82.3 s). The $\tau_2$ values for all the catalysts reduced in the presence of EG as compared to that obtained in its absence (Table 4.8). The decrease in $\tau_2$ indicated that electro-oxidation of EG was a faster process than the transport of ionic species. The lower values of $\tau_1$ and $\tau_2$ in the presence of EG depicted faster electrochemical process thereby resulting in higher current density, as observed from CV study (Figure 4.9a and b). Among all the studied catalysts, 20Cu-RGO with the lowest $\tau_1$ value (0.011 ms) generated the highest current density in acidic medium upon addition of EG (Table 4.6).

The EIS spectra of the supported copper catalysts in 0.1 M KOH in the absence and presence of EG are shown in Figure 4.14b and d, respectively. The nature of impedance pattern in basic medium was quite similar to that in acidic medium and also fitted the same equivalent

circuit (Figure 4.14e). The values of different components of the fitted circuit are tabulated in Table 4.9. The $R_S$ values of different supported catalysts in basic medium ranged from 4.9 to 6.6 Ω, while $R_1$ ranged from 7.2 to 20.3 Ω in the following order 20Cu-ALS-TC (7.2 Ω) < 20Cu-RGO (12.1 Ω) < 20Cu-VC (14.1 Ω) < 20Cu-AC (20.3 Ω). Admittance ($Y_1$) for different supported copper catalysts in basic medium varied from 23.8 to 387 $\Omega^{-1}s^n$ with $n_1$ fluctuating between 0.31 and 0.63. Time constant ($\tau_1$) for each catalyst was calculated from $R_1$ and $Q_1$ and it varied between 0.010 ms and 0.298 ms. 20Cu-RGO had the lowest $\tau_1$ (0.010 ms) followed by 20Cu-VC (0.022 ms), 20Cu-ALS-TC (0.037 ms) and 20Cu-AC (0.298 ms). The time required for the transport of ionic species in the absence of EG was represented by $\tau_2$, which was calculated from $R_2$ and $Q_2$. In basic medium, the $\tau_2$ values for different catalysts fluctuated from 1.4 to 1012s, with the increasing order of 20Cu-VC (1.4 s) < 20Cu-RGO (6.1 s) < 20Cu-AC (82.2) < 20Cu-ALS-TC (1012 s).

**Table 4.9: Parameters of equivalent circuit for different supported copper catalyst in 0.1 M KOH medium**

| Sample ID | $R_S$ (Ω) | $R_1$ (Ω) | $Q_1$ | | $\tau_1$ (ms) | $R_2$ (KΩ) | $Q_3$ | | $\tau_2$(s) |
|---|---|---|---|---|---|---|---|---|---|
| | | | $Y_1 \times 10^{-5}$ ($\Omega^{-1}s^n$) | $n_1$ | | | $Y_3 \times 10^{-5}$ ($\Omega^{-1}s^n$) | $n_3$ | |
| 20Cu-AC | 6.6 | 20.3 | 387 | 0.31 | 0.298 | 8.7 | 305 | 0.74 | 82.2 |
| 20Cu-RGO | 4.9 | 12.1 | 152 | 0.39 | 0.010 | 3.1 | 142 | 0.82 | 6.1 |
| 20Cu-ALS-TC | 6.0 | 7.2 | 23.8 | 0.63 | 0.037 | 6.1 | 242 | 0.39 | 1012 |
| 20Cu-VC | 5.6 | 14.1 | 116 | 0.39 | 0.022 | 1.6 | 86.6 | 0.86 | 1.4 |
| 20Cu-AC* | 6.4 | 29.5 | 259 | 0.32 | 0.318 | 2.3 | 174 | 0.75 | 6.4 |
| 20Cu-RGO* | 4.4 | 19.8 | 134 | 0.34 | 0.023 | 2.7 | 257 | 0.75 | 13.2 |
| 20Cu-ALS-TC* | 5.8 | 43.2 | 148 | 0.40 | 1.020 | 2.6 | 70.5 | 0.56 | 2.9 |
| 20Cu-VC* | 7.8 | 7.1 | 76.8 | 0.46 | 0.012 | 1.4 | 162 | 0.80 | 2.7 |

* In presence of 0.5 M EG

The transport of ionic species was a slower process in basic medium, as similar to that in acidic medium. Hence, the overall performance depended on the time constant $\tau_2$. It was observed that current density obtained from CV was inversely related to $\tau_2$ (Figure 4.9c, Table 4.6 and 4.9). The catalysts with lower $\tau_2$ values performed better electrochemically, as low $\tau_2$ values indicated faster transport process. Consequently, the catalysts with low $\tau_2$ values generated higher current density. In the presence of EG, the $R_S$ in basic medium remained more or less similar as that observed in the absence of EG (Figure 14.4d, Table 4.9). The $R_1$ for all the

catalysts experienced a slight increase upon the addition of EG, except for 20Cu-VC. The $R_1$ of 20Cu-VC decreased in presence of EG. The $Y_1$ also experienced a decrease for all the supported catalysts, except for 20Cu-ALS-TC. The $n_1$ values ranged from 0.32 to 0.46. In the basic medium, the $n_1$ value in the presence of EG remained almost same to that observed in the absence of EG. This demonstrated that addition of EG to basic medium had no effect on the double layer behaviour formed at the electrode-electrolyte interface. All the catalysts, except 20Cu-ALS-TC, showed negligible changes in $\tau_1$ values when EG was added to the basic medium. On the other hand, the $\tau_1$ value of 20Cu-ALS-TC increased significantly in the presence of EG. In the presence of EG in basic medium, the $\tau_2$ value, which is a measure of electrochemical reaction, decreased for 20Cu-ALS-TC and 20Cu-AC, while it increased for 20Cu-RGO and 20Cu-VC. All the catalysts experienced a decrease in current density, which could be explained by an increase in $\tau_1$ values upon addition of EG in basic medium. However, an increase in $\tau_2$ value for 20Cu-VC accounted for the decrease in current density, even though $\tau_1$ decreased minimally.

Comparing the performance of different catalysts in acidic and basic medium in the absence of EG, it was noted that all the catalysts generated higher current density in basic medium (Figure 4.9, Table 4.6). This was supported by their corresponding $\tau_1$ and $\tau_2$ values calculated from their respective equivalent circuit. Both the time constants were higher in acidic medium than in basic medium. Only for 20Cu-VC, $\tau_1$ was smaller in acidic medium than in basic medium, nevertheless $\tau_2$ was higher in acidic medium. The values of $\tau_1$ and $\tau_2$ decreased in acidic medium, but increased in basic medium in the presence of EG. Accordingly, CV showed better performance for all the catalysts in acidic medium with 0.5 M EG than in basic medium.

The study regarding effect of different support towards development of low cost transition metal based catalyst was systematically conducted for electro-oxidation of ethylene glycol. The results revealed that RGO was the best support for the electrocatalysts in both acidic and basic mediums. Moreover, the RGO supported enhanced activity in basic medium than in acidic medium for EG oxidation. The results were strongly supported by different physical as well as electrochemical characterisation.

## 4.3 Supported different metal catalysts

In the earlier section, the effect of support was discussed. Simultaneously, the effect of different metals was initially explored for low cost support. The study was conducted in both acidic and basic mediums to find out the most effective metal for electro-oxidation of EG.

### 4.3.1 Activated carbon supported different metal catalysts

#### 4.3.1.1 Physical characterization

The elemental composition of the electrocatalysts was determined by EDX analysis (Table 4.10). The metal content varied between 20.4 to 23.3 wt.%, while the oxygen content was in the range of 10.5 to 12.2 wt.%. The carbon content was obtained in the range of 65.9 - 69.1 wt.%.

**Table 4.10: Elemental composition of activated carbon supported different metal catalysts**

| Sample ID | Metal (wt.%) | C (wt.%) | O (wt.%) |
|---|---|---|---|
| 20Cu-AC | 23.3 | 65.9 | 10.8 |
| 20Ni-AC | 20.4 | 69.1 | 10.5 |
| 20Fe-AC | 20.4 | 68.0 | 11.6 |
| 20Co-AC | 20.4 | 67.4 | 12.2 |

The $N_2$ adsorption-desorption isotherms for the electrocatalysts were of Type II with H4 hysteresis loop, irrespective of the type of metal (Figure 4.15a). The presence of H4 hysteresis loop confirmed the existence of slit shaped porous structure. The isotherms for the electrocatalysts showed no significant variation except that for 20Ni-AC, which showed lower adsorption values. The BET surface area, pore volume, micropore area and average pore size of the catalysts are summarized in Table 4.11. The surface area and pore volume of the activated carbon were 986 $m^2/g$ and 0.6 $cm^3/g$, respectively. The surface area decreased with the addition of metals to carbon. This decrease in surface area for all the electrocatalysts with respect to carbon could be attributed to the partial pore blockage by the deposited metals. The surface area values of the electrocatalysts were in the order of 20Ni-AC (379 $m^2/g$) < 20Co-AC (526 $m^2/g$) < 20Cu-AC (566 $m^2/g$) < 20Fe-AC (615 $m^2/g$). The highest and the lowest surface area values were observed for 20Fe-AC and 20Ni-AC, respectively. The tendency of the deposited nickel to shrink on the surface after deposition might have resulted in increased pore blockage, thereby resulting in lowest surface area and pore volume for 20Ni-AC (Table 4.11). The pore size distribution of the electrocatalysts followed almost identical patterns, with

the majority of pores ranging in between 1 and 7 nm (Figure 4.15b). The 20Ni-AC had the lowest pore volume, while 20Fe-AC had the highest pore volume. The average pore size of the catalysts varied between 2.8 and 3.3 nm.

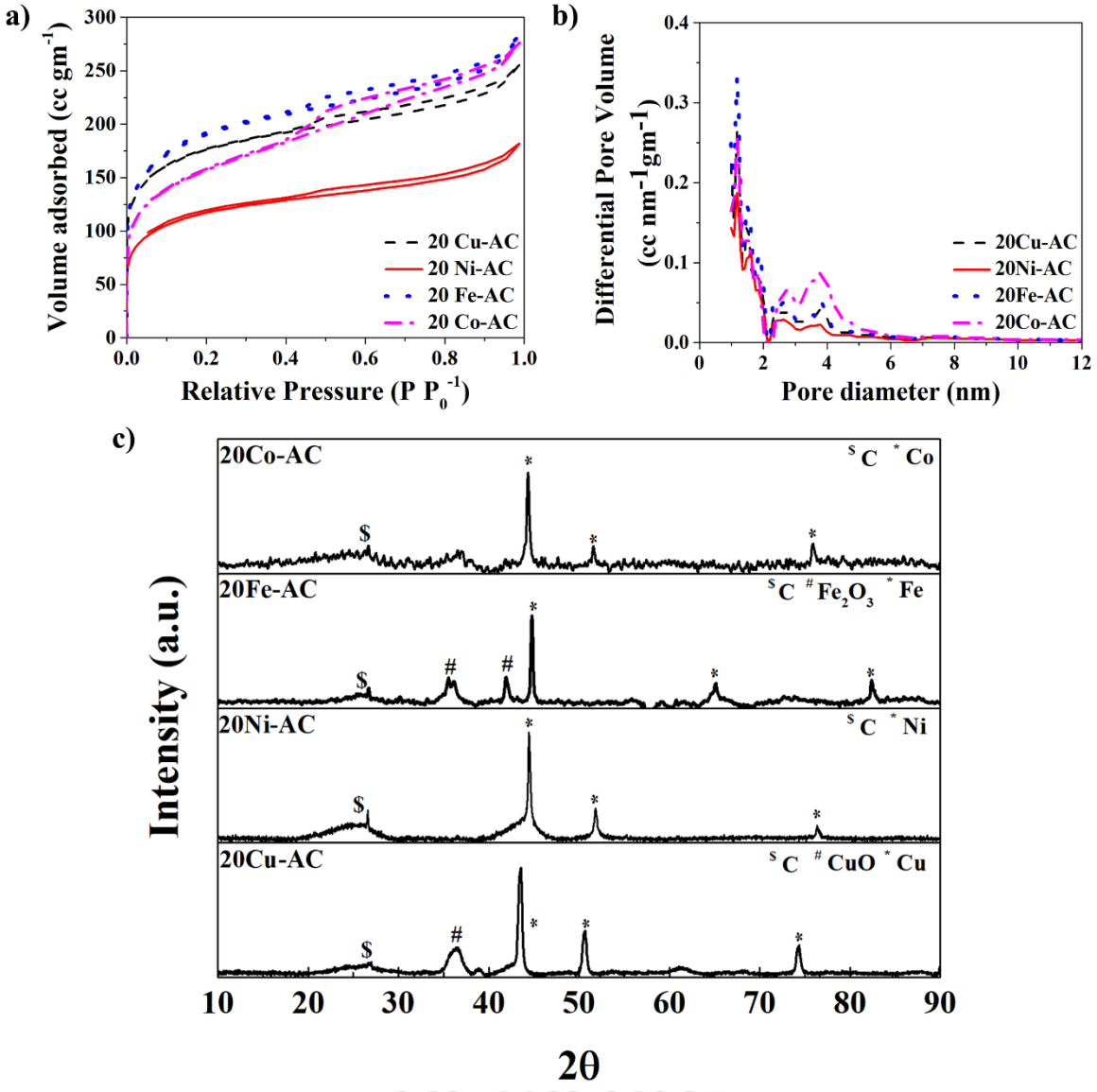


**Figure 4.15: a) $N_2$ adsorption-desorption isotherms, b) pore size distributions and c) XRD profiles of AC supported metal catalysts. (In all the isotherms the lower curves are for adsorption process and the upper curves for desorption process.)**

XRD profiles of electrocatalysts displayed a broad and low intensity graphitic peak between 24° to 27° corresponding to (002) plane of carbon (Figure 4.15c). The 20Cu-AC showed multiple peaks at 36.8°, 43.47°, 50.37° and 74° corresponding to (111) plane of CuO, (111), (200) and (220) planes of $Cu^0$ respectively (Ghouri et al., 2015). Multiple $Ni^0$ peaks were observed in 20Ni-AC at 44.49°, 51.89° and 76.34°, depicting (111), (200) and (220) planes,

respectively (Cui et al., 2015). The peaks at 35.7°, 41.7°, 44.82°, 65.23° and 82.36° in 20Fe-AC corresponded to (111), (113) planes of $Fe_2O_3$ and (110), (200), (211) planes of $Fe^0$ , respectively (Shi et al., 2015). The peaks for $Co^0$ of 20Co-AC were observed at 44.2°, 51.59° and 75.89° relating to (111), (200) and (220) planes, respectively (Cui et al., 2015). The d-spacing of metals for all electrocatalysts is tabulated in Table 4.11. The d-spacing values of metals in 20Cu-AC, 20Ni-AC, 20Fe-AC and 20Co-AC, calculated from the corresponding highest intensity peaks, were 0.208, 0.220, 0.219 and 0.220 nm, respectively. The dotted circular rings observed in the SAED patterns (Figure 4.17) confirmed that all the electrocatalysts were polycrystalline in nature and the planes were in compliance with that detected by XRD analysis. The crystallite size of AC supported catalysts varied from 17.6 to 33.9 nm.

**Table 4.11: Physical properties of AC supported metal catalysts**

| Sample ID | BET surface area ($m^2/g$) | Total Pore Volume ($cm^3/g$) | Micropore area ($m^2/g$) | Average pore size (nm) | Metal d-spacing* (nm) | $D_{TEM}$ (%) | $\phi$ (eV) |
|---|---|---|---|---|---|---|---|
| AC | 986 | 0.6 | 231 | 2.6 | - | - | - |
| 20Cu-AC | 566 | 0.39 | 95 | 2.8 | 0.208 | 15.8 | 4.415 |
| 20Ni-AC | 379 | 0.28 | 22 | 3.0 | 0.220 | 5.8 | 4.565 |
| 20Fe-AC | 615 | 0.44 | 43 | 2.9 | 0.219 | 6.4 | 4.211 |
| 20Co-AC | 526 | 0.43 | 26 | 3.3 | 0.220 | 9.7 | 4.517 |

*Metal d-spacing was calculated from XRD.

The FESEM images of electrocatalysts are shown in Figure 4.16a-d. All the electrocatalysts showed agglomerated porous morphology with varying degrees of porosity. All the catalysts showed a distinct spherical entity, which might be attributed to agglomerated metal particles. The agglomerated nature of the particles was more evident in 20Ni-AC with larger openings.

The FETEM images of the electrocatalysts are displayed in Figure 4.16e-h. The appearance of dense spheres in the FETEM images verified the presence of metal particles in the electrocatalysts . The size distributions of metal particles for all the catalysts are shown in Figure 4.16i-l. The size distributions of the metal particles for 20Cu-AC, 20Ni-AC, 20Fe-AC and 20Co-AC ranged from 4 to 12, 5 to 21, 9 to 21 and 6 to 16 nm, with corresponding average metal particle size of 7.8, 16.3, 14.4 and 9.4 nm, respectively. The corresponding metal dispersion values, calculated from Equation (3.2), are tabulated in Table 4.11. The 20Cu-AC showed the highest metal dispersion of 15.8%, while 20Ni-AC showed the lowest of 5.8%. The metal dispersion values of 20Fe-AC and 20Co-AC were 6.4% and 9.7%, respectively. The d-

spacing values, obtained from high resolution FETEM images (Figure 4.18), for 20Cu-AC, 20Ni-AC, 20Fe-AC and 20Co-AC were 0.25, 0.23, 0.22 and 0.22 nm, respectively, which are in agree,ent with the values obtained from XRD analysis.

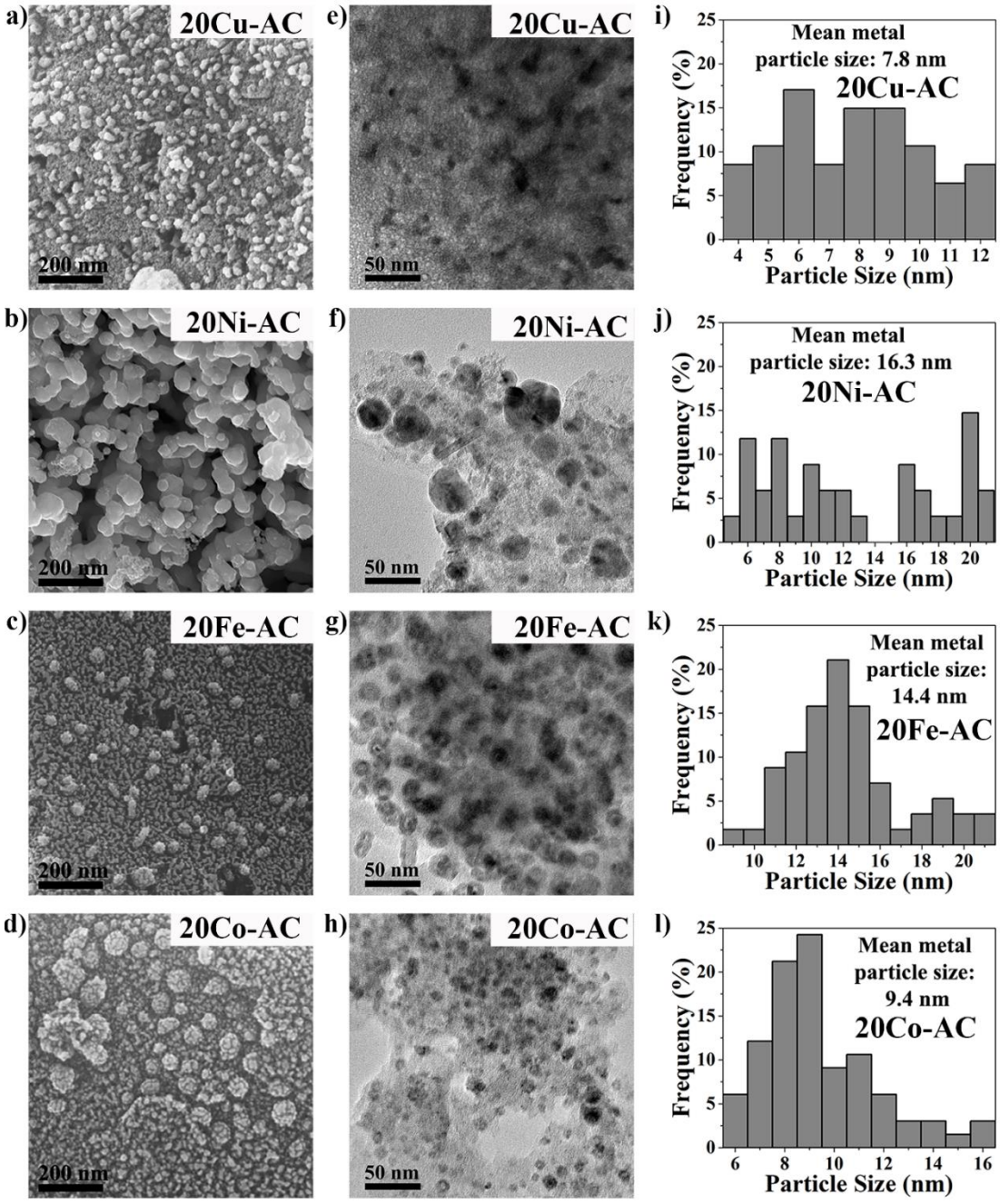


**Figure 4.16: a-d) FESEM images, e-h) FETEM images and corresponding i-l) particle size distribution of AC supported metal catalysts.**

The KPFM analysis of different catalysts are shown in Figure 4.19. The mapping of contact potential difference (CPD) values indicated variation in the surface charge for different catalysts, which might be attributed to the presence of different metals on the surface of the

catalysts. The CPD distribution of 20Cu-AC, 20Ni-AC, 20Fe-AC and 20Co-AC varied from 0.33 to 0.35 V, 0.17 to 0.24 V, 0.54 to 0.56 V and 0.19 to 0.27 V, respectively.

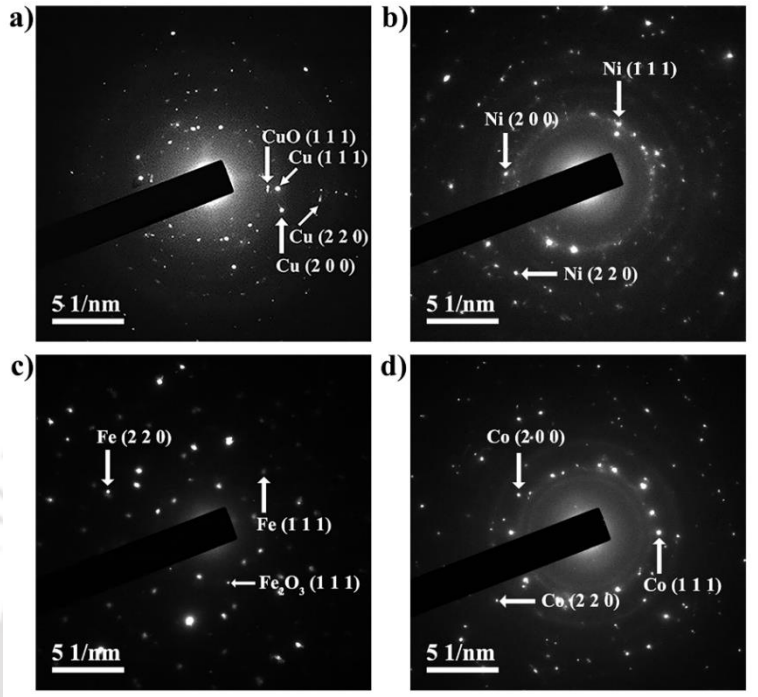


**Figure 4.17: SAED pattern from FETEM of electrocatalysts a) 20Cu-AC, b) 20Ni-AC, c) 20Fe-AC and d) 20Co-AC.**

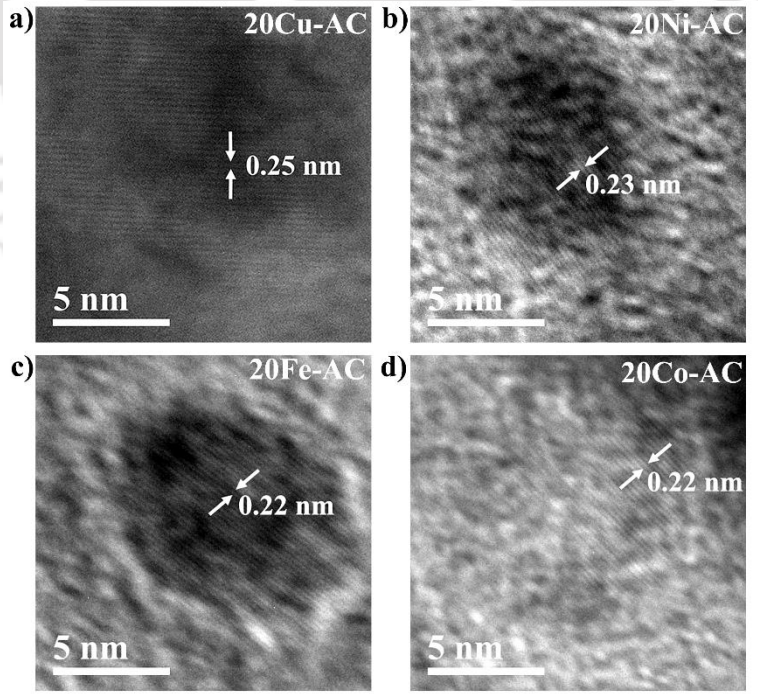


**Figure 4.18: High resolution FETEM images of electrocatalysts a) 20Cu-AC, b) 20Ni-AC, c) 20Fe-AC and d) 20Co-AC.**

The corresponding average CPD values obtained for different catalysts were in the order of 20Ni-AC (0.195 V) < 20Co-AC (0.243 V) < 20Cu-AC (0.345 V) < 20Fe-AC (0.549 V). The work function of different catalysts were calculated from these values using the Equation (3.4), as discussed in the experimental section. The order of work functions for different catalysts were 20Fe-AC (4.211 eV) < 20Cu-AC (4.415 eV) < 20Co-AC (4.517 eV) < 20Ni-AC (4.565 eV). The higher work function values generally corresponded to the higher electrochemical activity of the catalysts (Patel et al., 2016).

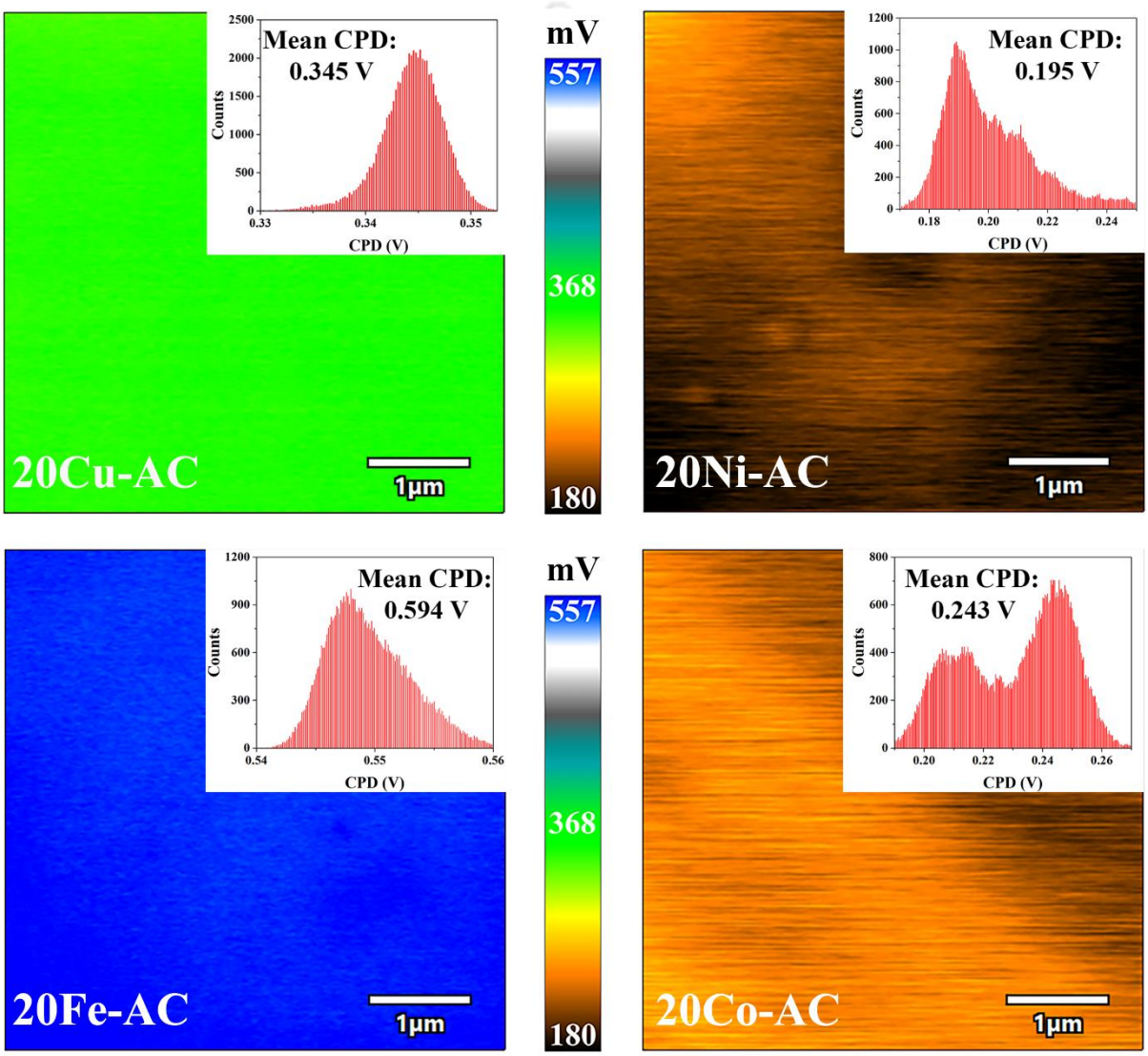


**Figure 4.19: KPFM images of AC supported metal catalysts and their corresponding distribution of contact potential difference (CPD) in inset.**

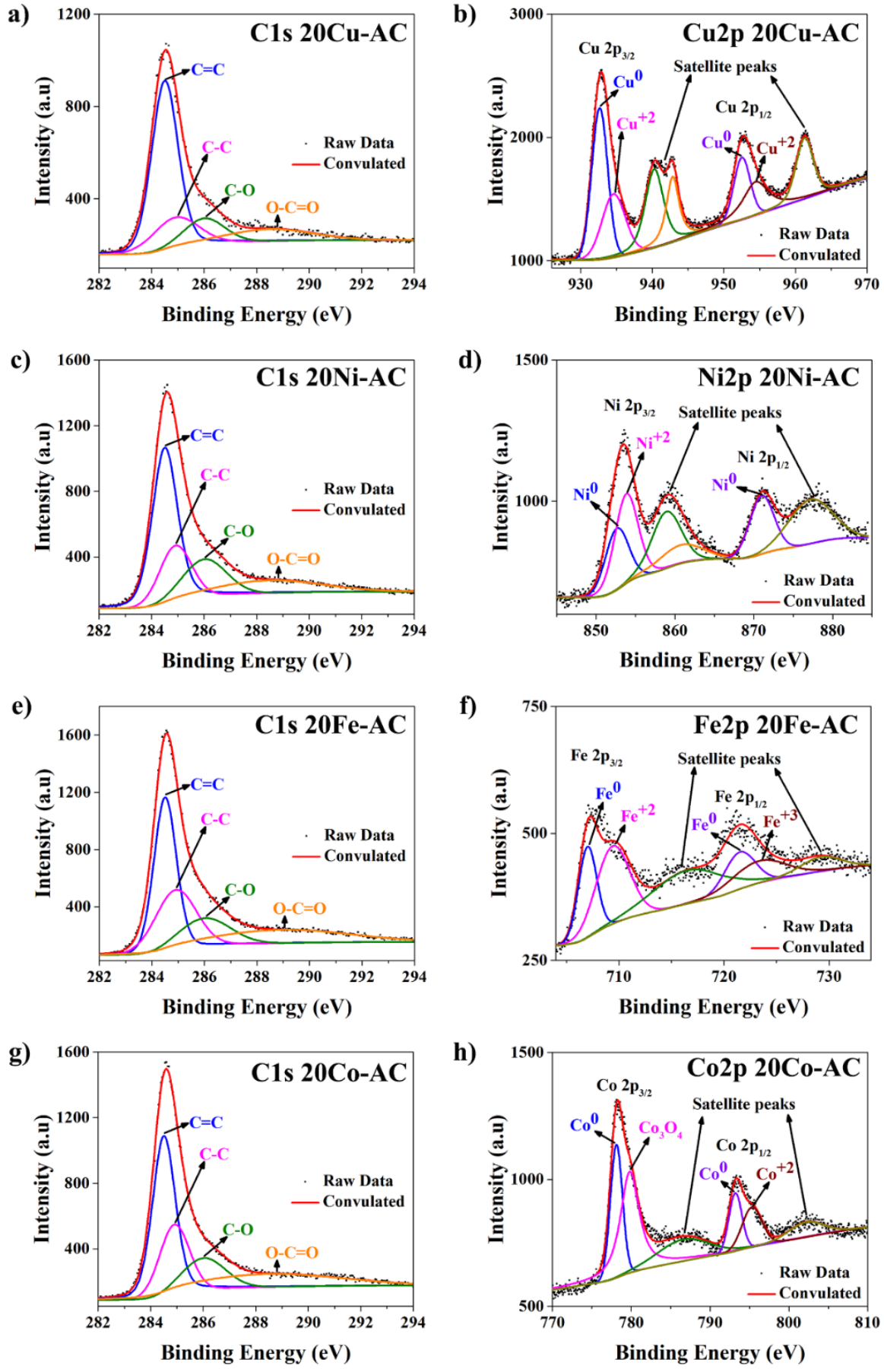


**Figure 4.20: XPS spectra of various AC supported metal catalysts.**

The XPS spectra of different catalysts are shown in Figure 4.20. The C1s of different metal catalysts were deconvoluted to understand the presence of different functional groups. All the catalysts showed four peaks at 284.5, 284.9, 286.0 and 288.8 eV, representing C=C, C-C, C-O and O=C-O functional groups, respectively (Zhang et al., 2018b). These peaks might have originated from the oxygen-containing functional groups present on the surface of carbon. The relative contribution of the different functional groups varied with the catalysts (Table 4.12). The difference might be explained by interactions of different metals with AC support. The relative contribution of oxygen-containing functional groups was highest for 20Fe-AC and 20Co-AC (35%), followed by 20Ni-AC (33%) and 20Cu-AC (26%).

**Table 4.12: Binding energy and relative contribution of different functional group present in AC supported different metal catalysts**

| Sample ID | C=C eV (%)* | C-C eV (%) | C-O eV(%) | O=C-O eV (%) |
|---|---|---|---|---|
| 20Cu-AC | 284.5 (59) | 285 (16) | 286 (13) | 288.7 (13) |
| 20Ni-AC | 284.5 (48) | 285 (19) | 286.1 (18) | 288.8 (15) |
| 20Fe-AC | 284.5 (39) | 284.9 (26) | 286 (15) | 289 (20) |
| 20Co-AC | 284.5 (43) | 284.9 (22) | 286 (14) | 288.8 (21) |

*the percent contribution of each peak is given in bracket.

All the metals showed 2p spectra, consisting of $2p_{3/2}$ and $2p_{1/2.}$ The deconvoluted $Cu2p_{3/2}$ spectra showed four peaks at 932.7, 934.7, 940.3 and 942.8 eV representing $Cu^0$, $Cu^{+2}$ and two satellite peaks, whereas $Cu2p_{1/2}$ revealed three peaks at 952.5, 954.6 and 961.3 eV representing $Cu^0$, $Cu^{+2}$ and one satellite peak, respectively (Xu et al., 2018b). The $Ni2p_{3/2}$ spectra exhibited four peaks at 852.7, 853.9, 859.1 and 861.2 eV depicting $Ni^0$, $Ni^{+2}$ and two satellite peaks, while $Ni2p_{1/2}$ displayed peaks at 872.1 and 877.4 eV, indicating $Ni^0$ and one satellite peak, respectively (Biesinger et al., 2011). The $Fe2p_{3/2}$ spectra showed three peaks at 707.1, 709.6 and 716.3 eV denoting $Fe^0$, $Fe^{+2}$ and one satellite peak, respectively. The $Fe2p_{1/2}$ spectra revealed three peaks at 721.6, 723.5 and 725.5 eV corresponding to $Fe^0$, $Fe^{+3}$ and one satellite peak, respectively (Mills and Sullivan, 1983). The $Co2p_{3/2}$ spectra exhibited three peaks at 778.1, 779.6, and 787 eV representing $Co^0$, $Co_3O_4$ and one satellite peak, whereas three peaks at 793.2, 795.5 and 802.3 eV were observed for $Co^0$, $Co^{+2}$ and one satellite peak in $Co2p_{1/2}$ region, respectively (Zafeiratos et al., 2010). In comparison to pure metals, all the metal peaks in the catalysts were shifted to higher binding energy (Mills and Sullivan, 1983; Xu et al., 2018b). This suggested strong interaction of metal particles with the carbon. The relative contribution of different oxidation states varied depending on the type of metal and is tabulated

in Table 4.13. The contribution of zero oxidation state, *i.e.* the metallic form, were 35, 57, 42 and 40% in 20Cu-AC, 20Ni-AC, 20Fe-AC and 20Co-AC, respectively.

**Table 4.13: Binding energies and relative contribution of different metal oxidation states present in the AC supported metal catalysts**

| Sample ID | Metal Oxidation State | $2p_{3/2}$ B.E (eV) | $2p_{1/2}$ B.E (eV) | Relative Metal Content (%) |
|---|---|---|---|---|
| 20Cu-AC | $Cu^0$ | 932.7 | 952.5 | 35 |
| | $Cu^{2+}$ | 934.7 | 954.6 | 65 |
| 20Ni-AC | $Ni^0$ | 852.7 | 872.1 | 57 |
| | $Ni^{2+}$ | 853.9 | - | 43 |
| 20Fe-AC | $Fe^0$ | 707.1 | 721.6 | 42 |
| | $Fe^{2+}$ | 709.6 | - | 40 |
| | $Fe^{3+}$ | - | 723.5 | 18 |
| 20Co-AC | $Co^0$ | 778.1 | - | 40 |
| | $Co^{2+}$ | - | 795.5 | 14 |
| | $Co_3O_4$ | 779.6 | - | 46 |

### 4.3.1.2 Electrochemical characterization

The CV curves of electrocatalysts recorded in acidic (0.1 M $H_2SO_4$) medium are shown in Figure 4.21a. The corresponding anodic peak potential and current density values are tabulated in Table 4.14. The anodic peaks were observed between 0.1 and 0.55 V. Ni exhibited two anodic peaks, one at 0.13 V representing its oxidation to $Ni^+$ ions and the other at 0.39 V denoting subsequent conversion to $Ni^{2+}$ ions. Similar to Ni, Cu also exhibited two oxidation states, one at 0.16 V and the other at 0.4 V, which corresponded with the formation potential of +1 and +2 ionic states, respectively. On the other hand, Fe and Co showed only one peak at 0.53 V and 0.37 V, respectively. These peak potentials of Fe and Co corresponded to their higher oxidation states. Similar peak potentials for Fe and Co were also reported and assigned to their higher oxidation states (Ebersbach et al., 1967). For the reduction of Cu, Fe and Co in acidic medium, only one peak was detected at 0.27, 0.25 and 0.22 V, respectively. The Ni, on the other hand, showed two reduction peaks at 0.25 and -0.1 V. The onset potential for the electrocatalysts also varied as 0.15 V for 20Cu-AC, -0.01 V for 20Ni-AC, 0.19 V for 20Fe-AC and 0.12 V for 20Co-AC. The anodic current densities varied as 20Ni-AC (0.97 $mA/cm^2$) > 20Fe-AC (0.87 $mA/cm^2$) >20Co-AC (0.82 $mA/cm^2$) > 20Cu-AC (0.18 $mA/cm^2$). Thus, in acidic medium, 20Ni-AC showed the highest anodic current density and 20Cu-AC the lowest. For all the electrocatalysts, there was an initial rise in current density at lower potential range

(0 to 0.3 V), which might have corresponded to the formation of $M^+$ ions from M**.** At potential around and above 0.4 V, the oxidation peaks were detected for all the electrocatalysts. These peaks are associated with formation of higher oxidation states of the metals. The formation of more number of higher oxidation states, would lead to more electron transfer for any metal. The higher number of transferred electrons could be directly related to the current density produced by any catalysts. All the catalysts showed reduction peaks around 0.3 V. Futhermore, 20Ni-AC showed an additional reduction peak at -0.09 V.

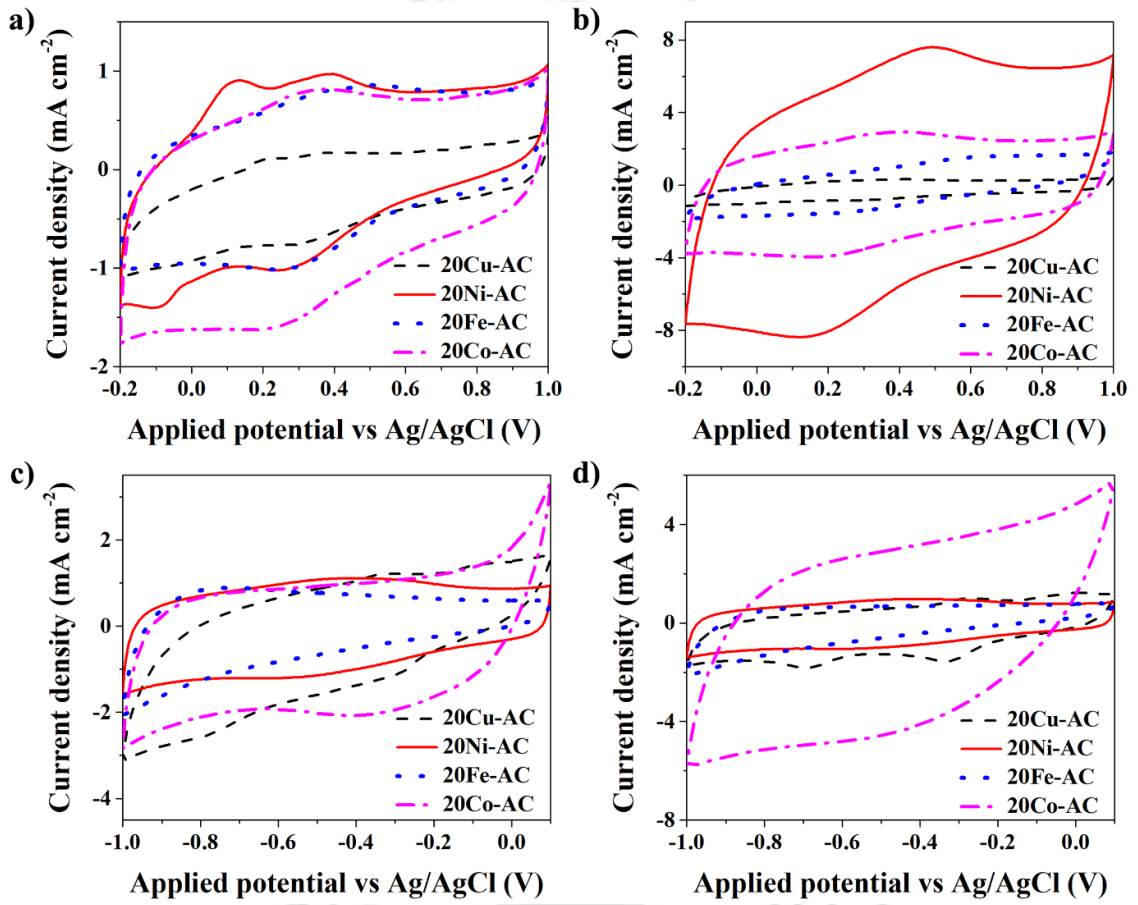


**Figure 4.21: Cyclic voltammetry of AC supported metal catalysts a) in 0.1 M $H_2SO_4$ without EG and b) in 0.1 M $H_2SO_4$ with 0.5 M EG, c) in 0.1 M KOH without EG, d) in 0.1 M KOH with 0.5 M EG.**

The CV studies conducted in acidic medium in the presence of 0.5 M EG are shown in Figure 4.21b. In presence of EG, the carbon showed no activity in acidic medium (Figure 4.3a). In acidic medium, the anodic peak potential shifted to a higher value in the presence of EG. However, the shift was negligible in case of 20Cu-AC. Table 4.14 provides an overview of the values for anodic potential and current density. The peak potential of 20Ni-AC shifted to 0.49 V, whereas it shifted to 0.67 V and 0.4 V for 20Fe-AC and 20Co-AC, respectively. The

potential shift was maximum for 20Fe-AC. In general, the applied potential could be related to the activation energy required for the catalysts to undergo any reaction. Thus, in the presence of EG, an increase in applied potential indicated an increase in activation energy for oxidation reactions. The activation energy was maximum for 20Fe-AC. The current density corresponding to the respective anodic peak potentials increased as EG underwent reaction on the surface of electrocatalysts. It was observed that 20Ni-AC generated a current density of 7.62 $mA/cm^2$, which was the highest in this medium followed by that of 20Co-AC (3.01 $mA/cm^2$), 20Fe-AC (1.67 $mA/cm^2$) and 20Cu-AC (0.32 $mA/cm^2$). The mass activity for EG oxidation shown by different electrocatalysts in acidic medium is tabulated in Table 4.15. The mass activity of the catalysts followed similar trend as that of current density. The highest mass activity of 47.2 $mA/mg_m$ was observed for 20Ni-AC in acidic medium. The higher percentage of metallic states along with higher work function value might be responsible for the highest current density in 20Ni-AC, while corresponding lower values for 20Cu-AC resulted in its lowest current density in acidic medium, both in absence and presence of EG. This also proved that the 20Ni-AC had the best catalytic activity among the studied electrocatalysts for EG electro-oxidation in acidic environment.

**Table 4.14: Anodic peak potential and current density observed from cyclic voltammetry of AC supported metal catalysts in acidic and basic media**

| Sample ID | In $H_2SO_4$ medium | | | | In KOH medium | | | |
|---|---|---|---|---|---|---|---|---|
| | Without EG | | With EG | | Without EG | | With EG | |
| | $E_{Pa}$ (V) | $J_{Pa}$ ($mA/cm^2$) | $E_{Pa}$ (V) | $J_{Pa}$ ($mA/cm^2$) | $E_{Pa}$ (V) | $J_{Pa}$ ($mA/cm^2$) | $E_{Pa}$ (V) | $J_{Pa}$ ($mA/cm^2$) |
| 20Cu-AC | 0.41 | 0.18 | 0.40 | 0.32 | -0.34 | 1.21 | -0.27 | 1.02 |
| 20Ni-AC | 0.39 | 0.97 | 0.49 | 7.62 | -0.44 | 1.12 | -0.42 | 1.02 |
| 20Fe-AC | 0.53 | 0.87 | 0.67 | 1.67 | -0.74 | 0.91 | -0.69 | 0.66 |
| 20Co-AC | 0.37 | 0.82 | 0.40 | 3.01 | - | - | - | - |

$E_{Pa}$ is anodic peak potential, $J_{Pa}$ is anodic current density.

The CV curves for basic medium are shown in Figure 4.21c. The peak potentials of different electrocatalysts varied distinctly. The 20Cu-AC, 20Ni-AC and 20Fe-AC showed anodic peaks at -0.34, -0.44 and -0.74 V, respectively. However, 20Co-AC did not exhibit any proper peak over the applied potential range. In addition to the aforementioned peak, 20Cu-AC also displayed a secondary peak at -0.075 V. Similarly, 20Cu-AC showed two reduction peaks at -0.29 V and -0.8 V. On the other hand, only one reduction peak was observed for 20Ni-AC and 20Co-AC at -0.56 V and -0.41 V, respectively. No prominent reduction peak was detected from the CV of 20Fe-AC in basic medium. The anodic peaks for 20Cu-AC at -0.34 V and -0.075 V

may be attributed to the formation of $Cu^{+}$ and $Cu^{+2}$ ions, respectively. For 20Ni-AC, the peak at -0.44 V could be assigned to α-$Ni(OH)_2$ formation. Similarly, anodic oxidation of 20Fe-AC in basic environment resulted in the formation of $Fe(OH)_2$ at a potential of -0.74 V. The absence of prominent peaks in 20Co-AC suggested weak transition of Co from metallic to oxidized state in basic medium. The current density generated in basic medium follows the following trend as: 20Cu-AC (1.21 mA/cm$^2$) > 20Ni-AC (1.12 mA/cm$^2$) > 20Fe-AC (0.91 mA/cm$^2$). This trend suggested that Cu showed higher activity in basic medium trailed by Ni and Fe. It is evident from Table 4.14 that current density generated in basic medium was higher than that in acidic medium. In basic medium, there was a scope of transition between different forms of hydroxides involving the transfer of electrons. These additional electron transfer might have resulted in higher current density observed in the basic medium. The ability of copper to undergo transition between various oxidation states might have resulted in slightly higher current density for 20Cu-AC than 20Ni-AC in basic medium.

**Table 4.15: Electrochemical properties and catalytic activity of AC supported metal catalysts**

| Sample ID | Mass activity (mA/mg$_m$) | | ECSA (cm$^2$) | Specific ECSA (m$^2$/g) |
|---|---|---|---|---|
| | $H_2SO_4$ medium | KOH medium | | |
| 20Cu-AC | 2.85 | 61 | 32.5 | 33.9 |
| 20Ni-AC | 76.2 | 110 | 42.5 | 44.3 |
| 20Fe-AC | 16.7 | 59 | 20 | 20.8 |
| 20Co-AC | 30.1 | 66 | 27.5 | 28.7 |

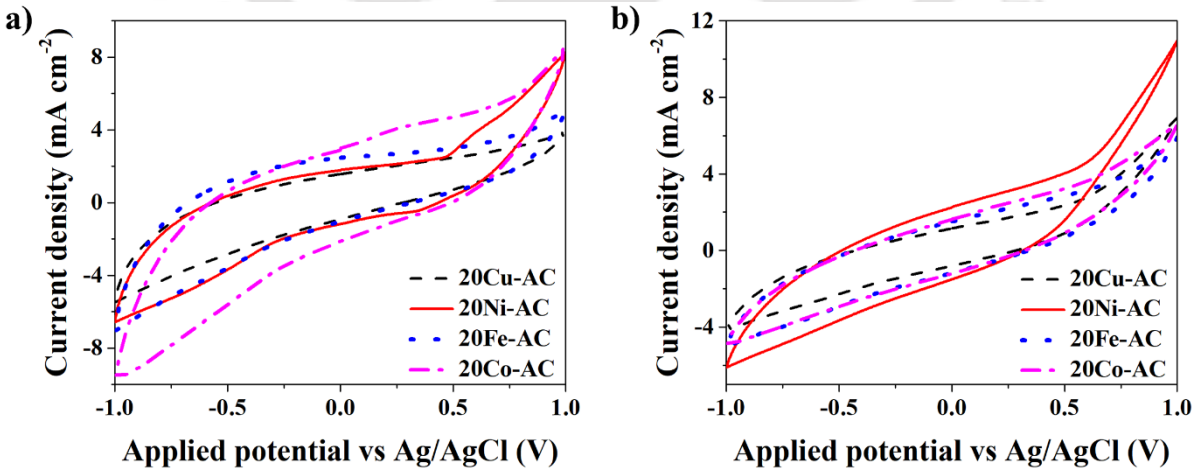


**Figure 4.22: Cyclic voltammetry of different AC supported metal catalysts in a) 0.1 M KOH and b) 0.5 M EG & 0.1 M KOH.**

In contrast to the behaviour of the electrocatalysts in acidic medium, the introduction of EG resulted in a shift of potential to lower values in basic medium. The CV studies conducted in basic medium with 0.5 M EG are shown in Figure 4.21d. Carbon showed negligible acitvity in basic medium with EG (Figure 4.3b). The 20Cu-AC, 20Ni-AC and 20Fe-AC exhibited anodic peaks at -0.27 V, -0.42 V and -0.69 V, respectively. However, 20Co-AC also did not generate any peak in presence of EG. Thus, the activation energy required to electro-oxidize EG was slightly reduced in basic environment, as suggested from the decrease in potential value. On the other hand, the current density generated at the peak potentials were not enhanced in presence of EG.

During electro-oxidation of EG in basic medium, 20Fe-AC generated a current density of 0.66 mA/cm$^2$. The 20Ni-AC and 20Cu-AC produced the same current density of 1.02 mA/cm$^2$. These results suggested that the used potential range was insufficient to undergo electro-oxidation of EG in basic medium. Hence, CV in basic medium was also performed in the range of -1 to 1 V in the absence and presence of EG (Figure 4.22). The low intensity peaks in these profiles, as discussed above, were not distinct. A new oxidation peak at 0.6 V with an onset potential of 0.46 V was detected for 20Ni-AC along with a reduction peak at 0.33 V. The oxidation peak of Ni may be attributed to the formation of NiOOH from $Ni(OH)_2$ (Cui et al., 2015). A current density of 3.98 mA/cm$^2$ was observed at this peak potential. Similarly, 20Co-AC showed an oxidation peak at 0.27 V, with an onset potential of 0.07 V. The current density associated with this peak was 4.2 mA/cm$^2$. However, no detectable peaks were present for 20Cu-AC and 20Fe-AC at higher potential. In the presence of 0.5 M EG and 0.1 M KOH, a steep rise in current density was observed at potential above 0.5 V for all the electrocatalysts. This suggested accelerated oxidation of EG at higher potential, which might be associated with the formation of higher order metal oxides at these potentials. The current density obtained for different catalysts at 1 V in presence of EG in basic medium followed the trend as: 20Fe-AC (5.9 mA/cm$^2$) < 20Co-AC (6.6 mA/cm$^2$) < 20Cu-AC (6.9 mA/cm$^2$) < 20Ni-AC (11 mA/cm$^2$).

The ECSA calculated from the linear relationship of current and scan rate was shown in Figure 4.23e. The CV studies showed increased current density with an increase in scan rate (30-80 mV/s) (Figure 4.23a-d). The ECSA values are tabulated in Table 4.15. The specific ECSA for different electrocataysts followed the increasing trend as: 20Fe-AC (20.8 m$^2$/g) < 20Co-AC (28.7 m$^2$/g) < 20Cu-AC (33.9 m$^2$/g) < 20Ni-AC (44.3 m$^2$/g). The increasing current density trend in basic medium was also supported by the increasing trend of ECSA for various electrocatalysts. The mass activity of different electrocatalysts in basic medium is summarized

in Table 4.15. 20Ni-AC had the highest mass activity of 110 mA/$mg_m$, followed by 20Co-AC (66 mA/$mg_m$), 20Cu-AC (61 mA/$mg_m$) and 20Fe-AC (59 mA/$mg_m$).

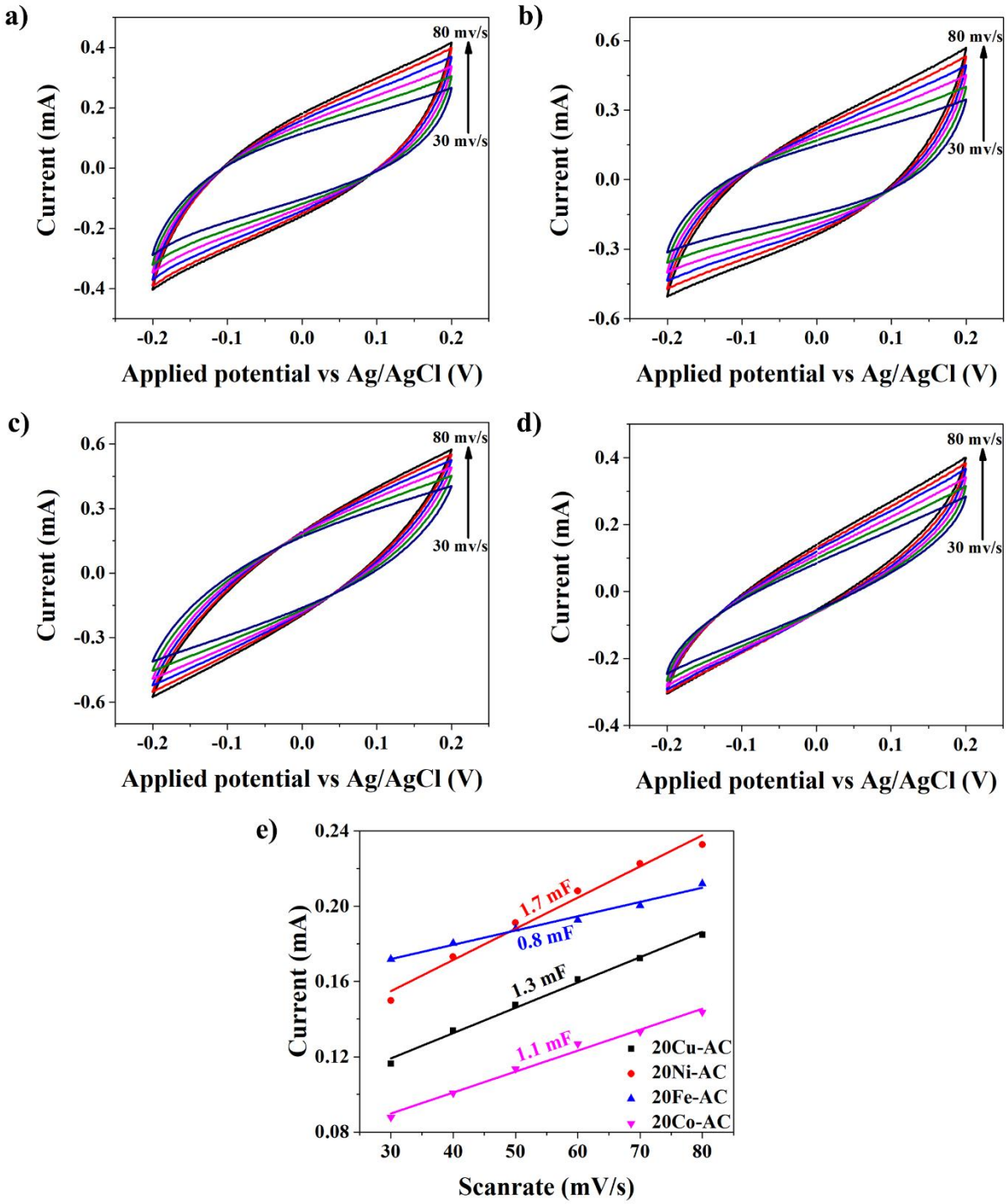


**Figure 4.23: Cyclic voltammetry at different scan rates for electrocatalysts a) 20Cu-AC and b) 20Ni-AC, c) 20Fe-AC, d) 20Fe-AC and e) relationship between current and scan rate for AC supported metal catalysts.**

Comparing the performance of all the electrocatalysts in both the media conditions, it was observed that all metals showed better activity in basic medium than in acidic medium at higher potential. Literature suggested the transformation of metals to higher metal oxides during electro-oxidation of organic compounds. This transformation to higher metal oxides was proposed irrespective of the type of transition metals (especially for Cu, Ni, Fe and Co) or the type of supports (Gayathri et al., 2022; Hameed et al., 2022; Rajeshkhanna and Ranga Rao, 2018). Increased formation of these oxides facilitated the electro-oxidation of EG. In contrast to acidic nedium, the enhanced activity of the metal catalysts in basic medium suggested that at higher potential, basic medium facilitated the formation of these metal oxides. Despite lower surface area and slightly lower metal dispersion, 20Ni-AC exhibited the highest activity towards anodic oxidation of EG and this might be attributed to its higher work function, ease of formation of higher oxidation states, *etc*. On the other hand, despite of having the highest surface area, 20Fe-AC displayed the least current density in presence of EG. The lower electrochemical activity of 20Fe-AC might be correlated to its lowest work function and most difficulty in the formation of higher oxidation states, as was evident from highest required onset potential. In basic medium, 20Cu-AC showed significantly higher activity, next to 20Ni-AC and as discussed earlier, this might have been associated with its ability to transform into different oxidation states.

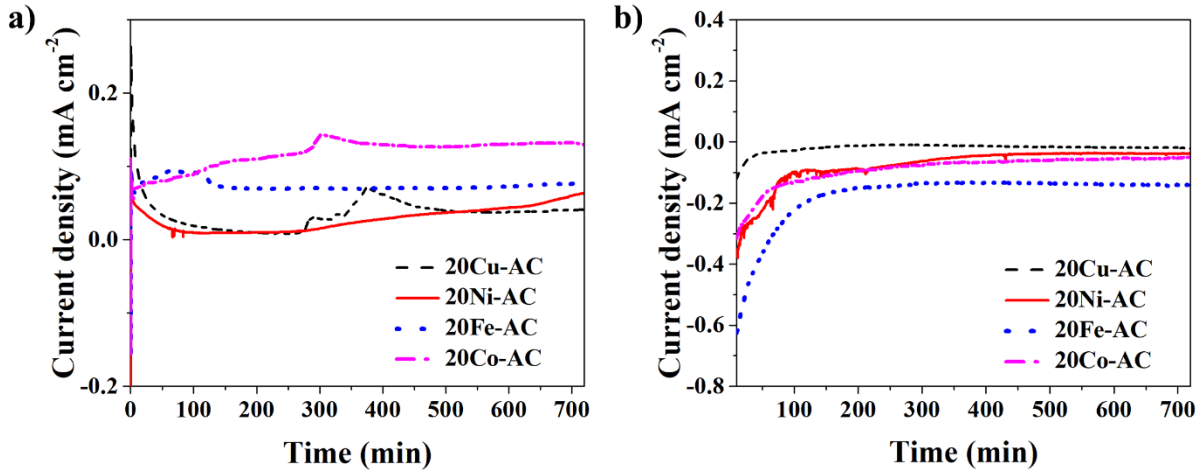


**Figure 4.24: Chronoamperometry for AC supported metal catalysts in presence of 0.5 M EG using a) 0.1 M $H_2SO_4$ and b) 0.1 M KOH as electrolyte.**

Chronoamperometric (CA) studies of electrocatalysts were carried out for 12 h in the presence of 0.5 M EG in acidic or basic medium and the plots are represented in Figure 4.24a and b, respectively. The acidic and basic medium were maintained at 0.1 M. In acidic medium with EG, the electrocatalysts were stabilised after 30 mins. The 20Co-AC catalyst showed the

highest current density and stability in acidic medium, followed by 20Fe-AC. 20Ni-AC and 20Cu-AC showed similar current density and stability. In basic medium, different catalysts attained stability at different times. The 20Cu-AC attained stability in shortest amount of time but had the lowest current density. 20Fe-AC performed the best in basic medium, although taking the maximum time to stabilize. The better stability of 20Fe-AC in basic medium suggested lower passivation of 20Fe-AC than other catalysts. The 20Ni-AC and 20Co-AC showed moderate performance in basic medium.

The EIS spectra of electrocatalysts in acidic medium are displayed in Figure 4.25a. All the electrocatalysts exhibited similar EIS pattern with two semi-circles. One semicircle was at higher frequency and other at lower frequency. All the spectra were fitted with equivalent circuit as shown in Figure 4.25e. The constant phase elements (CPE), $Q_1$ and $Q_2$, consisted of two components, admittance (Y) and phase angle (n). Phase angle values varied for CPE with respect to its capacitance, resistance or inductance nature. Time constants ($\tau_1$ and $\tau_2$) were calculated from their respective R and Q components, and were associated with the rate involved in respective processes. Lower time constant for a process suggests it to be faster (Kim and Park, 2005).

The circuit fitted values for acidic medium are represented in Table 4.16 (Figure 4.25a). The solution resistance ($R_S$) values of various metal-based electrocatalysts ranged from 15.1 to 24.8 Ω, indicating that the differences were not significant. The charge transfer resistance, $R_1$, was lowest for 20Cu-AC at 300 Ω, followed by 20Ni-AC (336 Ω), 20Co-AC (601 Ω), and the highest for 20Fe-AC at 801 Ω. The admittance $Y_1$ varied between 172 $\times 10^{-5}$ and 653 $\times 10^{-5}$ $\Omega^{-1}s^n$, whereas $n_1$ ranged from 0.26 to 1. The $\tau_1$ values of different metals followed the increasing trend as: 20Ni-AC (0.27 s) < 20Cu-AC (13.2 s) < 20Co-AC (22 s) < 20Fe-AC (87.3 s). Thus, it could be suggested that in acidic medium, the charge transfer process of 20Ni-AC was fastest in comparison to other catalysts. This was consistent with CV analysis, which showed that 20Ni-AC generated higher current in acidic medium than other catalysts (Figure 4.21a). $R_2$ for different electrocatalysts ranged between 2.5 and 18.7 KΩ, $Y_2$ varied from 185 to 713 $\times 10^{-5}$ $\Omega^{-1}s^n$, whereas $n_2$ varied from 0.4 to 0.87. The corresponding time constant $\tau_2$ of different metals followed the increasing trend as: 20Cu-AC (61 s) < 20Co-AC (137.8 s) < 20Ni-AC (150.1 s) < 20Fe-AC (4260 s). It could be concluded that the ionic transport of 20Cu-AC was faster compared to the other catalysts, followed by 20Co-AC and 20Ni-AC. It was also observed that 20Fe-AC had the slowest rates of charge transfer as well as ionic transport. The increasing trend in current density, as observed in CV study (Figure 4.21a), might be associated with decreasing $\tau_1$ values for the catalysts, except for 20Cu-AC. The current density observed in

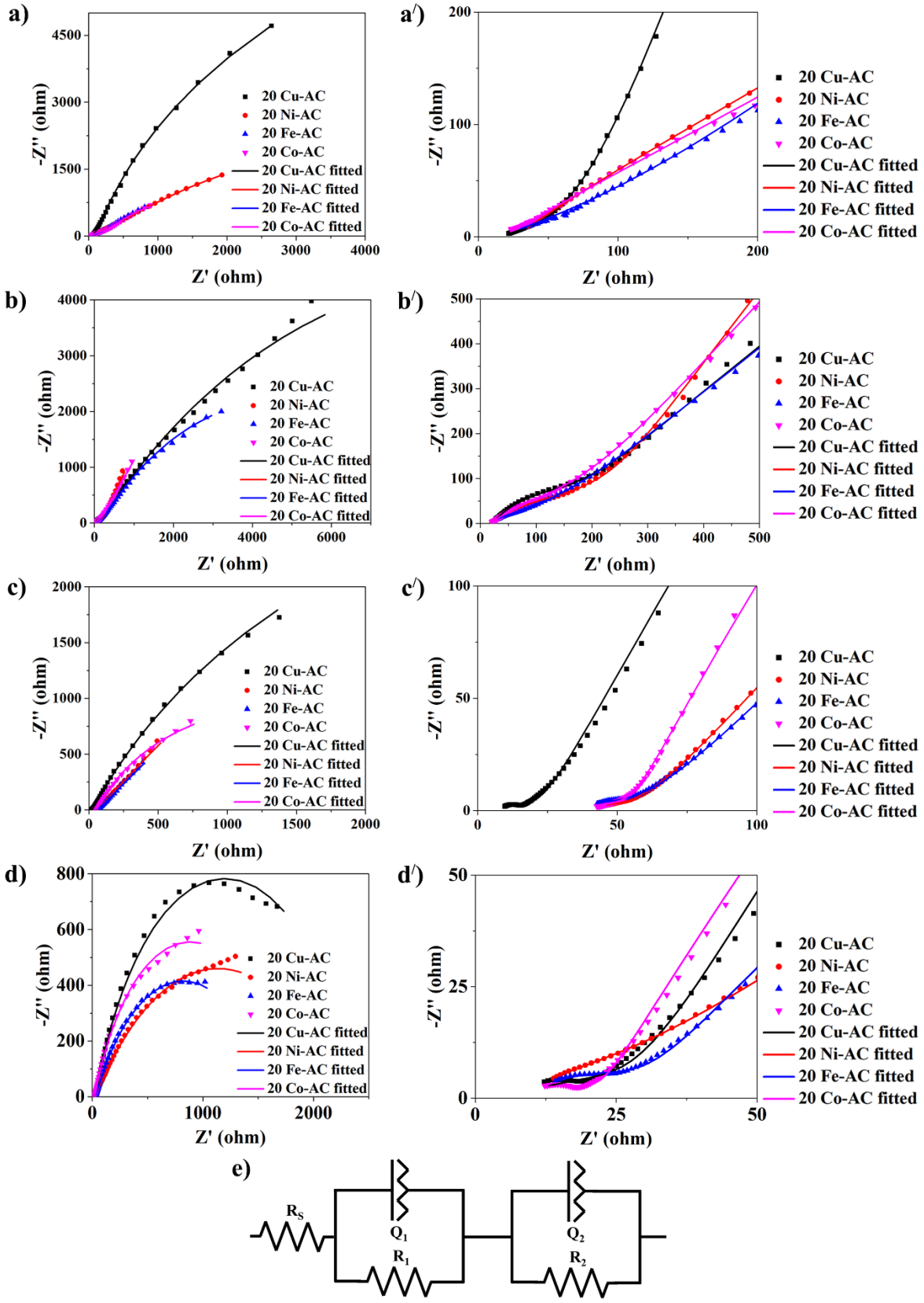


**Figure 4.25: EIS spectra of AC supported metal catalysts in a) without EG, b) with 0.5 M EG in 0.1 M $H_2SO_4$ c) without EG, d) with 0.5 M EG in 0.1 M KOH, e) corresponding equivalent circuit diagram. Points indicate experimental data and solid lines indicate fitting values and a/-d/) Zoomed view of higher frequencies.**

acidic medium was lowest for 20Cu-AC, despite its lower $\tau_1$ and $\tau_2$ values. As discussed earlier, the lower percentage of metallic states and lower work function for 20Cu-AC might have contributed to its lower performance. This could also suggest slower conversion of copper (Cu) into its different ionic states.

**Table 4.16. Fitted values of different equivalent circuit components for AC supported metal catalysts in 0.1 M $H_2SO_4$ and 0.1 M KOH medium in absence and presence of EG.**

| Sample ID | $R_S$ (Ω) | $R_1$ (Ω) | $Q_1$ | | $\tau_1$ (s) | $R_2$ (KΩ) | $Q_2$ | | $\tau_2$(s) |
|---|---|---|---|---|---|---|---|---|---|
| | | | $Y_1$ x $10^{-5}$ ($\Omega^{-1}s^n$) | $n_1$ | | | $Y_2$ x $10^{-5}$ ($\Omega^{-1}s^n$) | $n_2$ | |
| **In acidic medium** | | | | | | | | | |
| 20Cu-AC | 15.1 | 300 | 653 | 0.26 | 13.2 | 18.7 | 191 | 0.87 | 61.0 |
| 20Ni-AC | 21.0 | 336 | 172 | 0.43 | 0.27 | 8.9 | 185 | 0.56 | 150.1 |
| 20Fe-AC | 24.8 | 801 | 454 | 0.29 | 87.3 | 20 | 713 | 0.59 | 4260 |
| 20Co-AC | 16.8 | 601 | 498 | 1.00 | 22.0 | 2.5 | 281 | 0.40 | 137.8 |
| **In acidic medium + 0.5 M EG** | | | | | | | | | |
| 20Cu-AC* | 22.1 | 114 | 4.8 | 0.70 | 0.563 | 19.9 | 41.9 | 0.53 | 53.1 |
| 20Ni-AC* | 16.7 | 247 | 128 | 0.46 | 0.081 | 10.0 | 688 | 0.73 | 334 |
| 20Fe-AC* | 9.6 | 212 | 102 | 0.32 | 0.008 | 9.3 | 105 | 0.57 | 54.7 |
| 20Co-AC* | 17.8 | 191 | 171 | 0.46 | 0.090 | 15.0 | 435 | 0.65 | 623 |
| **In basic medium** | | | | | | | | | |
| 20Cu-AC | 6.6 | 20.3 | 387 | 0.31 | 0.298 | 8.7 | 305 | 0.74 | 82.2 |
| 20Ni-AC | 34.3 | 44 | 887 | 0.18 | 5.016 | 15 | 714 | 0.62 | 1980 |
| 20Fe-AC | 32.1 | 41.4 | 531 | 0.30 | 1.742 | 55 | 926 | 0.58 | 48015 |
| 20Co-AC | 40.5 | 17.2 | 402 | 0.41 | 1.565 | 2.7 | 628 | 0.76 | 40.8 |
| **In basic medium + 0.5 M EG** | | | | | | | | | |
| 20Cu-AC* | 6.4 | 29.5 | 259 | 0.32 | 0.318 | 2.3 | 174 | 0.75 | 6.4 |
| 20Ni-AC* | 6.3 | 26.2 | 110 | 0.40 | 0.130 | 2.2 | 131 | 0.50 | 8.3 |
| 20Fe-AC* | 8.5 | 22.0 | 3.43 | 0.50 | 0.051 | 1.58 | 223 | 0.62 | 7.8 |
| 20Co-AC* | 7.6 | 15.5 | 9.47 | 0.42 | 0.041 | 1.72 | 374 | 0.73 | 12.8 |

* Denotes values obtained in presence of EG.

The EIS spectra of electrocatalysts in acidic medium in the presence of 0.5 M EG is shown in Figure 4.25b. Addition of EG in the acidic medium did not change the nature of EIS spectra of the electrocatalysts. Hence, the spectra were fitted with the same equivalent circuit as used earlier (Figure 4.25e). The corresponding fitted values are shown in Table 4.16. The $R_S$ values were not affected significantly by the addition of EG, with the exception of 20Fe-AC; for which it decreased from 24.8 to 9.6 Ω. The charge transfer resistance $R_1$ and corresponding constant

phase element component $Y_1$ for all the catalysts decreased with respect to that obtained in the absence of EG.

The $R_1$ for 20Cu-AC was the lowest at 114 Ω, followed by 20Co-AC (191 Ω), 20Fe-AC (212 Ω) and 20Ni-AC (247 Ω). The $Y_1$ of different electrocatalysts fluctuated between 4.8 $\times 10^{-5}$ to 171 $\times 10^{-5}$ $\Omega^{-1}s^n$, while $n_1$ ranged from 0.32 to 0.70. The respective $\tau_1$ values deceased drastically in presence of EG compared to that obtained in its absence, suggesting faster charge transfer process in the presence of EG. The $\tau_1$ value was lowest for 20Fe-AC (0.008 s), followed by 20Ni-AC (0.081 s), 20Co-AC (0.090 s) and 20Cu-AC (0.563 s). The electrochemical reaction resistance $R_2$ values increased upon addition of EG, except for 20Fe-AC and $Y_2$ values increased for 20Ni-AC and 20Co-AC but decreased for 20Cu-AC and 20Fe-AC. The overall impact of $R_2$ and $Y_2$ could be observed from $\tau_2$ values, which increased for 20Ni-AC and 20Co-AC and decreased significantly for 20Cu-AC and 20Fe-AC. Both in the absence and presence of EG, the $\tau_1 << \tau_2$ for all the electrocatalysts confirmed that main resistances to the process were due to reaction resistances or resistance to ionic transport. In the presence of EG, the lowest time constants for 20Fe-AC may explain its better performance over longer period during CA study (Figure 4.24a). The drastic increase in current density for 20Ni-AC and 20Co-AC upon EG addition, as observed during CV study (Figure 4.21b), might be explained by the rapid decrease in $\tau_1$.

The EIS spectra of electrocatalysts in basic medium are shown in Figure 4.25c. The trend of EIS spectra in basic medium was similar to that observed in acidic medium. The fitted values of equivalent circuit components are tabulated in Table 4.16. The $R_S$ of electrocatalysts were between 6.6 and 40.5 Ω and all the values were higher compared to that in acidic medium, except for 20Cu-AC. The $R_1$ in basic medium followed the increasing trend of 20Co-AC (17.2 Ω) < 20Cu-AC (20.3 Ω) < 20Fe-AC (41.4 Ω) < 20Ni-AC (44 Ω). All these $R_1$ values were lower than the corresponding values in acidic medium. The $Y_1$ values ranged from 387 $\times 10^{-5}$ to 887 $\times 10^{-5}$ $\Omega^{-1}s^n$, while $n_1$ varied between 0.18 and 0.41. The $\tau_1$ for all the electrocatalysts in basic medium varied from 0.298 ms to 5.016 ms. These $\tau_1$ values were significantly lower than those obtained in acidic medium, with the exception of 20Ni-AC, where the $\tau_1$ value increased significantly. The $\tau_1$ value was the lowest for 20Cu-AC and highest for 20Ni-AC. The $\tau_2$ calculated from $R_2$ and $Q_2$ was significantly higher than $\tau_1$, as was also observed in acidic medium. The $\tau_2$ values for the electrocatalysts ranged from 40.8 to 48015 s in basic medium. The increasing order of $\tau_2$ was 20Co-AC (40.8 s) < 20Cu-AC (82.2 s) < 20Ni-AC (1980 s) < 20Fe-AC (48015 s) and could be used to explain the decreasing current density observed for the catalysts during CV analysis (Figure 4.21c).

The EIS spectra in basic medium with 0.5 M EG is shown in Figure 4.25d. Irrespective of the catalysts, it was observed that incorporation of EG to the basic medium decreased the $R_S$ values. $R_1$ and $Y_1$ also decreased for the catalysts, except 20Cu-AC. Accordingly, $\tau_1$ also got reduced in the presence of EG. Thus, the introduction of EG lowered the charge transfer resistance in basic medium for all the catalysts, except 20Cu-AC. The introduction of EG in basic medium resulted in a decrease in the $R_2$, $Y_2$ and corresponding $\tau_2$ values. This lowering of $\tau_2$ value indicated that the electrochemical reaction became fast as EG was introduced in basic medium particularly at higher potential. The addition of EG decreased the values of both $\tau_1$ and $\tau_2$ with $\tau_1 << \tau_2$. The higher values of $\tau_2$ compared to $\tau_1$ also suggested that resistance to ionic transport or reaction resistance was the controlling resistance in basic medium as well.

### 4.3.2 Reduced graphene oxide supported different metal catalysts

The study on the effect of support (Section 4.2) concluded RGO as the best support. It was also found out that in basic medium, the electrocatalysts showed better performance. Hence, the effect of various metals was also investigated in basic medium using RGO as a support to better understand the electrochemical behaviour of EG oxidation.

#### 4.3.2.1 Physical characterization

The RGO consisted of 85.7% carbon and 14.3% oxygen. The metal content of several catalysts varied from 22.5 to 25.7%. The oxygen content of the catalysts was almost in similar range (15-16%), except for 20Cu-RGO (10.2%). The addition of metal had no negative effect on the oxygen content of the catalysts. The EDX analysis of RGO and electrocatalysts are summarized in Table 4.17.

**Table 4.17: Elemental composition of RGO and RGO supported metal catalysts**

| Sample ID | Metal (wt.%) | C (wt.%) | O (wt.%) |
|---|---|---|---|
| RGO | - | 85.7 | 14.3 |
| 20Cu-RGO | 24.7 | 65.1 | 10.2 |
| 20Ni-RGO | 22.5 | 61.7 | 15.8 |
| 20Fe-RGO | 25.7 | 58.8 | 15.5 |
| 20Co-RGO | 23.4 | 61.5 | 15.1 |

The FESEM images of different electrocatalysts are depicted in Figure 4.26a-d. RGO demonstrated an agglomerated stack like structure (Figure 4.2b). Metal/RGO was found to deposit distinct spherical metal particles on RGO stacks. The extent of metal agglomeration depended on the type of metal. Agglomeration was higher for Fe and Co than for Ni and Cu. It

was also observed that 20Cu-RGO and 20Ni-RGO electrocatalysts were comparatively more porous in nature than 20Fe-RGO and 20Co-RGO electrocatalysts.

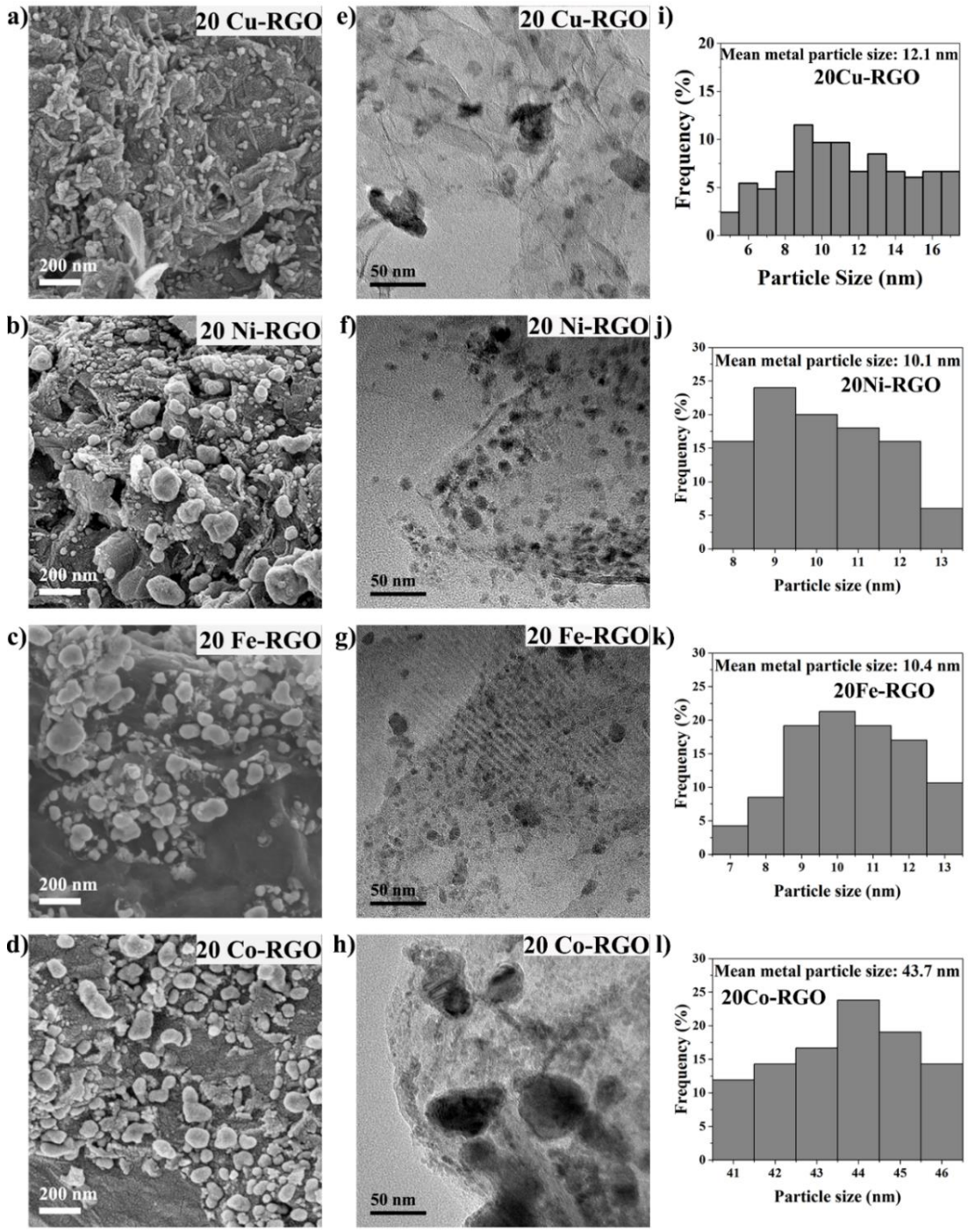


**Figure 4.26: a-d) FESEM images, e-h) FETEM images and i-l) their corresponding particle size distribution of RGO supported metal catalysts.**

The FETEM images of electrocatalysts are represented in Figure 4.26e-h. All the electrocatalysts displayed a sheet-like structure due to RGO (Figure 4.2f). The presence of metal particles was confirmed by dark spherical particles observed in the images of different

electrocatalysts. The metal size distribution of the electrocatalysts are shown in Figure 4.26i-l. The metal particles in 20Cu-RGO, 20Ni-RGO, 20Fe-RGO and 20Co-RGO had average sizes of 12.1, 10.1, 10.4 and 43.7 nm, respectively. The dispersion values of various catalysts, calculated using Equation (3.2), are tabulated in Table 4.18. The dispersion was highest for 20Cu-RGO (10.2%), followed by 20Ni-RGO (9.3%), 20Fe-RGO (8.9%) and 20Co-RGO (2.1%). The dotted circular ring observed in the SAED images of the catalysts (Figure 4.27) confirmed their polycrystalline nature. Moreover, the planes obtained for different catalysts were aligned with those observed in XRD. The d-spacing of metal crystallites for different catalysts, as observed from FETEM images, are shown in Figure 4.27. The d-spacing of 20Cu-RGO, 20Ni-RGO, 20Fe-RGO and 20Co-RGO were 0.26, 0.23, 0.22 and 0.23 nm, respectively. The d-spacing obtained from FETEM differed slightly from the XRD results (Table 4.18).

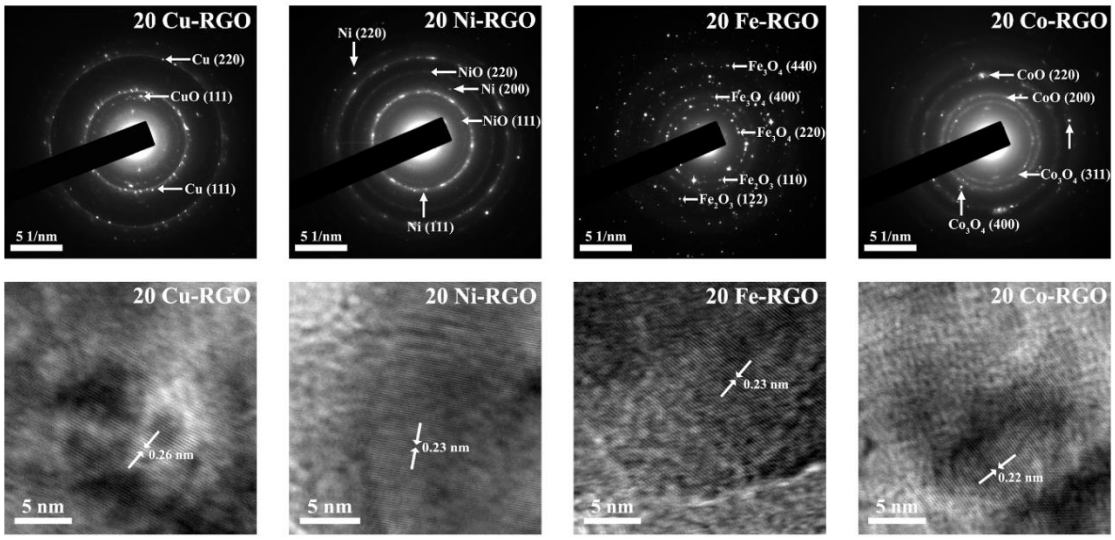


**Figure 4.27: SAED and d-spacing of RGO supported metal catalyst obtained from FETEM.**

The $N_2$ adsorption-desorption isotherms and pore size distribution of electrocatalysts are depicted in Figure 4.28a and b. The RGO exhibited Type II isotherm and H4 hysteresis loop (Figure 4.1a). The surface area of RGO was 487 $m^2/g$. All the electrocatalysts with H4 hysteresis loop showed a Type II isotherm, similar to that of RGO. The electrocatalysts formed slit shaped porous structure, as suggested by the presence of an H4 hysteresis loop. The incorporation of metal into RGO decreased the $N_2$ adsorption for all the electrocatalysts. The volume of $N_2$ adsorbed depended on the type of metal. The 20Ni-RGO and 20Cu-RGO gave higher $N_2$ adsorption, while 20Fe-RGO and 20Co-RGO showed very low $N_2$ adsorption. Accordingly, the surface area of different electrocatalysts showed the following trend as: 20Ni-RGO (200 $m^2/g$) > 20Cu-RGO (142 $m^2/g$) > 20Fe-RGO (17.4 $m^2/g$) > 20Co-RGO (9.2 $m^2/g$).

The surface area, average pore size and total pore volume are tabulated in Table 4.18. The metal particles deposited on RGO might have blocked the smaller pores of RGO, thereby lowering the surface area of the catalysts. Extremely low surface area for 20Fe-RGO and 20Co-RGO indicated metal sintering and excessive blockage of the pores.

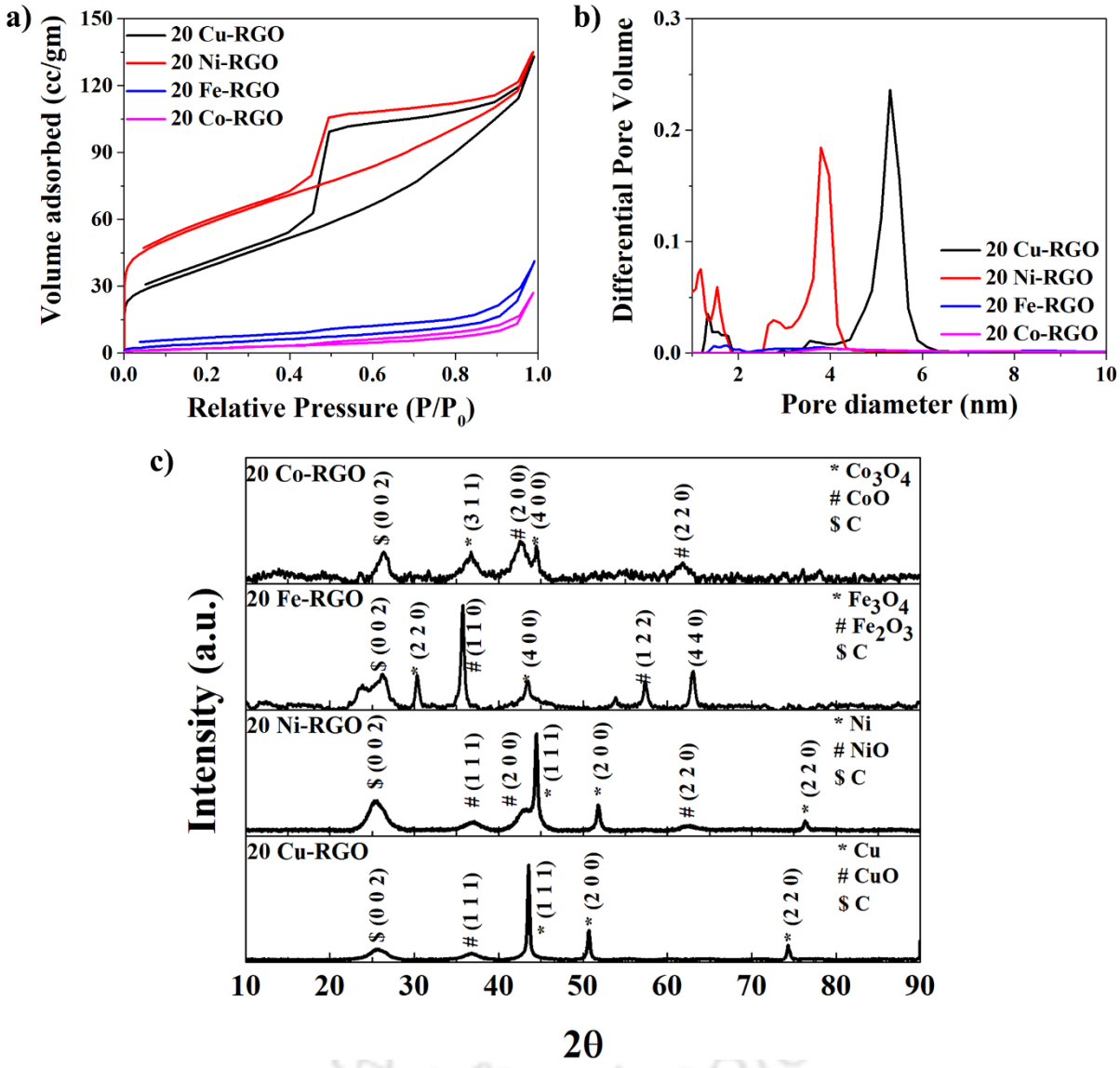


**Figure 4.28: a) $N_2$ adsorption-desorption isotherms, b) pore size distribution and c) XRD profiles of RGO supported metal catalysts. (In all the isotherms the lower curves are for adsorption process and the upper curves for desorption process.)**

The pore size distribution is shown in Figure 4.28b. RGO had an average pore size of 4 nm and pore volume of 0.5 $cm^3/g$. The pores of 20Ni-RGO were observed to be below 5 nm. The pore sizes in 20Cu-RGO varied between 3 and 6.5 nm. On the other hand, 20Fe-RGO and 20Co-RGO had wide pore size distribution with very low pore volume. These results agreed with the earlier observation of extensive pore blockages for these catalysts. 20Ni-RGO and 20Cu-RGO had similar pore volumes of 0.2 $cm^3/g$. The average pore size of 20Co-RGO was 18 nm,

followed by 20Fe-RGO (14 nm), 20Cu-RGO (5.8 nm) and 20Ni-RGO (4 nm). The average pore size increased and pore volume decreased with the addition of metals into RGO. This confirmed the blockage of smaller pores by metal incorporation.

**Table 4.18: Physical properties of RGO supported metal catalysts**

| Sample ID | BET surface area ($m^2/g$) | Total Pore Volume ($cm^3/g$) | Micropore area ($m^2/g$) | Average pore size (nm) | Metal d-spacing* (nm) | $D_{TEM}$ (%) |
|---|---|---|---|---|---|---|
| RGO | 487 | 0.5 | 67 | 4 | - | - |
| 20Cu-RGO | 142 | 0.2 | 11 | 5.8 | 0.21 | 10.2 |
| 20Ni-RGO | 200 | 0.2 | 34 | 4 | 0.20 | 9.3 |
| 20Fe-RGO | 17.4 | 0.06 | 0 | 14 | 0.25 | 8.9 |
| 20Co-RGO | 9.2 | 0.04 | 0 | 18 | 0.22 | 2.1 |

* d-spacing of different metals calculated from XRD

The XRD profiles of different electrocatalysts are represented in Figure 4.28c. The catalysts showed (002) peak of graphitic carbon between 25-27° which confirmed the presence of RGO (Singh and De, 2020). The peaks at 43.5°, 50.6° and 74.3° for 20Cu-RGO corresponded to the (111), (200) and (220) planes of $Cu^0$, respectively, whereas the peaks at 36.7° (111) might be assigned to CuO (Ghouri et al., 2015). The 36.9°, 42.7° and 62.4° peaks for 20Ni-RGO are assigned to (111), (200) and (220) planes of NiO, respectively. The 44.5°, 51.7° and 76.3° peaks corresponded to (111), (200) and (220) planes of $Ni^0$, respectively (Ullah et al., 2019). The peaks at 35.7° and 57.3°corresponded to the (110) and (122) planes of $Fe_2O_3$ in 20Fe-RGO. The 30.42°, 43.47° and 63° in 20Fe-RGO have already been reported to be assigned to (220), (400) and (440) planes of $Fe_3O_4$, respectively (Ai et al., 2019). The 20Co-RGO revealed peaks for the (200) and (220) planes of CoO at 42.7° and 62.1°, while peaks at 36.8° and 44.5° corresponded to the (311) and (400) planes of $Co_3O_4$, respectively (Alex et al., 2020). The metal d-spacing of different electrocatalysts are displayed in Table 4.18, which varied from 0.20 to 0.25 nm. The crystallite size of RGO supported catalysts varied between 7.4 to 26.3 nm.

The XPS spectra of electrocatalysts are shown in Figure 4.29. The C1s spectra revealed the presence of C=C, C-C, C-O and O=C-O functional groups, whose peaks were observed around 284.6, 285, 286 and 288 eV, respectively (Singh and De, 2020). Table 4.19 tabulates the relative contribution of these functional groups, which ranged from 27 to 33% and did not vary significantly from one another.

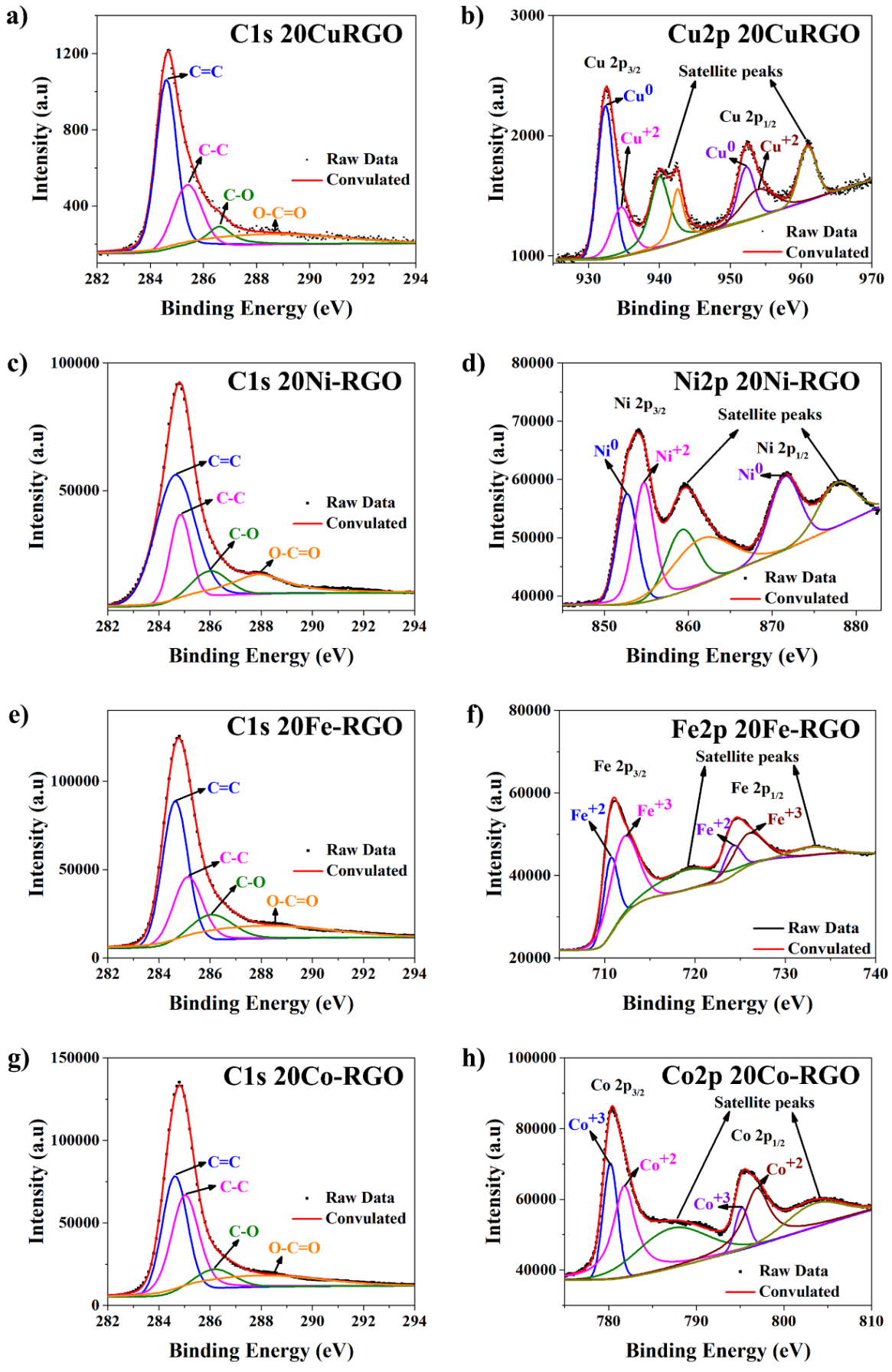


**Figure 4.29: XPS spectra of different RGO supported metal catalysts.**

The transition metals (Cu, Ni, Fe and Co) present in the different electrocatalysts showed their respective 2p spectra, which consisted of $2p_{3/2}$ and $2p_{1/2}$ regions. The 20Cu-RGO showed peaks for $Cu^0$ at 932.4 and 952.5 eV, while that for $Cu^{2+}$ at 934.7 and 954.6 eV. The satellite peaks of Cu were observed at 940.3, 942.8 and 961.3 eV (Xu et al., 2018b). The 20Ni-RGO produced peaks for $Ni^0$ at 852.7 and 871.6 eV, and for $Ni^{2+}$ at 854.6 eV. Three satellite peaks were detected at 859.4, 862.2 and 877.9 eV (Biesinger et al., 2011). The 20Fe-RGO displayed $Fe^{2+}$ peaks at 710.7 and 724.3 eV, and $Fe^{3+}$ peaks at 712.4 and 726.1 eV, whereas the satellite peaks were observed at 719.3 and 732.9 eV (Ai et al., 2019). The $Co^{2+}$ peaks of 20Co-RGO were observed at 781.8 and 796.8 eV, while $Co^{3+}$ peaks were detected at 780.2 and 795.2 eV. The satellite peaks were observed at 787.8 and 804 eV (Alex et al., 2020). The peaks observed for various metals in composite electrocatalysts were shifted to the higher binding energies as compared to those reported for pure metals (Biesinger et al., 2011; Xu et al., 2018b). This observation inferred strong metal-RGO interaction in the electrocatalysts. Table 4.20 summarizes the relative contribution of different oxidation states of metals.

**Table 4.19: Binding energy and relative contribution of carbon functional groups present in RGO supported metal catalysts**

| Sample ID | C=C eV (%)* | C-C eV (%) | C-O eV(%) | O=C-O eV (%) |
|---|---|---|---|---|
| 20Cu-RGO | 284.6 (49) | 285.8(23) | 286.6 (9) | 288.4 (19) |
| 20Ni-RGO | 284.6 (54) | 284.8 (19) | 286 (10) | 287.9 (17) |
| 20Fe-RGO | 284.6 (42) | 285.1 (26) | 286 (13) | 288.5 (20) |
| 20Co-RGO | 284.6 (35) | 285 (37) | 286.2 (10) | 288.3 (18) |

**Table 4.20: Binding energies and relative contribution of different metal oxidation states present in RGO supported metal catalysts**

| Sample ID | Metal Oxidation State | $2p_{3/2}$ B.E (eV) | $2p_{1/2}$ B.E (eV) | Relative Metal Content (%) |
|---|---|---|---|---|
| 20Cu-RGO | $Cu^0$ | 932.4 | 952.5 | 35 |
| | $Cu^{2+}$ | 934.7 | 954.6 | 65 |
| 20Ni-RGO | $Ni^0$ | 852.7 | 871.6 | 62 |
| | $Ni^{2+}$ | 854.6 | - | 38 |
| 20Fe-RGO | $Fe^{2+}$ | 710.7 | 724.3 | 32 |
| | $Fe^{3+}$ | 712.4 | 726.1 | 68 |
| 20Co-RGO | $Co^{2+}$ | 781.8 | 796.8 | 69 |
| | $Co^{3+}$ | 780.2 | 795.2 | 31 |

KPFM images of RGO supported catalysts are represented in Figure 4.30. The incorporation of different types of metal in RGO support resulted in significant variation in CPD values, which in turn resulted in variation in the work function of the catalysts. The work function of different catalysts followed the increasing trend as: 20Cu-RGO (4.481 eV) < 20Fe-RGO (4.628

eV) < 20Co-RGO (4.704 eV) < 20Ni-RGO (4.824 eV). The high work function of the catalyst accounts for its high electrocatalytic activity. Hence, 20Ni-RGO with the highest work function resulted in high electrocatalytic behaviour, as observed from CV in the later section.

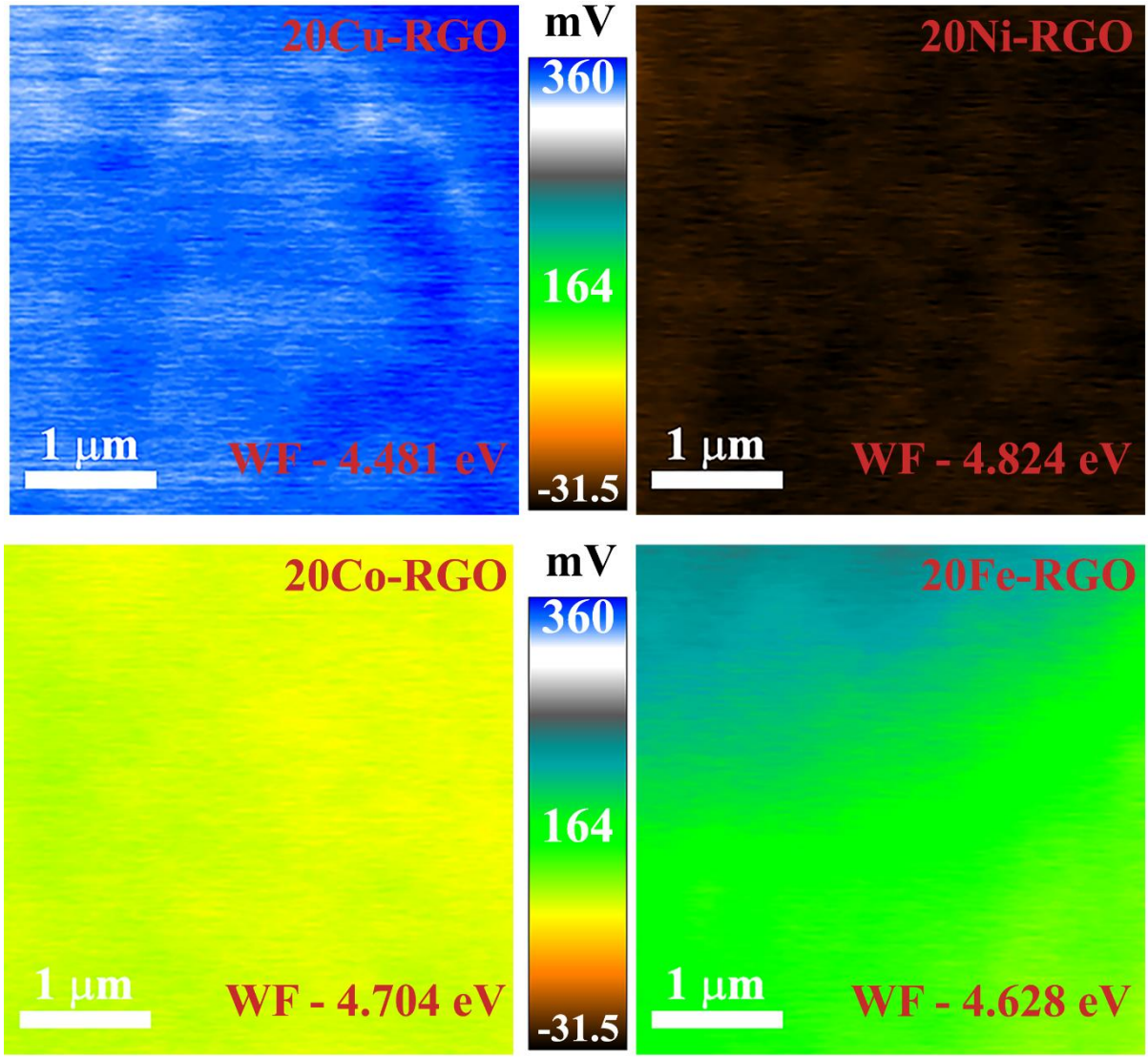


**Figure 4.30: KPFM images of different RGO supported metal catalysts.**

### 4.3.2.2 Electrochemical characterization

The CV of electrocatalysts was conducted in basic medium in the presence and absence of EG. The CV of the electrocatalysts in 0.1 M KOH is shown in Figure 4.32a. In basic medium (0.1 M KOH), 20Ni-RGO showed one oxidation peak at 0.62 V, corresponding to the formation of nickel oxyhydroxide (Cui et al., 2015; Zhu et al., 2017). The 20Ni-RGO experienced one reduction peak at 0.37 V, which related to the reduction of nickel oxyhydroxide. The reaction involving Ni is given below (Zhu et al., 2017):

$$Ni(OH)_2 + OH^- \rightleftarrows NiOOH + H_2O + e^- \quad (4.6)$$

The 20Co-RGO showed a small hump-like peak at 0.47 V, which corresponded to cobalt oxyhydroxide formation. The reaction of Co in basic medium was given as (Cui et al., 2015):

$$Co_3O_4 + OH^- + H_2O \rightarrow 3CoOOH + e^- \quad (4.7)$$

However, peaks were not detected for 20Cu-RGO and 20Fe-RGO at lower potential under the used CV conditions. A steep rise in current density was observed for all the electrocatalysts after a certain potential. At higher potential, Fe might have undergone the following reaction (Dai et al., 2021):

$$Fe(OH)_2 + OH^- \rightarrow FeOOH + H_2O + e^- \quad (4.8)$$

The ferrous hydroxide undergone transformation to iron oxy hydroxide. Similarly, the steep rise of potential in case of copper (Cu) based catalyst in basic medium might have led to the reactions according to Equation (4.2) and (4.3) (Leckie, 1970). The copper hydroxide, formed at relatively lower potential, might had undergone formation of $Cu_2O_3$, which is very unstable in nature, at higher potential. The onset potential and the peak current density are tabulated in Table 4.21 for all the electrocatalysts. The onset potentials of 20Cu-RGO, 20Ni-RGO, 20Fe-RGO and 20Co-RGO were obtained at 0.75, 0.47, 0.78 and 0.20 V, respectively. The peak current density for all the catalysts was observed at 1 V. The peak current density of different electrocatalysts followed the increasing trend as 20FeRGO (4.1 mA/cm$^2$) < 20Co-RGO (4.8 mA/cm$^2$) < 20Cu-RGO (5.4 mA/cm$^2$) < 20Ni-RGO (7.4 mA/cm$^2$). The current density obtained from CV did not follow the trend with the onset potentials observed for the catalysts (Table 4.21). The CV of different catalysts was conducted in different scan rate (10 – 80 mV/s) over non-faradic region (Figure 4.32a-d). The linear relationship between current density and scan rate for different catalysts is shown in Figure 4.32e. The ECSA, specific ECSA, and RF of electrocatalysts are tabulated in Table 4.22.

The ESCA of the catalysts showed an increasing trend as: 20Fe-RGO (14 cm$^2$) < 20Co-RGO (17.3 cm$^2$) < 20Cu-RGO (19.3 cm$^2$) < 20Ni-RGO (44.3 cm$^2$). The RF also followed the same trend as ECSA. The ECSA and RF of different catalysts were directly related to their catalytic performance in basic medium. The Tafel slopes of different catalysts in 0.1 M KOH are depicted in Figure 4.31c and Table 4.22. The Tafel slope was the lowest for 20Ni-RGO (179 mV/dec), followed by 20Cu-RGO (266 mV/dec), 20Co-RGO (275 mV/dec) and 20Fe-RGO (310 mV/dec). The higher Tafel slope indicated slower catalytic kinetics. Thus, lowest Tafel slope for 20Ni-RGO implies faster kinetics and hence improved performance, as was

observed in CV in terms of highest current density. The increasing trend of Tafel slope corresponded to the decreasing catalytic activity in basic medium, as demonstrated in CV study (Figure 4.31a). The charge transfer coefficient was calculated using Butler-Volmer equation (Equation 3.6). In basic medium, the α values for different catalysts followed the increasing trend as: 20Fe-RGO (0.19) < 20Co-RGO (0.21) < 20Cu-RGO (0.22) < 20Ni-RGO (0.33). Higher α value indicated increased electrochemical activity.

**Table 4.21: Onset potential and current density observed from cyclic voltammetry for RGO supported metal catalysts in basic medium**

| Sample ID | In 0.1 M KOH | | In 0.5 M EG + 0.1 M KOH | |
|---|---|---|---|---|
| | $E_{Onset}^{*}$ (V) | $J_{Pa}$ (mA/cm$^2$) | $E_{Onset}$ (V) | $J_{Pa}$ (mA/cm$^2$) |
| 20Cu-RGO | 0.75 | 5.4 | 0.59 | 9.1 |
| 20Ni-RGO | 0.47 | 7.4 | 0.54 | 12.7 |
| 20Fe-RGO | 0.78 | 4.1 | 0.78 | 8.0 |
| 20Co-RGO | 0.20 | 4.8 | 0.55 | 5.8 |

*$E_{onset}$ is onset potential.

The CV of the electrocatalysts in 0.1 M KOH with 0.5 M EG is shown in Figure 4.31b. The onset potential of 20Ni-RGO and 20Co-RGO in presence of EG increased to 0.54 V and 0.55 V, respectively. However, the onset potential of 20Cu-RGO decreased to 0.59 V upon addition of EG. There was no change in the onset potential of 20Fe-RGO. This suggested that 20Ni-RGO and 20Co-RGO required higher energy for EG oxidation. The 20Cu-RGO required less energy to oxidise EG with respect to the energy required for oxidation in 0.1 M KOH without EG. The onset potential was lowest for 20Ni-RGO (0.54 V) followed by 20Co-RGO (0.55 V), 20Cu-RGO (0.59 V) and 20Fe-RGO (0.78 V) (Table 4.21). In basic medium, the current density of 20Cu-RGO, 20Ni-RGO and 20Co-RGO increased with the addition of 0.5 M EG. Negligible change of current density was observed for 20Fe-RGO. At 1 V, 20Ni-RGO had the highest peak current density (12.7 mA/cm$^2$), followed by 20Cu-RGO (9.1 mA/cm$^2$), 20Co-RGO (8 mA/cm$^2$) and 20Fe-RGO (5.8 mA/cm$^2$). The 20Ni-RGO with lowest onset potential showed the highest current density in presence of EG. Higher current density of the electrocatalysts can be directly related to their ECSA (Figure 4.32g). Different electrochemical parameters in the presence of EG are listed in Table 4.22. The Tafel slope obtained in the presence of EG also supported the current density behaviour observed for different electrocatalysts. The Tafel slope decreased for all the catalysts, except 20Fe-RGO (Table 4.22). The decrease in Tafel slope upon addition of EG indicated faster catalytic activity (Figure 4.31d). In the presence of EG, the value of α also increased for all electrocatalysts, except for

20Fe-RGO, which is in accordance with their better catalytic activity. There was no change of α for 20Fe-RGO, which echoed its poor performance, as observed by the negligible

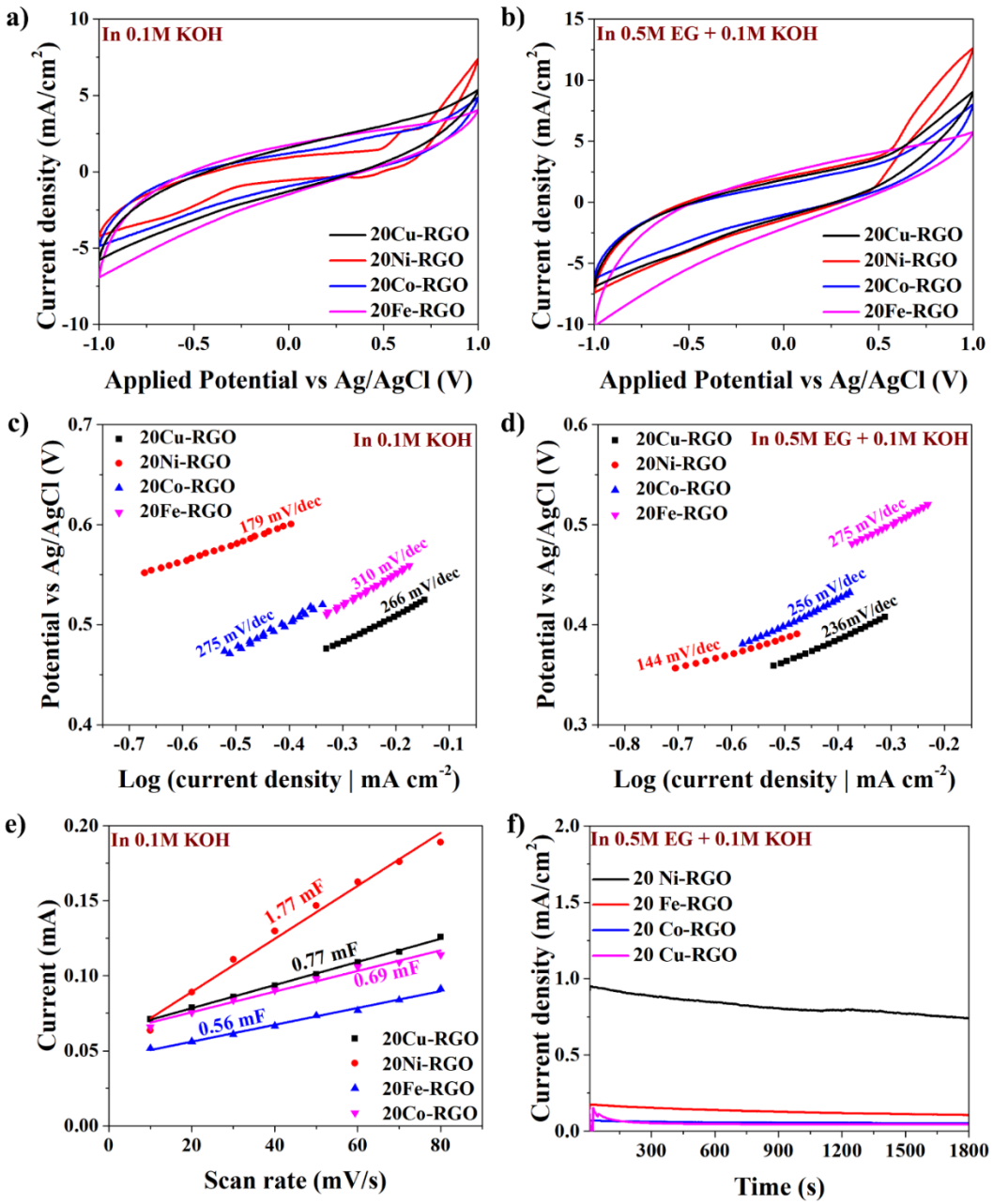


**Figure 4.31: Cyclic voltammetry of RGO supported metal catalysts in a) 0.1 M KOH and b) 0.5 M EG + 0.1 M KOH mediums. Tafel slope of different electrocatalysts shown in c) 0.1 M KOH and d) 0.5 M EG + 0.1 M KOH mediums, e) linear relationship of current and scan rate at 0 V vs Ag/AgCl and (f) chronoamperometry of different RGO supported metal catalysts in presence of 0.5 M EG in 0.1 M KOH.**

change of current density when EG was added (Figure 4.31b). The better electrocatalytic activity of the catalysts was related to the formation of metal oxyhydroxides or higher order metal oxides (Cui et al., 2015; Dai et al., 2021; Leckie, 1970; Zhu et al., 2017). These metal

oxides reacted with EG at higher potentials (above 0.5 V), which in turn helped in generating high current density (Cui et al., 2015; Dai et al., 2021; Dantas et al., 2012; Hassanzadeh et al., 2019). Higher ECSA accounted for increased electrochemical activity in the presence of EG. Moreover, metal dispersion of various electrocatalysts also influenced the electrochemical performance. The higher ECSA (44.3 $cm^2$) and moderate dispersion (9.3%) of 20Ni-RGO might have resulted in its higher current density. The 20Cu-RGO with an ECSA of 19.3 $cm^2$ and a dispersion of 10.2% was the second best.

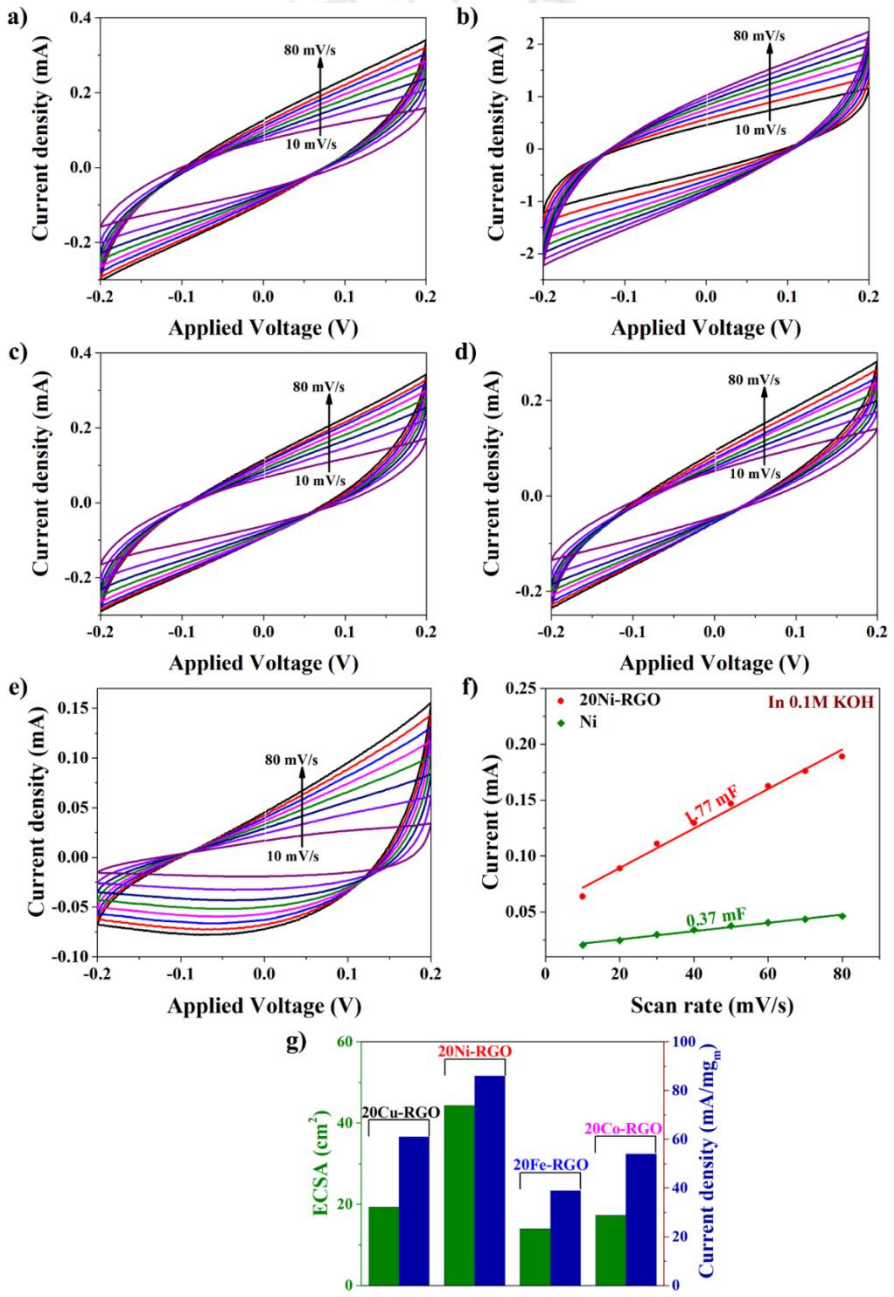

**Figure 4.32: Cyclic voltammetry at different scan rate for a) 20Cu-RGO, b) 20Ni-RGO, c) 20Co-RGO, d) 20Fe-RGO, e) Ni, f) comparison of linear relationship of current and scan rate between 20Ni-RGO and Ni, g) relation of different metal RGO electrocatalysts between ECSA and current density in 0.5 M EG + 0.1 M KOH.**

**Table 4.22: Electrochemical properties of RGO supported metal catalysts**

| Sample ID | ECSA ($cm^2$) | Specific ECSA ($m^2/g$) | RF | Tafel Slope (mV/dec) | | $\alpha^*$ | |
|---|---|---|---|---|---|---|---|
| | | | | In 0.1 M KOH | In 0.5 M EG + 0.1 M KOH | In 0.1 M KOH | In 0.5 M EG + 0.1 M KOH |
| 20Cu-RGO | 19.3 | 20.1 | 98.2 | 266 | 236 | 0.22 | 0.25 |
| 20Ni-RGO | 44.3 | 46.1 | 225.8 | 179 | 144 | 0.33 | 0.41 |
| 20Fe-RGO | 14 | 14.6 | 71.4 | 310 | 315 | 0.19 | 0.19 |
| 20Co-RGO | 17.3 | 18 | 88 | 275 | 256 | 0.21 | 0.23 |

*α is charge transfer co-efficient.

CA profiles of electrocatalysts in basic medium (0.1 M KOH) with 0.5 M EG is shown in Figure 4.31f. All the electrocatalysts attained stability within 60 s, except 20Cu-RGO which attained stability after 190 s. It was also observed that each catalyst was stable for at least 1800 s. After this time period, 20Ni-RGO had the highest current density (0.74 $mA/cm^2$), followed by 20Fe-RGO (0.11 $mA/cm^2$), 20Co-RGO (0.05 $mA/cm^2$) and 20Cu-RGO (0.04 $mA/cm^2$).

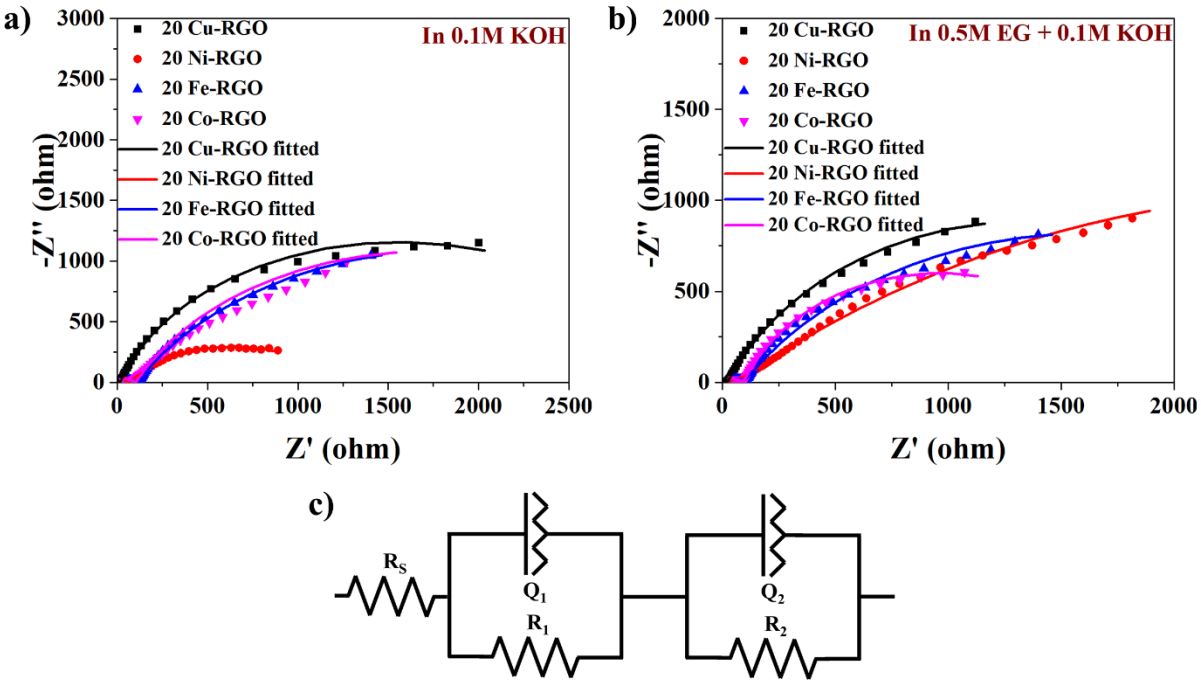


**Figure 4.33: EIS of different RGO supported metal catalysts in a) 0.1 M KOH, b) 0.5 M EG + 0.1 M KOH and c) equivalent circuit diagrams.**

The EIS of electrocatalysts in 0.1 M KOH is shown in Figure 4.33a. All the electrocatalysts showed similar EIS spectra with two depleted semicircles, one at high frequency region and the other at low frequency region. The EIS spectra were fitted with an equivalent circuit shown in Figure 4.33c, where $R_S$ is the solution resistance, $R_1$ and $Q_1$ are resistance and constant phase element (CPE) corresponding to charge transfer, $R_2$ and $Q_2$ are the resistances developed due to ionic transport and electrochemical reaction (only in presence of EG). The fitted parameters of the equivalent circuit are tabulated in Table 4.23. The $R_S$ values for different catalysts ranged between 4.9 and 24 Ω. The charge transfer resistance ($R_1$) was the lowest for 20Cu-RGO (12.1 Ω), followed by 20Ni-RGO (45.7 Ω), 20Co-RGO (81.6 Ω) and 20Fe-RGO (88.7 Ω). The admittance ($Y_1$) component of $Q_1$ ranged from 3.1 to 152 $\times 10^{-5}\ \Omega^{-1}s^n$, while phase angle ($n_1$) varied from 0.39 to 0.55. The combined effect of both $R_1$ and $Q_1$, estimated by time constant ($\tau_1$), was almost similar for all the electrocatalysts (0.01-0.014 ms). This suggested that the charge transfer process was almost similar for all the catalysts in basic medium, irrespective of the type of metal. The ionic transport resistance ($R_2$) varied between 1.2 and 3.6 KΩ. The $Y_2$ ranged from 142 to 283 $\times 10^{-5}\ \Omega^{-1}s^n$, whereas $n_2$ was between 0.6 and 0.82. The time constant $\tau_2$ for 20Ni-RGO was the lowest (4.6 s), followed by 20Cu-RGO (6.1 s), 20Fe-RGO (10.7 s) and 20Co-RGO (20 s). The lowest time constant of 20Ni-RGO accounted for the best performance observed in CV (Figure 4.31a). Since $\tau_1$ was substantially smaller than $\tau_2$ for all the catalysts, thus it could be concluded that ionic transport was slower and controlling process in basic medium.

**Table 4.23: Parameters of equivalent circuit for RGO supported metal catalysts**

| Sample ID | $R_S$ (Ω) | $R_1$ (Ω) | $Q_1$ | | $\tau_1$ (ms) | $R_2$ (KΩ) | $Q_2$ | | $\tau_2$ (s) |
|---|---|---|---|---|---|---|---|---|---|
| | | | $Y_1 \times 10^{-5}$ ($\Omega^{-1}s^n$) | $n_1$ | | | $Y_2 \times 10^{-5}$ ($\Omega^{-1}s^n$) | $n_2$ | |
| **In 0.1 M KOH** | | | | | | | | | |
| 20Cu-RGO | 4.9 | 12.1 | 152 | 0.39 | 0.010 | 3.1 | 142 | 0.82 | 6.1 |
| 20Ni-RGO | 23.9 | 45.7 | 4 | 0.55 | 0.011 | 1.2 | 215 | 0.60 | 4.6 |
| 20Fe-RGO | 24 | 88.7 | 5.4 | 0.48 | 0.014 | 3.6 | 146 | 0.70 | 10.7 |
| 20Co-RGO | 24 | 81.6 | 3.1 | 0.52 | 0.011 | 3.3 | 283 | 0.74 | 20 |
| **In 0.5 M EG + 0.1 M KOH** | | | | | | | | | |
| 20Cu-RGO* | 4.4 | 19.8 | 134 | 0.34 | 0.023 | 2.7 | 257 | 0.75 | 13.2 |
| 20Ni-RGO* | 25.4 | 40 | 7.7 | 0.55 | 0.026 | 5.6 | 120 | 0.46 | 63.1 |
| 20Fe-RGO* | 21.9 | 72.6 | 2.2 | 0.57 | 0.012 | 3 | 91 | 0.63 | 5 |
| 20Co-RGO* | 14 | 80.4 | 5.4 | 0.49 | 0.015 | 1.7 | 218 | 0.77 | 5.7 |

* In presence of 0.5 M EG, $\tau = (Y \times R)^{\frac{1}{n}}$

The EIS spectra after addition of EG in the same basic medium is shown in Figure 4.33b. There was no alteration in the nature of the EIS curves of different electrocatalysts, hence the curves were fitted with the same equivalent circuit shown in Figure 4.33c. The introduction of EG resulted in very minor changes in resistances $R_S$ and $R_1$. The $Y_1$ values of $Q_1$ also showed minor variation. The $n_1$ values for the electrocatalysts ranged from 0.34 to 0.57. The addition of EG resulted in an increase in time constant $\tau_1$ for 20Cu-RGO, 20Ni-RGO and 20Co-RGO, whereas it slightly decreased for 20Fe-RGO. The $\tau_1$ varied between 0.012 and 0.026 ms. The $R_2$, which contributed to the resistance towards electrochemical oxidation, decreased for all the catalysts, except 20Ni-RGO. The $R_2$ for different electrocatalysts followed the increasing trend as: 20Co-RGO (1.7 KΩ) < 20Cu-RGO (2.7 KΩ) < 20Fe-RGO (3 KΩ) < 20Ni-RGO (5.6 KΩ). The $Y_2$ values varied from 91 to 257 $\times 10^{-5}$ $\Omega^{-1}s^n$ whereas $n_2$ ranged from 0.46 to 0.77. The $\tau_2$ values increased for 20Cu-RGO (13.2 s) and 20Ni-RGO (63.1 s), whereas it decreased for 20Fe-RGO (5 s) and 20Co-RGO (5.7s). The $\tau_2$ values were inversely related to the average pore sizes of the electrocatalysts (Table 4.18). 20Fe-RGO and 20Co-RGO having higher pore size had lower $\tau_2$ values, while 20Ni-RGO and 20Cu-RGO with smaller pore size resulted in higher $\tau_2$ values. The larger pore size is predicted to help the transport of large EG molecules to the active metal site, thereby facilitating the electro-oxidation process. However, the present results suggested that the intrinsic catalytic activity of individual metal played more dominating role in current generation. As a result, 20Fe-RGO and 20Co-RGO had significantly lower current density, although having larger pore sizes, which could be related to their reduced catalytic activity. The electro-oxidation process was also observed to be the slowest step, with $\tau_1 << \tau_2$ for all the electrocatalysts both in the absence and presence of EG.

The effect of different metals supported on activated carbon as well as on RGO showed that Ni was the best performing metal for EG oxidation in basic medium. It was also observed that RGO supported Ni catalysts performed better than the other catalysts. This inference was backed by different physical and electrochemical characterisation as discussed in above sections.

## 4.4 Effect of metal loading

The study of various metals for EG electro-oxidation revealed that Ni was the best performing metal among other transition metals (Cu, Co and Fe). Hence the study of metal loading was carried out using Ni as the active metal and RGO as support

### 4.4.1 Physical characterization

The 20Ni-RGO was thus the best catalyst both in terms of current density and stability in the presence of EG. In order to investigate the effect of nickel loading, the loading was varied between 20 and 40 wt.%. The elemental analysis by EDX of these catalysts are included in Table 4.24.

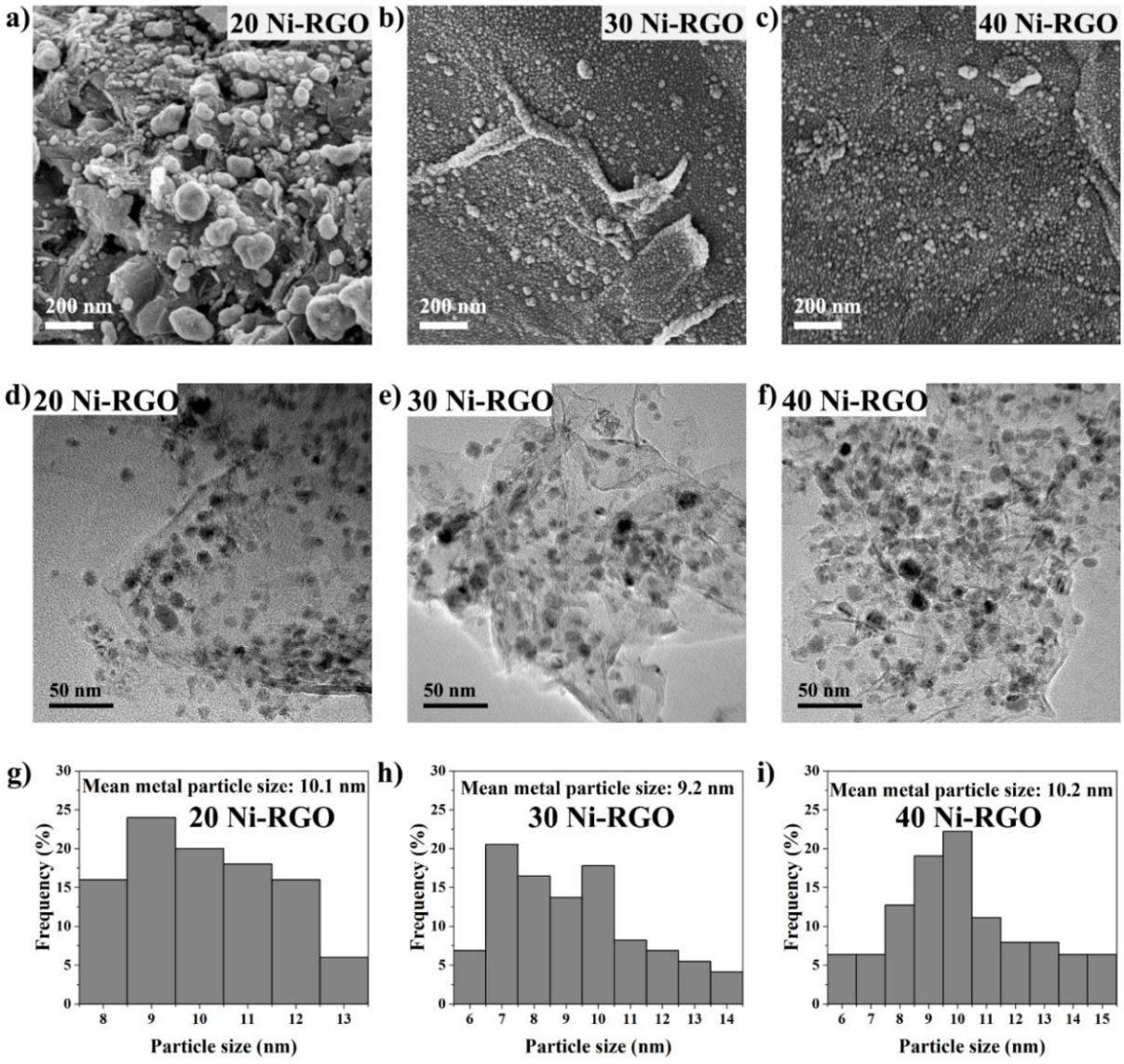


**Figure 4.34: a-c) FESEM images and d-f) FETEM image and g-i) the particle size distribution of Ni-RGO with different Ni loading.**

**Table 4.24: Elemental composition of Ni-RGO with different metal loadings**

| Sample ID | Metal (wt.%) | C (wt.%) | O (wt.%) |
|---|---|---|---|
| 20Ni-RGO | 22.5 | 61.7 | 15.8 |
| 30Ni-RGO | 35.5 | 54.4 | 10.1 |
| 40Ni-RGO | 39.7 | 51.0 | 9.3 |

The FESEM images of the Ni-RGO catalysts with different percentages of Ni loading showed spherical Ni particles of various sizes (Figure 4.34a-c). With the increase in Ni loading, the porous nature of RGO became less visible due to the formation of thick metal/metal oxide layer on the RGO. The appearance of dark spheres in the FETEM images of different Ni-loaded electrocatalysts (Figure 4.34d-f) confirmed the presence of Ni particles incorporated within the sheet-like structures of RGO. The variation in Ni loading did not significantly affect the average particle size of the deposited Ni, which ranged between 9 and 10 nm (Figure 4.34g-i). However, the distribution of the particles became denser with the increase in Ni loading. The metal dispersion for the catalysts, as calculated by Equation (3.2), was 9-10% (Table 4.25).

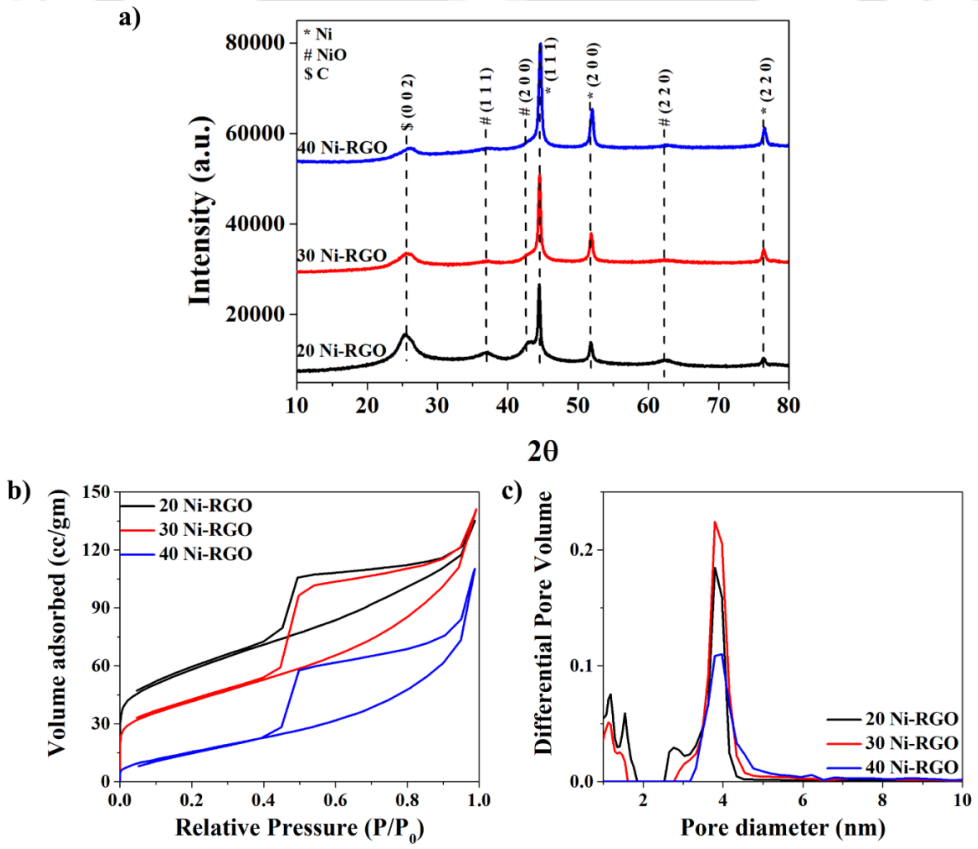


**Figure 4.35: a) XRD pattern, b) $N_2$ adsorption-desorption isotherm and c) pore size distribution of Ni-RGO with different Ni loadings. (In all the isotherms the lower curves are for adsorption process and the upper curves for desorption process.)**

The XRD profiles of electrocatalysts showed peaks at the same position irrespective of Ni loadings, as discussed earlier (Figure 4.35a). No shift of peaks was observed. However, the peak intensity of the Ni peaks increased slightly upon increasing the Ni loading. At 0.2nm, the metal d-spacing values for different Ni-loaded catalysts were same with respect to the peak at 44.5°, which corresponded to $Ni^0$ (111) planes. This suggested no significant change in metallic structure with increased Ni loading in the range studied.

The $N_2$ adsorption-desorption isotherms of Ni-RGO with different Ni loadings showed decrease in adsorbed volume of $N_2$ with increasing metal loadings (Figure 4.35b). The surface area of the catalysts followed the increasing trend as: 40Ni-RGO (63 $m^2/g$) < 30Ni-RGO (146 $m^2/g$) < 20Ni-RGO (200 $m^2/g$) (Table 4.25). The pore size distribution of different Ni-loaded catalysts is shown in Figure 4.35c. Majority of the pores had sizes less than 7 nm (Figure 4.35c). As the loading of Ni increased, the density of deposited metal particles increased, as was also observed from the TEM images. This resulted in increased blockage of the finer pores of the substrate RGO, thereby reducing the surface area and increasing the average pore size. The effect was maximum at the highest Ni loading of 40 wt.%.

**Table 4.25: Physical properties of Ni-RGO catalysts with different metal loadings**

| Sample ID | BET surface area ($m^2/g$) | Total Pore Volume ($cm^3/g$) | Micropore area ($m^2/g$) | $Ni^0$ d-spacing* (nm) | $D_{TEM}$ (%) |
|---|---|---|---|---|---|
| 20Ni-RGO | 200 | 0.21 | 34 | 0.20 | 9.2 |
| 30Ni-RGO | 146 | 0.21 | 19 | 0.20 | 10.2 |
| 40Ni-RGO | 63 | 0.17 | 0 | 0.20 | 9.2 |

* d-spacing of $Ni^0$ calculated from XRD.

### 4.4.2 Electrochemical characterization

The CV of electrocatalysts, with different metal loadings, in basic medium is shown in Figure 4.36a. In 0.1 M KOH, all the electrocatalysts showed one oxidation and one reduction peak. The oxidation peak of Ni electrocatalysts was observed at around 0.6 V, while the reduction peak was at 0.37 V. The oxidation peak shifted to the higher side, whereas the reduction peak shifted to lower potential with an increase in Ni loading. The oxidation peaks of 20Ni-RGO, 30Ni-RGO and 40Ni-RGO were observed at 0.6, 0.63 and 0.7 V, whereas the reduction peaks were at 0.37, 0.36 and 0.31 V. The oxidation peak detected for Ni electrocatalysts depicted the formation of nickel oxyhydroxide, while the reduction peaks indicated the reduction of the same. However, nickel loading in basic medium had negligible effect on the anodic onset

potential. The onset potential and peak current density of Ni catalysts are tabulated in Table 4.26.

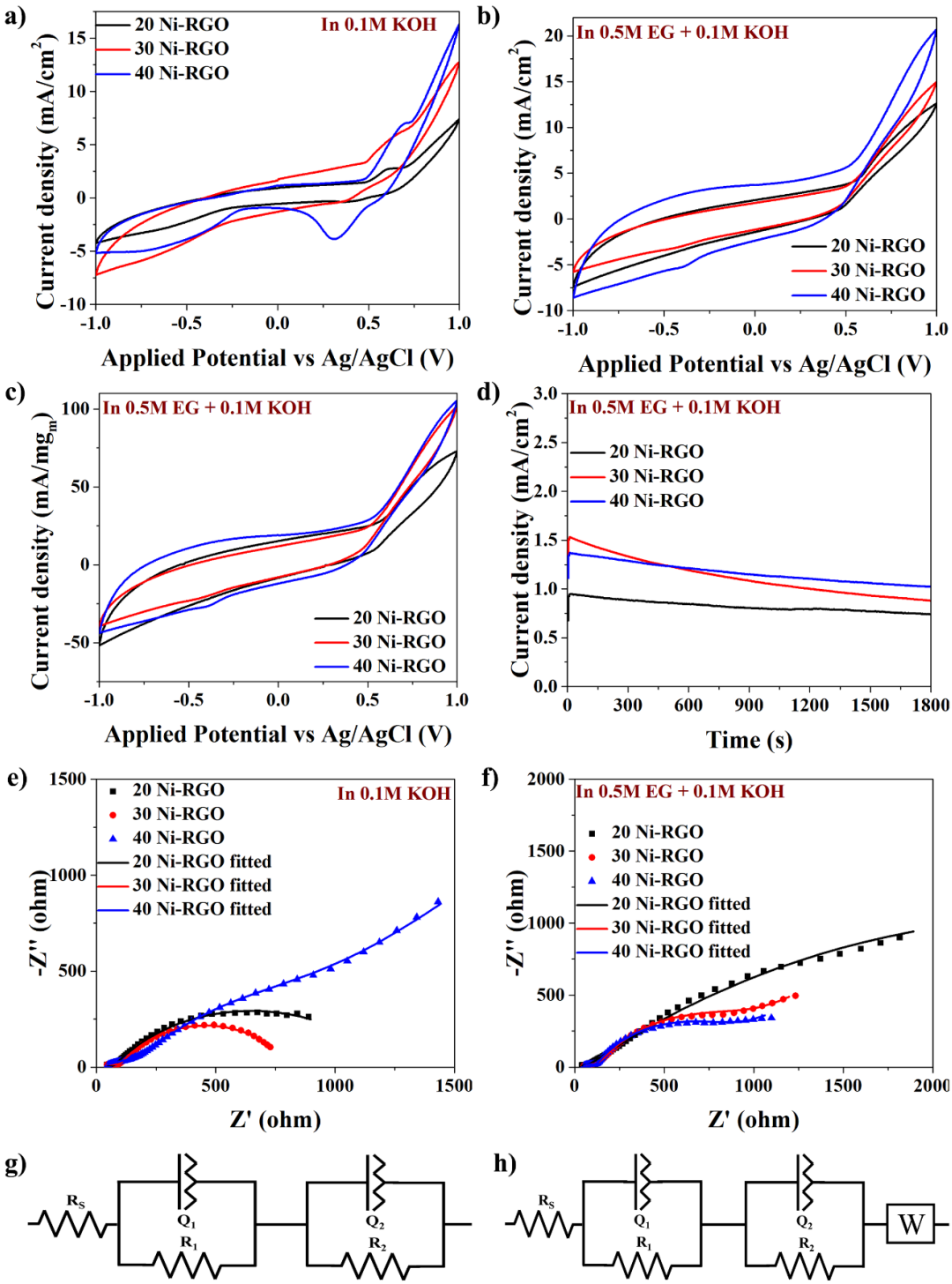


**Figure 4.36: Cyclic voltammetry of Ni-RGO with different Ni loading in a) 0.1 M KOH, b) 0.5 M + EG 0.1 M KOH, c) mass activity of the Ni-RGO in 0.5 M + EG 0.1 M KOH d) chronoamperometry in 0.5 M EG + 0.1 M KOH, EIS of Ni-RGO with different loading in e) 0.1 M KOH, f) 0.5 M EG + 0.1 M KOH and g-h) equivalent circuit diagram.**

The peak current density was observed at 1 V in 0.1 M KOH. 40Ni-RGO produced the highest current density (16.4 mA/cm$^2$), followed by 30Ni-RGO (12.8 mA/cm$^2$) and 20Ni-RGO (7.4 mA/cm$^2$). The CV of the catalysts in the presence of 0.5 M EG in basic medium is shown in Figure 4.36b. The current density observed in presence of EG increased with Ni loading. The onset potential also increased with the addition of EG.

The onset potential and current density in the presence of EG are shown in Table 4.26. The onset potential for Ni based catalysts increased in presence of EG suggesting the higher energy requirement for EG oxidation. The 30 and 40 wt.%. Ni-RGO had same low onset potential (0.50 V) whereas 20 wt.%. Ni-RGO had higher onset potential (0.54 V). The current density followed an increasing trend as: 20Ni-RGO (12.7 mA/cm$^2$) < 30Ni-RGO (15 mA/cm$^2$) < 40Ni-RGO (20.7 mA/cm$^2$). The current density observed was aligned with the onset potential. The mass activity of the catalysts is shown in Figure 4.34c. The mass activity also followed the similar trend as current density where 20Ni-RGO (86 mA/cm$^2$mg$_m$) < 30Ni-RGO (102 mA/mg$_m$) < 40Ni-RGO (106 mA/mg$_m$). The increase in mass activity with the increase in Ni loading from 30 to 40 wt.% was less than that for loading from 20 to 30 wt.%. A significant decrease in surface area for 40Ni-RGO might have contributed to its lower increase in current density. All the Ni catalysts which reacted with EG molecules produced Ni oxyhydroxides at potential above 0.5 V. The higher formation of nickel oxyhydroxides would result in more active sites for reaction with EG. Therefore, the current density trend obtained in Ni catalysts with varying concentration of Ni loading was due to the formation of nickel oxyhydroxides.

**Table 4.26: Onset peak potential and current density observed from cyclic voltammetry of Ni-RGO with different metal loadings**

| Sample ID | In 0.1 M KOH | | In 0.5 M EG + 0.1 M KOH | |
|---|---|---|---|---|
| | $E_{Onset}$ (V) | $J_{Pa}$ (mA/cm$^2$) | $E_{Onset}$ (V) | $J_{Pa}$ (mA/cm$^2$) |
| 20Ni-RGO | 0.47 | 7.4 | 0.54 | 12.7 |
| 30Ni-RGO | 0.46 | 12.8 | 0.50 | 15 |
| 40Ni-RGO | 0.46 | 16.4 | 0.50 | 20.7 |

The CA of Ni electrocatalysts with different loadings of Ni in the presence of 0.5 M EG in basic medium is shown in Figure 4.36d. The stability of the catalysts was achieved within 60 s. The amperogram revealed that the catalysts were stable for 1800 s. The current density observed after 1800 s was highest for 40Ni-RGO (1 mA/cm$^2$), followed by 30Ni-RGO (0.88 mA/cm$^2$) and 20Ni-RGO (0.74 mA/cm$^2$).

Figure 4.36e depicts the EIS spectra for all the Ni electrocatalysts with different concentrations of Ni loading. The EIS spectra of all the electrocatalysts showed one semicircle

at higher frequency and another at lower frequency. Aside from the aforementioned feature, 40Ni-RGO demonstrated an increase in impedance, forming a straight line in the extreme low frequency region. This occured in 40Ni-RGO due to Warburg resistance, mainly from the mass transport process. Therefore, the EIS spectra of the electrocatalysts were fitted with two different equivalent circuit, as shown in Figure 4.36g and h. The EIS spectra of 20Ni-RGO and 30Ni-RGO were fitted with equivalent circuit shown in Figure 4.34g, whereas the EIS spectra of 40Ni-RGO was fitted with equivalent circuit shown in Figure 4.36h. The equivalent circuit in Figure 4.36h consists of a Warburg resistance connected in series with the equivalent circuit shown in Figure 4.36g. Table 4.27 shows the circuit parameters for Ni-RGO electrocatalysts with varying Ni loadings. The $R_S$ of several Ni catalysts varied from 4 to 27.3 Ω. The $R_1$ was the least for 20Ni-RGO (45.7 Ω), followed by 30Ni-RGO (104 Ω) and 40Ni-RGO (170 Ω). The $Y_1$ values were similar to $R_1$ and ranged from 4 $\times 10^{-5}$ to 53.2 $\times 10^{-5}$ $\Omega^{-1}s^n$, whereas $n_1$ was between 0.31 and 0.55. The time constant $\tau_1$ for 20Ni-RGO, 30Ni-RGO and 40Ni-RGO was 0.011, 0.032 and 1.5 ms, respectively. Increasing Ni loading resulted in an increase in $\tau_1$. The $R_2$ for different electrocatalysts fluctuated between 1.2 to 0.51 KΩ. The $Y_2$ values varied from 200 $\times 10^{-5}$ to 220 $\times 10^{-5}$ $\Omega^{-1}s^n$, whereas $n_2$ was between 0.60 and 0.71. The $\tau_2$ values followed the increasing order as: 40Ni-RGO (1.2 s) < 30Ni-RGO (1.7 s) < 20Ni-RGO (4.6 s). Thus, $\tau_2$ decreased with the increase in metal loading. The Warburg resistance (W) generated only for 40Ni-RGO in 0.1 M KOH was 3.6 $\Omega^{0.5}$. The low surface area of 40Ni-RGO might had caused the mass transport resistance (Table 4.25). As $\tau_1 << \tau_2$, $\tau_2$ played the role of rate determining step in current generation for different electrocatalysts. The increasing trend of current density (Figure 4.36a) with metal loading could be explained by the decreasing trend of $\tau_2$. Lower $\tau_2$ values corresponded to faster processes and higher current generation. Although $\tau_2$ values were lower for 40Ni-RGO, the addition of Warburg resistance might had lowered the increment of mass activity compared to 30Ni-RGO.

The EIS spectra of different catalysts with 0.5 M EG in basic medium are shown in Figure 4.36f. All the EIS spectra exhibited by electrocatalysts were similar in nature. All the electrocatalysts showed two semicircles, with 30Ni-RGO and 40Ni-RGO exhibiting an additional straight line at extremely lower frequency. The EIS spectra of 20Ni-RGO was fitted with the equivalent circuit in Figure 4.36g, but the EIS of other two catalysts were fitted with the equivalent circuit in Figure 4.36h. The fitted values are included in Table 4.27. Addition of EG resulted in an increase in $R_S$. The $R_S$ values varied in the range of 25 to 40 Ω. The $R_1$ values

also increased and varied in between 40 to 124 Ω. However, the $R_1$ decreased for 40Ni-RGO. The $Y_1$ values also followed the same trend as $R_1$ and were between 7.7 and 73.5 $\times 10^{-5}$ $\Omega^{-1}s^n$. The $n_1$ ranged from 0.33 to 0.55. In the presence of EG, the $\tau_1$ values increased for 20Ni-RGO and 30Ni-RGO, but decreased for 40Ni-RGO. The $\tau_1$ values of 20Ni-RGO, 30Ni-RGO and 40Ni-RGO were 0.026, 0.655 and 0.165 ms, respectively. The electrochemical oxidation parameters ($R_2$ and $Y_2$) decreased in the presence of EG, thereby suggesting the feasibility of EG electro-oxidation for Ni-based catalysts with higher loading. The $R_2$ ranged from 0.45 to 5.6 KΩ, whereas $Y_2$ varied from 120 $\times 10^{-5}$ to 180 $\times 10^{-5}$ $\Omega^{-1}s^n$. The time constant $\tau_2$ decreased with EG addition, suggesting faster electrochemical process for 30Ni-RGO and 40Ni-RGO. The $\tau_2$ values for 30Ni-RGO and 40Ni-RGO were quite similar (approximately 1 s), while $\tau_2$ for 20Ni-RGO was high at 63.1 s. However, Warburg resistance was observed for 30Ni-RGO during EG electro-oxidation, indicating the role of mass transfer process. The Warburg resistance for 30Ni-RGO and 40Ni-RGO were 7 $\Omega^{-0.5}$ and 10 $\Omega^{-0.5}$, respectively. The addition of EG improved the Warburg resistance of 40Ni-RGO. The higher Warburg resistance of 40Ni-RGO might have also contributed to its lower performance in terms of current density despite having higher metal loading.

**Table 4.27: Parameters of equivalent circuit for Ni-RGO electrocatalysts with different Ni loadings**

| Sample ID | $R_S$ (Ω) | $R_1$ (Ω) | $Q_1$ | | $\tau_1$ (ms) | $R_2$ (KΩ) | $Q_2$ | | $\tau_2$ (s) | W ($\Omega^{-0.5}$) |
|---|---|---|---|---|---|---|---|---|---|---|
| | | | $Y_1 \times 10^{-5}$ ($\Omega^{-1}s^n$) | $n_1$ | | | $Y_2 \times 10^{-5}$ ($\Omega^{-1}s^n$) | $n_2$ | | |
| **In 0.1 M KOH** | | | | | | | | | | |
| 20Ni-RGO | 23.9 | 45.7 | 4 | 0.55 | 0.011 | 1.2 | 215 | 0.60 | 4.6 | |
| 30Ni-RGO | 4 | 104 | 37.4 | 0.31 | 0.032 | 0.71 | 200 | 0.70 | 1.7 | |
| 40Ni-RGO | 27.3 | 170 | 53.2 | 0.37 | 1.5 | 0.51 | 224 | 0.71 | 1.2 | 3.6 |
| **In 0.5 MEG + 0.1 M KOH** | | | | | | | | | | |
| 20Ni-RGO* | 25.4 | 40 | 7.7 | 0.55 | 0.026 | 5.6 | 120 | 0.46 | 63.1 | |
| 30Ni-RGO* | 30 | 124 | 73.5 | 0.33 | 0.655 | 0.70 | 180 | 0.76 | 1.36 | 7.0 |
| 40Ni-RGO* | 39.2 | 80 | 16.5 | 0.50 | 0.165 | 0.71 | 150 | 0.74 | 1.09 | 10 |

* In presence of 0.5 M EG

As 30Ni-RGO proved to be the best performing catalyst for the electro-oxidation of EG, hence detailed electrocatalytic investigation was conducted using the same catalyst in order to determine different kinetic parameters associated with EG oxidation.

The peak current density (anodic as well as cathodic) for 30Ni-RGO in basic medium increased with the increase in scan rate (Figure 4.37). At lower scan rate (5 to 100 mV/s), the peak current density was in linear relation with the scan rate (Figure 4.37a). This linearity indicated that the electrochemical activity of the catalyst was dependent on the redox species produced at the electrode surface. This could also be attributed to the reversibility of the redox process. The surface coverage of the redox species (Γ*) on 30Ni-RGO, calculated by the Equation (3.8), was $2.7\times10^{-8}$ mol/cm$^2$. At higher scan rate (100 to 1000 mV/s), the peak current density was linearly dependent on $\nu^{1/2}$ (Figure 4.37b). This trend provided insight into the diffusion-limiting process in the redox behaviour of 30Ni-RGO, which developed due to charge neutralisation of redox active species on the electrode surface during redox reaction.

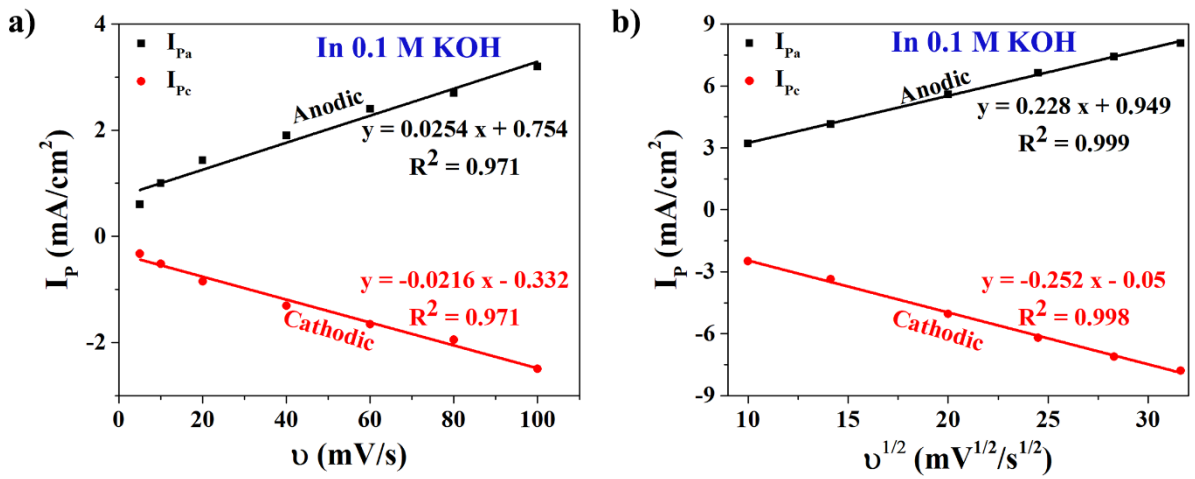


**Figure 4.37: a) Relationship between current density with scan rate at lower scan rate (5 to 100 mV/s) for 30Ni-RGO and b) relationship between current density with square root scan rate at higher scan rate (100 to 1000 mV/s) for 30Ni-RGO.**

The effect of different scan rates (5 to 1000 mV/s) were observed in presence of EG (Figure 4.38). The anodic current density increased with the increase in scan rate. The anodic peak for the oxidation of EG disappeared at higher scan rates (> 100 mV/s). The decrease in anodic peak could be related to the slower kinetics involved in the conversion of nickel hydroxides to nickel oxyhydroxides, which prevents adequate electron transfer within the electrode at higher scan rates (Azizi et al., 2013). Figure 4.38a and b represent the relationship between anodic peak current density with scan rate and square root of scan rate, respectively. If the current desnity is linear with scan rate, then the electrochemical process is surface adsorption controlled while it's linearity with square root of scan rate suggested diffuson controlled process. It was quite evident from Figure 4.38a that the current density was not linear with scan rate, hence, the process is not surface adsorption controlled. The linear fitting for Figure 4.38b

indicated that the peak current density was better fitted with the square root of scan rate. Thus, the electro-oxidation of EG by 30Ni-RGO was controlled by diffusion-limiting process rather than surface adsorption-controlled process. The relation between Log I and Log ν is shown in Figure 4.38c. The slope of Log I vs Log ν could give additional confirmation regarding diffusion-controlled and surface adsorption-controlled process. When the slope is 0.5, it indicates a diffusion-controlled process, whereas a slope of 1 is associated with adsorption-controlled process (Ma et al., 2021). In case of EG oxidation by 30Ni-RGO, the slope of Log I vs Log ν was 0.257, which was close to 0.5, thereby indicating that the electro-oxidation process was controlled by diffusion. The deviation of experimental slope value (0.257) from the theoretical value (0.5) was due to kinetics of the reaction. The diffusion coefficient of EG molecule calculated from the Equation (3.9) was between $2.35 \times 10^{-5}$ and $2.35 \times 10^{-8}$ $cm^2/s$, when n was varied between 1 and 10.

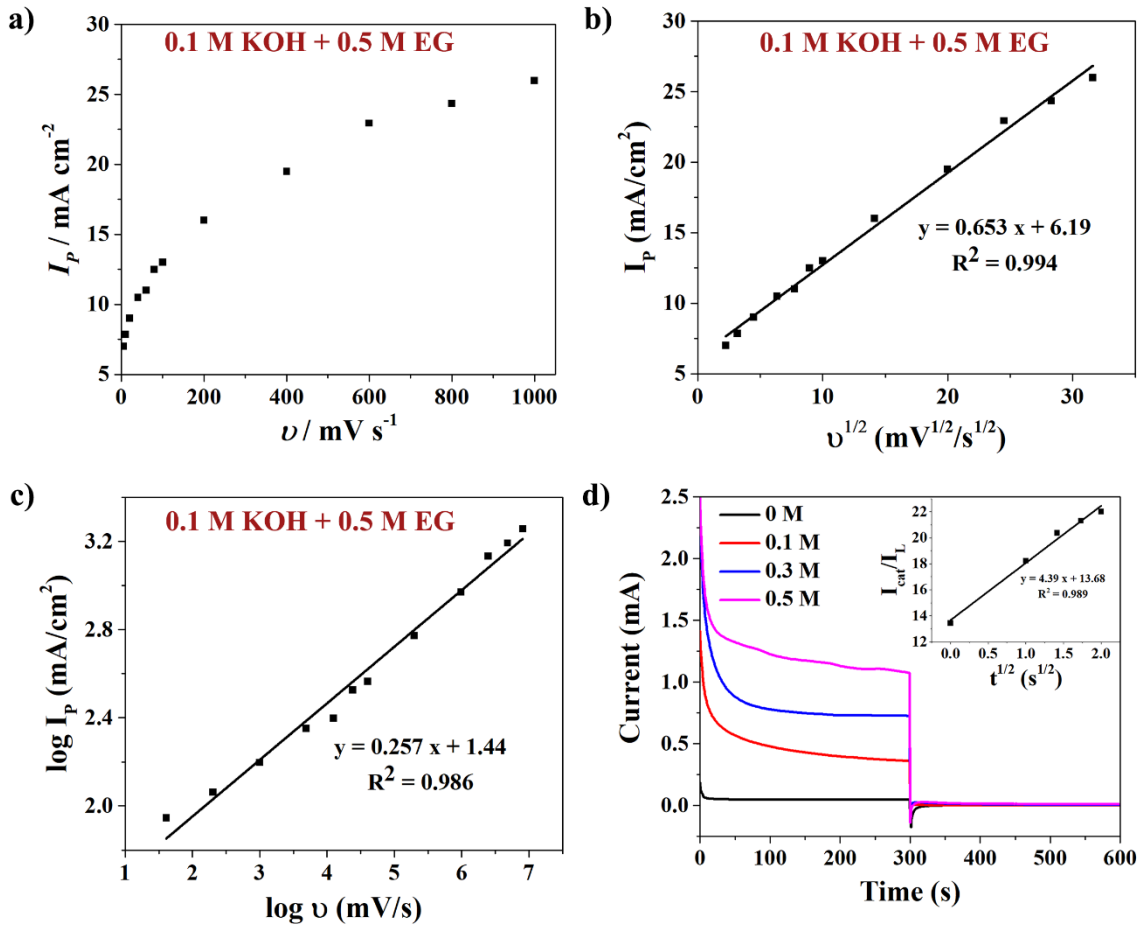


**Figure 4.38: Dependency of current density for 30Ni-RGO in 0.5 M EG 0.1 M KOH with a) scan rate, b) square root of scan rate, c) relationship between Log of current density with log of scan rate, d) dual potential chrono amperometry of 30Ni-RGO for different EG concentration in KOH. Relationship between $I_{cat}/I_L$ with $t^{1/2}$ of 0.5 M EG in inset. (EG= ethylene glycol)**

The EG reaction, like other reactions of organic molecules on the Ni surface, occurred in the presence of NiOOH and the oxidation process happened after the formation of NiOOH from $Ni(OH)_2$. The NiOOH then reacted with EG molecules resulting in subsequent regeneration of $Ni(OH)_2$. The proposed reaction mechanism for electro-oxidation of EG by Ni based catalyst is represented below:

$$Ni^{2+} + HOCH_2CH_2OH \rightarrow Ni^{2+}\text{-}(HOCH_2CH_2OH)_{ads} \quad (4.8)$$

$$Ni^{2+}\text{-}(HOCH_2CH_2OH)_{ads} + 2NiOOH \rightarrow Ni^{2+}\text{-}(HOCH_2CHO)_{ads} + 2Ni(OH)_2 \quad (4.9)$$

$$Ni^{2+}\text{-}(HOCH_2CHO)_{ads} + 2NiOOH \rightarrow Ni^{2+}\text{-}(HOCH_2COO^-)_{ads} + 2Ni(OH)_2 \quad (4.10)$$

$$Ni^{2+}\text{-}(HOCH_2COO^-)_{ads} + 2NiOOH \rightarrow Ni^{2+}\text{-}(OHCCOO^-)_{ads} + 2Ni(OH)_2 \quad (4.11)$$

$$Ni^{2+}\text{-}(OHCCOO^-)_{ads} + 2NiOOH + 3OH^- \rightarrow {}^-OOCCOO^- + 3Ni(OH)_2 \quad (4.12)$$

Dual step chronoamperometry was performed to investigate the electrochemical-chemical (EC) mechanism and determine the catalytic rate constant of 30Ni-RGO for EG oxidation. The chronoamperogram of 30Ni-RGO at varying concentrations of EG is shown in Figure 4.38d. The step potential was employed according to the peak potential observed from CV. The current density increased with increasing EG concentration. The rate at which current decreases slowed down as the concentration of EG increased. Thus, it could be inferred that NiOOH reacted with EG as soon as it formed on the surface of the electrode. When 0.3 V potential was applied, no significant cathodic current was observed, indicating the irreversibility of EG oxidation reaction. The exponential behaviour of I-V curve confirmed that the electrochemical process was diffusion-controlled and followed the Cottrell equation. Hence, the mean $k_{cat}$ of 30Ni-RGO for EG oxidation was $1.48 \times 10^4$ $cm^3$/mol.s, as calculated from Equation (3.10).

As previously noted, very limited studies have been conducted on the anodic oxidation of EG over transition metal-based catalysts. However, due to variations in operating parameters, it was difficult to make direct comparisons between different available literatures. Nonetheless, a comparative study was conducted using existing literature in order to provide insight into the catalytic performance of several monometallic electrocatalysts used in this study. On comparing the present results with that of the reported ones for transition metal-based catalysts (Table 4.28), it was observed that 30Ni-RGO and 40Ni-RGO developed in this work performed significantly better for EG oxidation in alkaline medium as compared to previously reported Ni-based catalysts. The higher current density observed in this study was associated with substantially higher EG/KOH. It was difficult to compare the various electrochemical parameters of the catalysts used in this study to those described in the

literature, as no such similar data was available. The ECSA for all catalysts reported in the present study was higher than that reported by Hameed et al. (Hameed et al., 2022). The reported current density for Fe/VC catalyst was higher than the present study *i.e.* for Fe/RGO (Gayathri et al., 2022). The observed difference could be due to difference in the nature of carbon and reaction conditions such as higher KOH and EG concentrations. There was no reported study comparing EG oxidation for Co/RGO and Cu/RGO.

**Table 4.28: Comparison of current density as reported for different transition metal based electrocatalysts for electro-oxidation of EG with that of present study**

| Catalyst | Electrolyte (Conc.) | EG (Conc.) | Current density ($mA/cm^2$) | References |
|---|---|---|---|---|
| Ni nanofiber | NaOH (0.2 M) | 0.03 M | 10.1 | Hosseini et al., 2017 |
| Ni/ITO | NaOH (0.2 M) | 0.03 M | 1.6 | Lin et al., 2017 |
| Ni/carbon nanofiber | NaOH (4 M) | 1 M | 0.86 | Hameed et al., 2022 |
| Fe/VC | KOH (0.5 M) | 1 M | 14.6 | Gayathri et al., 2022 |
| Ni SDS poly(o-aminophenol)/C | NaOH (0.1 M) | 0.28 M | 11.1 | Ojani et al., 2009 |
| Ni SDS (p-aminoacetanilide)/C | NaOH (0.1 M) | 0.25 M | 5.9 | Ojani et al., 2011 |
| Ni Trition X-100, poly (m-toluidine) | NaOH (0.1 M) | 0.06 M | 10.6 | Ojani et al., 2013 |
| Ni nanofibers | NaOH (0.2 M) | 0.03 M | 10 | Hosseini et al., 2017 |
| $Ni(OH)_2$/nano zeolite beta and MWCNT | NaOH (1.6 M) | 4 M | 12.52 | Eshagh-Nimvari and Karim Hassaninejad-Darzi, 2021 |
| **30Ni-RGO** | **KOH (0.1 M)** | **0.5 M** | **15** | **This work** |
| **40Ni-RGO** | **KOH (0.1 M)** | **0.5 M** | **20** | **This work** |
| **20Ni-RGO** | **KOH (0.1 M)** | **0.5 M** | **8.4** | **This work** |
| **20Cu-RGO** | **KOH (0.1 M)** | **0.5 M** | **6** | **This work** |
| **20Co-RGO** | **KOH (0.1 M)** | **0.5 M** | **5.3** | **This work** |
| **20Fe-RGO** | **KOH (0.1 M)** | **0.5 M** | **3.8** | **This work** |

## 4.5 Reduced graphene oxide supported bimetallic catalyst

The study of metal loading indicated that 30 wt.% was the most effective metal loading for EG oxidation. Taking this into account, the total metal loading was fixed at 30 wt.%, with Ni as the active metal. Thus, the effect of different co-metals (Cu, Co and Fe) on Ni was studied for EG oxidation.

### 4.5.1 Physical characterization

The elemental analysis of various bimetallic catalysts by EDX analysis confirmed the presence of Ni and different co-metals (Cu, Fe or Co) (Table 4.29). The total metal loading ranged between 30.2 and 32.6 wt.%. The Ni metal loading varied between 22.5 and 23.6 wt.%, while loading of co-doped metals was in the range of 8.4 to 8.9 wt.%. The ratio of Ni with co-doped metals varied within 2.6 to 2.7. The carbon content of catalysts ranged from 49.2 to 51.2 wt.%, while oxygen content was around 16-18 wt.%.

**Table 4.29: Elemental composition of bimetallic catalysts**

| Sample ID | Metal (wt.%) | C (wt.%) | O (wt.%) |
|---|---|---|---|
| NiCu-RGO | Ni (23.8), Cu (8.8) | 49.9 | 17.5 |
| NiFe-RGO | Ni (23.6), Fe (8.9) | 51.2 | 16.3 |
| NiCo-RGO | Ni (22.5), Co (8.4) | 50.7 | 18.4 |

The $N_2$ adsorption-desorption isotherms of bimetallic catalysts are shown in Figure 4.39a. All the bimetallic catalysts followed Type II isotherm having H4 hysteresis loop. This H4 hysteresis loop confirmed the formation of interconnected slit-shaped porous structure. The volume of adsorbed $N_2$ varied according to the type of co-doped metal. NiCo-RGO adsorbed the maximum volume of $N_2$, followed by NiCu-RGO and NiFe-RGO. Accordingly, the surface area of different bimetallic catalysts followed the order as: NiCo-RGO (186 $m^2/g$) < NiCu-RGO (151 $m^2/g$) < NiFe-RGO (145 $m^2/g$). The surface area, average pore size and pore volume of the catalysts are tabulated in Table 4.30. The pore size distribution of different bimetallic catalysts showed that all had similar pore size distribution (Figure 4.39b). The pores were mainly in the range of 3 to 5 nm. The total pore volume of the bimetallic catalysts were almost similar and within the range of 0.23 to 0.26 $cm^3/g$. The average pore size of NiFe-RGO, NiCu-RGO and NiCo-RGO were 6.8, 6.2 and 5.5 nm respectively. The results suggested that the partial blockage of pores was minimum in NiCo-RGO, resulting in its highest surface area and lowest average pore size.

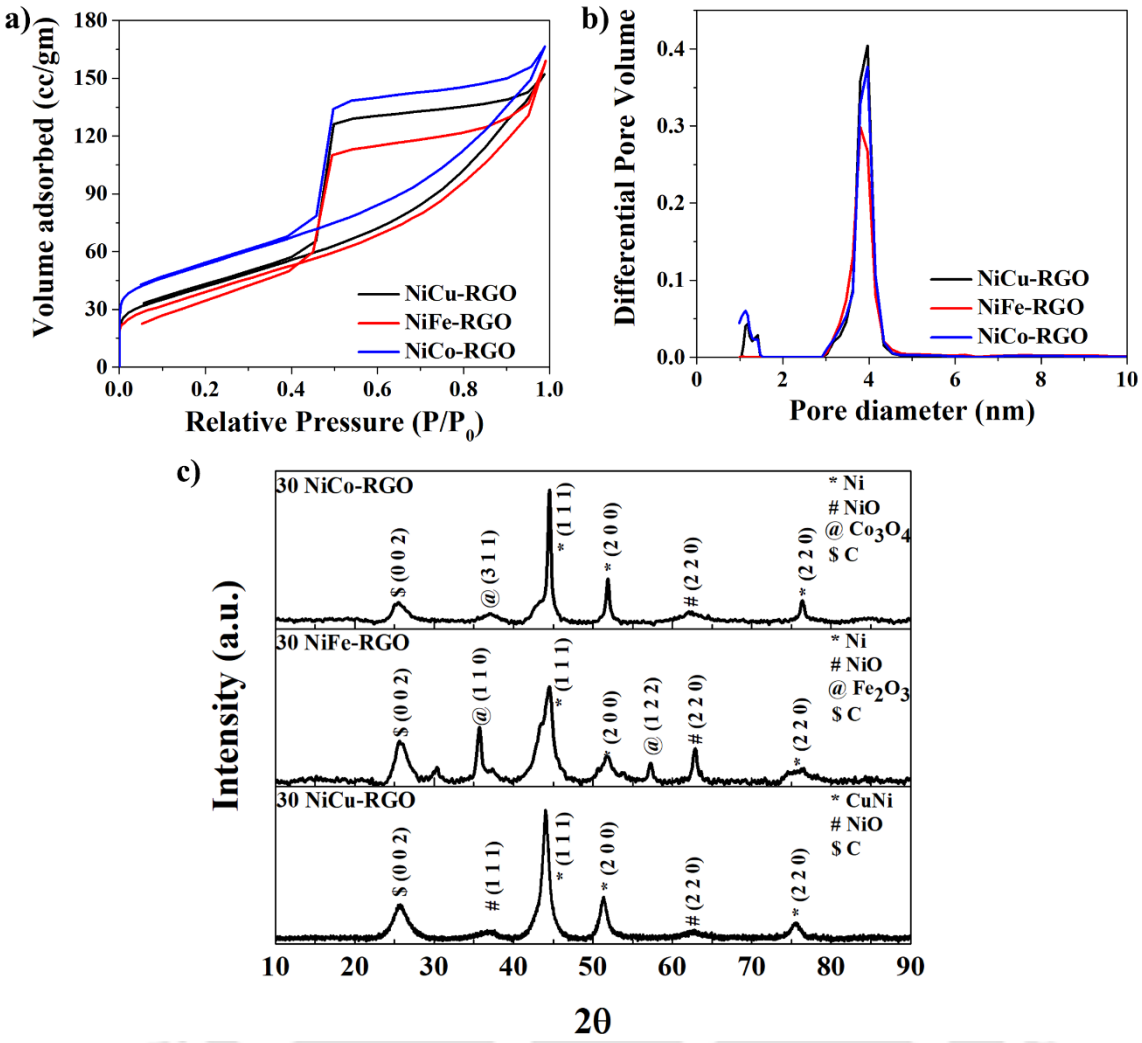


**Figure 4.39: a) $N_2$ adsorption and desorption, b) pore size distribution and c) XRD profile of bimetallic catalysts. (In all the isotherms the lower curves are for adsorption process and the upper curves for desorption process.)**

The XRD patterns of different bimetallic catalysts are shown in Figure 4.39c. All the bimetallic catalysts exhibited a graphitic peak of graphene at 25.5°, corresponding to the (002) plane of C (Singh and De, 2020). The XRD pattern of Ni-RGO revealed metallic $Ni^0$ peaks at 44.5°, 51.8° and 76.4°, which correspond to the (111), (200) and (220) planes, respectively (Figure 4.35a) (Ullah et al., 2019). The $Ni^0$ peaks of NiCu-RGO were observed at 43.9°, 51.3° and 75.5°, while the $Ni^0$ peaks of NiCo-RGO and NiFe-RGO were observed at the same positions as Ni-RGO. The NiO peak at 62.8° was also observed in all the bimetallic catalysts for the (220) plane. NiCu-RGO also showed a peak at 37.3°, corresponding to the (111) peak of NiO. The $Cu^0$ peak was reported at 43.5°, 50.6° and 74.3°, corresponding to (111), (200) and (220) planes, respectively (Ghouri et al., 2015). Since the $Ni^0$ and $Cu^0$ peaks were close to each other, they merged resulting in an apparent shift of $Ni^0$ peaks in NiCu-RGO compared to Ni-RGO.

The NiFe-RGO exhibited $Fe_2O_3$ peaks at 35.6° (110) and 57.3° (122) (Ai et al., 2019). The NiCo-RGO showed a peak at 37.2° relating to the (311) plane of $Co_3O_4$ (Alex et al., 2020). The Ni d-spacing was determined using the peak at 44.5° observed in all catalysts. The Ni d-spacing was ~0.203 nm (Table 4.30). The slightly higher Ni d-spacing (0.205 nm) for NiCu--RGO was due to the left shift of Ni peak in comparison to Ni-RGO. The crystallite size of bimetallic catalysts was in the range of 5.2 to 15 nm.

**Table 4.30: Physical properties of bimetallic catalysts**

| Sample ID | BET surface area ($m^2/g$) | Total Pore Volume ($cm^3/g$) | Micropore area ($m^2/g$) | Average pore size (nm) | Ni d-spacing (nm) | D (%) (TEM) |
|---|---|---|---|---|---|---|
| NiCu-RGO | 151 | 0.23 | 13 | 6.2 | 0.205 | 14.5 |
| NiFe-RGO | 145 | 0.25 | 2 | 6.8 | 0.203 | 13.3 |
| NiCo-RGO | 186 | 0.26 | 33 | 5.5 | 0.203 | 13.5 |

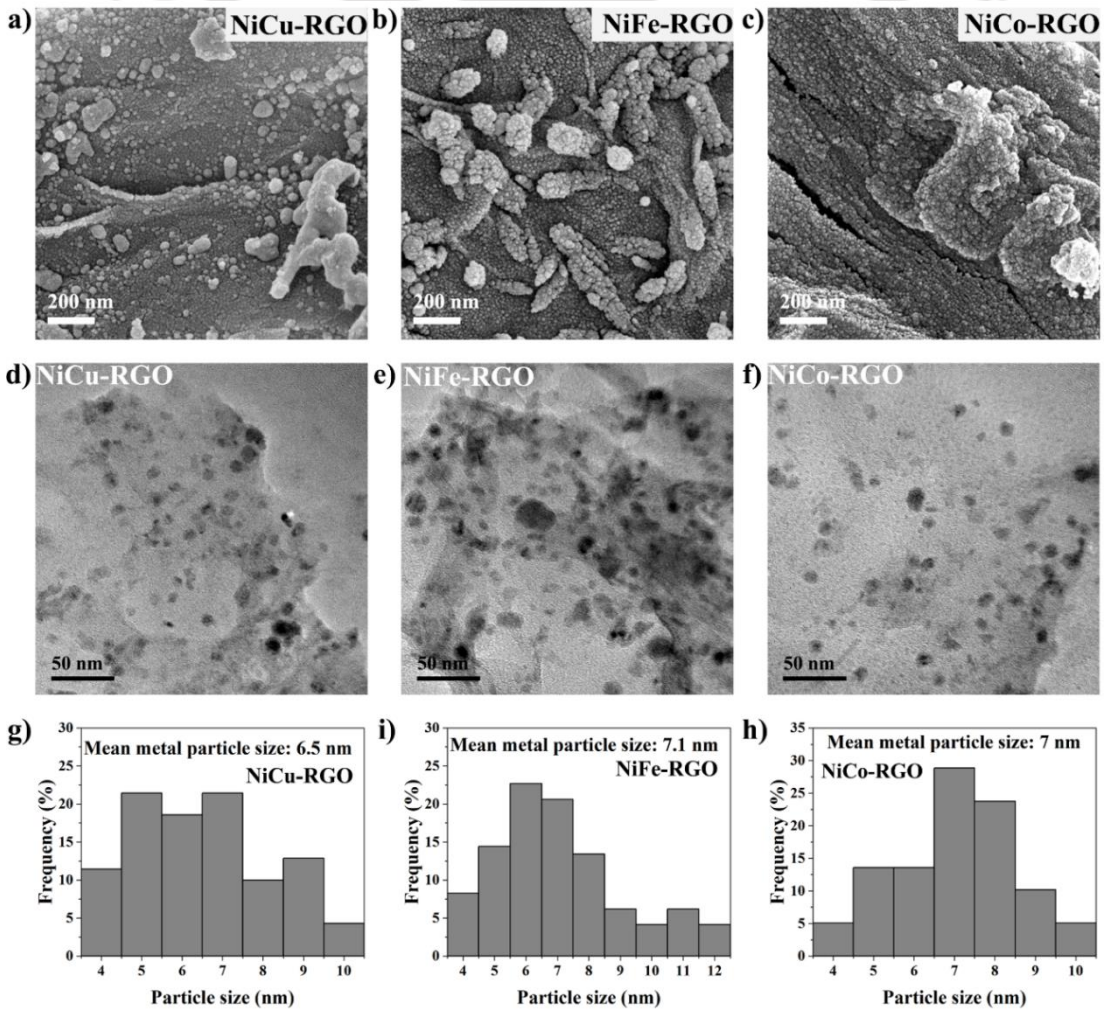


**Figure 4.40: a-c) FESEM images, d-f) FETEM images and g-i) their particle size distribution of bimetallic catalysts.**

The FESEM images of bimetallic catalysts are represented in Figure 4.40a-c. The support formed stacked sheet-like structure (Figure 4.2b). The deposited metals on the support had irregular agglomerated morphology, as observed in the images. This morphology might be due to high metal loading of 30 wt.%. Figure 4.40d-f shows the FETEM images of bimetallic catalysts. The graphene sheets were clearly visible in all the catalysts (Figure 4.2f). The dark irregular spherical-like structures were the metal particles dispersed on graphene sheets. The particle size distribution of various bimetallic catalysts as observed from the corresponding FETEM images are shown in Figure 4.40g-h. The particle size distribution of all the bimetallic catalysts were similar, ranging from 4 to 10 nm. NiCu-RGO had the lowest average particle size of 6.5 nm, while NiCo-RGO (7 nm) and NiFe-RGO (7.1 nm) had comparable average particle sizes. The dispersion was calculated by Equation (3.2) using FETEM images and tabulated in Table 4.30. No significant difference was observed in the dispersion of metals, which ranged from 13.3 to 14.5%. Thus, the presence of 25% of different co-metals in the bimetallic catalysts did not affect the overall morphology of the nickel metals or the catalysts.

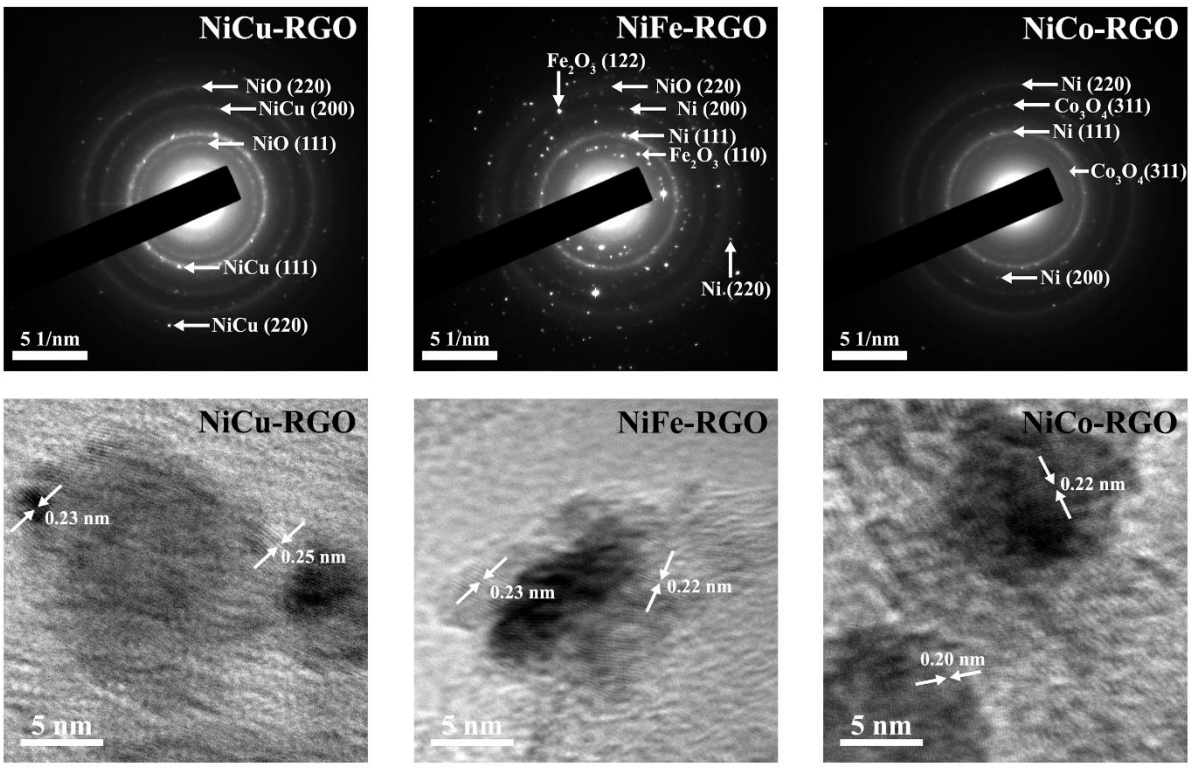


**Figure 4.41: SAED and d-spacing of different bimetallic catalysts.**

The SAED pattern of different bimetallic catalysts is displayed in Figure 4.41. The dotted circular ring observed in SAED images confirmed the polycrystalline nature of the catalysts.

The planes obtained from SAED images were found to be consistent with that observed in XRD. Figure 4.41 shows the d-spacing of various bimetallic catalysts and all of them exhibited two different d-spacing values. This observation confirmed the presence of different bimetals into the support. However, there was variation in the d-spacing values obtained from FETEM and XRD.

The XPS of different bimetallic catalysts is shown in Figure 4.42 and 4.43. The XPS spectra confirmed the presence of Ni and other co-metals (Cu, Co or Fe) on the support. The deconvolution spectra of C1s and Ni2p were similar for all the bimetallic catalysts. Deconvolution of C1s spectra established the presence of C=C (284.6 eV), C-C (285 eV), C-O (286.1 eV) and O-C=O (288.6 eV) (Figure 4.42) (Singh and De, 2020). However, the percentage contribution of carbon functional groups was different for different bimetallic catalysts (Table 4.31). In addition, the O1s spectra of the bimetallic catalysts was also deconvoluted to explore the oxygen functional groups (Figure 4.42). The oxygen functional groups were same for all the catalysts. After deconvolution, C-O-C, C-OH, C=O and O-C=O functional groups were observed at 533.8, 533, 532 and 531.1 eV respectively. NiCu-RGO had the highest percentage of oxygen containing functional groups (36%). The percentage oxygen functional groups in the other two bimetallic catalysts were similar, at around 25%.

**Table 4.31: Binding energy and relative contribution of carbon functional groups present in bimetallic catalysts**

| Sample Id | C=C eV (%)* | C-C eV (%) | C-O eV(%) | O=C-O eV (%) |
|---|---|---|---|---|
| NiCu-RGO | 284.6 (29) | 284.9 (35) | 286 (15) | 288.5 (21) |
| NiFe-RGO | 284.6 (52) | 284.9 (22) | 285.9 (18) | 288.2 (8) |
| NiCo-RGO | 284.6 (40) | 285 (35) | 286.1 (16) | 288.5 (9) |

*the percent contribution of each peak is given in bracket.

The Ni2p deconvolution exhibited same spectra for all the bimetallic catalysts. The $Ni^0$ spectra was observed in Ni-RGO at 852.5 ($2p_{3/2}$) and 871.3 eV ($2p_{1/2}$), while $Ni^{2+}$ was obtained at 854.4 eV ($2p_{3/2}$). Three satellite peaks were detected at 859.2, 862.4 and 877.4 eV (Figure 4.29d) (Biesinger et al., 2011).

$Cu^0$ peaks were observed at 932.7 ($2p_{3/2}$) and 952.6 eV ($2p_{1/2}$) in the Cu2p spectra in NiCu-RGO, while $Cu^{2+}$ peaks were seen at 934.4 ($2p_{3/2}$) and 954.6 eV ($2p_{1/2}$). Three satellite peaks were displayed at 941.5, 943.9 and 962.3 eV. The Co2p spectra, which showed $Co^{2+}$ peaks at 781.9 ($2p_{3/2}$) and 796.8 eV ($2p_{1/2}$), and $Co^{3+}$ at 780.4 ($2p_{3/2}$) and 795.6 eV ($2p_{1/2}$), confirmed the presence of cobalt in NiCo-RGO. Two satellite peaks of Co were spotted at

786.9 and 803 eV (Alex et al., 2020). No metallic state of Co was observed in NiCo-RGO. The incorporation of Fe in NiFe-RGO was confirmed by the $Fe^{2+}$ peaks at 710.8 ($2p_{3/2}$) and 724.4 eV ($2p_{1/2}$), and $Fe^{3+}$ peaks at 712.6 ($2p_{3/2}$) and 726.4 eV ($2p_{1/2}$). Two satellite peaks were obtained at 718.6 and 733.4 eV (Ai et al., 2019). The metallic state of Fe was also not observed for NiFe-RGO. Table 4.32 lists the relative contribution of various metal oxidation states.

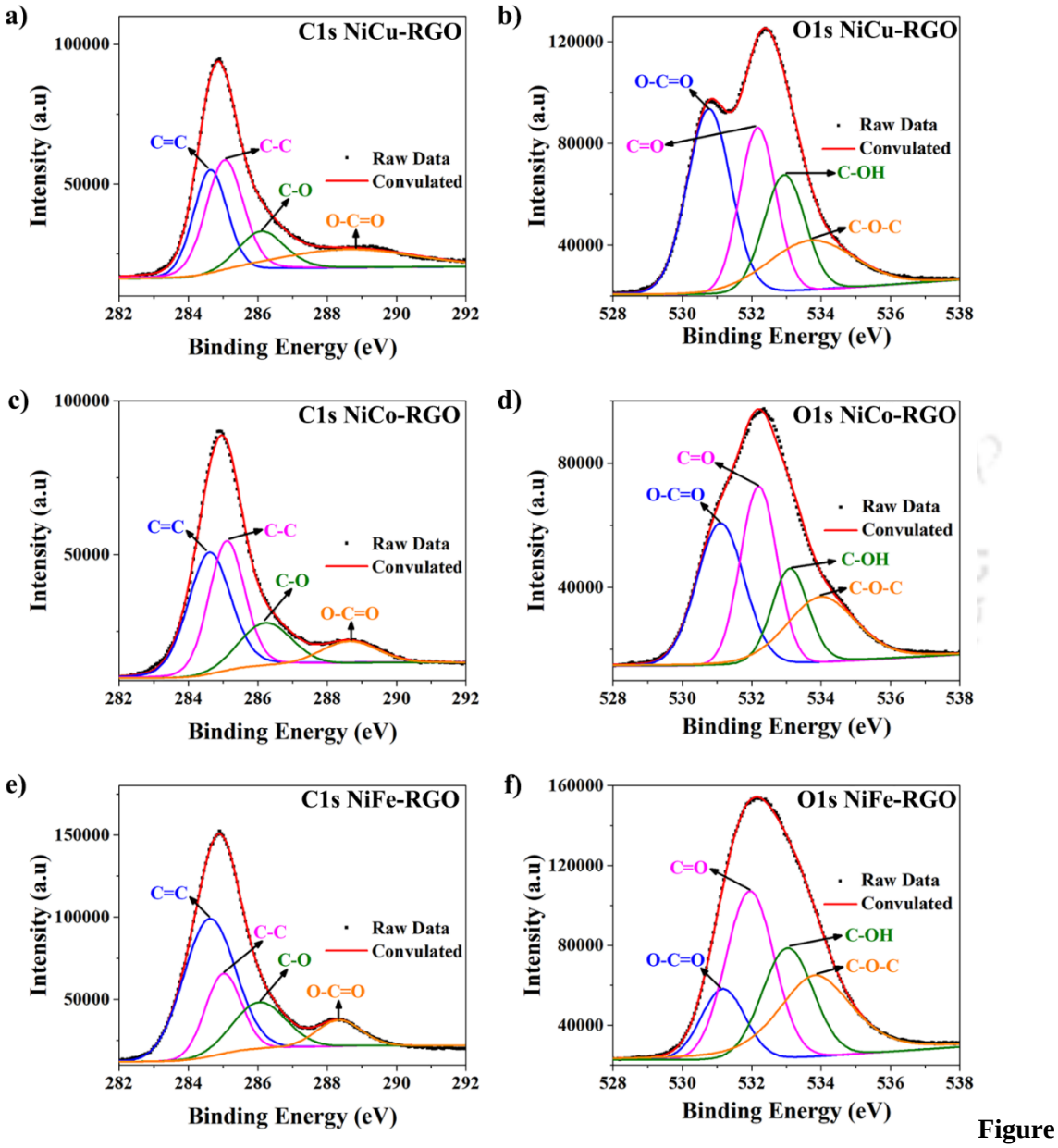


**Figure 4.42: C1s and O1s XPS of different bimetallic catalysts.**

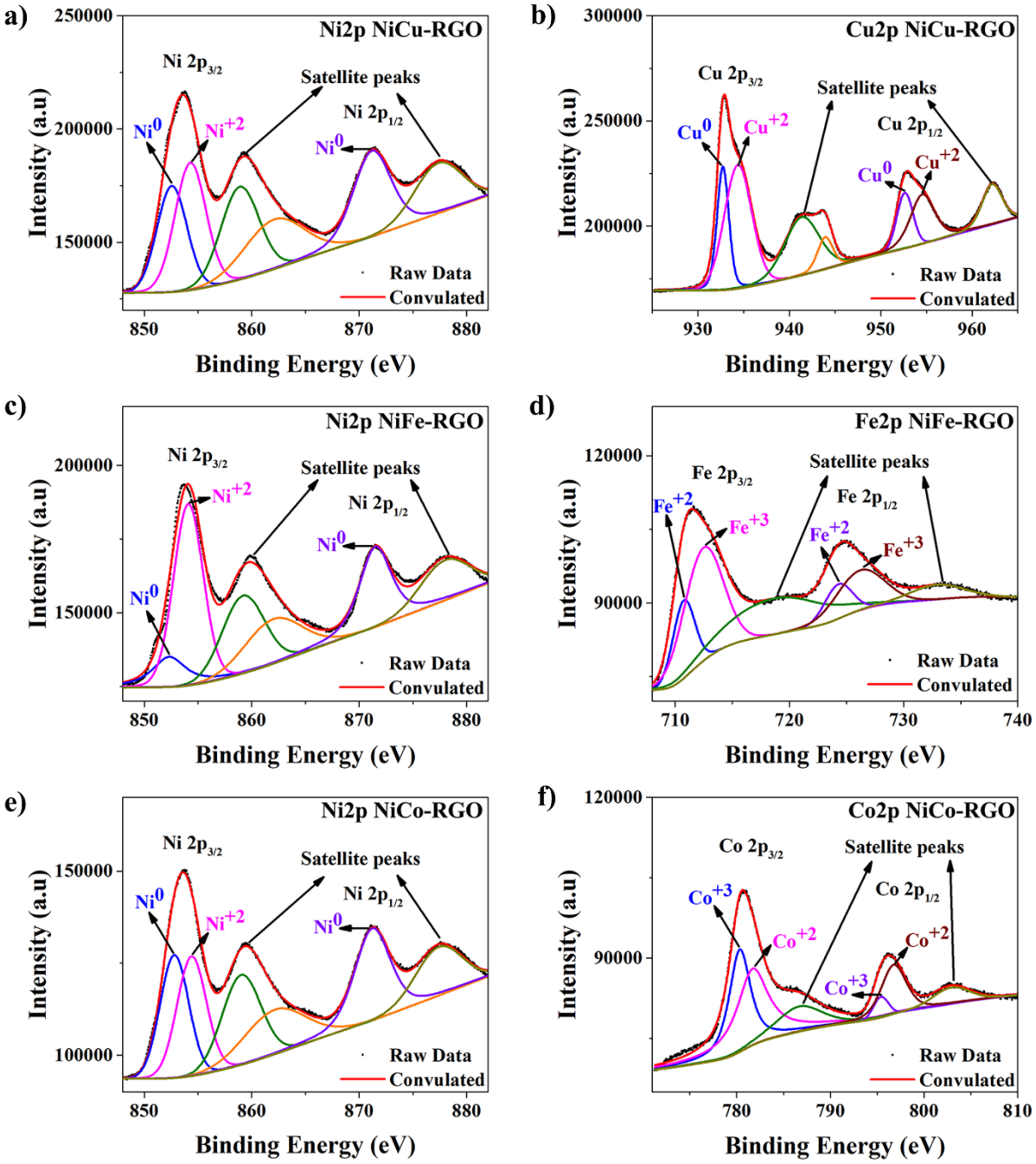


**Figure 4.43: Metal XPS spectra of different bimetallic catalysts.**

NiCu-RGO and NiCo-RGO exhibited a positive shift of 1 and 3 eV respectively in $Ni^0$ peaks, while NiFe-RGO showed a negative shift of 2 eV. This shift in $Ni^0$ peaks in the presence of co-metals (Cu, Co and Fe) would account for increased interaction of Ni with the co-metals. Moreover, higher the extent of shift in binding energy, stronger would be the interaction. Thus, Ni would have stronger interaction with Co as compared to Cu and Fe. However, a positive shift in $Ni^0$ peak also suggested stronger interaction of metal with the support. Therefore, the incorporation of Cu and Co contributed in the enhancement of metal-support interaction,

whereas addition of Fe accounted for a weaker metal-support interaction. The non-availability of metallic states of Fe and Co was due to the temperature at which the sample had been reduced.

**Table 4.32: Binding energies and relative contribution of different metal oxidation states present in the bimetallic catalysts**

| Sample Id | Metal Oxidation State | $2p_{3/2}$ B.E (eV) | $2p_{1/2}$ B.E (eV) | Relative Metal Content (%) |
|---|---|---|---|---|
| Ni-RGO | $Ni^0$ | 852.5 | 871.3 | 62 |
| | $Ni^{2+}$ | 854.4 | - | 38 |
| NiCu-RGO | $Ni^0$ | 852.6 | 871.4 | 63 |
| | $Ni^{2+}$ | 854.3 | / | 37 |
| | $Cu^0$ | 932.7 | 952.6 | 34 |
| | $Cu^{2+}$ | 934.4 | 954.6 | 66 |
| NiFe-RGO | $Ni^0$ | 852.3 | 871.5 | 46 |
| | $Ni^{2+}$ | 854.1 | / | 54 |
| | $Fe^{2+}$ | 710.8 | 724.4 | 30 |
| | $Fe^{3+}$ | 712.6 | 726.4 | 70 |
| NiCo-RGO | $Ni^0$ | 852.8 | 871.3 | 67 |
| | $Ni^{2+}$ | 854.5 | / | 33 |
| | $Co^{2+}$ | 781.9 | 796.8 | 61 |
| | $Co^{3+}$ | 780.4 | 795.6 | 39 |

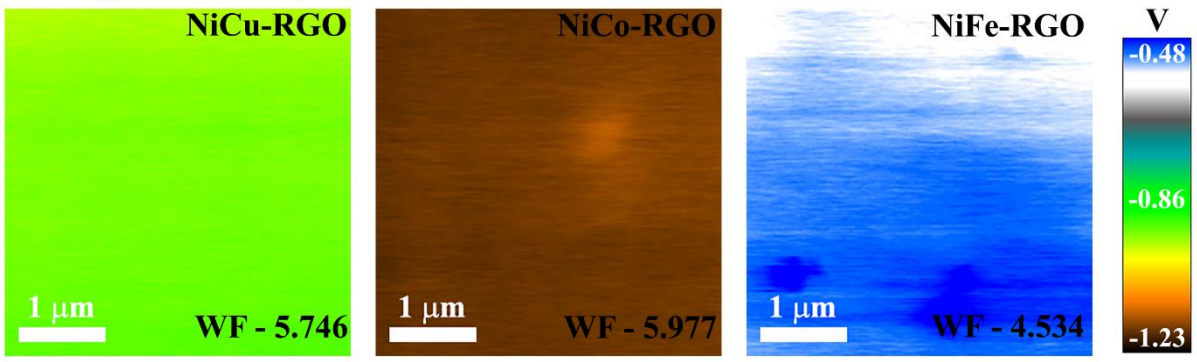


**Figure 4.44: KPFM images of bimetallic catalysts.**

The KPFM images of various bimetallic catalysts is shown in Figure 4.44. The CPD values varied significantly when co-metals were incorporated into the RGO support. Hence, there was difference in work function values among different bimetallic catalysts. The work function values of different bimetallic catalysts followed an increasing trend as: NiFe-RGO (4.534 eV) < NiCu-RGO (5.746 eV) < NiCo-RGO (5.977 eV). The presence of co-metals in the bimetallic catalysts affected the difference in work function values. Thus, co-metals played a crucial role in modifying the work function of the catalysts. It was already reported that the electrocatalytic

activity of catalyst increased with the increase in work function. Hence, it could be concluded that the NiCo-RGO with the highest work function would perform better than the other bimetallic catalysts. It was observed that the trend of electrocatalytic activity of different bimetallic catalysts (discussed in later section) followed the same trend as work function.

### 4.5.2 Electrochemical characterization

The CV of bimetallic catalysts in basic medium is shown in Figure 4.45a. All the catalysts showed one oxidation and one reduction peak. The possible reactions involving different metals in basic medium are already described in earlier section. Since Ni was present in higher amounts in all the bimetallic catalysts, the major peaks might be assigned to ionic changes associated with Ni. The anodic and cathodic peak potential of monometallic Ni-RGO catalysts were observed at 0.6 V and 0.37 V, respectively (Figure 4.36a). A shift in anodic peak potential was observed for all the bimetallic catalysts. The oxidation peak of NiCo-RGO was observed at 0.62 V, while the reduction peak at 0.22 V. The NiCu-RGO and NiFe-RGO exhibited oxidation peaks at 0.55 and 0.78 V, respectively whereas reduction peaks at 0.3 and 0.5 V, respectively. The shift of peak potential for the formation of nickel oxyhydroxides could be due to the interaction of nickel with co-doped metals. The onset potential of bimetallic catalysts also depended on the type of co-doping metal. NiCo-RGO had the lowest onset potential at 0.37 V, followed by NiCu-RGO (0.56 V) and NiFe-RGO (0.61 V). Table 4.33 lists the onset potential and current density of the bimetallic catalysts. The low onset potential could be related to the low energy required for the catalysts to undergo oxidation. This suggested that NiCo-RGO was the most active catalyst for electro-oxidation. The maximum current density was observed at 1 V for all the catalysts. The current density of bimetallic catalysts followed the following trend as: NiCu-RGO (16.7 $mA/cm^2$) > NiCo-RGO (12.9 $mA/cm^2$) > NiFe-RGO (9.3 $mA/cm^2$). The higher current density of NiCu-RGO in basic medium might be attributed to its moderate surface area, pore size and higher metal dispersion. The Tafel slopes obtained for NiCu-RGO, NiCo-RGO and NiFe-RGO in 0.1 M KOH were 152, 169, 185 mV/dec, respectively (Figure 4.45c). The increase in Tafel slope was inversely related to the generation of higher current density. The corresponding charge transfer coefficients (α) for NiCu-RGO, NiCo-RGO and NiFe-RGO were calculated to be 0.39, 0.35 and 0.32, respectively (Table 4.33). The charge transfer coefficient could be directly related to the catalytic activity of the bimetallic catalysts. Therefore, higher current density generated for NiCu-RGO might be correlated with its higher charge transfer coefficient and lower Tafel slope. The decreasing

trend of Tafel slope and increasing trend of α value supported the current density trend observed for different bimetallic catalysts.

The addition of EG in basic medium enhanced the current density for all bimetallic catalysts while lowering the onset potential. This suggested that the co-metals had influenced the EG oxidation and helped in lowering the energy requirement for EG oxidation. The CV analysis in the presence of EG is shown in Figure 4.45b. NiCo-RGO, NiCu-RGO and NiFe-RGO had onset potential of 0.35, 0.48 and 0.56 V, respectively. In the presence of EG, NiCo-RGO exhibited a peak at 0.75 V, whereas no peaks were observed for the other two catalysts. The current density generated from EG oxidation was highest for NiCo-RGO (24.2 $mA/cm^2$), followed by NiCu-RGO (19.2 $mA/cm^2$) and NiFe-RGO (12.2 $mA/cm^2$). The better catalytic activity could be related with the low onset potential of the bimetallic catalysts. The results demonstrated that the incorporation of different co-metals affected the current density of bimetallic catalysts.

The introduction of Co and Cu as co-metals to Ni-RGO resulted in significant increase in current density, whereas incorporation of Fe lowered the performance of Ni-RGO. In comparison to Ni-RGO, the addition of Co and Cu facilitated the formation of metal oxyhydroxides for bimetallic catalysts. The stronger interaction of Ni-Co and Ni-Cu, as observed from XPS, could have played a significant role in the formation of more metal oxyhydroxides. The greater number of metal hydroxides produced for NiCu-RGO and NiCo-RGO would account for better EG oxidation, thereby generating higher current density. The increasing trend of current density could also be related to the increase in surface area. The highest current density observed for NiCo-RGO might be because of its higher surface area (Table 4.30).

Furthermore, the higher metallic $Ni^0$ percentage of the bimetallic catalysts would also contribute towards better EG oxidation. The formation of nickel hydroxides from $Ni^0$ at lower potential resulted in the release of electrons which could be employed for EG oxidation. As a result, a catalyst with higher $Ni^0$ oxidation state would release more electrons during formation of nickel hydroxides. These electrons could be utilised for electro-oxidation of EG. The higher metallic $Ni^0$ content in different bimetallic catalysts was influenced by the nature of co-doped metals, as observed from XPS (Table 4.32). Therefore, NiCo-RGO having higher $Ni^0$ content, generated higher current density during EG oxidation.

The ECSA was calculated using the relationship between current and scan rate in 0.1 M KOH (Figure 4.45e). It was observed that current increased with increase in scan rate (Figure 4.46). The specific ECSA for bimetallic catalysts increased in the order of NiFe-RGO (30.5

$m^2/g$) < NiCu-RGO (34.9 $m^2/g$) < NiCo-RGO (39.6 $m^2/g$). The increasing trend of current density generation corresponded to the the increasing trend of ECSA. Higher ECSA provided more accessible sites for EG to get oxidised. Thus, NiCo-RGO with the highest ECSA (39.6 $m^2/g$) produced the maximum current density in the presence of EG.

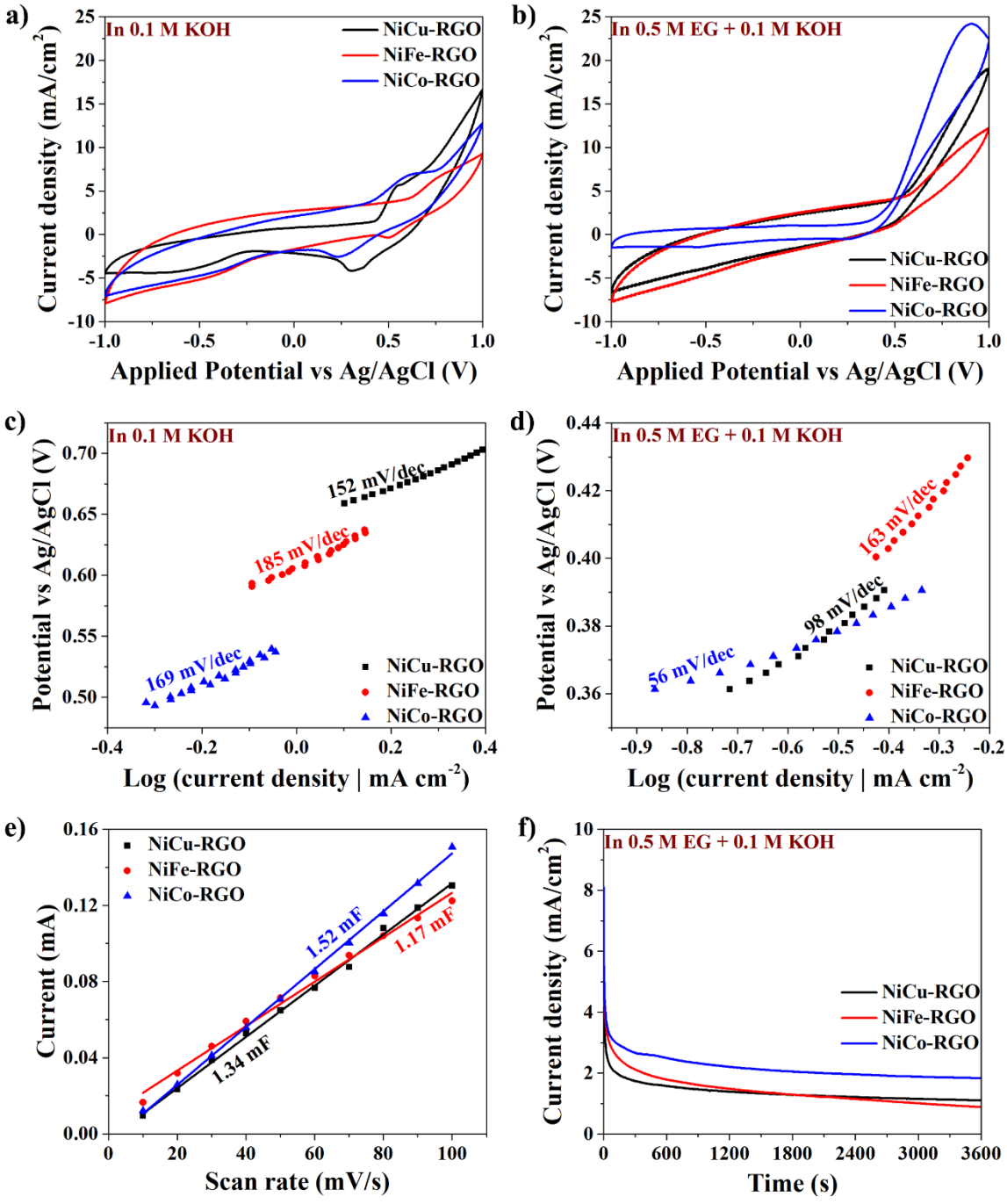


**Figure 4.45: Cyclic voltammetry of bimetallic catalysts a) 0.1 M KOH, b) 0.5 M EG 0.1M KOH, Tafel slope of bimetallic catalysts c) 0.1M KOH, d) 0.5 M EG 0.1 M KOH, e) relationship between current and scanrate in 0.1 M KOH and f) chronoamperometry of bimetallic catalysts in 0.5 M EG 0.1 M KOH.**

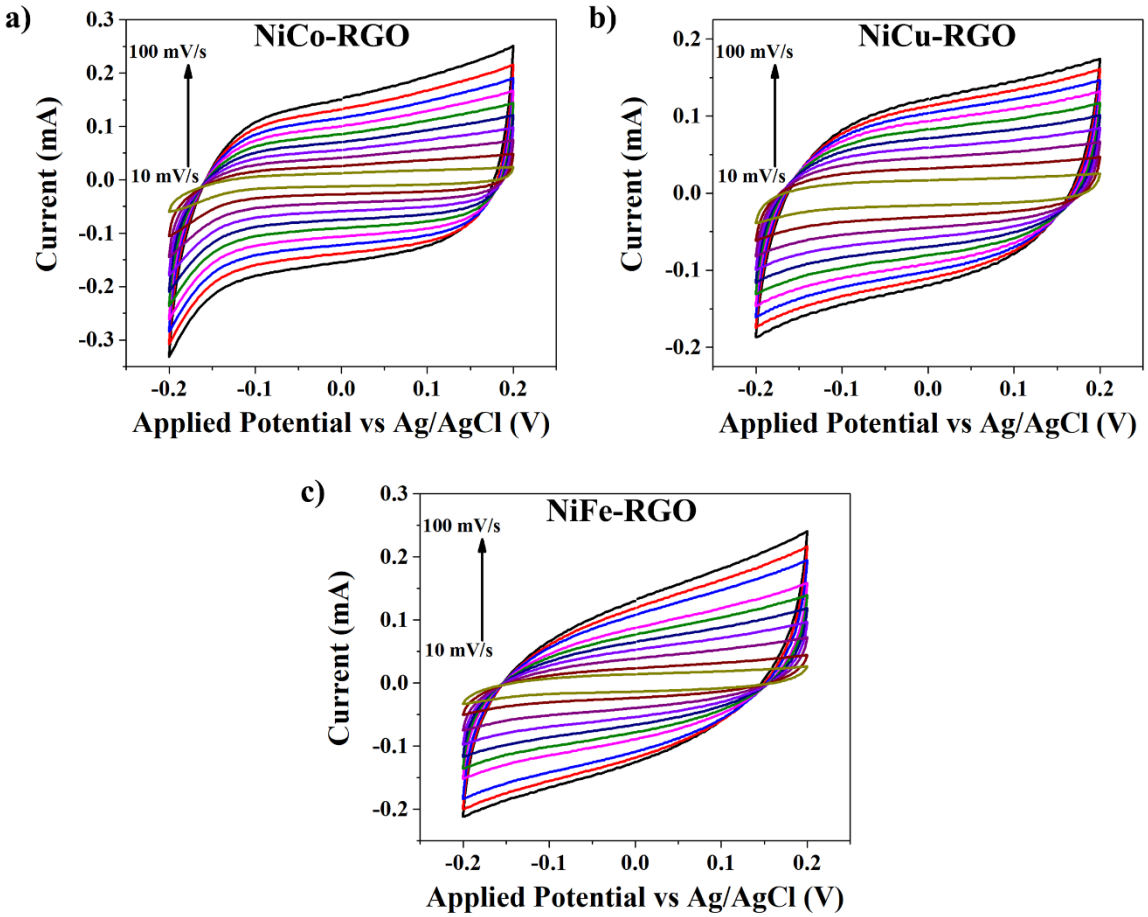


**Figure 4.46: Cyclic voltammetry of bimetallic catalysts at different scan rate.**

The Tafel slope of each bimetallic catalyst decreased upon addition of EG. NiCo-RGO exhibited the lowest Tafel slope of 56 mV/dec, followed by NiCu-RGO (98 mV/dec) and NiFe-RGO (163 mV/dec). The lowering of Tafel slope indicated a faster charge transfer effect for different bimetallic catalysts. Thus, the charge transfer coefficients of all bimetallic catalysts increased in the presence of EG. The α value was higher for NiCo-RGO, followed by NiCu-RGO and NiFe-RGO. The higher α value signified the ease of charge transfer during EG oxidation. So, NiCo-RGO having higher α value would transfer charge more easily compared to the other two bimetallic catalysts, which in turn would facilitate more current density generation during EG oxidation process. Thus, lowest Tafel slope and highest α value of NiCo-RGO accounted for the highest catalytic activity of the catalyst in presence of EG.

The stability of the catalysts was investigated by chronoamperometry, as shown in Figure 4.45f. In the presence of EG, all of the catalysts showed stability upto 1800s. The stabilisation time varied depending on the catalyst. NiCu-RGO and NiCo-RGO got stabilised almost after 120s, whereas NiFe-RGO stabilised after 300s. After 1800s, NiCo-RGO produced

a constant current of 1.83 mA/cm$^2$. On the other hand, NiCu-RGO and NiFe-RGO produced a constant current of 1.1 mA/ cm$^2$ and 0.88 mA/cm$^2$, respectively. Since NiCo-RGO had improved catalytic stability in 0.5 M EG, hence subsequent studies were carried out for the optimisation of different process parameters using the same NiCo-RGO catalyst.

**Table 4.33: Onset potential and anodic peak current density of bimetallic catalyst**

| Sample Id | ECSA ($m^2/g$) | In 0.1 M KOH | | | | In 0.5 M EG + 0.1 M KOH | | | |
|---|---|---|---|---|---|---|---|---|---|
| | | $E_{Onset}$ (V) | $J_{Pa}$ (mA/cm$^2$) | Tafel slope (mV/dec) | $\alpha^*$ | $E_{Onset}$ (V) | $J_{Pa}$ (mA/cm$^2$) | Tafel slope (mV/dec) | $\alpha^*$ |
| NiCu-RGO | 34.9 | 0.55 | 16.7 | 152 | 0.39 | 0.48 | 19.2 | 98 | 0.60 |
| NiFe-RGO | 30.5 | 0.61 | 9.3 | 185 | 0.32 | 0.56 | 12.2 | 163 | 0.36 |
| NiCo-RGO | 39.6 | 0.38 | 12.9 | 169 | 0.35 | 0.35 | 24.2 | 56 | 1.0 |

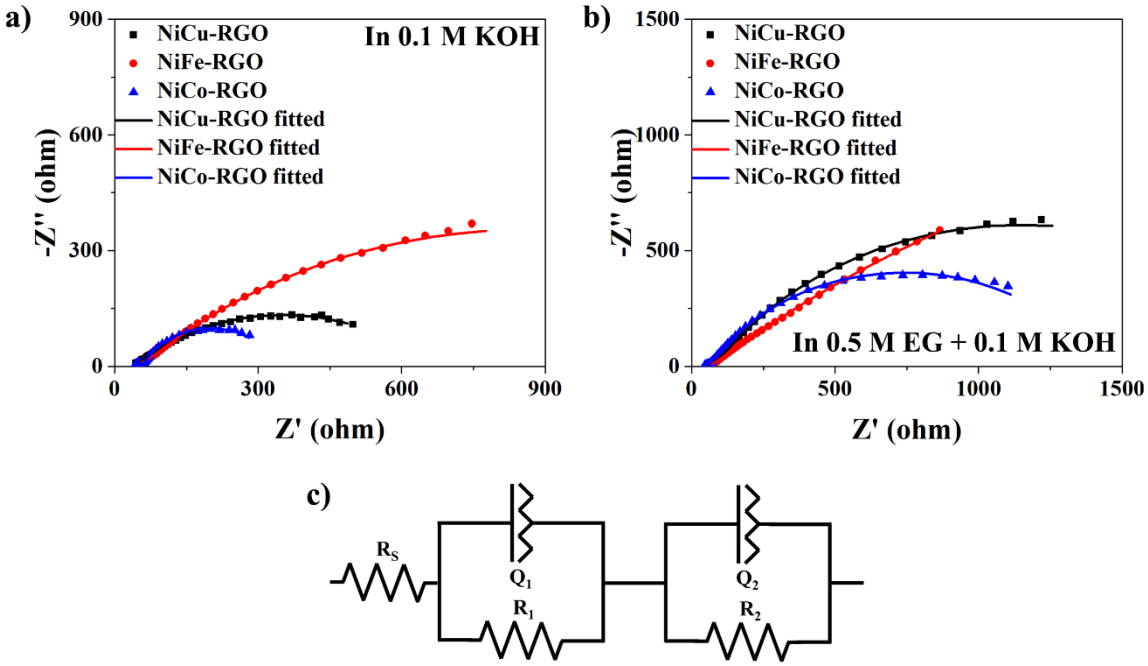


**Figure 4.47: EIS of bimetallic catalysts in a) 0.1 M KOH, b) 0.5 M EG and 0.1 M KOH and c) equivalent circuit diagram.**

The EIS of bimetallic catalysts in the absence and presence of EG is shown in Figure 4.47a and b, respectively. The EIS spectra formed two semicircles, one at lower frequency and the other at higher frequency. The EIS spectra were fitted using the circuit shown in Figure 4.47c. The fitted parameters for different spectra are tabulated in Table 4.34. The solution resistance ($R_S$) was almost same for NiCu-RGO and NiCo-RGO. However, there was a slight increase in $R_S$ for NiFe-RGO. In 0.1 M KOH, NiCu-RGO had the lowest charge transfer resistance ($R_1$) at

8.4 Ω, followed by NiFe-RGO (12 Ω) and NiCo-RGO (29 Ω). The $Y_1$ parameter of the constant phase element (CPE, $Q_1$) ranged from 0.11 to $0.92\times10^{-3}$ $\Omega^{-1}s^n$, whereas phase ($n_1$) lied between 0.52 and 0.73. The time constant obtained from equivalent circuit provided insight into how fast or slow the process of electrochemical interaction with the catalysts occurs. The time constant for charge transfer process ($\tau_1$) was least for NiCu-RGO (0.06 ms), followed by NiFe-RGO (0.2 ms) and NiCo-RGO (0.45 ms). This trend depicted that NiCu-RGO was faster in transferring electron from the electrode surface than other bimetallic catalysts and hence have higher current density in 0.1 M KOH medium. The resistance due to mass transfer process ($R_2$) in basic medium followed the increasing trend as: NiCo-RGO (0.275 KΩ) < NiCu-RGO (0.618 KΩ) < NiFe-RGO (1.63 KΩ). The $Y_2$ associated with CPE, which is responsible for mass transfer process, varied between 1.2 and $2.6\times10^{-3}$ $\Omega^{-1}s^n$ for all the catalysts, while $n_2$ ranged from 0.52 to 0.79. NiCu-RGO had the least time constant for mass transfer process ($\tau_2$) at 0.49 s, followed by NiCo-RGO (0.64 s) and NiFe-RGO (4.6 s). On the other hand, NiCu-RGO was able to accelerate the charge transfer process, followed by NiCo-RGO and NiFe-RGO. The catalyst with faster processes was able to generate higher current density more easily, and hence higher current density trend in the basic medium was supported by the faster mass transfer process of the catalysts and their catalytic activity.

The EIS patterns of different electrocatalysts in the presence of EG were similar to those in the absence of EG. The incorporation of EG decreased the $R_S$ value for NiCo-RGO (22 Ω) and NiFe-RGO (17 Ω), while it increased for NiCu-RGO (43.3 Ω). All the catalysts had similar $R_1$ values of approximately 46 Ω. The $Y_1$ values ranged from 0.04 to $0.95\times10^{-3}$ $\Omega^{-1}s^n$, while $n_1$ fluctuated between 0.32 and 0.71. The time constant ($\tau_1$) was lowest for NiFe-RGO (0.006 ms), followed by NiCo-RGO (0.06 ms) and NiCu-RGO (0.35 ms). The $R_2$ was associated with the electrochemical process in the presence of EG and varied from 1.35 to 6.02 KΩ. The $Y_2$ values ranged between 0.9 and $1.5\times10^{-3}$ $\Omega^{-1}s^n$, whereas $n_2$ varied from 0.47 to 0.69. The time constant for electrochemical oxidation of EG ($\tau_2$) followed the trend as: NiCu-RGO (2.5 s) < NiCo-RGO (4.2 s) < NiFe-RGO (110 s). The lower time constant accounted for faster electrochemical oxidation, which favoured the high current density as observed from CV (Figure 4.45b). Upon comparing the different time constants of bimetallic catalysts, it was observed that NiCo-RGO had moderate time constants for both the charge transfer and electrochemical oxidation process, which worked in favour of generating higher current density from EG oxidation. NiCu-RGO had faster electrochemical oxidation process but slower charge transfer process in presence of EG and thus it resulted to be second best in terms of catalytic activity towards EG electro-

oxidation. NiFe-RGO had the fastest charge transfer process but the time required for electrochemical oxidation process is too high, which resulted in the generation of least current density among different bimetallic catalysts.

**Table 4.34: EIS equivalent circuit fitting parameters for bimetallic catalyst**

| Sample Id | $R_S$ (Ω) | $R_1$ (Ω) | $Q_1$ | | $\tau_1$ (ms) | $R_2$ (KΩ) | $Q_2$ | | $\tau_2$(s) |
|---|---|---|---|---|---|---|---|---|---|
| | | | $Y_1 \times 10^{-3}$ ($\Omega^{-1}s^n$) | $n_1$ | | | $Y_2 \times 10^{-3}$ ($\Omega^{-1}s^n$) | $n_2$ | |
| NiCu-RGO | 35 | 8.4 | 0.92 | 0.73 | 0.06 | 0.618 | 1.2 | 0.52 | 0.49 |
| NiCo-RGO | 35 | 29 | 0.65 | 0.52 | 0.45 | 0.275 | 2.6 | 0.79 | 0.64 |
| NiFe-RGO | 44 | 12 | 0.11 | 0.78 | 0.2 | 1.63 | 1.4 | 0.52 | 4.6 |
| NiCu-RGO* | 43.3 | 45 | 0.81 | 0.42 | 0.35 | 2.12 | 0.9 | 0.67 | 2.5 |
| NiCo-RGO* | 22 | 46 | 0.95 | 0.32 | 0.06 | 1.35 | 2 | 0.69 | 4.2 |
| NiFe-RGO* | 17 | 48 | 0.04 | 0.71 | 0.006 | 6.02 | 1.5 | 0.47 | 110 |

* In presence of EG

One possible explanation for the faster electrochemical process could be the ease in the formation of higher metal oxyhydroxides in different catalysts. As discussed earlier, the ease in the formation of higher metal oxyhydroxides depended on the interaction of Ni with co-metals. In comparison to other co-metals, the stronger interaction between Ni and Co might have contributed to the formation of higher metal oxyhydroxides and an overall faster electrochemical process. The higher $Ni^0$ content in NiCo-RGO (Table 4.32) also might have led to the generation of more electrons for the electrochemical oxidation of EG. Moreover, the co-doped metals also influenced the BET surface area (Table 4.30) as well as ECSA (Table 4.33) of the electrocatalysts. Higher BET surface area and ECSA was observed when cobalt was used as the co-doped metal. The moderate $\tau_1$ and $\tau_2$ values of NiCo-RGO accounted for higher current density production. The NiCu-RGO had highest $\tau_1$ value which restricted the charge transfer process, however the electrochemical process was faster than NiCo-RGO. On the other hand, higher $\tau_2$ values suggested slower electrochemical process of NiFe-RGO in the presence of EG. Thus, it can be concluded that there was significant effect of co-metals in bimetallic catalyst on the electro-oxidation of EG.

Since NiCo-RGO proved to be the best catalyst, so further in-depth study towards EG oxidation was conducted using the same catalyst to determine the different electrocatalytic parameters.

The peak current density (anodic and cathodic) of NiCo-RGO in KOH medium increased with the increase in scan rate (Figure 4.48). At lower scan rates (5 to 100 mV/s), the

peak current density was linearly related to scan rate (Figure 4.48a). This linearity indicated that the electrochemical activity of the catalyst was dependent on surface adsorption process that is relied on the redox species formed on the electrode surface. This phenomenon could also be attributed to the reversibility of the redox process. The surface coverage of the redox species (Γ*) was calculated by Equation (3.8). The Γ* for NiCo-RGO was calculated to be $1.5\times10^{-7}$ mol/cm$^2$. At higher scan rates (100 to 1000 mV/s), the peak current density was linearly dependent on the square root of scan rate (Figure 4.48b), which indicated the diffusion-limiting process in the redox behaviour of NiCo-RGO. This limiting phenomenon resulted from the charge neutralisation of redox active species on the electrode surface during redox reaction.

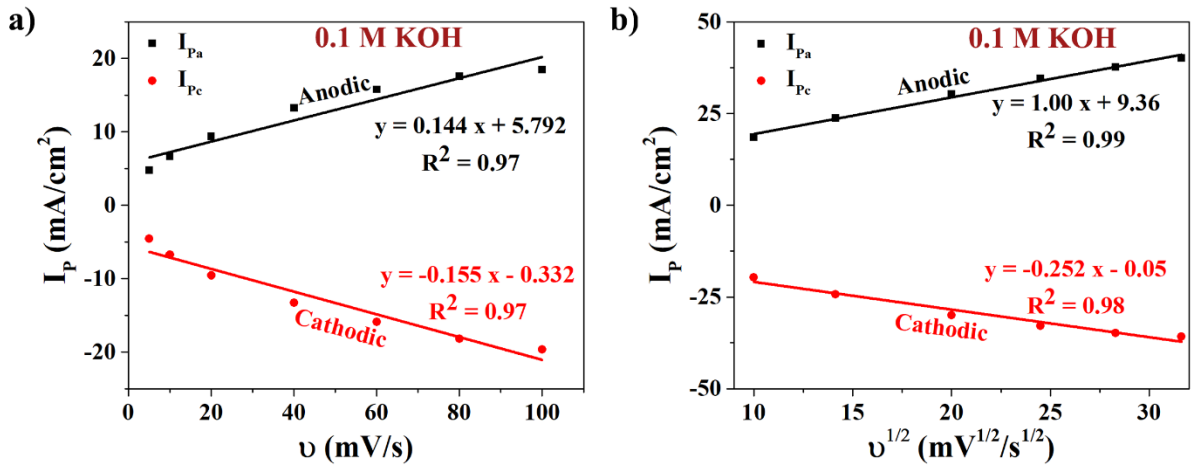


**Figure 4.48: a) Relationship between current density with scan rate at lower scan rate (5 to 100 mV/s) for NiCo-RGO and b) relationship between current density with square root scan rate at higher scan rate (100 to 1000 mV/s) for NiCo-RGO.**

Figure 4.49 depicts the effect of various scan rates (5 to 1000 mV/s) in the presence of EG. The anodic current density increased with the increase in scan rate. At higher scan rates (>100 mV/s), the anodic peak for EG oxidation disappeared. This disappearance of the anodic peak could be attributed to the slower kinetics involved in the conversion of metal hydroxides to metal oxyhydroxides, which prevents adequate electron transfer within the electrode at higher scan rates (Azizi et al., 2013). Figure 4.49a and b show the relationship between anodic peak current density with scan rate and square root of scan rate. If the current density is linear with scan rate, then the electrochemical process is surface adsorption controlled while it's linearity with square root of scan rate suggested diffusion controlled process. In Figure 4.49a, the linearity between current density and scan rate was not achieved, hence, the process was not surface adsorption controlled. The linear fitting for Figure 4.49b revealed that the peak current density was better fitted with respect to the square root of scan rate than the scan rate itself.

Thus, EG electro-oxidation by NiCo-RGO was controlled by diffusion-limiting process rather than surface adsorption-controlled process. The relation between Log I and Log ν is shown in Figure 4.49c. The slope of Log I vs Log ν also provided confirmation regarding diffusion and surface adsorption-controlled process. The slope of diffusion-controlled process is 0.5, whereas a slope is 1 indicates adsorption controlled process (Ma et al., 2021). The oxidation of EG by NiCo-RGO resulted in Log I vs Log ν slope of 0.36, which was closer to 0.5, indicating that the electro-oxidation process was controlled by diffusion. The deviation of experimental slope value (0.36) from theoretical value (0.5) could be due to kinetic process of the reaction. The diffusion coefficient ($D_0$) of EG molecules for NiCo-RGO catalyst, calculated from Equation (3.9), was between $9.53 \times 10^{-5}$ to $9.53 \times 10^{-8}$ $cm^2/s$, while n varied between 1 and 10.

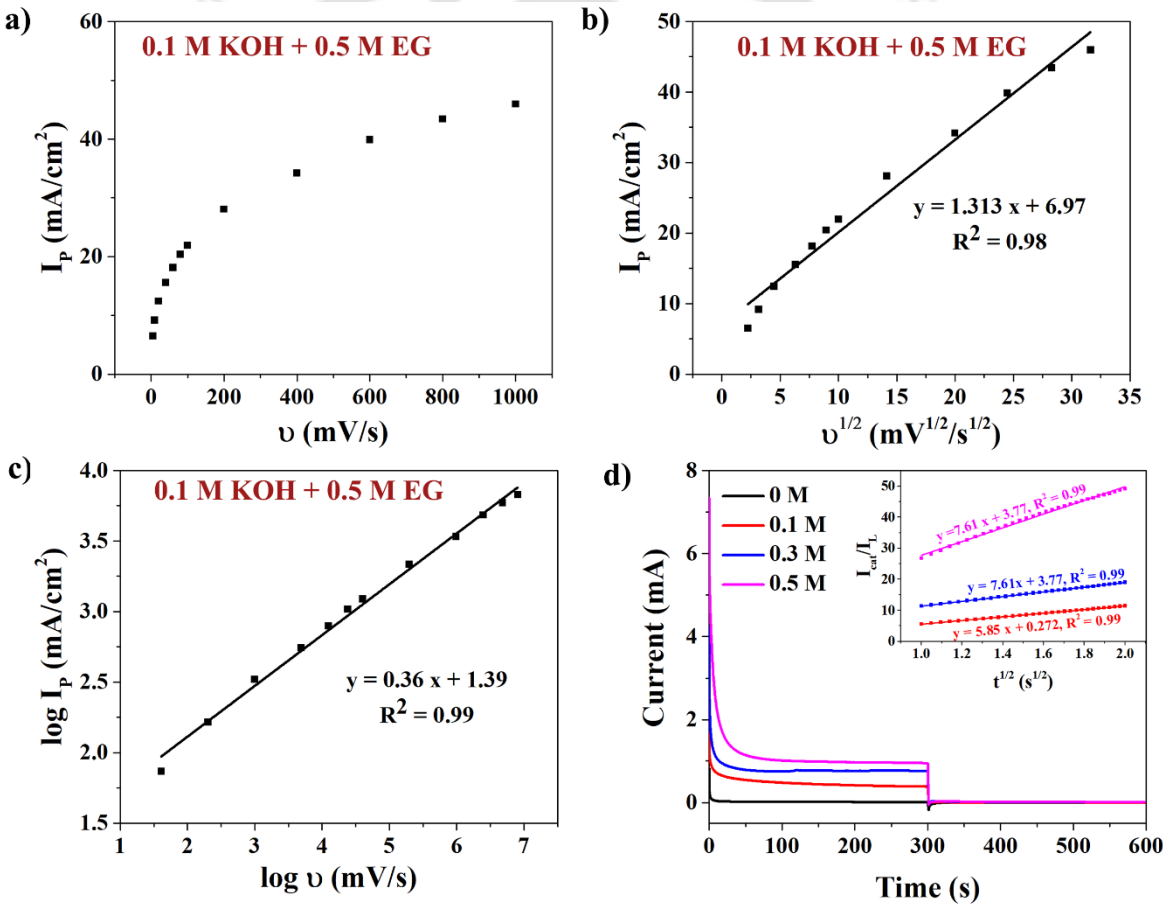


**Figure 4.49: Dependency of current density for NiCo-RGO in 0.5 M EG 0.1 M KOH with a) scan rate, b) square root of scan rate, c) relationship between Log of current density with log of scan rate, d) dual potential chronoamperometry of NiCo-RGO for different EG concentration in KOH. Relationship between $I_{cat}/I_L$ with $t^{1/2}$ of different EG concentration in inset. (EG= ethylene glycol)**

Dual step chronoamperometry for NiCo-RGO is shown in the Figure 4.49d. The study was performed to determine the catalytic rate constant of NiCo-RGO for EG oxidation, as well to

analyze the electrochemical-chemical mechanism. The step potential was employed based on the peak potential obtained from CV. It was found that current density increased with the increase in EG concentration. The rate at which current decreased also slowed down as the concentration of EG increased. Thus, it could be stated that metal oxyhydroxides reacted with EG as soon as they were formed on the surface of the electrode. When 0.3 V potential was applied, no significant cathodic current was observed, indicating the irreversible behaviour of EG oxidation reaction. The exponential behaviour of I-V curve confirmed that the electrochemical process was diffusion-controlled. This allowed the phenomenon to follow the Cottrell equation. Thus, the mean $k_{cat}$ of NiCo-RGO during EG oxidation was $1.71 \times 10^5$ $cm^3/mol.s$, as calculated from Equation (3.10). The different electrochemical parameters of the bimetallic catalyst NiCo-RGO improved when co-metals were introduced into the monometallic counterpart. This strongly validated the amplified electrocatalytic activity of the bimetallic catalyst.

## 4.6 Effect of process parameters

The study of RGO supported Ni-based bimetallic catalyst concluded that NiCo-RGO was the best performing catalyst for EG oxidation. Therefore, further research regarding the effect of different process parameters was carried out using NiCo-RGO as the bimetallic catalyst.

### 4.6.1 Effect of KOH concentration

The CV of NiCo-RGO at 25 °C in presence of 0.5 M EG and various KOH concentrations is shown in Figure 4.50a. In these conditions, NiCo-RGO exhibited one oxidation and one reduction peak. The anodic peak was observed at around 0.75 V, while the cathodic peak was detected at 0.21 V. The anodic peak of NiCo-RGO shifted to lower potential with an increase in KOH concentrations. The increase in KOH concentration increased the ionic concentration of the electrolyte, which created the possibility of increased metal hydroxides formation. This helped in easy generation of higher number of electrons from the catalyst surface. This easy formation of electrons which are available for EG oxidation could result in a reduction in the peak potential. The onset potential of NiCo-RGO decreased with the increase in KOH concentration. The onset potential and current density for different operating parameters are tabulated in Table 4.35. The onset potential at 0.1, 0.5 and 1 M KOH were 0.34, 0.30 and 0.27 V, respectively. The peak current density was observed at 1 V. Moreover, the current density also increased for NiCo-RGO with the increase in KOH concentration. The highest current density was observed at 1 M KOH (45.4 $mA/cm^2$), followed by 0.5 M KOH (32.7 $mA/cm^2$) and 0.1 M KOH (24.2 $mA/cm^2$). The current density trend could be related to the low onset potential trend. As the concentration of KOH increased, the number of hydroxyl ions also increased in the system, resulting in higher current density generation by facilitating more nickel oxyhydroxide formation.

The EIS spectra of NiCo-RGO at various KOH concentration is shown in Figure 4.50b. The EIS spectra showed two semicircles, one at higher frequency and the other at lower frequency. The fitted parameters of the equivalent circuit is tabulated in Table 4.36. The solution resistance ($R_S$) decreased with an increase in KOH concentration. As the concentration increased from 0.1 to 0.5 M KOH, the semicircle arc reduced drastically, resulting in a decrease in the charge transfer resistance from 35 to 11.6 Ω. The $Y_1$ parameter of $Q_1$ was between 0.65 and 1.38 $\times 10^{-3}$ $\Omega^{-1}s^n$, while $n_1$ varied from 0.52 to 0.79. The time constant ($\tau_1$), representing the charge transfer process, was almost similar and found to be between 0.4 and 0.5 ms. The resistance corresponding to electrochemical reaction ($R_2$) decreased with increase in KOH

concentration. The $Y_2$ varied from 2.6 to 4.1 $\times 10^{-3}$ $\Omega^{-1}s^n$, whereas $n_2$ values were almost similar. The time constant for electrochemical oxidation ($\tau_2$), representing electrochemical oxidation process, followed the increasing trend as: 0.64 s (1 M) < 0.11 s (0.5 M) < 0.09 s (0.1 M). The decreasing $\tau_2$ also agreed with the increase in current density (Figure 4.50a). The ion mobility also increased with the increase in KOH concentration, making hydroxyl ions more available at the solid-liquid interface. The hydroxyl ions generated also helped in the electrochemical reaction, resulting in the reduction of $\tau_2$. This reduction in $\tau_2$ values accounted for the production of high current density with increasing KOH concentration.

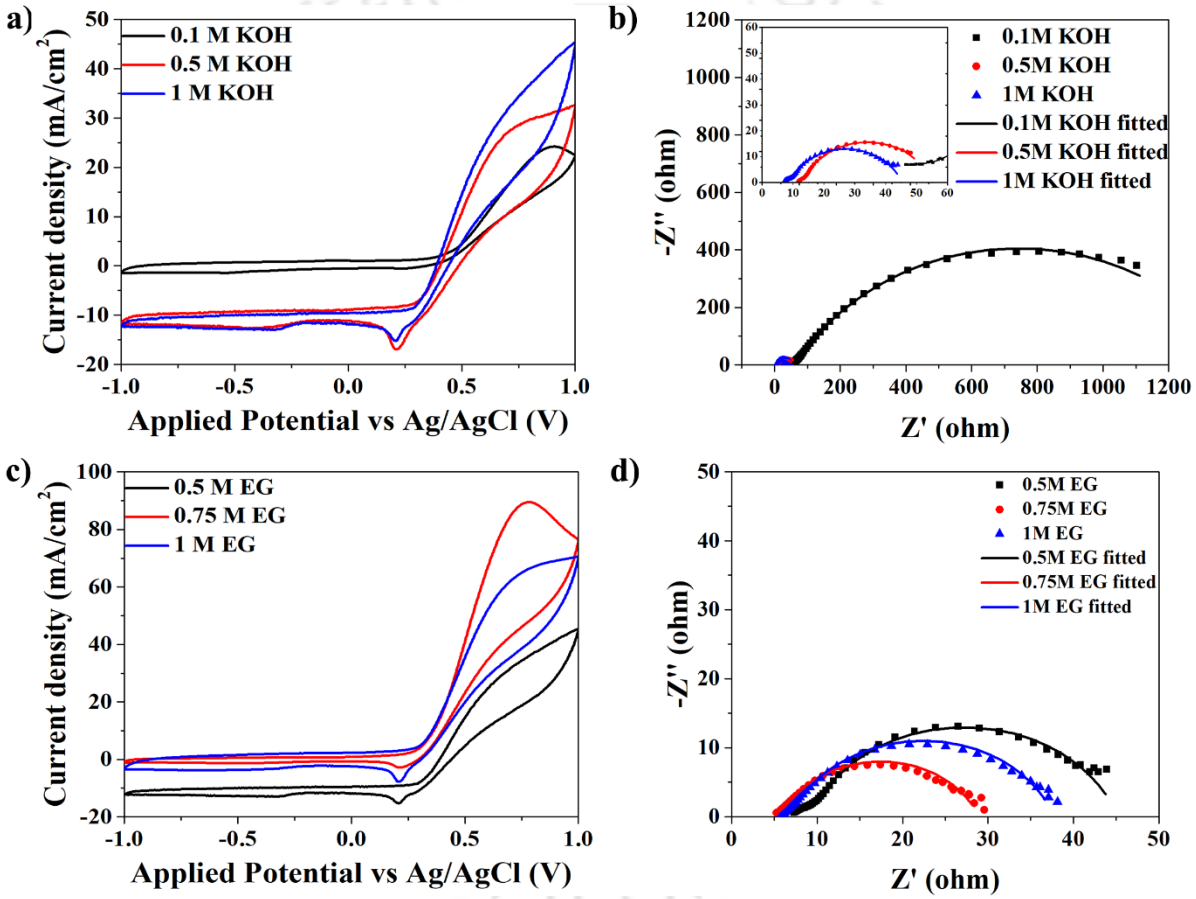


**Figure 4.50: a) Cyclic voltammetry, b) EIS of NiCo-RGO catalyst using different KOH concentrations in presence of 0.5 M EG at 25 °C. (Zoomed view of initial section of EIS in inset), c) Cyclic voltammetry and d) EIS of NiCo-RGO in presence of different EG concentrations in 1 M KOH at 25 °C.**

### 4.6.2 Effect of ethylene glycol (EG) concentration

The CV of NiCo-RGO recorded at 25°C in the presence of various concentrations of EG and 1 M KOH is shown in Figure 4.50c. The NiCo-RGO exhibited an oxidation and reduction peak at around 0.78 and 0.23 V, respectively. The peak current density was observed at 1 V for all

the EG concentrations, except 0.75 M (at 0.78 V). The increase in EG concentration slightly increased the onset potential of NiCo-RGO, which ranged between 0.27 and 0.30 V. As, the concentration increased, the energy requirement for oxidation also increased since the availability of EG molecules increased on the catalyst surface for oxidation. The current density for NiCo-RGO increased with increase in EG concentration, but decreased in after 0.75 M. The initial increase in EG concentration made more EG molecules available for oxidation, which enhanced the current density production. As the molar concentration of EG reached beyond 0.75 M, the available active sites on the catalyst might have become saturated with EG molecules, rendering them incapable of contributing further in current density generation. The decrease in current density above 0.75 M could possibly be attributed to limiting hydroxyl ions at higher concentration of EG. This limited availability of hydroxyl ions resulted in a restriction in the formation of required number of metal hydroxides needed for further enhancement of EG oxidation. The current density ($mA/cm^2$) in presence of different molar concentrations of EG followed the trend as: 89.4 (0.75 M) > 70.5 (1 M) > 45.4 (0.5 M).

**Table 4.35: Onset potential and peak current density for NiCo-RGO catalyst at different conditions**

| KOH Conc (M) | Alcohol Conc (M) | Temperature (°C) | Type of Alcohol | $E_{Onset}$ (V) | $J_{Pa}$ ($mA/cm^2$) |
|---|---|---|---|---|---|
| 0.1 | 0.5 | 25 | EG | 0.34 | 24.2 |
| 0.5 | 0.5 | 25 | EG | 0.30 | 32.7 |
| 1 | 0.5 | 25 | EG | 0.27 | 45.4 |
| 1 | 0.75 | 25 | EG | 0.29 | 89.4 |
| 1 | 1 | 25 | EG | 0.30 | 70.5 |
| 1 | 0.75 | 50 | EG | 0.23 | 170.6 |
| 1 | 0.75 | 75 | EG | 0.18 | 198.7 |
| 1 | 0.75 | 75 | Gly | 0.13 | 290.1 |
| 1 | 0.75 | 75 | 1,2 PD | 0.30 | 169.9 |

The EIS of NiCo-RGO in the presence of varying EG concentrations and 1 M KOH at 25°C is shown in Figure 4.50d. With the increase in EG concentration, the EIS spectra exhibited a similar pattern of having two semicircles, one at the higher frequency and the other at the lower frequency. Table 4.36 shows the parameter of an equivalent circuit. The solution resistance ($R_S$) changed minimally with an increase in EG conentration. The charge transfer resistance reduced with decrease in EG concentration as: 0.75 M (0.84 Ω) < 0.5 M (2.5 Ω) < 1 M (5.1 Ω). The $Y_1$ varied between 0.78 and $1.51\times10^{-3}$ $\Omega^{-1}s^n$, while $n_1$ ranged from 0.66 to 0.8. The $\tau_1$ was least at 0.75 M (0.11 ms), followed by 0.4 ms at 0.5 M and 0.65 ms at 1 M. The electrochemical oxidation resistance ($R_2$) values followed the same trend as charge transfer

resistance and varied from 0.023 to 0.055 KΩ. The $Y_2$ values were in between 0.9 and $4.1\times10^{/3}$ $\Omega^{/1}s^n$, while change of $n_2$ was negligible. The $\tau_2$ values were least for 0.75 M (0.01 s), followed by 1 M (0.02 s) and 0.5 M (0.09 s). The increase in $\tau_2$ values indicated a slower electrochemical oxidation. So based on the time constant values, it was concluded that the overall electrochemical process was faster for 0.75 M EG compared to other EG concentrations. The increased $\tau_2$ for 1 M EG confirmed that more EG molecules produced beyond 0.75 M increased the impedance of the electrochemical process, thereby inhibiting current density production. Since $\tau_2 > \tau_1$, therefore $\tau_2$ played the limiting role for the generation of current density and hence the inverse trend of $\tau_2$ confirmed the higher current density generation in 0.75 M EG (Figure 4.50a).

**Table 4.36: Fitted parameters of equivalent circuit for NiCo-RGO catalyst different conditions**

| Effect of parmeters | $R_S$ (Ω) | $R_1$ (Ω) | $Q_1$ | | $\tau_1$ (ms) | $R_2$ (KΩ) | $Q_2$ | | $\tau_2$ (s) |
|---|---|---|---|---|---|---|---|---|---|
| | | | $Y_1\times10^{-3}$ ($\Omega^{-1}s^n$) | $n_1$ | | | $Y_2\times10^{-3}$ ($\Omega^{-1}s^n$) | $n_2$ | |
| **Effect of KOH concentration (M)** | | | | | | | | | |
| 0.1 | 35.0 | 29 | 0.65 | 0.52 | 0.450 | 0.275 | 2.6 | 0.79 | 0.640 |
| 0.5 | 11.6 | 2.0 | 1.38 | 0.79 | 0.500 | 0.041 | 4.0 | 0.82 | 0.110 |
| 1 | 7.0 | 2.5 | 0.94 | 0.77 | 0.400 | 0.036 | 4.1 | 0.80 | 0.090 |
| **Effect of Ethylene Glycol concentration (M)** | | | | | | | | | |
| 0.5 | 7.0 | 2.5 | 0.94 | 0.77 | 0.400 | 0.036 | 4.1 | 0.80 | 0.090 |
| 0.75 | 5.0 | 0.8 | 0.78 | 0.80 | 0.110 | 0.023 | 1.5 | 0.77 | 0.010 |
| 1 | 6.4 | 5.1 | 1.51 | 0.66 | 0.650 | 0.055 | 0.9 | 0.78 | 0.020 |
| **Effect of temperature (°C)** | | | | | | | | | |
| 25 | 5.0 | 0.8 | 0.78 | 0.80 | 0.110 | 0.023 | 1.5 | 0.77 | 0.010 |
| 50 | 3.2 | 0.8 | 1.31 | 0.42 | 0.020 | 0.014 | 2.4 | 0.70 | 0.009 |
| 75 | 2.8 | 0.5 | 0.01 | 1.00 | 0.015 | 0.012 | 0.4 | 0.85 | 0.002 |
| **Effect of type of Alcohol** | | | | | | | | | |
| Ethylene glycol | 2.8 | 0.5 | 0.01 | 1.00 | 0.015 | 0.012 | 0.4 | 0.85 | 0.002 |
| Glycerol | 2.1 | 0.8 | 0.03 | 1.00 | 0.007 | 0.035 | 0.2 | 0.79 | 0.001 |
| Propane-1,2-diol | 3.2 | 0.5 | 0.27 | 0.93 | 0.068 | 0.010 | 2.0 | 0.74 | 0.005 |

### 4.6.3 Effect of temperature

The CV of NiCo-RGO at different temperatures in 1 M KOH and 0.75 M EG is shown in Figure 4.51a. At all the studied temperatures, one oxidation and one reduction peaks were observed. The onset potential shifted to lower potential with the increase in temperature. The onset potentials for 25, 50 and 75 °C were 0.29, 0.23 and 0.18 V respectively. As, the temperature increased the energy required for oxidation of EG decreased.The peak was observed at ~ 0.78 V for all the temperatures. The current density increased with increase in

temperature. The current density followed the increasing trend as: 89.4 mA/cm$^2$ (25 °C) < 170.6 mA/cm$^2$ (50 °C) < 198.7 mA/cm$^2$ (75 °C). Even at 0.6 V, the current denisties at 50°C (138.7 mA/cm$^2$) and 75°C (154.2 mA/cm$^2$) were much higher than that observed for 25 °C at 0.78 V (89.4 mA/cm$^2$). The increase in temperature allowed the catalyst to overcome the activation barrier required for EG oxidation more easily and thereby enhanced the performance of the catalyst.

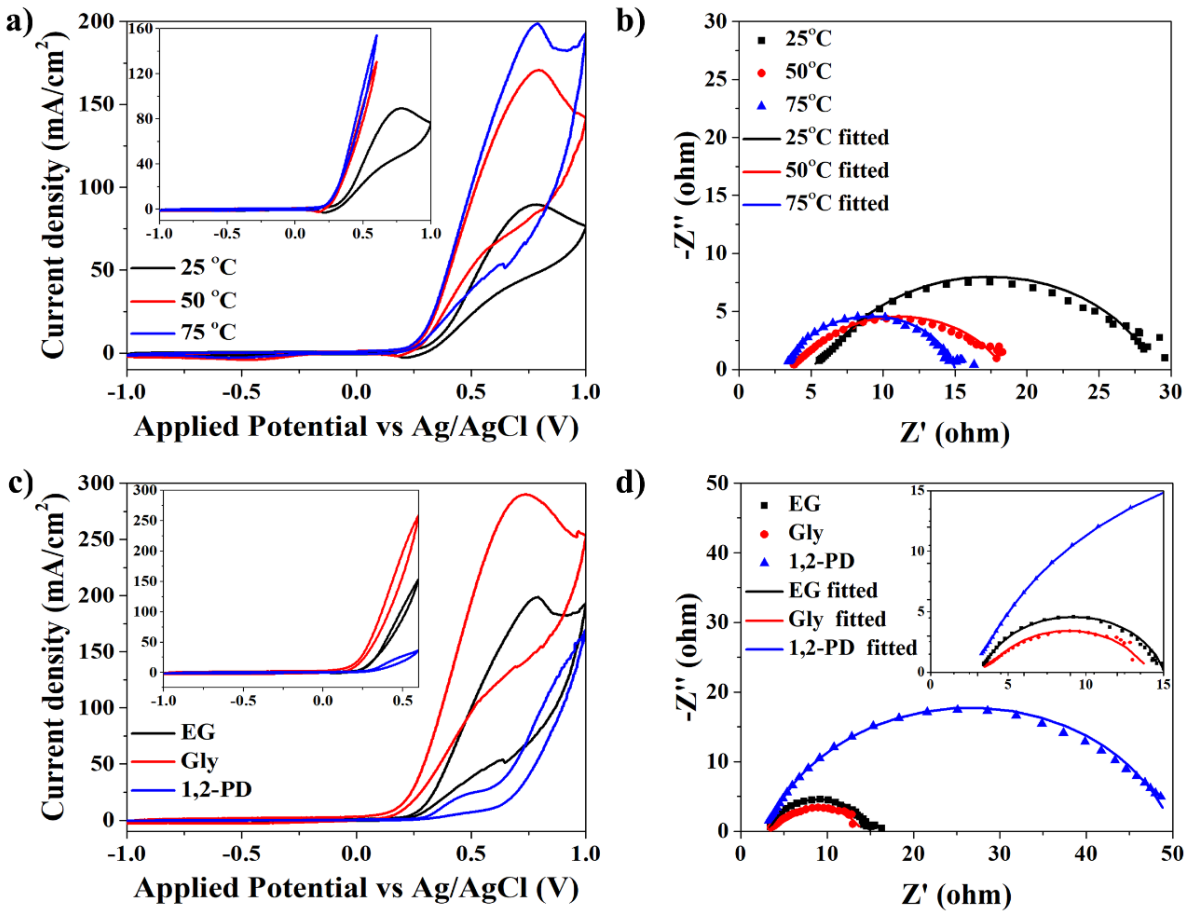


**Figure 4.51: a) Cyclic voltammetry and b) EIS of NiCo-RGO at different temperatures in 1M KOH with 0.75 M EG (cyclic voltammetry upto 0.6 V at 50 °C and 75 °C in inset) c) Cyclic voltammetry (upto 0.6 V in inset) and d) EIS (zoomed view in inset) of NiCo-RGO for different 0.75 M polyhydric alcohols in 1 M KOH at 75 °C.**

The EIS spectra of NiCo-RGO obtained at different temperatures is shown in Figure 4.51b. The behaviour of EIS spectra acquired at different temperatures was similar, with one semicircle at higher frequency and one semicircle at lower frequency. The parameters of an equivalent circuit is tabulated in Table 4.36. The solution resistance, $R_S$, decreased with increase in temperature and ranged from 2.8 to 5 Ω. The charge transfer resistance values were similar for 25°C and 50°C (0.84 Ω), but reduced to 0.5 Ω for 75°C. The $Y_1$ values ranged from

0.01 to $1.31\times10^{-3}$ $\Omega^{-1}s^n$, while $n_1$ varied from 0.42 to 1. The $\tau_1$ values decreased drastically with increasing temperature and followed the trend as: 75°C (0.015 ms) < 50°C (0.02 ms) < 25°C (0.11 ms). This trend was inversely related to the current density produced at different temperatures. The $R_2$ values ranged from 0.012 to 0.023 KΩ and decreased with increase in temperature. The $Y_2$ values ranged from 0.38 to $2.4\times10^{-3}$ $\Omega^{-1}s^n$ with $n_2$ of 0.7 to 0.85. The decrease in $\tau_2$ values was also observed with increase in temperature, with 75°C showing the least decrease (0.002 s), followed by 50°C (0.009 s) and 25°C (0.01 s). The increase in temperature provides additional energy, which also increased the randomness and mobility of ions into the system. The higher mobility of ions reduced the mass transfer effect as well as activation energy required for NiCo-RGO to electro-oxidise EG and thus the electrochemical process become faster with increase in temperature. The lowering of both $\tau_1$ and $\tau_2$ strongly supported the increase in current density with increasing temperature, thereby facilitating higher current density generation. Thus, it could be concluded that the optimal operating parameter for electrochemical oxidation of EG would be 0.75 M EG in 1 M KOH at 75 °C.

### 4.6.4 Effect of different polyhydric alcohol

The activity of the bimetallic catalyst was further checked with other polyhydric alcohols in order to determine its efficacy for the electro-oxidation of polyhydric alcohols. The onset potential was lowest for glycerol (0.13 V) followed by ethylene glycol (0.18 V) and propane-1,2-diol (0.30 V). The CV of NiCo-RGO for several polyhydric alcohols at 0.75 M concentration in a basic medium at 75°C is shown in Figure 4.51c. In the presence of glycerol (Gly) and propane-1,2-diol (1,2 PD), NiCo-RGO catalysts showed a single oxidation peak. The oxidation peak potential for each alcohol was different and the potentials were 0.78 V for EG, 0.73 V for glycerol and 0.5 V for propane-1,2-diol. Glycerol and EG had the highest current density at peak potential, but for propane-1,2-diol, it was observed at 1 V. The current density was highest for glycerol (290.1 $mA/cm^2$), followed by EG (198.7 $mA/cm^2$) and propane-1,2-diol (169.9 $mA/cm^2$). Even at a lower potential 0.6 V, the current density followed the similar trend, with EG, glycerol and propane-1,2-diol having current densities of 154.2, 259.5 and 36.8 $mA/cm^2$ respectively. The higher density produced for glycerol and EG, even at lower potential, suggested that these alcohols were more easily electrochemically oxidized by NiCo-RGO than propane-1,2-diol. Upon comparing different polyhydric alcohols, it was observed that glycerol generated higher current density than EG, however propane-1,2-diol produced lower current density than ethylene glycol. Glycerol have more volumetric density as well as

more hydroxyl group than ethylene glycol, which contributed to the generation of more current density than EG. On the other hand, propane-1,2-diol have more volumetric density but same number of hydroxyl groups as EG. The higher volumetric density of propane-1,2-diol is due to the presence of extra alkyl groups. However, the oxidation of alkyl groups (-$CH_3$) was much more difficult, which resulted in a lower current density than EG. The similar observation was also obtained from the onset potential for alcohol oxidation.

The EIS of NiCo-RGO for various polyhydric alcohols in basic medium is shown in Figure 4.51d. Similar EIS patterns were observed in the presence of all alcohols. The EIS pattern consisted of two semicircles. The fitted parametric values are tablated in Table 4.36. The time constant for charge transfer process ($\tau_1$) values was lowest for glycerol (0.007 ms), followed by EG (0.015 ms) and propane-1,2-diol (0.068 ms). The $\tau_2$ followed the increasing order as: glycerol (0.001 s) < EG (0.002 s) < propane-1,2-diol (0.005 s). The lower $\tau_1$ and $\tau_2$ signified that the overall process was faster for glycerol and EG as compared to propane-1,2-diol. Glycerol has a higher number of alcohol sites as well as carbon number, which facilitated the transfer of higher number of electrons than EG and propane-1,2-diol. This could have accelerated the electrochemical process and higher current denisty generation, as evident from EIS and CV. On the other hand, propane-1,2-diol has more carbon number than EG, but equal number of alcohol groups. Higher number of carbon in propane-1,2-diol made its oxidation difficult due to the requirement of higher activation energy to break the alkyl bond. This slowed down the overall electrochemical process and resulted in lower current density. This might be due to the difficulty in breaking -$CH_3$ bond present in propane-1,2-diol. The decreasing trend of $\tau_1$ and $\tau_2$ values for different alcohols supported the increased current density production from various alcohols, as observed in CV (Figure 4.51c).

The present study was compared with other catalysts for EG electro-oxidation (Table 4.37). There have been few studies using a similar combination of non-noble metal-based bimetallic catalysts for EG oxidation. Therefore, catalytic activity was compared with different non-noble metal-based bimetallic catalysts. Moreover, direct comparison with the reported study was difficult as the oxidation conditions were different. The present study could be directly compared to NiCo/SS as published by Sun et al., (2015) and could be concluded that the present study reported 11 mA/$cm^2$ more current density from EG oxidation at room temperature. In comparison to other combination of non-noble metal-based catalysts, the present study demonstrated two to three times better catalytic activity for EG oxidation. Only the $NiPbO_2$ showed at per activity as the reported catalyst, whereas $NiPbO_2$-graphene showed

higher activity than NiCo-RGO for electro-oxidation of EG. Thus, it could be concluded that NiCo-RGO proved to be a better catalyst than others reported in the existing literature, and hence could be employed as a catalyst for DAFC with higher catalytic activity.

**Table 4.37: Comparison of current density as reported for different transition metal based bimetallic electrocatalysts for electro-oxidation of EG with that of present study**

| Catalyst | Electrolyte (Conc.) | EG (Conc.) | Current density ($mA/cm^2$) | References |
|---|---|---|---|---|
| NiTi/ITO | NaOH (0.1 M) | 0.7 M | 1.2 | Yu et al., 2019 |
| NiCo/SS | KOH (1 M) | 0.5 M | 75 | Sun et al., 2015 |
| NiMn/carbon nanofiber | NaOH (4 M) | 1 M | 15.95 | Hameed et al., 2022 |
| CoMn/Mt | NaOH (0.1 M) | 0.8 M | 6 | Abbaci et al., 2022 |
| FeNi/VC | KOH (0.5 M) | 1 M | 28.2 | Gayathri et al., 2022 |
| FeCo/VC | KOH (0.5 M) | 1 M | 36.6 | Gayathri et al., 2022 |
| NiMn/RGO | KOH (0.5 M) | 1 M | 38 | Hefnawy et al., 2021 |
| $NiPbO_2$ | NaOH (1 M) | 1 M | 87 | Sultan et al., 2023 |
| $NiPbO_2$/graphene | NaOH (1M) | 1M | 172 | Sultan et al., 2023 |
| **NiCu-RGO** | **KOH (0.1 M)** | **0.5 M** | **19.2** | **This work** |
| **NiFe-RGO** | **KOH (0.1 M)** | **0.5 M** | **12.2** | **This work** |
| **NiCo-RGO** | **KOH (0.1 M)** | **0.5 M** | **24.2** | **This work** |
| **NiCo-RGO** | **KOH (1M)** | **0.75 M** | **86** | **This work** |
| **NiCo-RGO (at 75°C)** | **KOH (1M)** | **0.75 M** | **198.7** | **This work** |

## 4.7 Reaction study and stability of the catalyst

### 4.7.1 Reaction study

Following chronoamperometry of the bimetallic catalysts, the reaction samples for the electro-oxidation of EG by different bimetallic catalysts were analysed using HPLC. The selectivity of various products formed during EG oxidation is shown in Figure 4.52. The variation of products among different bimetallic catalysts could be attributed to the effect of different co-metals. Glycoldehyde was found to be the most abundant product in all the bimetallic catalysts. The selectivity of glycoldehyde was highest for NiFe-RGO (98.3%), followed by NiCo-RGO (95.8%) and NiCu-RGO (91.3%). In addition to glycoldehyde, all the catalysts produced oxalic acid. The NiCo-RGO and NiCu-RGO catalysts produced glycolic acid, whereas NiCu-RGO primarily produced glyoxylic acid. NiCo-RGO and NiFe-RGO generated only trace amount of glyoxylic acid. The reaction pathways for different bimetallic catalysts are illustrated in scheme 1.

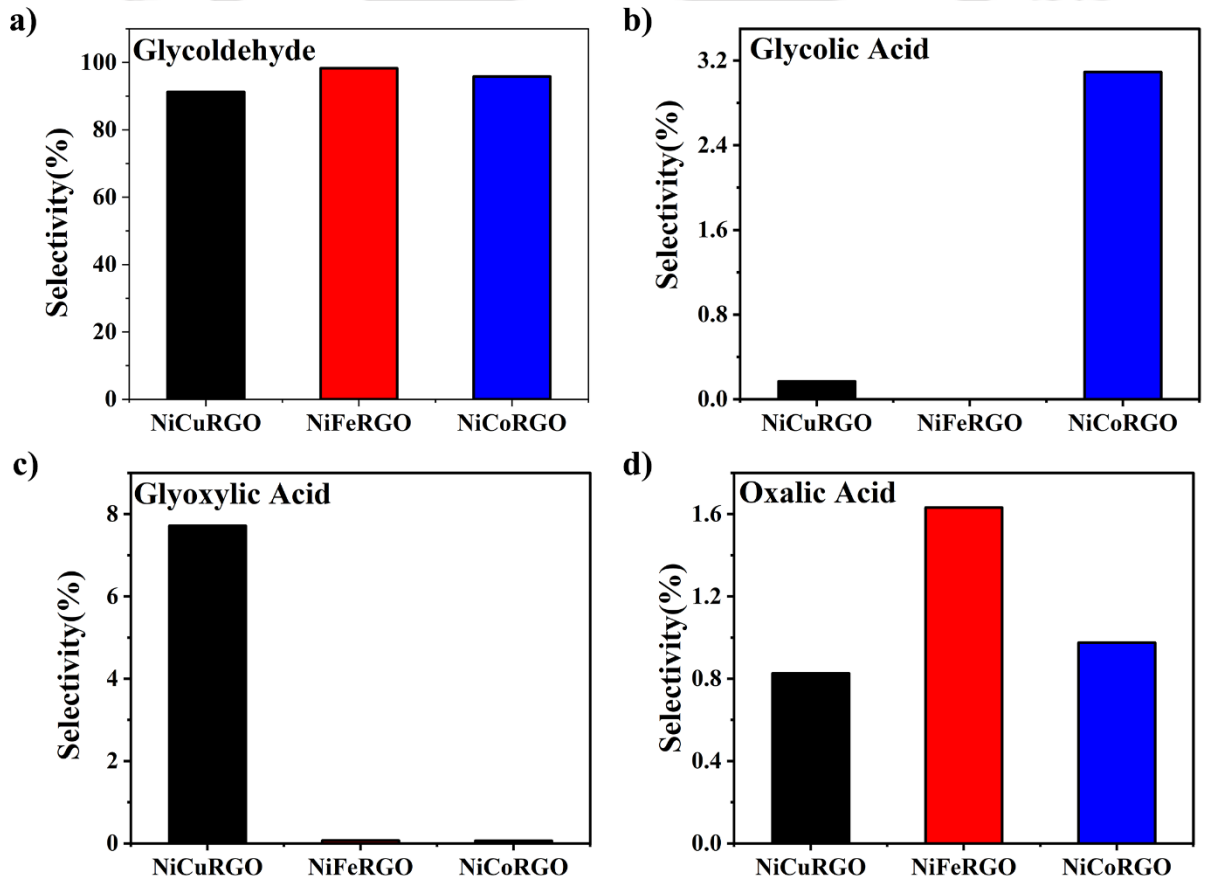


**Figure 4.52: Selectivity of a) glycoldehyde, b) glycolic acid, c) glyoxylic acid and d) Oxalic acid for different bimetallic catalysts.**

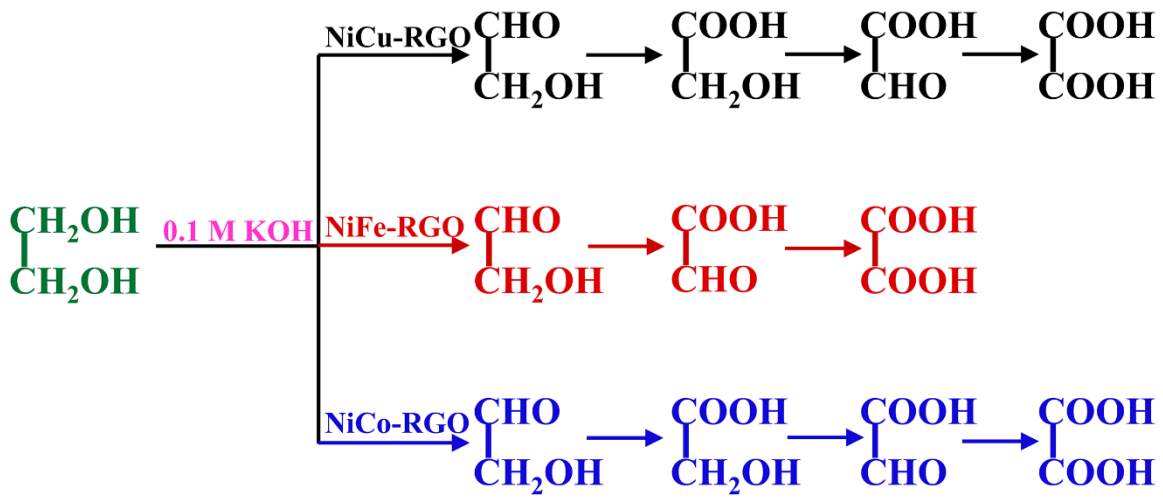


**Scheme 1: Reactions involved for ethylene glycol oxidation in basic medium by bimetallic catalysts.**

### 4.7.2 Stability of catalysts

The CO stripping test was performed for 20Cu-RGO in both acidic and basic media to determine the tolerance of the electrode towards CO poisoning. The CV showed CO oxidation peaks at 0.18 V in acidic medium and -0.54 V in basic medium (Figure 4.53). The difference in peak current density between the 1st and 2nd cycles suggested that the presence of CO had a negligible effect on the performance of 20Cu-RGO in both acidic and basic media.

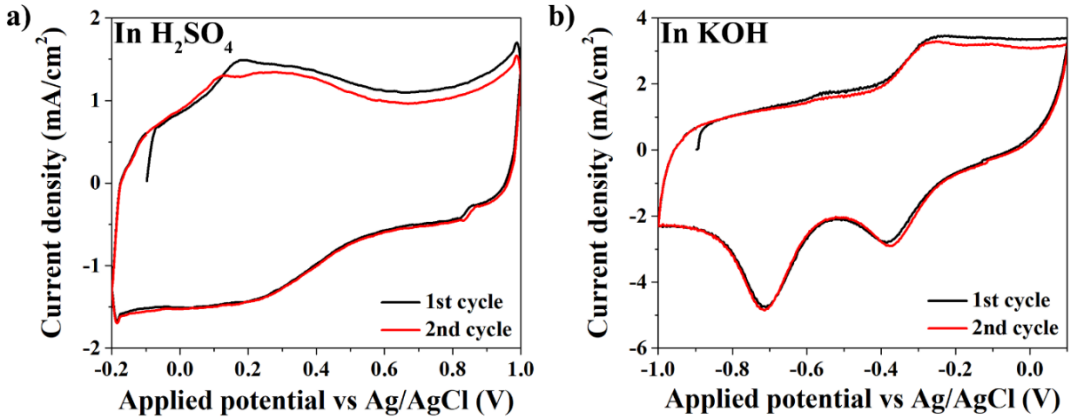


**Figure 4.53: CO stripping voltammetry of 20Cu-RGO in a) 0.1 M $H_2SO_4$ and b) 0.1 M KOH medium.**

The physical and chemical stability of 20Cu-RGO in acidic and basic media were analysed using FETEM images (Figure 4.54) and XPS profiles (Figure 4.55), obtained before and after EG oxidation. The FETEM images revealed a small increase in the average size of metal particles in both the media conditions, indicating that the metal tended to agglomerate slightly

after exposure to the oxidation process. The average metal size increased from 6.5 nm to 8.1 nm and 7.6 nm after EG oxidation in acidic and basic medium, respectively.

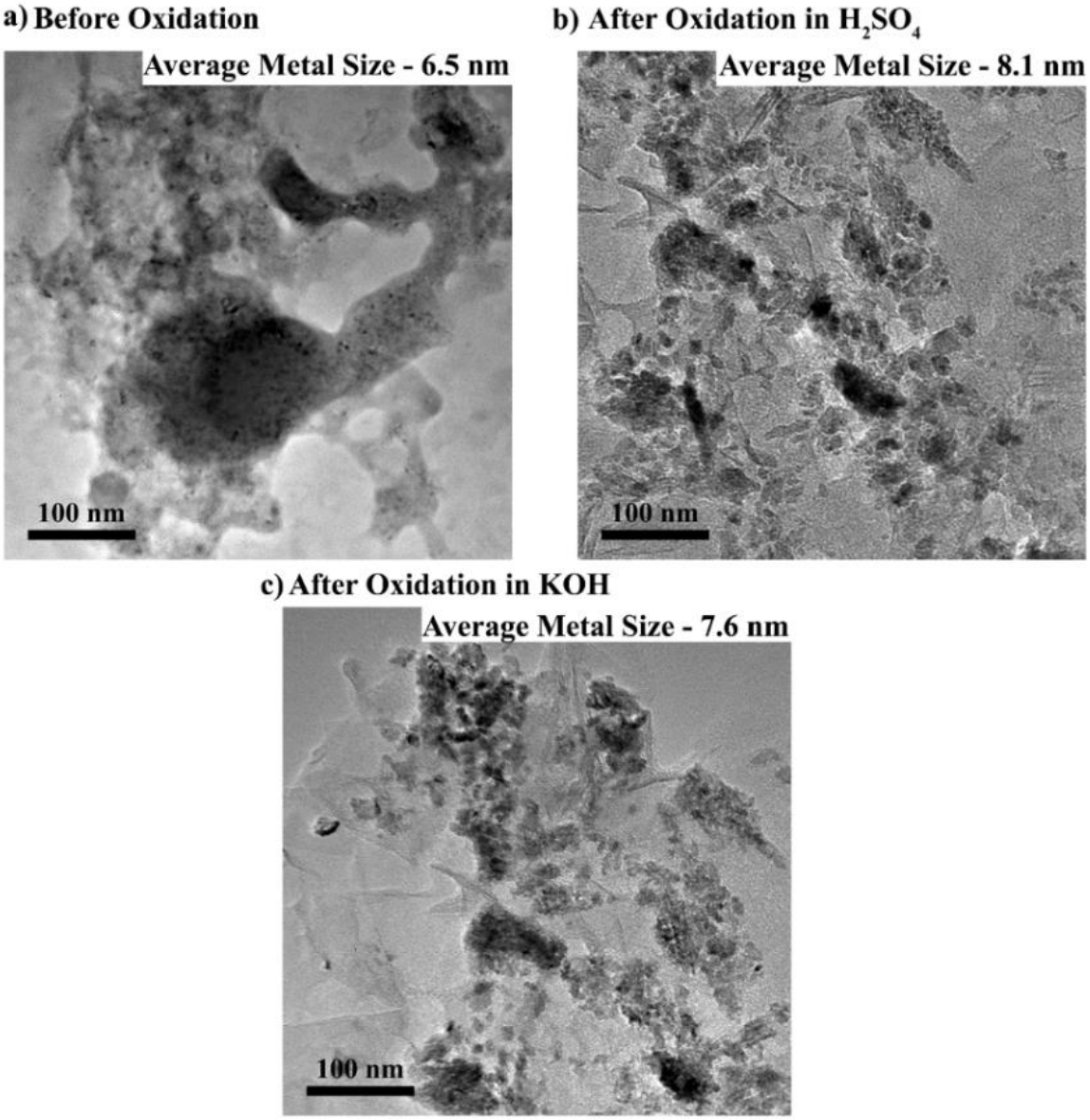


**Figure 4.54: FETEM images of 20Cu-RGO a) before oxidation, b) after EG oxidation in acidic medium and c) after EG oxidation in basic medium.**

The deconvoluted XPS spectra for Cu2p showed similar profiles before and after electro-oxidation of EG (Figure 4.55). The variation in the atomic weight percent of Cu was very small due to exposure to the oxidation process. The Cu content reduced from 1.39 wt.% for fresh catalyst to 1.34 and 1.37 wt.% after electro-oxidation of EG in acidic and basic media, respectively. The higher reduction in copper content in acidic medium might be due to the

leaching of copper into the electrolytic solution. These results suggested that 20Cu-RGO was both physically and chemically stable during EG oxidation.

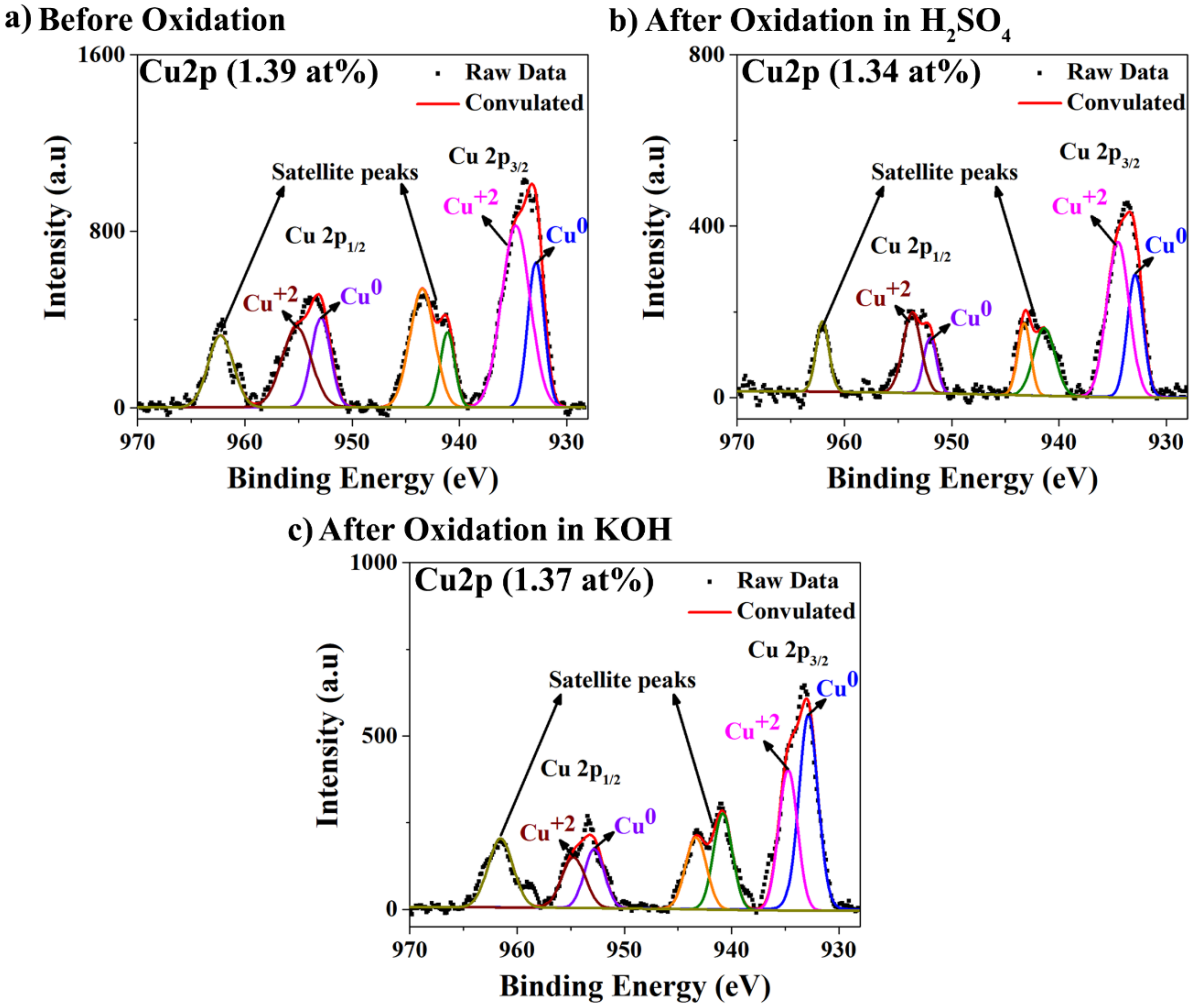


**Figure 4.55: $Cu_2p$ XPS spectra of 20Cu-RGO a) before oxidation, b) after EG oxidation in acidic medium and c) after EG oxidation in basic medium.**

The structural stability of 20Ni-AC was assessed using FETEM images with EDS mapping. The images of 20Ni-AC as anode electrode were collected and mapping was done both before and after the exposure to EG oxidation reaction in basic medium (Figure 4.56). The FETEM images and EDS mapping of the sample revealed that EG oxidation reaction had no significant effect on the structure or composition of 20Ni-AC. Slight metal agglomeration was observed, as indicated by an increase in the average metal size from 9.6 nm before oxidation to 10.2 nm after oxidation reaction. A slight aggregation of Ni was also observed in the mapping image for Ni.

Similarly, FETEM images of 30Ni-RGO were investigated before and after electro-oxidation of EG (Figure 4.57a and b). The average metal size increased to 8.5 nm from 8.1 nm after EG oxidation. The image of 30Ni-RGO after oxidation also showed some agglomeration.

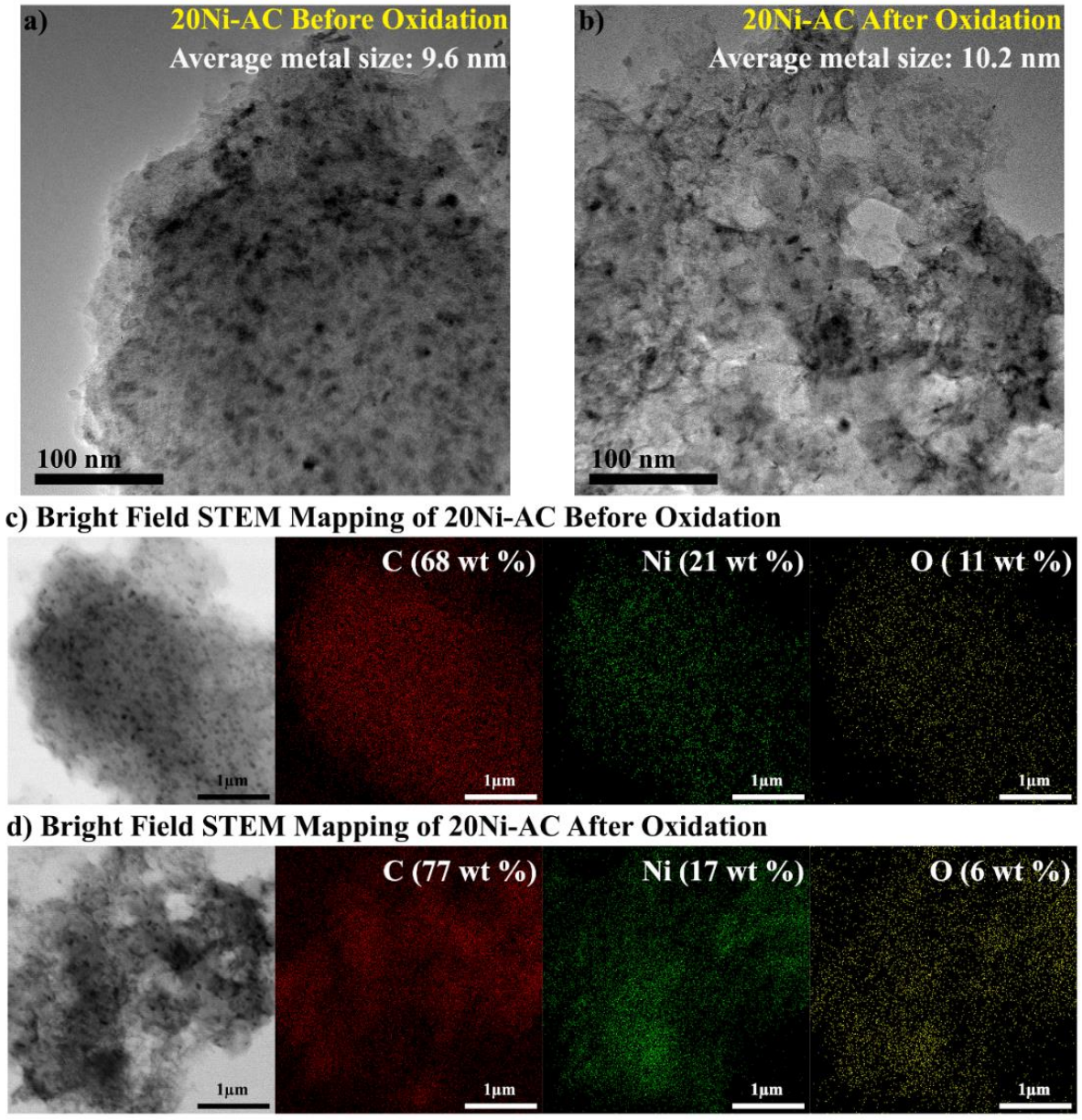


**Figure 4.56: FETEM images of 20Ni-AC a) before and b) after EG oxidation in basic medium. Bright Field STEM Mapping of 20Ni-AC c) before and d) after EG oxidation in basic medium.**

The stability of the bimetallic catalyst (NiCo-RGO) was investigated using FETEM analysis. The FETEM images of NiCo-RGO before and after electro-oxidation of EG is depicted in Figure 4.57c and d. The average metal size of the catalyst was determined to study the effect of EG reaction on the electrocatalyst. The average metal size shifted from 7.8 nm to 8.2 nm

after the electro-oxidation of EG. The FETEM images of NiCo-RGO revealed trace amounts of agglomeration upon EG oxidation. However, no other changes were observed in the bimetallic catalyst.

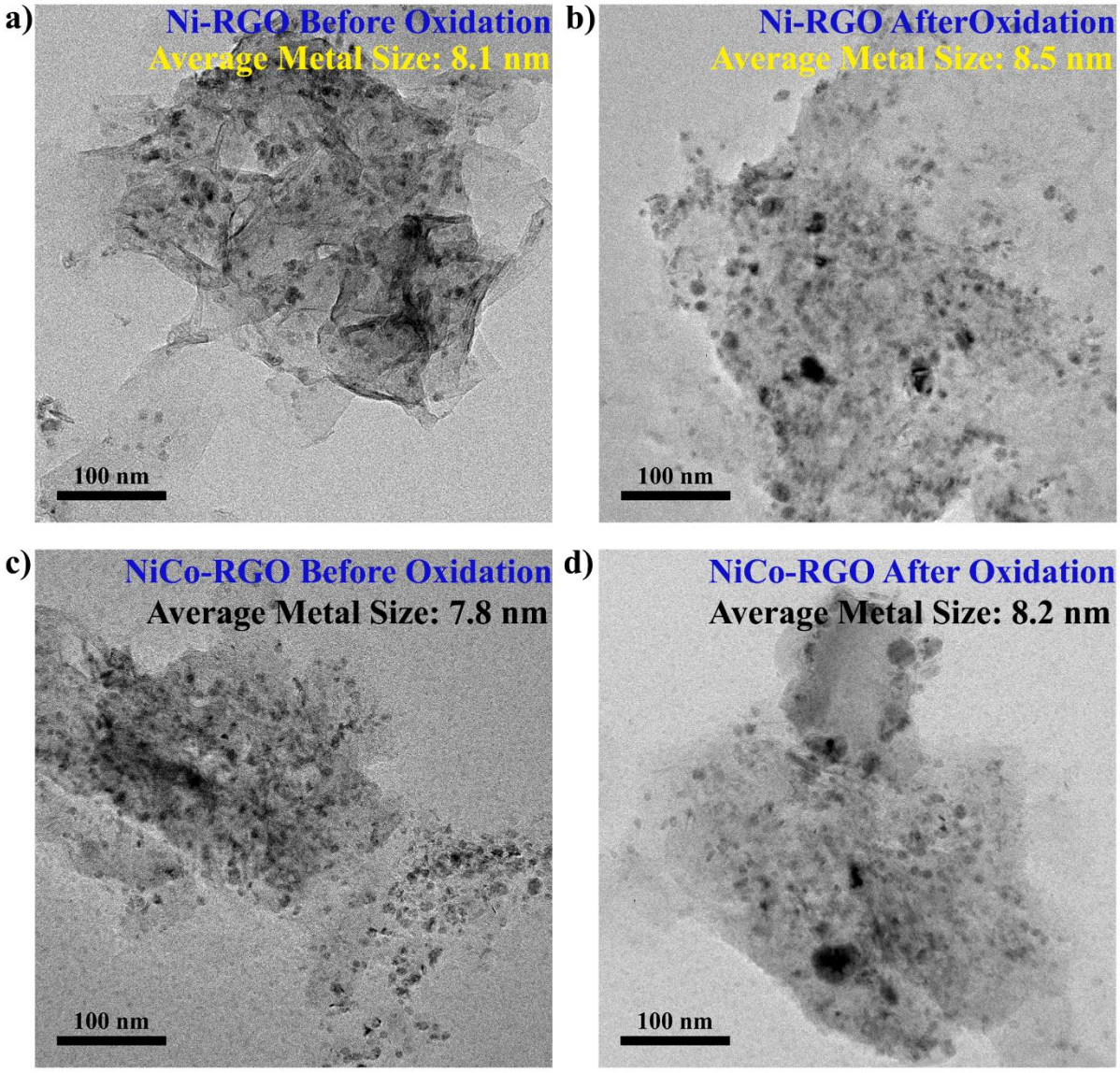


**Figure 4.57: FETEM images of 30Ni-RGO a) before and b) after EG oxidation in basic medium. FETEM images of NiCo-RGO c) before and d) after EG oxidation in basic medium.**

## 4.8 Fuel cell study

The single cell FC study was conducted with the best bimetallic catalyst (NiCo-RGO) at the optimal conditions obtained from the effect of process parameters. In order to gain insight about the real time system, the FC study was carried out for several polyhydric alcohols. The polarisation curve for different alcohols is shown in Figure 4.58a. Propane-1,2-diol had the highest open circuit potential (OCP) of 0.84 V, followed by ethylene glycol (0.80 V) and glycerol (0.75 V). However, ethylene glycol had the highest current density (40.72 mA/cm$^2$ at 0.16 V), followed by glycerol (30.62 mA/cm$^2$ at 0.2 V) and propane-1,2-diol (18.85 mA/cm$^2$ at 0.16 V). Figure 4.58b displays the power density curve of different polyhydric alcohols. The maximum power density was observed at different current densities and cell voltages for different alcohols. The highest power density for ethylene glycol was observed at 31.63 mA/cm$^2$ and 0.22 V, whereas the maximum power density for glycerol was obtained at 27.64 mA/cm$^2$ and 0.22 V. Further, propane-1,2-diol displayed the peak power density at 13.38 mA/cm$^2$ and 0.28 V. Ethylene glycol generated the highest power density (7.07 mW/cm$^2$), followed by glycerol (6.11 mW/cm$^2$) and propane-1,2-diol (3.71 mW/cm$^2$).

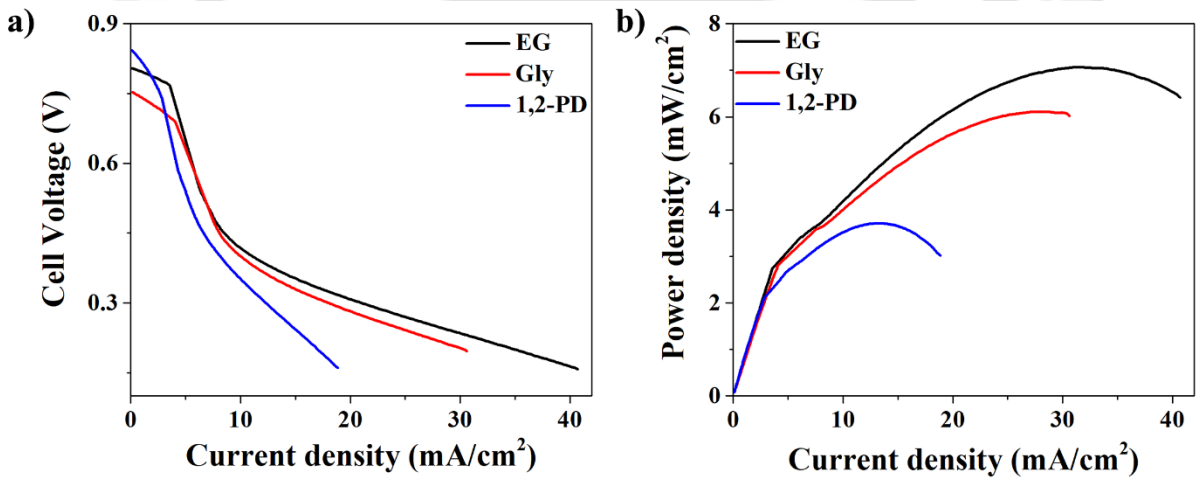


**Figure 4.58: a) Polarisation curve of NiCo-RGO for different polyhydric alcohol and b) power density curve of NiCo-RGO for different alcohol (EG = ethylene glycol, Gly = glycerol, 1,2-PD = propane-1,2-diol).**

# *Chapter 5 Conclusions and Future WorK*

# 5. Conclusion and Future Work

## 5.1 Conclusion

- The effect of various supports on electro-oxidation of ethylene glycol was investigated using copper as the active metal in acidic and basic media. In acidic medium, 20Cu-RGO generated a current density of 5.61 mA/cm$^2$, whereas 20Cu-VC produced 2.59 mA/cm$^2$. The order of current density in basic medium was 20Cu-ALS-TC (0.73 mA/cm$^2$) < 20Cu-AC (1.23 mA/cm$^2$) < 20Cu-VC (1.61 mA/cm$^2$) < 20Cu-RGO (2.78 mA/cm$^2$). The mass activity of 20Cu-RGO was 47.8 mA/mg$_{Cu}$ and 23.7 mA/mg$_{Cu}$ in acidic and basic medium, respectively. This study revealed that RGO provides the best support for electro-oxidation of ethylene glycol.
- Different transition metal-based catalysts (Cu, Ni, Co, or Fe) were evaluated with low-cost commercial activated carbon support. The supported metal catalysts performed exceedingly well as compared to the individual components in the electro-oxidation of ethylene glycol. The electrochemical activity was evaluated in both acidic and basic environments, with and without ethylene glycol. In acidic medium with ethylene glycol, 20Ni-AC generated the maximum current density (7.62 mA/cm$^2$ at 0.49 V), followed by 20Co-AC, 20Fe-AC and 20Cu-AC. On the other hand, in basic medium containing ethylene glycol, 20Ni-AC produced highest current density of 11 mA/cm$^2$ at 1 V, followed by 20Cu-AC (6.9 mA/cm$^2$), 20Co-AC (6.6 mA/cm$^2$) and 20Fe-AC (5.9 mA/cm$^2$). Ni was found to be the most active metal for ethylene glycol oxidation
- The performance of various transition metals (Cu, Ni, Fe and Co) for the electro-oxidation of ethylene glycol was then assessed on the most active support RGO. The cyclic voltammetry of RGO supported different metal catalysts in basic medium revealed that 20Ni-RGO exhibited the highest mass activity of 86 mA/mg$_m$., followed by 20Cu-RGO (61 mA/mg$_m$), 20Co-RGO (54 mA/mg$_m$) and 20Fe-RGO (39 mA/mg$_m$). So, Ni-RGO was came out to be the best performing catalysts for ethylene glycol oxidation
- Furthermore, the effect of metal loading was examined in order to determine the optimum loading for monometallic catalyst in the range of 20 to 40 wt. %. The current density of Ni-RGO varied with nickel loading. In the presence of ethylene glycol, the current density increased to 102 and 106 mA/mg$_m$ for nickel loadings of 30 and 40 wt. %, respectively. So, it was concluded that 30 wt. % was the most effective metal loading as there was minimal increment in mass activity on increasing nickel loading to 40 wt.%.

- The detailed electrochemical analysis found surface coverage of redox species, diffusion coefficient of ethylene glycol molecule and mean electrocatalytic rate constant for 30Ni-RGO was $2.7\times10^{-8}$ mol/cm$^2$, $2.35 \times 10^{-5}$ to $2.35 \times 10^{-8}$ cm$^2$/s and $1.48 \times 10^4$ cm$^3$/mol.s respectively. Further investigation explored that the electro-oxidation of EG over 30Ni-RGO followed the electrochemical-chemical mechanism controlled by diffusion and accordingly reaction mechanism for EG oxidation was proposed.
- Nickel was observed to be the most active metal with RGO as a support, hence Ni-based bimetallic catalysts were prepared with Co, Cu and Fe as co-metals. The metal loading was maintained at 30 wt. %, with Ni to co-metal ratio of 3:1. Cyclic voltammetry results showed that NiCo-RGO had the highest current density, followed by NiCu-RGO and NiFe-RGO. This observation was also supported by the surface area obtained for different catalysts. Thus, it could be concluded that NiCo-RGO was the best catalyst examined for the electro-oxidation of ethylene glycol.
- The detailed electrochemical analysis of NiCo-RGO revealed that surface coverage of redox species, diffusion coefficient of ethylene glycol molecule and mean electrocatalytic rate constant for NiCo-RGO was $1.5\times10^{-7}$ mol/cm$^2$, $9.53 \times 10^{-5}$ to $9.53 \times 10^{-8}$ cm$^2$/s and $1.71 \times 10^5$ cm$^3$/mol.s respectively. These parameters were significantly higher than that observed for Ni-RGO, explained the enhanced activity of NiCo-RGO.
- The effect of process parameters such as temperature, concentration of KOH and ethylene glycol was investigated using NiCo-RGO. It was observed that increasing KOH concentration and temperature boosted the current density of the electrochemical process. However, the same linearity was not observed upon changing the ethylene glycol concentration. The current density tends to decrease after 0.75 M EG. The results of cyclic voltammetry were validated by electrochemical impedance spectroscopy data. As a result, the most suitable conditions for electro-oxidation were determined to be 1 M KOH with 0.75 M EG at 75 °C in the studied range.
- Under the suitable conditions, the NiCo-RGO generated 198.7 mA/cm$^2$ current density at 0.78 V through electro-oxidation of ethylene glycol. Moreover, NiCo-RGO demonstrated significant activity for the electro-oxidation of glycerol as well as propane-1,2-diol, generating 290.1 mA/cm$^2$ and 169.9 mA/cm$^2$ current density respectively.
- The product analysis after ethylene glycol oxidation confirmed the presence of glycoldehyde, glycolic, glyoxylic and oxalic acids. Glycoldehyde selectivity was the

highest for all the bimetallic catalysts. However, the selectivity of other products varied depending on the co-metal used.

- The catalysts also had negligible CO poisoning effect, as evidenced by CO stripping voltammetry. The analysis of the electrodes before and after ethylene glycol oxidation revealed that the catalysts were both physically and chemically stable throughout the process. This study demonstrated the effectiveness of supported transition metal based catalysts for ethylene glycol inelectro-oxidation, which can be implemented to direct alcohol fuel cell using polyhydric alcohol as fuel.
- The single cell fuel cell study of NiCo-RGO gave an idea about the power generation of the best bimetallic catalyst. The study showed that highest power density was generated for ethylene glycol (7.07 $mW/cm^2$) followed by glycerol (6.11 $mW/cm^2$) and propane-1,2-diol (3.71 $mW/cm^2$). Hence, the catalyst could be employed for commercial fuel cell application with polyhydric alcohol as fuel.

## 5.2 Recommendation for future work.

The study revealed that nickel-based bimetallic catalyst was the most efficient catalyst for the electro-oxidation of alcohols. In continuation of this work, the following future work could be recommended.

- The optimisation of the bimetal ratio could be explored for more effective oxidation of alcohols.
- Other low-cost transition metals could also be investigated as co-metals with nickel for electro-oxidation of alcohol.
- The parametric study of single cell fuel cell using transition metal-based catalyst could be conducted for finding the optimized conditions to generate power.
- Multi stack fuel cell studies of direct alcohol fuel cells with transition metal-based catalyst could be conducted for commercial applications.

# *References*

Abbaci A, Bouremmad F, Bouznit Y (2022) New efficient and low cost electro catalyst for ethanol and ethylene glycol oxidation based on Mn(II)Co(II)-modified montmorillonite. *International Journal of Environmental Science and Technology* 19:10855-10868.

Ahmad MS, Cheng CK, Kumar R, Singh S, Saeed KA, Ong HR, Abdullah H, Khan MR (2020) Pd/CNT Catalysts for Glycerol Electro-oxidation: Effect of Pd Loading on Production of Valuable Chemical Products. *Electroanalysis* 32:1139-1147.

Ai Q, Yuan Z, Huang R, Yang C, Jiang G, Xiong J, Huang Z, Yuan S (2019) One-pot co-precipitation synthesis of Fe3O4 nanoparticles embedded in 3D carbonaceous matrix as anode for lithium ion batteries. *Journal of Materials Science* 54:4212-4224.

Akbarfallahi S, Hosseini SR, Ghasemi S (2020) Improved electrocatalytic activity of ethanol oxidation over Pd/TiO2 nanofibers-carbon black nanocomposite. *Materials Chemistry and Physics* 252:123317.

Al-Enizi AM, Ghanem MA, El-Zatahry AA, Al-Deyab SS (2014) Nickel oxide/nitrogen doped carbon nanofibers catalyst for methanol oxidation in alkaline media. *Electrochimica Acta* 137:774-780.

Alex C, Sarma SC, Peter SC, John NS (2020) Competing Effect of Co3+ Reducibility and Oxygen-Deficient Defects Toward High Oxygen Evolution Activity in Co3O4 Systems in Alkaline Medium. *ACS Applied Energy Materials* 3:5439-5447.

Almeida TS, Yu Y, de Andrade AR, Abruña HD (2019) Employing iron and nickel to enhance ethanol oxidation of Pd-based anodes in alkaline medium. *Electrochimica Acta* 295:751-758.

Amin RS, Abdel Hameed RM, El-Khatib KM, Elsayed Youssef M (2014) Electrocatalytic activity of nanostructured Ni and Pd–Ni on Vulcan XC-72R carbon black for methanol oxidation in alkaline medium. *International Journal of Hydrogen Energy* 39:2026-2041.

Anantharaj S, Sugime H, Noda S (2020) Ultrafast Growth of a Cu(OH)2–CuO Nanoneedle Array on Cu Foil for Methanol Oxidation Electrocatalysis. *ACS Applied Materials & Interfaces* 12:27327-27338.

Arjona N, Guerra-Balcázar M, Álvarez-Contreras L (2022) Hierarchical Pd and Pt structures obtained on 3D carbon electrodes as electrocatalysts for the ethylene glycol electro-oxidation. *Applied Surface Science* 571:151246.

Arunachalam P, Ghanem MA, Al-Mayouf AM, Al-shalwi M (2017) Enhanced electrocatalytic performance of mesoporous nickel-cobalt oxide electrode for methanol oxidation in alkaline solution. *Materials Letters* 196:365-368.

Ashok A, Kumar A (2021) Ag/Co3O4 as an effective catalyst for glycerol electro-oxidation in alkaline medium. *International Journal of Hydrogen Energy* 46:4788-4797.

Ashok A, Kumar A, Ponraj J, Mansour S, F T (2018) Single Step Synthesis of Porous NiCoO 2 for Effective Electrooxidation of Glycerol in Alkaline Medium. *Journal of The Electrochemical Society* 165:J3301-J3309.

Askari MB, Salarizadeh P, Seifi M, Rozati SM (2019) Ni/NiO coated on multi-walled carbon nanotubes as a promising electrode for methanol electro-oxidation reaction in direct methanol fuel cell. *Solid State Sciences* 97:106012.

Atar N, Eren T, Yola ML, Karimi-Maleh H, Demirdögen B (2015) Magnetic iron oxide and iron oxide@gold nanoparticle anchored nitrogen and sulfur-functionalized reduced graphene oxide electrocatalyst for methanol oxidation. *RSC Advances* 5:26402-26409.

Azizi SN, Ghasemi S, Chiani E (2013) Nickel/mesoporous silica (SBA-15) modified electrode: An effective porous material for electrooxidation of methanol. *Electrochimica Acta* 88:463-472.

Barakat NAM, Al-Mubaddel FS, Rezual Karim M, Alrashed M, Yong Kim H (2018) Influence of Sn content on the electrocatalytic activity of NiSn alloy nanoparticles-incorporated carbon

nanofibers toward methanol oxidation. *International Journal of Hydrogen Energy* 43:21333-21344.

Baronia R, Goel J, Tiwari S, Singh P, Singh D, Singh SP, Singhal SK (2017) Efficient electro-oxidation of methanol using PtCo nanocatalysts supported reduced graphene oxide matrix as anode for DMFC. *International Journal of Hydrogen Energy* 42:10238-10247.

Bauen A, Hart D, Chase A (2003) Fuel cells for distributed generation in developing countries—an analysis. *International Journal of Hydrogen Energy* 28:695-701.

Benipal N, Qi J, Liu Q, Li W (2017) Carbon nanotube supported PdAg nanoparticles for electrocatalytic oxidation of glycerol in anion exchange membrane fuel cells. *Applied Catalysis B: Environmental* 210:121-130.

Biesinger MC, Payne BP, Grosvenor AP, Lau LWM, Gerson AR, Smart RSC (2011) Resolving surface chemical states in XPS analysis of first row transition metals, oxides and hydroxides: Cr, Mn, Fe, Co and Ni. *Applied Surface Science* 257:2717-2730.

Boudghene Stambouli A, Traversa E (2002) Fuel cells, an alternative to standard sources of energy. *Renewable and Sustainable Energy Reviews* 6:295-304.

Busó-Rogero C, Herrero E, Feliu JM (2014) Ethanol Oxidation on Pt Single-Crystal Electrodes: Surface-Structure Effects in Alkaline Medium. *ChemPhysChem* 15:2019-2028.

Caglar B, Hassan Y, Basak O, Hepbasli A (2021) Electrooxidation of Glycerol on Monometallic and Bimetallic Catalysts-Containing Porous Carbon Cloth Electrodes in an Alkaline Medium. *Journal of The Electrochemical Society* 168:084506.

Caneppele GL, Almeida TS, Zanata CR, Teixeira-Neto É, Fernández PS, Camara GA, Martins CA (2017) Exponential improving in the activity of Pt/C nanoparticles towards glycerol electrooxidation by Sb ad-atoms deposition. *Applied Catalysis B: Environmental* 200:114-120.

CarAndBike Team An NDTV Ventrure. “Tata Motors Reveals India's First Hydrogen Fuel Cell Bus.” NDTV, 25th January 2017 https://www.carandbike.com/news/tata-motors-reveals-indias-first-hydrogen-fuel-cell-bus-1652559 (accessed 12.07.2024)

Carrión-Satorre S, Montiel M, Escudero-Cid R, Fierro JLG, Fatás E, Ocón P (2016) Performance of carbon-supported palladium and palladiumruthenium catalysts for alkaline membrane direct ethanol fuel cells. *International Journal of Hydrogen Energy* 41:8954-8962.

Chang G, Cai Z, Jia H, Zhang Z, Liu X, Liu Z, Zhu R, He Y (2018) High electrocatalytic performance of a graphene-supported PtAu nanoalloy for methanol oxidation. *International Journal of Hydrogen Energy* 43:12803-12810.

Chen C, Jin L, Shang H, Song T, Gao F, Zhang Y, Wang C, Wang C, Du Y (2019) Monodispersed bimetallic platinum-copper alloy nanospheres as efficient catalysts for ethylene glycol electrooxidation. *Journal of Colloid and Interface Science* 551:81-88.

Chen DP, Liu XC, Liu XD, Yuan L, Zhong ML, Wang CY (2021) Pd nanoparticles on self-doping-defects mesoporous carbon supports for highly active ethanol oxidation and ethylene glycol oxidation. *International Journal of Hydrogen Energy* 46:30455-30466.

Chen H, Xing Z, Zhu S, Zhang L, Chang Q, Huang J, Cai W-B, Kang N, Zhong C-J, Shao M (2016) Palladium modified gold nanoparticles as electrocatalysts for ethanol electrooxidation. *Journal of Power Sources* 321:264-269.

Chen S-S, Yang Z-Z, Wang A-J, Fang K-M, Feng J-J (2018) Facile synthesis of bimetallic gold-palladium nanocrystals as effective and durable advanced catalysts for improved electrocatalytic performances of ethylene glycol and glycerol oxidation. *Journal of Colloid and Interface Science* 509:10-17.

Chen W, Zhang Y, Wei X (2015) Catalytic performances of PdNi/MWCNT for electrooxidations of methanol and ethanol in alkaline media. *International Journal of Hydrogen Energy* 40:1154-1162.

Choudhary AK, Pramanik H (2020) Enhancement of ethanol electrooxidation in half cell and single direct ethanol fuel cell (DEFC) using post-treated polyol synthesized Pt-Ru nano electrocatalysts supported on HNO3-functionalized acetylene black carbon. *International Journal of Hydrogen Energy* 45:574-594.

Corchado-García J, Cabrera CR (2014) Ethylene Glycol Oxidation at Pt/TiO2/Carbon Hybrid Catalysts Modified Glassy Carbon Electrodes in Alkaline Media. *Electrocatalysis* 5:402-407.

Coutanceau C, Demarconnay L, Lamy C, Léger JM (2006) Development of electrocatalysts for solid alkaline fuel cell (SAFC). *Journal of Power Sources* 156:14-19.

Cowey K, Green KJ, Mepsted GO, Reeve R (2004) Portable and military fuel cells. *Current Opinion in Solid State and Materials Science* 8:367-371.

Crowe BJ, 1973. Fuel cells: a survey. NASA.

Cui X, Guo W, Zhou M, Yang Y, Li Y, Xiao P, Zhang Y, Zhang X (2015) Promoting Effect of Co in NimCon (m + n = 4) Bimetallic Electrocatalysts for Methanol Oxidation Reaction. *ACS Applied Materials & Interfaces* 7:493-503.

Cuña A, Reyes Plascencia C, da Silva EL, Marcuzzo J, Khan S, Tancredi N, Baldan MR, de Fraga Malfatti C (2017) Electrochemical and spectroelectrochemical analyses of hydrothermal carbon supported nickel electrocatalyst for ethanol electro-oxidation in alkaline medium. *Applied Catalysis B: Environmental* 202:95-103.

Dai Y, Ding J, Li J, Li Y, Zong Y, Zhang P, Wang Z, Liu X (2021) N, S and Transition-Metal Co-Doped Graphene Nanocomposites as High-Performance Catalyst for Glucose Oxidation in a Direct Glucose Alkaline Fuel Cell. *Nanomaterials (Basel)* 11:202.

Dalbay N, Kadirgan F (1990) The properties of palladium electrodes for electrooxidation of ethylene glycol. *Journal of Electroanalytical Chemistry and Interfacial Electrochemistry* 296:559-569.

Danaee I, Jafarian M, Forouzandeh F, Gobal F, Mahjani MG (2009) Electrochemical impedance studies of methanol oxidation on GC/Ni and GC/NiCu electrode. *International Journal of Hydrogen Energy* 34:859-869.

Dantas LMF, De Souza APR, Castro PS, Paixão TRLC, Bertotti M (2012) SECM Studies on the Electrocatalytic Oxidation of Glycerol at Copper Electrodes in Alkaline Medium. *Electroanalysis* 24:1778-1782.

Das S, Dutta K, Kundu PP (2016) Sulfonated polypyrrole matrix induced enhanced efficiency of Ni nanocatalyst for application as an anode material for DMFCs. *Materials Chemistry and Physics* 176:143-151.

Dash S, Munichandraiah N (2015) Nanoflowers of PdRu on PEDOT for Electrooxidation of Glycerol and Its Analysis. *Electrochimica Acta* 180:339-352.

Deng Z, Yi Q, Zhang Y, Nie H (2017) NiCo/C-N/CNT composite catalysts for electro-catalytic oxidation of methanol and ethanol. *Journal of Electroanalytical Chemistry* 803:95-103.

dos Santos JRN, Alves ICB, Marques ALB, Marques EP (2022) Ni–Ag Supported on Reduced Graphene Oxide as Efficient Electrocatalyst for Alcohol Oxidation Reactions. *Electrocatalysis* 13:713-730.

Du X, Cai W, Zhang Q, Yang L, He H (2021) Rhodium Nanoflowers on Three-Dimensional Graphitic Carbon Nitride Nanosheets/Graphene Hybrid Aerogels as Electrocatalysts for Methanol Oxidation. *ACS Applied Nano Materials* 4:9729-9737.

Duan Y, Yu Z-Y, Yang L, Zheng L-R, Zhang C-T, Yang X-T, Gao F-Y, Zhang X-L, Yu X, Liu R, Ding H-H, Gu C, Zheng X-S, Shi L, Jiang J, Zhu J-F, Gao M-R, Yu S-H (2020) Bimetallic nickel-

molybdenum/tungsten nanoalloys for high-efficiency hydrogen oxidation catalysis in alkaline electrolytes. *Nature Communications* 11:4789.

Dutta A, Datta J (2013) Significant role of surface activation on Pd enriched Pt nano catalysts in promoting the electrode kinetics of ethanol oxidation: Temperature effect, product analysis & theoretical computations. *International Journal of Hydrogen Energy* 38:7789-7800.

Dutta A, Mondal A, Broekmann P, Datta J (2017) Optimal level of Au nanoparticles on Pd nanostructures providing remarkable electro-catalysis in direct ethanol fuel cell. *Journal of Power Sources* 361:276-284.

Ebersbach U, Schwabe K, Ritter K (1967) On the kinetics of the anodic passivation of iron, cobalt and nickel. *Electrochimica Acta* 12:927-938.

El-Jemni MA, Abdel-Samad HS, AlKordi MH, Hassan HH (2022) Normalization of the EOR catalytic efficiency measurements based on RRDE study for simply fabricated cost-effective Co/graphite electrode for DAEFCs. *Journal of Electroanalytical Chemistry* 918:116488.

El-Nowihy GH, Mohammad AM, Khalil MMH, Sadek MA, El-Deab MS (2017) Promising ethylene glycol electro-oxidation at tailor-designed NiOx/Pt nanocatalyst. *International Journal of Hydrogen Energy* 42:5095-5104.

El Attar A, Oularbi L, Chemchoub S, El Rhazi M (2020) Preparation and characterization of copper oxide particles/polypyrrole (Cu2O/PPy) via electrochemical method: Application in direct ethanol fuel cell. *International Journal of Hydrogen Energy* 45:8887-8898.

Elgrishi N, Rountree KJ, McCarthy BD, Rountree ES, Eisenhart TT, Dempsey JL (2018) A Practical Beginner's Guide to Cyclic Voltammetry. *Journal of Chemical Education* 95:197-206.

Eshagh-Nimvari S, Karim Hassaninejad-Darzi S (2021) Synergistic effects of nanozeolite beta-MWCNTs on the electrocatalytic oxidation of ethylene glycol: Experimental design by response surface methodology. *Materials Science and Engineering: B* 268:115125.

Estudillo-Wong LA, Vargas-Gómez AM, Arce-Estrada EM, Manzo-Robledo A (2013) TiO2/C composite as a support for Pd-nanoparticles toward the electrocatalytic oxidation of methanol in alkaline media. *Electrochimica Acta* 112:164-170.

Fan D, Teng Y, Wang C, Xu D (2023) Facile synthesis of large-size Pd nanosheets-assembled nanofilms with enhanced electrocatalytic performance. *Materials Letters* 333:133686.

Farsadrooh M, Torrero J, Pascual L, Peña MA, Retuerto M, Rojas S (2018) Two-dimensional Pd-nanosheets as efficient electrocatalysts for ethanol electrooxidation. Evidences of the CC scission at low potentials. *Applied Catalysis B: Environmental* 237:866-875.

Fathirad F, Mostafavi A, Afzali D (2017) Bimetallic Pd–Mo nanoalloys supported on Vulcan XC-72R carbon as anode catalysts for direct alcohol fuel cell. *International Journal of Hydrogen Energy* 42:3215-3221.

Feng Y-Y, Song G-H, Zhang Q, Hu H-S, Feng M-Y, Wang J-Y, Kong D-S (2017) Catalytic performance of non-alloyed bimetallic PtAu electrocatalysts for methanol oxidation reaction. *International Journal of Hydrogen Energy* 42:30109-30118.

Fleischmann M, Korinek K, Pletcher D (1972) The kinetics and mechanism of the oxidation of amines and alcohols at oxide-covered nickel, silver, copper, and cobalt electrodes. *Journal of the Chemical Society, Perkin Transactions 2*:1396-1403.

Frota Jr. EF, Silva de Barros VV, de Araújo BRS, Gonzaga Purgatto Â, Linares JJ (2017) Pt/C containing different platinum loadings for use as electrocatalysts in alkaline PBI-based direct glycerol fuel cells. *International Journal of Hydrogen Energy* 42:23095-23106.

Gao F, Xu H, Zhang Y, Wang J, Wang C, Du Y (2018) Facile construction of pompon-like PtAg alloy catalysts for enhanced ethylene glycol electrooxidation. *International Journal of Hydrogen Energy* 43:9644-9651.

Gao F, Zhang Y, Zou B, Jiang F, Li Z, Du Y (2022) Facile synthesis of low-dimensional PdPt nanocrystals for high-performance electrooxidation of C 2 alcohols. *Journal of Colloid and Interface Science* 610:271-279.

García-Mateos FJ, Cordero-Lanzac T, Berenguer R, Morallón E, Cazorla-Amorós D, Rodríguez-Mirasol J, Cordero T (2017) Lignin-derived Pt supported carbon (submicron)fiber electrocatalysts for alcohol electro-oxidation. *Applied Catalysis B: Environmental* 211:18-30.

Gayathri A, Kiruthika S, Selvarani V, AlSalhi MS, Devanesan S, Kim W, Muthukumaran B (2022) Evaluation of iron-based alloy nanocatalysts for the electrooxidation of ethylene glycol in membraneless fuel cells. *Fuel* 321:124059.

Geraldes AN, Furtunato da Silva D, Martins da Silva JC, Antonio de Sá O, Spinacé EV, Neto AO, Coelho dos Santos M (2015) Palladium and palladium–tin supported on multi wall carbon nanotubes or carbon for alkaline direct ethanol fuel cell. *Journal of Power Sources* 275:189-199.

Ghouri ZK, Al-Meer S, Barakat NAM, Kim HY (2017) ZnO@C (core@shell) microspheres derived from spent coffee grounds as applicable non-precious electrode material for DMFCs. *Scientific Reports* 7:1738.

Ghouri ZK, Barakat NAM, Kim HY (2015) Influence of copper content on the electrocatalytic activity toward methanol oxidation of CoχCuy alloy nanoparticles-decorated CNFs. *Scientific Reports* 5:16695.

Ghouri ZK, Barakat NAM, Kim HY, Park M, Khalil KA, El-Newehy MH, Al-Deyab SS (2016) Nano-engineered ZnO/CeO2 dots@CNFs for fuel cell application. *Arabian Journal of Chemistry* 9:219-228.

Gong Y, Ma N, Yin Y, Xue J, Dong C, Guo P (2019) Synthesis of PdCu nanowire assembly and their catalytic activity toward ethanol oxidation. *Colloids and Surfaces A: Physicochemical and Engineering Aspects* 583:123909.

Gottesfeld S, Zawodzinski TA (1997) Polymer electrolyte fuel cells. 5:195-301.

Goyal A, Bondue CJ, Graf M, Koper MTM (2022) Effect of pore diameter and length on electrochemical CO2 reduction reaction at nanoporous gold catalysts. *Chemical Science* 13:3288-3298.

Grishina EP, Udalova AM, Rumyantsev EM (2002) Anodic Oxidation of Copper in Concentrated Sulfuric Acid Solutions. *Russian Journal of Electrochemistry* 38:1041-1045.

Guo X, Liang T, Zhang D, Zhang M, Lin Y, Lai C (2019a) Facile fabrication of 3D porous nickel networks for electro-oxidation of methanol and ethanol in alkaline medium. *Materials Chemistry and Physics* 221:390-396.

Guo X, Shang H, Guo J, Xu H, Du Y (2019b) Ultrafine two-dimensional alloyed PdCu nanosheets-constructed three-dimensional nanoflowers enable efficient ethylene glycol electrooxidation. *Applied Surface Science* 481:1532-1537.

Guo Y, Sun X, Liu Y, Wang W, Qiu H, Gao J (2012) One pot preparation of reduced graphene oxide (RGO) or Au (Ag) nanoparticle-RGO hybrids using chitosan as a reducing and stabilizing agent and their use in methanol electrooxidation. *Carbon* 50:2513-2523.

Habekost A (2016) Experimental Investigations of Alkaline Silver-zinc and Copper-zinc Batteries. *World Journal of Chemical Education* 4:4-12.

Habibi E (2017) Kinetics of ethylene glycol electrooxidation on the noble metal-based nano-catalysts. *Journal of the Iranian Chemical Society* 14:1983-1991.

Hameed RMA (2019) Nickel Oxide Nanoparticles Supported on Graphitized Carbon for Ethanol Oxidation in NaOH Solution. *Journal of Cluster Science* 30:1003-1016.

Hameed RMA, Abutaleb A, Zouli N, Yousef A (2022) Facile synthesis of electrospun transition metallic nanofibrous mats with outstanding activity for ethylene glycol electro-oxidation in alkaline solution. *Molecular Catalysis* 522:112186.

Hameed RMA, El-Sherif RM (2015) Microwave irradiated nickel nanoparticles on Vulcan XC-72R carbon black for methanol oxidation reaction in KOH solution. *Applied Catalysis B: Environmental* 162:217-226.

Hameed RMA, Fetohi AE, El-Khatib KM, Amin RS (2019) Preparation, characterization and electrocatalytic activity of transition metal @ platinum on carbon support for alkaline ethanol electro-oxidation. *Journal of Porous Materials* 26:971-986.

Han X, Sheng H, Yu C, Walker TW, Huber GW, Qiu J, Jin S (2020) Electrocatalytic Oxidation of Glycerol to Formic Acid by CuCo2O4 Spinel Oxide Nanostructure Catalysts. *ACS Catalysis* 10:6741-6752.

Hassanzadeh V, Sheikh-Mohseni MA, Habibi B (2019) Catalytic oxidation of ethanol by a nanostructured Ni-Co/RGO composite: Electrochemical construction and investigation. *Journal of Electroanalytical Chemistry* 847:113200.

Hassen D, El-Safty SA, Tsuchiya K, Chatterjee A, Elmarakbi A, Shenashen MA, Sakai M (2016) Longitudinal Hierarchy Co3O4 Mesocrystals with High-dense Exposure Facets and Anisotropic Interfaces for Direct-Ethanol Fuel Cells. *Scientific Reports* 6:24330.

He Q, Ji J, Zhang Q, Yang X, Lin Y, Meng Q, Zhang Y, Xu M (2020) PdMn and PdFe nanoparticles over a reduced graphene oxide carrier for methanol electro-oxidation under alkaline conditions. *Ionics* 26:2421-2433.

Hefnawy MA, Fadlallah SA, El-Sherif RM, Medany SS (2021) Nickel-manganese double hydroxide mixed with reduced graphene oxide electrocatalyst for efficient ethylene glycol electrooxidation and hydrogen evolution reaction. *Synthetic Metals* 282:116959.

Hernandez-Fernandez P, Lund PB, Kallesøe C, Clausen HF, Christensen LH (2015) Supported Pt-based nanoparticulate catalysts for the electro-oxidation of methanol: An experimental protocol for quantifying its activity. *International Journal of Hydrogen Energy* 40:284-291.

Hosseini SR, Ghasemi S, Kamali-Rousta M, Nabavi SR (2017) Preparation of NiO nanofibers by electrospinning and their application for electro-catalytic oxidation of ethylene glycol. *International Journal of Hydrogen Energy* 42:906-913.

Hosseini SR, Raoof J-B, Ghasemi S, Gholami Z (2015) Synthesis of Pt–Cu/poly (o-Anisidine) nanocomposite onto carbon paste electrode and its application for methanol oxidation. *International Journal of Hydrogen Energy* 40:292-302.

Houache MSE, Cossar E, Ntais S, Baranova EA (2018) Electrochemical modification of nickel surfaces for efficient glycerol electrooxidation. *Journal of Power Sources* 375:310-319.

Houache MSE, Hughes K, Safari R, Botton GA, Baranova EA (2020) Modification of Nickel Surfaces by Bismuth: Effect on Electrochemical Activity and Selectivity toward Glycerol. *ACS Applied Materials & Interfaces* 12:15095-15107.

Houache MSE, Sandoval MG, Safari R, Gaztañaga F, Escudero F, Hernández-Laguna A, Sainz-Díaz CI, Botton GA, Jasen PV, González EA, Juan A, Baranova EA (2021) Morphology alteration of nickel microstructures for glycerol electrooxidation. *Journal of Catalysis* 404:348-361.

Hu C, Zhou Y, Xiao M, Yu G (2020) Precise size and dominant-facet control of ultra-small Pt nanoparticles for efficient ethylene glycol, methanol and ethanol oxidation electrocatalysts. *International Journal of Hydrogen Energy* 45:4341-4354.

Hu G, Nitze F, Sharifi T, Barzegar HR, Wågberg T (2012) Self-assembled palladium nanocrystals on helical carbon nanofibers as enhanced electrocatalysts for electro-oxidation of small molecules. *Journal of Materials Chemistry* 22:8541-8548.

Hu T, Wang Y, Xiao H, Chen W, Zhao M, Jia J (2018) Shape-control of super-branched Pd–Cu alloys with enhanced electrocatalytic performance for ethylene glycol oxidation. *Chemical Communications* 54:13363-13366.

*Hydrogen Energy and Fuel Cells In India – A Way Forward*. Steering Committee on Hydrogen Energy and Fuel Cells, Ministry of New and Renewable Energy, Government of India, 2016.

Iida H, Igarashi A (2006) Characterization of a Pt/TiO2 (rutile) catalyst for water gas shift reaction at low-temperature. *Applied Catalysis A: General* 298:152-160.

Ji J, Dong P, Lin Y, Zeng X, Li X, Yang X, He Q, Zhang Y, Xu M (2018) One-pot synthesis of PdM/RGO (M=Co, Ni, or Cu) catalysts under the existence of PEG for electro-oxidation of methanol. *Journal of Nanoparticle Research* 20:192.

Jia J, Zhao L, Chang Y, Jia M, Wen Z (2020) Understanding the growth of NiSe nanoparticles on reduced graphene oxide as efficient electrocatalysts for methanol oxidation reaction. *Ceramics International* 46:10023-10028.

Jin C, Zhu J, Dong R, Chen Z, Huo Q (2016) Modification of Ag nanoparticles/reduced graphene oxide nanocomposites with a small amount of Au for glycerol oxidation. *International Journal of Hydrogen Energy* 41:16851-16857.

Ju K-J, Liu L, Feng J-J, Zhang Q-L, Wei J, Wang A-J (2016) Bio-directed one-pot synthesis of Pt-Pd alloyed nanoflowers supported on reduced graphene oxide with enhanced catalytic activity for ethylene glycol oxidation. *Electrochimica Acta* 188:696-703.

Kakaei K, Marzang K (2016) One – Step synthesis of nitrogen doped reduced graphene oxide with NiCo nanoparticles for ethanol oxidation in alkaline media. *Journal of Colloid and Interface Science* 462:148-153.

Kamarudin MZF, Kamarudin SK, Masdar MS, Daud WRW (2013) Review: Direct ethanol fuel cells. *International Journal of Hydrogen Energy* 38:9438-9453.

Karuppasamy L, Chen CY, Anandan S, Wu JJ (2017) High index surfaces of Au-nanocrystals supported on one-dimensional MoO3-nanorod as a bi-functional electrocatalyst for ethanol oxidation and oxygen reduction. *Electrochimica Acta* 246:75-88.

Karuppasamy L, Lee G-J, Anandan S, Wu JJ (2020) Synthesis of shape-controlled Pd nanocrystals on carbon nanospheres and electrocatalytic oxidation performance for ethanol and ethylene glycol. *Applied Surface Science* 519:146266.

Kasturi PR, Harivignesh R, Lee YS, Kalai Selvan R (2020) Polyol assisted formaldehyde reduction of bi-metallic Pt-Pd supported agro-waste derived carbon spheres as an efficient electrocatalyst for formic acid and ethylene glycol oxidation. *Journal of Colloid and Interface Science* 561:358-371.

Kautek W, Gordon JG (1990) XPS Studies of Anodic Surface Films on Copper Electrodes. *Journal of The Electrochemical Society* 137:2672.

Kazan ES, Bayramoğlu M (2021) Molybdenum compound cocatalyzed Ni-based anode electrocatalysts for EOR in alkaline media. *International Journal of Energy Research* 45:12806-12824.

Khalafallah D, Alothman OY, Fouad H, Abdelrazek Khalil K (2018) Hierarchical Co3O4 decorated PPy nanocasting core-shell nanospheres as a high performance electrocatalysts for methanol oxidation. *International Journal of Hydrogen Energy* 43:2742-2753.

Kianfar S, Golikand AN, ZareNezhad B (2021) Bimetallic-metal oxide nanoparticles of Pt-M (M: W, Mo, and V) supported on reduced graphene oxide (rGO): radiolytic synthesis and methanol oxidation electrocatalysis. *Journal of Nanostructure in Chemistry* 11:287-299.

Kien NT, Hashisake K, Chiku M, Higuchi E, Inoue H (2022) Activity and durability of intermetallic PdZn electrocatalyst for ethanol oxidation reaction. *Research on Chemical Intermediates* 48:3795-3810.

Kim J-W, Park S-M (2005) Electrochemical Oxidation of Ethanol at Nickel Hydroxide Electrodes in Alkaline Media Studied by Electrochemical Impedance Spectroscopy. *Journal of The Korean Chemical Society* 8:117-124.

Kordesch K, Simader G (1996) Fuel cells and their applications.

Kottayintavida R, Gopalan NK (2021) PdAu alloy nano wires for the elevated alcohol electro-oxidation reaction. *Electrochimica Acta* 384:138405.

Krittayavathananon A, Sawangphruk M (2016) Electrocatalytic oxidation of ethylene glycol on palladium coated on 3D reduced graphene oxide aerogel paper in alkali media: Effects of carbon supports and hydrodynamic diffusion. *Electrochimica Acta* 212:237-246.

Kumar A, Jena HM, (2015) High surface area microporous activated carbons prepared from Fox nut (Euryale ferox) shell by zinc chloride activation. *Applied Surface Science* 356:753-761.

Kumar VS, Kummari S, Yugender Goud K, Satyanarayana M, Vengatajalabathy Gobi K (2020) One-pot synthesis of Pd20-xAux nanoparticles embedded in nitrogen doped graphene as high-performance electrocatalyst toward methanol oxidation. *International Journal of Hydrogen Energy* 45:1018-1029.

Lam BTX, Chiku M, Higuchi E, Inoue H (2015) Preparation of PdAg and PdAu nanoparticle-loaded carbon black catalysts and their electrocatalytic activity for the glycerol oxidation reaction in alkaline medium. *Journal of Power Sources* 297:149-157.

Larminie J, Dicks A, McDonald MS (2003). Fuel cell systems explained. J. Wiley Chichester, UK.

Leckie HP (1970) The Anodic Polarization Behavior of Copper. *Journal of The Electrochemical Society* 117:1478.

Lee D, Kim Y, Kwon Y, Lee J, Kim T-W, Noh Y, Kim WB, Seo MH, Kim K, Kim HJ (2019) Boosting the electrocatalytic glycerol oxidation performance with highly-dispersed Pt nanoclusters loaded on 3D graphene-like microporous carbon. *Applied Catalysis B: Environmental* 245:555-568.

Li M, Zheng H, Han G, Xiao Y, Li Y (2017a) Facile synthesis of binary PtRu nanoflowers for advanced electrocatalysts toward methanol oxidation. *Catalysis Communications* 92:95-99.

Li N, Xia W-Y, Xu C-W, Chen S (2017b) Pt/C and Pd/C catalysts promoted by Au for glycerol and CO electrooxidation in alkaline medium. *Journal of the Energy Institute* 90:725-733.

Li S-S, Hu Y-Y, Feng J-J, Lv Z-Y, Chen J-R, Wang A-J (2014) Rapid room-temperature synthesis of Pd nanodendrites on reduced graphene oxide for catalytic oxidation of ethylene glycol and glycerol. *International Journal of Hydrogen Energy* 39:3730-3738.

Li X-r, Jiang Y-h, Wang P-z, Mo Y, Lai W-d, Li Z-j, Yu R-j, Du Y-t, Zhang X-r, Chen Y (2020) Effect of the oxygen functional groups of activated carbon on its electrochemical performance for supercapacitors. *New Carbon Materials* 35:232-243.

Li X, Ning S, Liu X, Shangguan E, Wu C, Li J, Wang Z, Li Q (2019a) Insights into the electrode reaction process of nickel nanoparticles @reduced graphene oxide catalyst for ethanol oxidation in alkaline solution. *Ionics* 25:3775-3786.

Li X, Tian H, Yan S, Shi H, Wu J, Sun Y, Xing Y, Bai H, Zhang H, (2024) Micropores enriched ultra-high specific surface area activated carbon derived from waste peanut shells boosting performance of hydrogen storage. *International Journal of Hydrogen Energy* 50:324-336.

Li Y, Gao W, Ci L, Wang C, Ajayan PM (2010) Catalytic performance of Pt nanoparticles on reduced graphene oxide for methanol electro-oxidation. *Carbon* 48:1124-1130.

Li Y, Han L, An B, Wang Y, Wang L, Yin X, Lu J (2016) Preparation of platinum catalysts supported on functionalized graphene and the electrocatalytic properties for ethanol oxidation in direct ethanol fuel cell. *Journal of Materials Science: Materials in Electronics* 27:6208-6215.

Li Z, Zhao X, Zhang Y, Wu J (2019b) One-pot construction of N-doped graphene supported 3D PdAg nanoflower as efficient catalysts for ethylene glycol electrooxidation. *Colloids and Surfaces A: Physicochemical and Engineering Aspects* 562:409-415.

Liming H (2009) Financing rural renewable energy: A comparison between China and India. *Renewable and Sustainable Energy Reviews* 13:1096-1103.

Lin J-L, Ren J, Tian N, Zhou Z-Y, Sun S-G (2013) In situ FTIR spectroscopic studies of ethylene glycol electrooxidation on Pd electrode in alkaline solution: The effects of concentration. *Journal of Electroanalytical Chemistry* 688:165-171.

Lin Q, Wei Y, Liu W, Yu Y, Hu J (2017) Electrocatalytic oxidation of ethylene glycol and glycerol on nickel ion implanted-modified indium tin oxide electrode. *International Journal of Hydrogen Energy* 42:1403-1411.

Liu B, Wu C, Wen C, Li H, Shimura Y, Tatsuoka H, Sa B (2022) Promoting effect of (Co, Ni)O solid solution on Pd catalysts for ethylene glycol electrooxidation in alkaline solution. *Electrochimica Acta* 408:139965.

Liu C, Hirohara M, Maekawa T, Chang R, Hayashi T, Chiang C-Y (2020) Selective electro-oxidation of glycerol to dihydroxyacetone by a non-precious electrocatalyst – CuO. *Applied Catalysis B: Environmental* 265:118543.

Liu Q, Xu Y-R, Wang A-J, Feng J-J (2016a) Simple wet-chemical synthesis of core–shell Au–Pd@Pd nanocrystals and their improved electrocatalytic activity for ethylene glycol oxidation reaction. *International Journal of Hydrogen Energy* 41:2547-2553.

Liu S, Tian N, Xie A-Y, Du J-H, Xiao J, Liu L, Sun H-Y, Cheng Z-Y, Zhou Z-Y, Sun S-G (2016b) Electrochemically Seed-Mediated Synthesis of Sub-10 nm Tetrahexahedral Pt Nanocrystals Supported on Graphene with Improved Catalytic Performance. *Journal of the American Chemical Society* 138:5753-5756.

Liu W, Qin X, Zhang X, Shao Z, Yi B (2017) Wormholelike mesoporous carbon supported PtRu catalysts toward methanol electrooxidation. *Journal of Energy Chemistry* 26:200-206.

López-Coronel A, Torres-Pacheco LJ, Bañuelos JA, Álvarez-López A, Guerra-Balcázar M, Álvarez-Contreras L, Arjona N (2020) Highly active PdNi bimetallic nanocubes electrocatalysts for the ethylene glycol electro-oxidation in alkaline medium. *Applied Surface Science* 530:147210.

López–Coronel A, Ortiz–Ortega E, Torres–Pacheco LJ, Guerra–Balcázar M, Arriaga LG, Álvarez–Contreras L, Arjona N (2019) High performance of Pd and PdAg with well–defined facets in direct ethylene glycol microfluidic fuel cells. *Electrochimica Acta* 320:134622.

Łuczak T, Bułat K (2016) Gold Surface Functionalization with S-containing Organic Compounds and Gold Nanoparticles for Ethylene Glycol Electrooxidation. *Electroanalysis* 28:711-717.

Luo H, Yukuhiro VY, Fernández PS, Feng J, Thompson P, Rao RR, Cai R, Favero S, Haigh SJ, Durrant JR, Stephens IEL, Titirici M-M (2022) Role of Ni in PtNi Bimetallic Electrocatalysts for Hydrogen and Value-Added Chemicals Coproduction via Glycerol Electrooxidation. *ACS Catalysis* 12:14492-14506.

Ma J, Wang X, Chu Z, Zhang J, Du P, Zhang Q, Cao F, Liu J (2021) Electrocatalytic Oxidation of Methanol over An Electrode with Ni-MOF-74 Catalyst. *ChemCatChem* 13:4824-4832.

Maksic A, Rakocevic Z, Smiljanic M, Nenadovic M, Strbac S (2015) Methanol oxidation on Pd/Pt(poly) in alkaline solution. *Journal of Power Sources* 273:724-734.

Mari E, Tsai P-C, Eswaran M, Ponnusamy VK (2020) Efficient electro-catalytic oxidation of ethylene glycol using flower-like graphitic carbon nitride/iron oxide/palladium nanocomposite for fuel cell application. *Fuel* 280:118646.

Marioli JM, Kuwana T (1992) Electrochemical characterization of carbohydrate oxidation at copper electrodes. *Electrochimica Acta* 37:1187-1197.

Martín-Yerga D, Henriksson G, Cornell A (2019) Effects of Incorporated Iron or Cobalt on the Ethanol Oxidation Activity of Nickel (Oxy)Hydroxides in Alkaline Media. *Electrocatalysis* 10:489-498.

McCrory CCL, Jung S, Peters JC, Jaramillo TF (2013) Benchmarking Heterogeneous Electrocatalysts for the Oxygen Evolution Reaction. *Journal of the American Chemical Society* 135:16977-16987.

Mehek R, Iqbal N, Noor T, Nasir H, Mehmood Y, Ahmed S (2017) Novel Co-MOF/Graphene Oxide Electrocatalyst for Methanol Oxidation. *Electrochimica Acta* 255:195-204.

Mekhilef S, Saidur R, Safari A (2012) Comparative study of different fuel cell technologies. *Renewable and Sustainable Energy Reviews* 16:981-989.

Miao Z, Xu C, Zhan J, Xu Z (2021) Morphology-control and template-free fabrication of bimetallic Cu–Ni alloy rods for ethanol electro-oxidation in alkaline media. *Journal of Alloys and Compounds* 855:157438.

Mills P, Sullivan JL (1983) A study of the core level electrons in iron and its three oxides by means of X-ray photoelectron spectroscopy. *Journal of Physics D: Applied Physics* 16:723.

Mohanapriya S, Gopi D (2022) Microwave assisted synthesis of core-shell Ni-Co/graphene nano sheets and their catalytic activity for methanol electro-oxidation. *Materials Today: Proceedings* 51:1797-1801.

Moreira AH, Benedetti AV, Cabot PL, Sumodjo PTA (1993) Electrochemical behaviour of copper electrode in concentrated sulfuric acid solutions. *Electrochimica Acta* 38:981-987.

Mukherjee A, Su W-N, Pan C-J, Basu S (2021) One pot synthesis of Pd@CuO core-shell nanoparticles for electro catalytic oxidation of ethylene glycol for alkaline direct fuel cell. *Journal of Electroanalytical Chemistry* 882:115006.

Nacef M, Chelaghmia ML, Khelifi O, Pontié M, Djelaibia M, Guerfa R, Bertagna V, Vautrin-Ul C, Fares A, Affoune AM (2021) Electrodeposited Ni on pencil graphite electrode for glycerol electrooxidation in alkaline media. *International Journal of Hydrogen Energy* 46:37670-37678.

Nakayama M, Suzuki K, Fujii K (2019) Single-ion catalyst of Ni2+ anchored in the interlayer space of layered MnO2 for electro-oxidation of ethanol in alkaline electrolyte. *Electrochemistry Communications* 105:106492.

Nguyen MTX, Nguyen M-K, Pham PTT, Huynh HKP, Pham HH, Vo CC, Nguyen ST (2021) High-performance Pd-coated Ni nanowire electrocatalysts for alkaline direct ethanol fuel cells. *Journal of Electroanalytical Chemistry* 888:115180.

Nie Y, Qi X, Wu R, Yang R, Wang H, Deng M, Zhang S, Lu S, Gu Z, Liu X (2021) Structurally ordered PtFe intermetallic nanocatalysts toward efficient electrocatalysis of methanol oxidation. *Applied Surface Science* 569:151004.

Noor T, Zaman N, Nasir H, Iqbal N, Hussain Z (2019) Electro catalytic study of NiO-MOF/rGO composites for methanol oxidation reaction. *Electrochimica Acta* 307:1-12.

Obradović MD, Stančić ZM, Lačnjevac UČ, Radmilović VV, Gavrilović-Wohlmuther A, Radmilović VR, Gojković SL (2016) Electrochemical oxidation of ethanol on palladium-nickel nanocatalyst in alkaline media. *Applied Catalysis B: Environmental* 189:110-118.

Oh LS, Park M, Park YS, Kim Y, Yoon W, Hwang J, Lim E, Park JH, Choi SM, Seo MH, Kim WB, Kim HJ (2023) How to Change the Reaction Chemistry on Nonprecious Metal Oxide

Nanostructure Materials for Electrocatalytic Oxidation of Biomass-Derived Glycerol to Renewable Chemicals. *Advanced Materials* 35:2203285.

Ojani R, Raoof J-B, Fathi S (2009) Poly(o-aminophenol) film prepared in the presence of sodium dodecyl sulfate: Application for nickel ion dispersion and the electrocatalytic oxidation of methanol and ethylene glycol. *Electrochimica Acta* 54:2190-2196.

Ojani R, Raoof J-B, Goli M, Alinezhad A (2013) High electrocatalysis of ethylene glycol oxidation based on nickel particles electrodeposited into poly (m-toluidine)/Triton X-100 composite. *Journal of Applied Electrochemistry* 43:927-937.

Ojani R, Raoof J-B, Rahemi V (2011) Evaluation of sodium dodecyl sulfate effect on electrocatalytic properties of poly (4-aminoacetanilide)/nickel modified carbon paste electrode as an efficient electrode toward oxidation of ethylene glycol. *International Journal of Hydrogen Energy* 36:13288-13294.

Oliveira VL, Morais C, Servat K, Napporn TW, Tremiliosi-Filho G, Kokoh KB (2013) Glycerol oxidation on nickel based nanocatalysts in alkaline medium – Identification of the reaction products. *Journal of Electroanalytical Chemistry* 703:56-62.

Oliveira VL, Morais C, Servat K, Napporn TW, Tremiliosi-Filho G, Kokoh KB (2014) Studies of the reaction products resulted from glycerol electrooxidation on Ni-based materials in alkaline medium. *Electrochimica Acta* 117:255-262.

Ormerod RM (2003) Solid oxide fuel cells. *Chemical Society Reviews* 32:17-28.

Patel MA, Luo F, Khoshi MR, Rabie E, Zhang Q, Flach CR, Mendelsohn R, Garfunkel E, Szostak M, He H (2016) P-Doped Porous Carbon as Metal Free Catalysts for Selective Aerobic Oxidation with an Unexpected Mechanism. *ACS Nano* 10:2305-2315.

Patil AS, Dubois TG, Sifer N, Bostic E, Gardner K, Quah M, Bolton C (2004) Portable fuel cell systems for America's army: technology transition to the field. *Journal of Power Sources* 136:220-225.

Pattanayak P, Pramanik N, Kumar P, Kundu PP (2018) Fabrication of cost-effective non-noble metal supported on conducting polymer composite such as copper/polypyrrole graphene oxide (Cu2O/PPy–GO) as an anode catalyst for methanol oxidation in DMFC. *International Journal of Hydrogen Energy* 43:11505-11519.

Pieta IS, Rathi A, Pieta P, Nowakowski R, Hołdynski M, Pisarek M, Kaminska A, Gawande MB, Zboril R (2019) Electrocatalytic methanol oxidation over Cu, Ni and bimetallic Cu-Ni nanoparticles supported on graphitic carbon nitride. *Applied Catalysis B: Environmental* 244:272-283.

Priya R, Berchmans S (2012) CuO Microspheres Modified Glassy Carbon Electrodes as Sensor Materials and Fuel Cell Catalysts. *Journal of The Electrochemical Society* 159:F73.

Qi J, Xin L, Chadderdon DJ, Qiu Y, Jiang Y, Benipal N, Liang C, Li W (2014) Electrocatalytic selective oxidation of glycerol to tartronate on Au/C anode catalysts in anion exchange membrane fuel cells with electricity cogeneration. *Applied Catalysis B: Environmental* 154-155:360-368.

Qi Z (2009) APPLICATIONS–TRANSPORTATION| Light Traction: Fuel Cells.

Qian H, Huang H, Wang X (2015) Design and synthesis of palladium/graphitic carbon nitride/carbon black hybrids as high-performance catalysts for formic acid and methanol electrooxidation. *Journal of Power Sources* 275:734-741.

Qin Y-H, Li Y, Lv R-L, Wang T-L, Wang W-G, Wang C-W (2014) Pd-Au/C catalysts with different alloying degrees for ethanol oxidation in alkaline media. *Electrochimica Acta* 144:50-55.

Radi A-E, Ashour WF-D, Elshafey R (2022) Glycerol Electrocatalytic Oxidation on Nickel Hydroxide Nanoparticles/Poly-Eriochrome Black T Modified Electrode. *Electrocatalysis* 13:653-662.

Rahim MAA, Abdel Hameed RM, Khalil MW (2004) Nickel as a catalyst for the electro-oxidation of methanol in alkaline medium. *Journal of Power Sources* 134:160-169.

Rajeshkhanna G, Ranga Rao G (2018) Micro and nano-architectures of Co3O4 on Ni foam for electro-oxidation of methanol. *International Journal of Hydrogen Energy* 43:4706-4715.

Ren G, Liu Y, Wang W, Wang M, Zhou Y, Wu S, Shen J (2018) Facilitated Utilization of Active Sites with Core-Shell PdPt@Pt/RGO Nanocluster Structures for Improved Electrocatalytic Ethylene Glycol Oxidation. *ChemElectroChem* 5:2645-2652.

Rezaee S, Shahrokhian S (2019) Facile synthesis of petal-like NiCo/NiO-CoO/nanoporous carbon composite based on mixed-metallic MOFs and their application for electrocatalytic oxidation of methanol. *Applied Catalysis B: Environmental* 244:802-813.

Rizk MR, Abd El-Moghny MG (2021) Controlled galvanic decoration boosting catalysis: Enhanced glycerol electro-oxidation at Cu/Ni modified macroporous films. *International Journal of Hydrogen Energy* 46:645-655.

Ruiz-Camacho B, Medina-Ramírez A, Villicaña Aguilera M, Minchaca-Mojica JI (2019) Pt supported on mesoporous material for methanol and ethanol oxidation in alkaline medium. *International Journal of Hydrogen Energy* 44:12365-12373.

Sankar S, Watanabe N, Anilkumar GM, Nair BN, Sivakamiammal SG, Tamaki T, Yamaguchi T (2019) Electro-oxidation competency of palladium nanocatalysts over ceria–carbon composite supports during alkaline ethylene glycol oxidation. *Catalysis Science & Technology* 9:493-501.

Santos JRN, Viégas DSS, Alves ICB, Rabelo AD, Costa WM, Marques EP, Zhang L, Zhang J, Marques ALB (2019) Reduced Graphene Oxide-Supported Nickel(II)-Bis(1,10-Phenanthroline) Complex as a Highly Active Electrocatalyst for Ethanol Oxidation Reaction. *Electrocatalysis* 10:560-572.

Satyanarayana M, Rajeshkhanna G, Sahoo MK, Rao GR (2018) Electrocatalytic Activity of Pd20–xAgx Nanoparticles Embedded in Carbon Nanotubes for Methanol Oxidation in Alkaline Media. *ACS Applied Energy Materials* 1:3763-3770.

Sedighi M, Rostami AA, Alizadeh E (2017) Enhanced electro-oxidation of ethanol using Pt–CeO2 electrocatalyst prepared by electrodeposition technique. *International Journal of Hydrogen Energy* 42:4998-5005.

Shamsipur M, Najafi M, Milani Hosseini M-R (2013) Electrooxidation of alcohols at a nickel oxide/multi-walled carbon nanotube-modified glassy carbon electrode. *Journal of Applied Electrochemistry* 43:1027-1033.

Sharaf OZ, Orhan MF (2014) An overview of fuel cell technology: Fundamentals and applications. *Renewable and Sustainable Energy Reviews* 32:810-853.

Shi SQ, Che W, Liang K, Xia C, Zhang D (2015) Phase transitions of carbon-encapsulated iron oxide nanoparticles during the carbonization of cellulose at various pyrolysis temperatures. *Journal of Analytical and Applied Pyrolysis* 115:1-6.

Shi W, Wang Q, Qin F, Yu J, Jia M, Gao H, Zhang Y, Zhao Y, Li G (2017) N-doped carbon encapsulated nickel nanoparticles: rational fabrication and ultra-high performance for ethanol oxidation. *Electrochimica Acta* 232:332-338.

Shi Y-C, Feng J-J, Lin X-X, Zhang L, Yuan J, Zhang Q-L, Wang A-J (2019) One-step hydrothermal synthesis of three-dimensional nitrogen-doped reduced graphene oxide hydrogels anchored PtPd alloyed nanoparticles for ethylene glycol oxidation and hydrogen evolution reactions. *Electrochimica Acta* 293:504-513.

Shu J, Yuan J, Xie S, Yue R, Zhang R, Xu J (2022) Robust poly(3,4-ethylenedioxythiophene) granules loaded Cu/Ni-doped Pd catalysts for high-efficiency electrooxidation of ethylene glycol. *Journal of Colloid and Interface Science* 628:745-757.

Sikeyi LL, Adekunle AS, Maxakato NW (2019) Electro-catalytic Activity of Carbon Nanofibers Supported Palladium Nanoparticles for Direct Alcohol Fuel Cells in Alkaline Medium. *Electrocatalysis* 10:420-428.

Sikeyi LL, Matthews T, Adekunle AS, Maxakato NW (2020) Electro-oxidation of Ethanol and Methanol on Pd/C, Pd/CNFs and Pd−Ru/CNFs Nanocatalysts in Alkaline Direct Alcohol Fuel Cell. *Electroanalysis* 32:2681-2692.

Sikeyi LL, Ntuli TD, Mongwe TH, Maxakato NW, Carleschi E, Doyle BP, Coville NJ, Maubane-Nkadimeng MS (2021) Microwave assisted synthesis of nitrogen doped and oxygen functionalized carbon nano onions supported palladium nanoparticles as hybrid anodic electrocatalysts for direct alkaline ethanol fuel cells. *International Journal of Hydrogen Energy* 46:10862-10875.

Silva JCM, Ntais S, Rajaraman V, Teixeira-Neto É, Teixeira-Neto ÂA, Neto AO, Antoniassi RM, Spinacé EV, Baranova EA (2019) The Catalytic Activity of Pt:Ru Nanoparticles for Ethylene Glycol and Ethanol Electrooxidation in a Direct Alcohol Fuel Cell. *Electrocatalysis* 10:203-213.

Singh SB, De M (2018) Alumina based doped templated carbons: A comparative study with zeolite and silica gel templates. *Microporous and Mesoporous Materials* 257:241-252.

Singh SB, De M (2020) Thermally exfoliated graphene oxide for hydrogen storage. *Materials Chemistry and Physics* 239:122102.

Singhal SC (2000) Advances in solid oxide fuel cell technology. *Solid State Ionics* 135:305-313.

Sitta E, Nagao R, Varela H (2013) The Electro-Oxidation of Ethylene Glycol on Platinum over a Wide pH Range: Oscillations and Temperature Effects. *PLOS ONE* 8:e75086.

Sitta E, Varela H (2010) Beta Oscillations in the Electro-oxidation of Ethylene Glycol on Platinum. *Electrocatalysis* 1:19-21.

Soliman AB, Abdel-Samad HS, Abdel Rehim SS, Ahmed MA, Hassan HH (2016) High performance nano-Ni/Graphite electrode for electro-oxidation in direct alkaline ethanol fuel cells. *Journal of Power Sources* 325:653-663.

Sultan MA, Hassan HB, Tammam RH (2023) Stimulation of ethylene glycol electrooxidation on electrodeposited Ni–PbO2–GN nanocomposite in alkaline medium. *Journal of Applied Electrochemistry* 53:463-486.

Sun H, Ye Y, Liu J, Tian Z, Cai Y, Li P, Liang C (2018) Pure Ni nanocrystallines anchored on rGO present ultrahigh electrocatalytic activity and stability in methanol oxidation. *Chemical Communications* 54:1563-1566.

Sun S, Sun L, Xi S, Du Y, Anu Prathap MU, Wang Z, Zhang Q, Fisher A, Xu ZJ (2017) Electrochemical oxidation of C3 saturated alcohols on Co3O4 in alkaline. *Electrochimica Acta* 228:183-194.

Sun S, Xu ZJ (2015) Composition dependence of methanol oxidation activity in nickel–cobalt hydroxides and oxides: an optimization toward highly active electrodes. *Electrochimica Acta* 165:56-66.

Sun S, Zhou Y, Hu B-L, Zhang Q, Xu Z (2015) Ethylene Glycol and Ethanol Oxidation on Spinel Ni-Co Oxides in Alkaline. *Journal of The Electrochemical Society* 163:H99-H104.

Suzuki NY, Santiago PVB, Galhardo TS, Carvalho WA, Souza-Garcia J, Angelucci CA (2016) Insights of glycerol electrooxidation on polycrystalline silver electrode. *Journal of Electroanalytical Chemistry* 780:391-395.

Tammam RH, Fekry AM, Saleh MM (2015) Electrocatalytic oxidation of methanol on ordered binary catalyst of manganese and nickel oxide nanoparticles. *International Journal of Hydrogen Energy* 40:275-283.

Tan JL, De Jesus AM, Chua SL, Sanetuntikul J, Shanmugam S, Tongol BJV, Kim H (2017) Preparation and characterization of palladium-nickel on graphene oxide support as anode catalyst for alkaline direct ethanol fuel cell. *Applied Catalysis A: General* 531:29-35.

Tarrús X, Montiel M, Vallés E, Gómez E (2014) Electrocatalytic oxidation of methanol on CoNi electrodeposited materials. *International Journal of Hydrogen Energy* 39:6705-6713.

Thamer BM, El-Newehy MH, Barakat NAM, Al-Deyab SS, Kim HY (2017) Preparation of zero-valent Co/N-CNFs as an immobilized thin film onto graphite disc for methanol electrooxidation. *Fibers and Polymers* 18:696-705.

*The Fuel Cell Industry Review*, E4Tech, 2016

Tian M-H, Yang Y, Desmond C, Liu F, Zhu Z-Q, Li Q-X (2020) Pt-Surface-Enriched Platinum–Tungsten Bimetallic Nanoparticles Catalysts on Different Carbon Supports for Electro-Oxidation of Ethanol. *Catalysis Letters* 150:3386-3393.

Tran G-S, Vo T-G, Chiang C-Y (2021) Earth-abundant manganese oxide nanoneedle as highly efficient electrocatalyst for selective glycerol electro-oxidation to dihydroxyacetone. *Journal of Catalysis* 404:139-148.

Tromans D, Ahmed T (1998) Active/Passive Behavior of Copper in Strong Sulfuric Acid. *Journal of The Electrochemical Society* 145:601.

Ullah N, Xie M, Oluigbo CJ, Xu Y, Xie J, Rasheed HU, Zhang M (2019) Nickel and cobalt in situ grown in 3-dimensional hierarchical porous graphene for effective methanol electro-oxidation reaction. *Journal of Electroanalytical Chemistry* 838:7-15.

Varkaraki E, Lymberopoulos N, Zachariou A (2003) Hydrogen based emergency back-up system for telecommunication applications. *Journal of Power Sources* 118:14-22.

Velázquez-Hernández I, Álvarez-López A, Álvarez-Contreras L, Guerra-Balcázar M, Arjona N (2021) Electrocatalytic oxidation of crude glycerol from the biodiesel production on Pd-M (M = Ir, Ru or Pt) sub-10 nm nanomaterials. *Applied Surface Science* 545:149055.

Velázquez-Hernández I, Torres-Pacheco L, Álvarez-López A, Álvarez-Contreras L, Guerra-Balcázar M, Arjona N (2022) Sustainable energy conversion of crude glycerol as biofuel employing PdBi nanomaterials. *Applied Surface Science* 602:154385.

Vulcu A, Radu T, Porav AS, Berghian-Grosan C (2021) Low-platinum catalyst based on sulfur doped graphene for methanol oxidation in alkaline media. *Materials Today Energy* 19:100588.

Wang C, Bukhvalov D, Goh MC, Du Y, Yang X (2022a) Hierarchical AgAu alloy nanostructures for highly efficient electrocatalytic ethanol oxidation. *Chinese Journal of Catalysis* 43:851-861.

Wang C, Wu C, Xing L, Duan W, Zhang X, Cao Y, Xia H (2020a) Facet-Dependent Long-Term Stability of Gold Aerogels toward Ethylene Glycol Oxidation Reaction. *ACS Applied Materials & Interfaces* 12:39033-39042.

Wang H, Ding J, Kannan P, Subramanian P, Ji S (2020b) Nitrogen-doped mesoporous carbon nanosheet network entrapped nickel nanoparticles as an efficient catalyst for electro-oxidation of glycerol. *International Journal of Hydrogen Energy* 45:28821-28835.

Wang H, Guan A, Zhang J, Mi Y, Li S, Yuan T, Jing C, Zhang L, Zhang L, Zheng G (2022b) Copper-doped nickel oxyhydroxide for efficient electrocatalytic ethanol oxidation. *Chinese Journal of Catalysis* 43:1478-1484.

Wang H, Thia L, Li N, Ge X, Liu Z, Wang X (2015) Selective electro-oxidation of glycerol over Au supported on extended poly(4-vinylpyridine) functionalized graphene. *Applied Catalysis B: Environmental* 166-167:25-31.

Wang W, Jing W, Liu Y, Wang Y, Zhao J, Lei Z (2018) Supporting Pd nanoparticles on riboflavin-derived carbon: an efficient electrocatalyst for ethylene glycol oxidation. *Ionics* 24:1745-1754.

Wang X-Y, Han Z, Duan J-J, Feng J-J, Huang H, Wang A-J (2020c) Facile construction of 3D hyperbranched PtRh nanoassemblies: A bifunctional electrocatalyst for hydrogen evolution and polyhydric alcohol oxidation reactions. *International Journal of Hydrogen Energy* 45:8433-8443.

*World Energy Resources*, World Energy Council, 2016.

Xia D, Jeong H, Hou D, Tao L, Li T, Knight K, Hu A, Kamphaus EP, Nordlund D, Sainio S, Liu Y, Morris JR, Xu W, Huang H, Li L, Xiong H, Cheng L, Lin F (2024) Self-terminating, heterogeneous solid-electrolyte interphase enables reversible Li-ether cointercalation in graphite anodes. *Proc Natl Acad Sci U S A* 121:e2313096121.

Xie S, Deng L, Huang H, Yuan J, Xu J, Yue R (2022a) One-pot synthesis of porous Pd-polypyrrole/nitrogen-doped graphene nanocomposite as highly efficient catalyst for electrooxidation of alcohols. *Journal of Colloid and Interface Science* 608:3130-3140.

Xie S, Huang H, Deng L, Li J, Yue R, Xu J (2022b) Crinkly Polypyrrole-Modified reduced graphene oxide loaded Pd nanoparticles as Highly efficient electrocatalyst for ethylene glycol oxidation. *Applied Surface Science* 598:153879.

Xin L, Zhang Z, Qi J, Chadderdon D, Li W (2012) Electrocatalytic oxidation of ethylene glycol (EG) on supported Pt and Au catalysts in alkaline media: Reaction pathway investigation in three-electrode cell and fuel cell reactors. *Applied Catalysis B: Environmental* 125:85-94.

Xu H, Song P, Fernandez C, Wang J, Zhu M, Shiraishi Y, Du Y (2018a) Sophisticated Construction of Binary PdPb Alloy Nanocubes as Robust Electrocatalysts toward Ethylene Glycol and Glycerol Oxidation. *ACS Applied Materials & Interfaces* 10:12659-12665.

Xu H, Yan B, Wang J, Zhang K, Li S, Xiong Z, Wang C, Shiraishi Y, Du Y, Yang P (2017a) Self-supported porous 2D AuCu triangular nanoprisms as model electrocatalysts for ethylene glycol and glycerol oxidation. *Journal of Materials Chemistry A* 5:15932-15939.

Xu H, Yan B, Yang J, Li S, Wang J, Du Y, Ren F (2018b) Exceptional ethylene glycol electrooxidation activity enabled by sub-16 nm dendritic Pt–Cu nanocrystals catalysts. *International Journal of Hydrogen Energy* 43:1489-1496.

Xu H, Yan B, Zhang K, Wang J, Li S, Wang C, Shiraishi Y, Du Y, Yang P (2017b) Ultrasonic-assisted synthesis of N-doped graphene-supported binary PdAu nanoflowers for enhanced electro-oxidation of ethylene glycol and glycerol. *Electrochimica Acta* 245:227-236.

Xu M, Lei S, Jin C (2021) Titanium dioxide as support material for Pt1Pd3 toward methanol oxidation. *International Journal of Hydrogen Energy* 46:5390-5397.

Xu X, Wang X, Huo S, Chen Z, Zhao H, Xu J (2018c) Facile synthesis of PdIr nanoporous aggregates as highly active electrocatalyst towards methanol and ethylene glycol oxidation. *Catalysis Today* 318:157-166.

Yang F, Cheng K, Ye K, Xiao X, Guo F, Yin J, Wang G, Cao D (2013) Electrocatalytic properties of carbon fiber cloth-supported flower-like Au nanostructures towards ethanol electrooxidation. *Electrochimica Acta* 114:478-483.

Yang H, Geng L, Zhang Y, Chang G, Zhang Z, Liu X, Lei M, He Y (2019) Graphene-templated synthesis of palladium nanoplates as novel electrocatalyst for direct methanol fuel cell. *Applied Surface Science* 466:385-392.

Yang J-M, Wang S-A, Sun C-L, Ger M-D (2014) Synthesis of size-selected Pt nanoparticles supported on sulfonated graphene with polyvinyl alcohol for methanol oxidation in alkaline solutions. *Journal of Power Sources* 254:298-305.

Yang Y, Wang W, Liu Y, Wang F, Chai D, Lei Z (2015a) Pd nanoparticles supported on phenanthroline modified carbon as high active electrocatalyst for ethylene glycol oxidation. *Electrochimica Acta* 154:1-8.

Yang Y, Wang W, Liu Y, Wang F, Zhang Z, Lei Z (2015b) Carbon supported heterostructured Pd–Ag nanoparticle: Highly active electrocatalyst for ethylene glycol oxidation. *International Journal of Hydrogen Energy* 40:2225-2230.

Yang Z-Z, Lin X-X, Zhang X-F, Wang A-J, Zhu X-Y, Feng J-J (2018) Bimetallic PtPd alloyed core-shell nanodendrites supported on reduced graphene oxide: One-pot green synthesis and efficient

electrocatalytic performances for glycerol oxidation and hydrogen evolution. *Journal of Alloys and Compounds* 735:2123-2132.

Yang Z-Z, Liu L, Wang A-J, Yuan J, Feng J-J, Xu Q-Q (2017) Simple wet-chemical strategy for large-scaled synthesis of snowflake-like PdAu alloy nanostructures as effective electrocatalysts of ethanol and ethylene glycol oxidation. *International Journal of Hydrogen Energy* 42:2034-2044.

Yao W, Jiang X, Li M, Li Y, Liu Y, Zhan X, Fu G, Tang Y (2021) Engineering hollow porous platinum-silver double-shelled nanocages for efficient electro-oxidation of methanol. *Applied Catalysis B: Environmental* 282:119595.

Yaqoob L, Noor T, Iqbal N, Nasir H, Mumtaz A (2021) Electrocatalytic performance of NiNH2BDC MOF based composites with rGO for methanol oxidation reaction. *Scientific Reports* 11:13402.

Yoo S, Cho S, Kim D, Ih S, Lee S, Zhang L, Li H, Lee JY, Liu L, Park S (2019) 3D PtAu nanoframe superstructure as a high-performance carbon-free electrocatalyst. *Nanoscale* 11:2840-2847.

Yu L, Zhang L, Zhang X, Dai G, Zhang J, Wang X, You H (2020) Hollow AuAg Alloy Nanourchins: Twin Plane and Surface Treatment for Enhanced Methanol Electrooxidation Performance. *ACS Applied Energy Materials* 3:723-732.

Yu Y, Zhai M, Hu J (2019) Electrocatalytic oxidation of ethanol and ethylene glycol on bimetallic Ni and Ti nanoparticle-modified indium tin oxide electrode in alkaline solution. *Progress in Natural Science: Materials International* 29:511-516.

Yu Z-N, Zhang Z, Lv Z-S, Liu M-T, Zhang L, Wang A-J, Jiang L-Y, Feng J-J (2018) Platinum69-cobalt31 alloyed nanosheet nanoassemblies as advanced bifunctional electrocatalysts for boosting ethylene glycol oxidation and oxygen reduction. *Journal of Colloid and Interface Science* 525:216-224.

Zafeiratos S, Dintzer T, Teschner D, Blume R, Hävecker M, Knop-Gericke A, Schlögl R (2010) Methanol oxidation over model cobalt catalysts: Influence of the cobalt oxidation state on the reactivity. *Journal of Catalysis* 269:309-317.

Zaher A, El Rouby WMA, Barakat NAM (2020) Tungsten incorporation in nickel doped carbon nanofibers as efficient electrocatalyst for ethanol oxidation. *Fuel* 280:118654.

Zalineeva A, Serov A, Padilla M, Martinez U, Artyushkova K, Baranton S, Coutanceau C, Atanassov PB (2015) Glycerol electrooxidation on self-supported Pd1Snx nanoparticules. *Applied Catalysis B: Environmental* 176-177:429-435.

Zhai C, Hu J, Zeng L, Fu N, Du Y, Zhu M (2019) One-pot fabrication of Nitrogen-doped graphene supported binary palladium-sliver nanocapsules enable efficient ethylene glycol electrocatalysis. *Journal of Colloid and Interface Science* 535:392-399.

Zhang D, Zhang L, Zhang W, Huo M, Yin J, Dang G, Ren Z, Zhang Q, Xie J, Mao SS (2017a) Morphology-dependent electrocatalytic performance of Fe2(MoO4)3 for electro-oxidation of methanol in alkaline medium. *Journal of Materiomics* 3:135-143.

Zhang J-h, Zhu T, Liang Y-j, Zhang C-j, Shi S-t, Xu C-w (2016) CeO2 promoted Au/C catalyst for glycerol electro-oxidation in alkaline medium. *Journal of the Energy Institute* 89:325-329.

Zhang J-M, Sun S-N, Li Y, Zhang X-J, Zhang P-Y, Fan Y-J (2017b) A strategy in deep eutectic solvents for carbon nanotube-supported PtCo nanocatalysts with enhanced performance toward methanol electrooxidation. *International Journal of Hydrogen Energy* 42:26744-26751.

Zhang J, Qu X, Han Y, Shen L, Yin S, Li G, Jiang Y, Sun S (2020a) Engineering PtRu bimetallic nanoparticles with adjustable alloying degree for methanol electrooxidation: Enhanced catalytic performance. *Applied Catalysis B: Environmental* 263:118345.

Zhang J, Shen Y (2021) Electro-Oxidation of Glycerol into Formic Acid by Nickel-Copper Electrocatalysts. *Journal of The Electrochemical Society* 168.

Zhang K, Xu H, Yan B, Wang J, Du Y, Liu Q (2018a) Superior ethylene glycol oxidation electrocatalysis enabled by hollow PdNi nanospheres. *Electrochimica Acta* 268:383-391.

Zhang L, Tu L-y, Liang Y, Chen Q, Li Z-s, Li C-h, Wang Z-h, Li W (2018b) Coconut-based activated carbon fibers for efficient adsorption of various organic dyes. *RSC Advances* 8:42280-42291.

Zhang Q, Chen T, Jiang R, Jiang F (2020b) Comparison of electrocatalytic activity of Pt1−xPdx/C catalysts for ethanol electro-oxidation in acidic and alkaline media. *RSC Advances* 10:10134-10143.

Zhang W, Huang H, Li F, Deng K, Wang X (2014a) Palladium nanoparticles supported on graphitic carbon nitride-modified reduced graphene oxide as highly efficient catalysts for formic acid and methanol electrooxidation. *Journal of Materials Chemistry A* 2:19084-19094.

Zhang Y, Chang G, Shu H, Oyama M, Liu X, He Y (2014b) Synthesis of Pt–Pd bimetallic nanoparticles anchored on graphene for highly active methanol electro-oxidation. *Journal of Power Sources* 262:279-285.

Zhang Z, Xin L, Qi J, Chadderdon DJ, Li W (2013) Supported Pt, Pd and Au nanoparticle anode catalysts for anion-exchange membrane fuel cells with glycerol and crude glycerol fuels. *Applied Catalysis B: Environmental* 136-137:29-39.

Zheng J-N, Li S-S, Chen F-Y, Bao N, Wang A-J, Chen J-R, Feng J-J (2014) Facile synthesis of platinum–ruthenium nanodendrites supported on reduced graphene oxide with enhanced electrocatalytic properties. *Journal of Power Sources* 266:259-267.

Zheng Y, Chen F, Liu X, Guo X, Ying Y, Wu Y, Wen Y, Yang H (2020) Rational design of PdRu/TiO2 composite material for advancing electrochemical catalysis of methanol oxidation. *Journal of Power Sources* 472:228517.

Zhiani M, Majidi S, Rostami H, Taghiabadi MM (2015) Comparative study of aliphatic alcohols electrooxidation on zero-valent palladium complex for direct alcohol fuel cells. *International Journal of Hydrogen Energy* 40:568-576.

Zhou W, Li M, Zhang L, Chan SH (2014) Supported PtAu catalysts with different nano-structures for ethanol electrooxidation. *Electrochimica Acta* 123:233-239.

Zhu H, Wang J, Liu X, Zhu X (2017) Three-dimensional porous graphene supported Ni nanoparticles with enhanced catalytic performance for Methanol electrooxidation. *International Journal of Hydrogen Energy* 42:11206-11214.

Zhu X-Y, Zhang L, Yuan P-X, Feng J-J, Yuan J, Zhang Q-L, Wang A-J (2018) Hollow Ag44Pt56 nanotube bundles with high electrocatalytic performances for hydrogen evolution and ethylene glycol oxidation reactions. *Journal of Colloid and Interface Science* 532:571-578.

Zou B, Zhang Y, Gao F, Li Z, Wang C, Wu Z, Wang D, Du Y (2022) 3D PdPb nanochain networks with efficient catalytic performance for ethylene glycol electrooxidation. *International Journal of Hydrogen Energy* 47:33329-33337.

# Appendices

**Appendix A: Temperature programmed reduction profiles of metal salt impregnated on carbon**

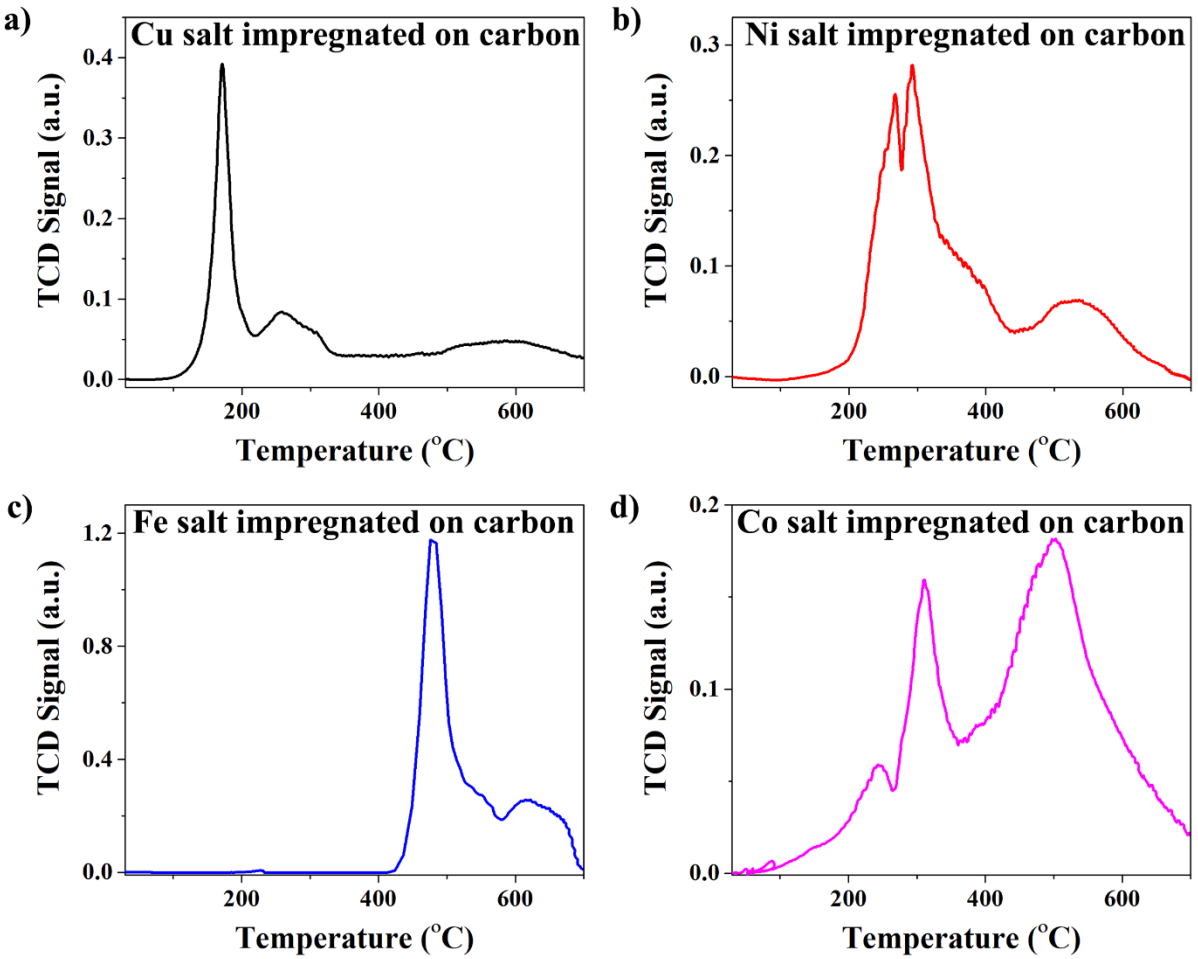


**Figure A1: Temperature programmed reduction profiles of different metal salt impregnated on carbon**

Temperature programmed reduction (TPR) was done using Chemisorb 2720 (Micromeritics). The required amount of samples was kept in quartz tube, degassed at 150°C for 2 h with the flow of He gas. Then the sample was heated from room temperature to 700°C at 10°C/min heating rate with a desired carrier gas. Based on the TPR data, different metal catalyst was reduced.

**Appendix B: Sample calculations for determining crystallite size from XRD**

The 20Cu-AC sample for crystallite size ($D_c$) is shown below (section 4.2.1). The metal dispersion was calculated using the following formulae described in the experimental section 3.5.1:

$$D_C = \frac{K\lambda}{\beta\cos\theta} \qquad \text{(A1)}$$

Where K is the dimensionless shape factor, λ is the wavelength, β is the full width half maxima of the peak and θ is the Bragg's angle.

For, 20Cu-AC, K was considered as 0.9, λ = 0.154 nm, β = 0.0086 rad and θ = 21.78°

Therefore, Dc for 20Cu-AC is

$$D_C = \frac{0.9 \times 0.154}{0.0086 \times \cos(21.78)} = 18.2 \text{ nm}$$

**Appendix C: Sample calculations for determining metal dispersion from FETEM images**

The 20Cu-AC sample for metal dispersion is shown below (section 4.2.1). The metal dispersion was calculated using the following formulae described in the experimental section 3.5.1:

$$D_{TEM} = \frac{C}{d} \qquad (A2)$$

where, d = mean diameter of metal particles (m) calculated from FETEM images.
For, 20Cu-AC d = 7.8 nm obtained from FETEM image (Figure 4.5i) and

$$C = \frac{6 \times M}{N \times \rho \times \delta} \qquad (A3)$$

where, M = atomic weight of the metal, N = Avagadro's no, ρ = density of different metals ($g/m^3$), and δ = cross-sectional area of different metal atoms ($m^2$).

For Cu, M = 63.456 g/mol, $\rho = 8.96 \times 10^6$ $g/m^3$, $\delta = 5.72 \times 10^{-20}$ $m^2$ and $N = 6.022 \times 10^{23}$.

Hence, the constant C for Cu metal is

$$C = \frac{6 \times 63.456}{6.022 \times 10^{23} \times 8.96 \times 10^6 \times 6.60 \times 10^{-20}} = 1.23 \text{ nm}$$

Therefore, $D_{TEM}$ for 20Cu-AC is

$$D_{TEM} = \frac{1.23}{7.8} = 0.16$$

**Appendix D: Sample calculations for determining work function from KPFM images**

The 20Cu-AC sample for work function is shown below (section 4.2.1). The mean CPD obtained from KPFM image (Figure 4.8) was 0.345 V. The work function was calculated using the following formulae described in the experimental section 3.5.1:

$$CPD = \frac{(\phi_{tip} - \phi_{sample})}{e} \qquad (A4)$$

where, $\phi_{tip}$ and $\phi_{sample}$ were work function of the tip and sample respectively.

Here, $\phi_{tip}$ = 4.76 eV (for the Pt/Ir tip used).

Hence, the work function of 20Cu-AC is

$$\phi_{sample} = 4.76 - 0.345 = 4.415 \text{ eV}$$

**Appendix E: Sample calculations for determining ECSA and RF**

The 20Cu-AC sample for ECSA and RF is shown below (section 4.2.2). The double layer capacitance ($C_{dl}$) was obtained from the relationship between current density and scan rates (Figure 4.11. The $C_{dl}$ for 20Cu-AC was 1.4 mF. The ECSA was calculated using the following formulae described in the experimental section 3.5.2:

$$\text{ECSA } (cm^2) = \frac{C_{dl}}{c_s} \qquad \text{(A5)}$$

where, $C_{dl}$ is double layer capacitance and is defined as the slope between current and scan rate for different electrocatalysts, $c_s$ is the specific charge density and is taken as 0.04 mF/cm2 for all the catalysts

For 20Cu-AC, $C_{dl}$ = 1.4 mF and $c_s$ = 0.04 mF/cm$^2$.

Hence, the ECSA for 20Cu-AC is

$$\text{ECSA} = \frac{1.4}{0.04} = 35 \text{ cm}^2$$

The RF was calculated using the formulae described in experimental section 3.5.2:

$$\text{RF} = \frac{\text{ECSA } (cm^2)}{\text{SA } (cm^2)} \qquad \text{(A6)}$$

where, SA is geometrical cross-sectional area of the electrode. Here SA = 0.196 cm$^2$.

Therefore, RF for 20Cu-AC is

$$\text{RF} = \frac{35}{0.196} = 178.6$$

**Appendix F: Zoomed view of the EIS of different supported copper catalyst.**

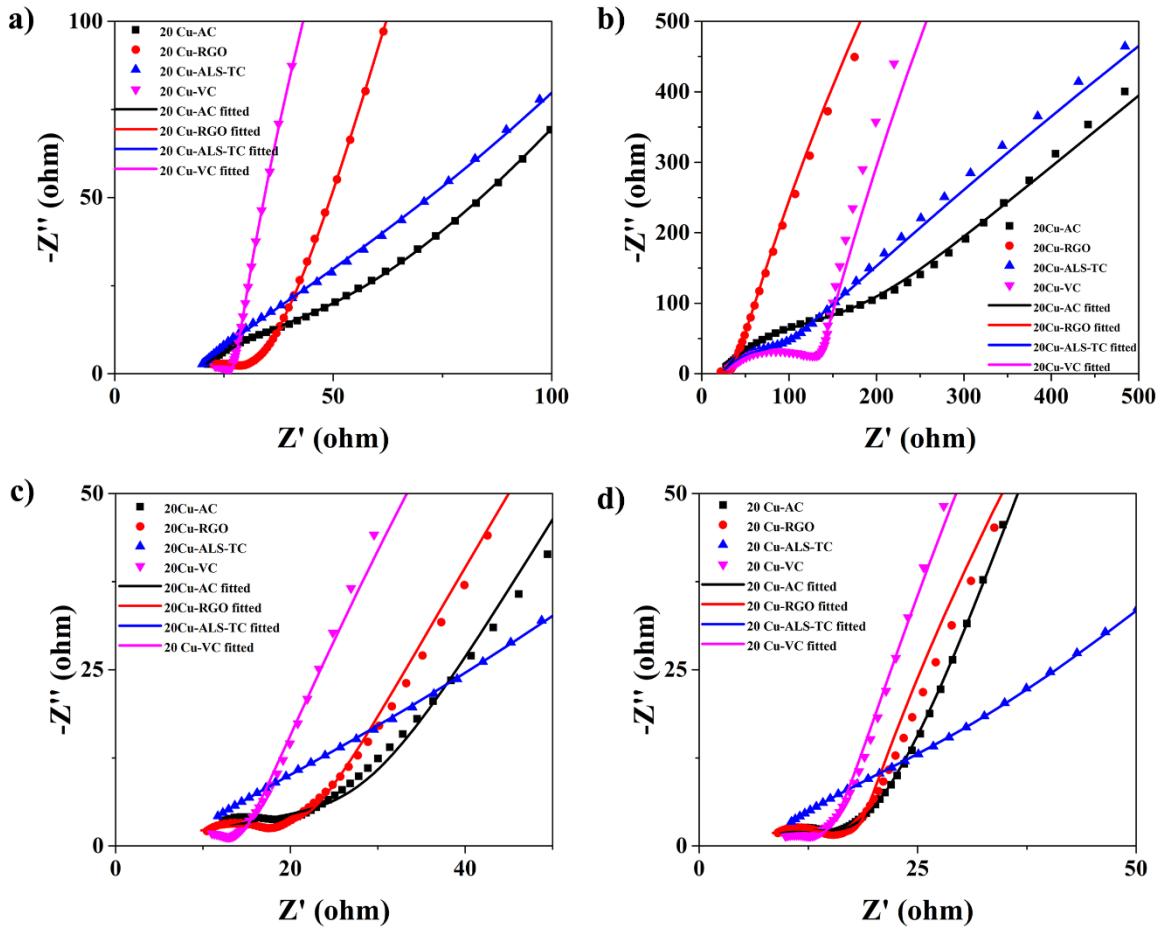


**Figure F1: Zoomed view of electrochemical impedance spectra of different supported copper catalysts in a, b) without EG and c, d) with 0.5 M EG in 0.1 M $H_2SO_4$ and 0.1 M KOH respectively and e) corresponding equivalent circuit diagram.**

**Appendix G: Sample calculations for determining charge transfer coefficient using Butler-Volmer equation**

The sample calculation for charge transfer coefficient is shown for 20Cu-RGO (section 4.3.2.2). The calculation was done using Butler-Volmer equation described in the experimental section 3.5.2 and from Tafel slope (Figure 4.31c).

$$\text{Log } i = \text{Log } i_0 + \alpha nF\eta/2.303RT \qquad \text{(A7)}$$

where, $i_o$ is the exchange current density, R is the universal gas constant, F is Faraday constant, T is temperature in K, η is overpotential, α is charge transfer coefficient and n is the number of electrons transferred.

Here, F = 96485.33 A.s/mol, n = 1, R = 8.314 J/mol.K and T = 298.15 K

For 20Cu-RGO in 0.1 M KOH, Tafel slope = 266 mV/dec

Therefore, charge transfer coefficient (α) for 20Cu-RGO is

$$\alpha = \frac{2.303 \times 8.314 \times 298.15}{96485.33 \times 0.266} = 0.22$$

**Appendix H: Sample calculations for determining surface coverage of redox species.**

The surface coverage of redox species was calculated for 30Ni-RGO (section 4.3.2). This was done using equation described in the experimental section 3.5.2.

$$I_P = \frac{n^2F^2}{4RT}\nu A\Gamma^* \qquad (A8)$$

where, $I_P$ is peak current, ν is scan rate, A is electrode area, R is the universal gas constant, F is Faraday constant, T is temperature and Γ* is surface coverage of redox species

Here, n = 1, F = 96485.33 A.s/mol, n = 1, R = 8.314 J/mol.K and T =298.15 K

For 30Ni-RGO, the slope between $I_p$ vs ν (Figure 4.37a) = 0.0254.

Hence, the surface coverage of redox species (Γ*) for 30Ni-RGO is

$$\Gamma^* = \frac{0.0254 \times 4 \times 8.314 \times 298.15}{1^2 \times 96485.33^2} = 2.71 \times 10^{-8}\ \text{mol/cm}^2$$

**Appendix I: Sample calculations for determining diffusion coefficient of ethylene glycol molecules.**

The diffusion coefficient of ethylene glycol molecules was calculated for 30Ni-RGO (section 4.3.2). This was done using Randels-Sevcik equation described in the experimental section 3.5.2.

$$I_P = 2.69 \times 10^5 \, n^{3/2} A D_0^{1/2} \nu^{1/2} C_0 \qquad (A9)$$

where, $I_P$ is peak current, ν is scan rate, A is electrode area, $C_0$ is the concentration, n is the number of electron tansfered and $D_0$ is the diffusion coefficient.

Here, $C_0 = 0.5 \times 10^{-3}$ $m^3$ and n will vary from 1 to 10

For 30Ni-RGO in 0.1 M KOH and 0.5 M EG, slope of $I_p$ vs ν (Figure 4.37a) = 0.653.

When n = 1, then the diffusion coefficient of ethylene glycol ($D_0$) molecules is

$$D_0 = \left(\frac{0.653}{2.69 \times 10^5 \times 1^{3/2} \times 0.5 \times 10^{-3}}\right)^2 = 2.35 \times 10^{-5} \text{ cm}^2/\text{s}$$

**Appendix J: Sample calculations for determining electrocatalytic rate constant for ethylene glycol oxidation.**

The electrocatalytic rate constant for ethylene glycol oxidation was calculated for 30Ni-RGO (section 4.3.2). This was done using Cottrell equation described in the experimental section 3.5.2. Dual chronoamperogram (Figure 4.38d) was also used to calculate the electrocatalytic rate constant.

$$\frac{I_{cat}}{I_L} = \pi^{1/2}(k_{cat}C \times t)^{1/2} \qquad (A10)$$

where, $I_{cat}$ and $I_L$ is the current in presence and absence of ethylene glycol, $k_{cat}$ is the electrocatalytic rate constant, C is the concentration of EG and t is the elapsed time.

Here the slope of $I_{cat}/I_L$ vs $t^{1/2}$ for ethylene glycol concentration of 0.1 M is 2.272

Therefore, the electrocatalytic rate constant for ethylene glycol oxidation by 30Ni-RGO is

$$k_{cat} = \left(\frac{2.272}{(3.14 \times 0.1 \times 10^{-3})^{1/2}}\right)^2 = 1.64 \times 10^4 \text{ cm}^3/\text{mol.s}$$

**Appendix K: Zoomed view of the EIS of RGO supported bimetallic catalyst.**

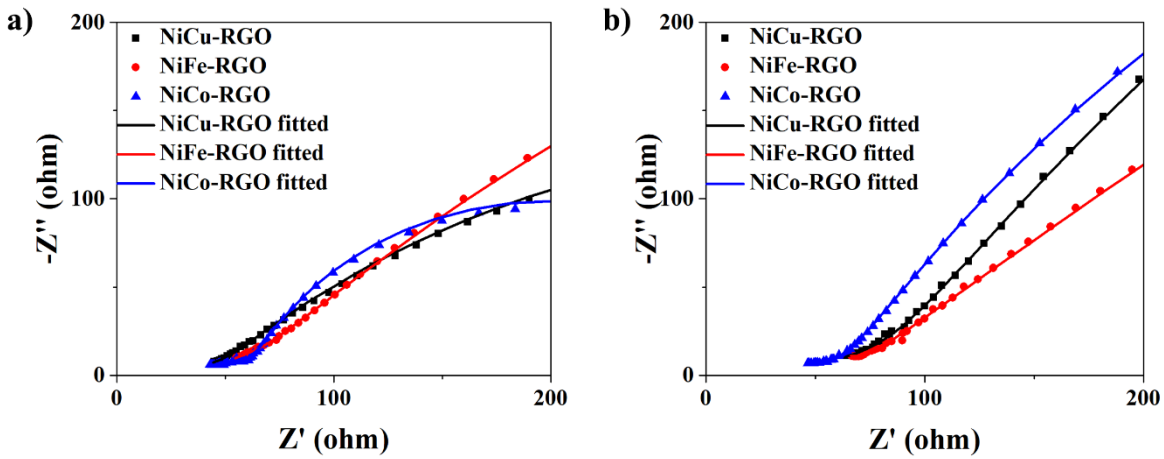


**Figure K1: Zoomed view of EIS for bimetallic catalysts in a) 0.1 M KOH, b) 0.5 M EG and 0.1 M KOH and c) equivalent circuit diagram.**